ADVANCES IN ASPHALT EMULSION MATERIALS FOR COLD PAVING TECHNOLOGIES

EDITED BY: Jian Ouyang, Yiqiu Tan and Dae-Wook Park
PUBLISHED IN: Frontiers in Materials

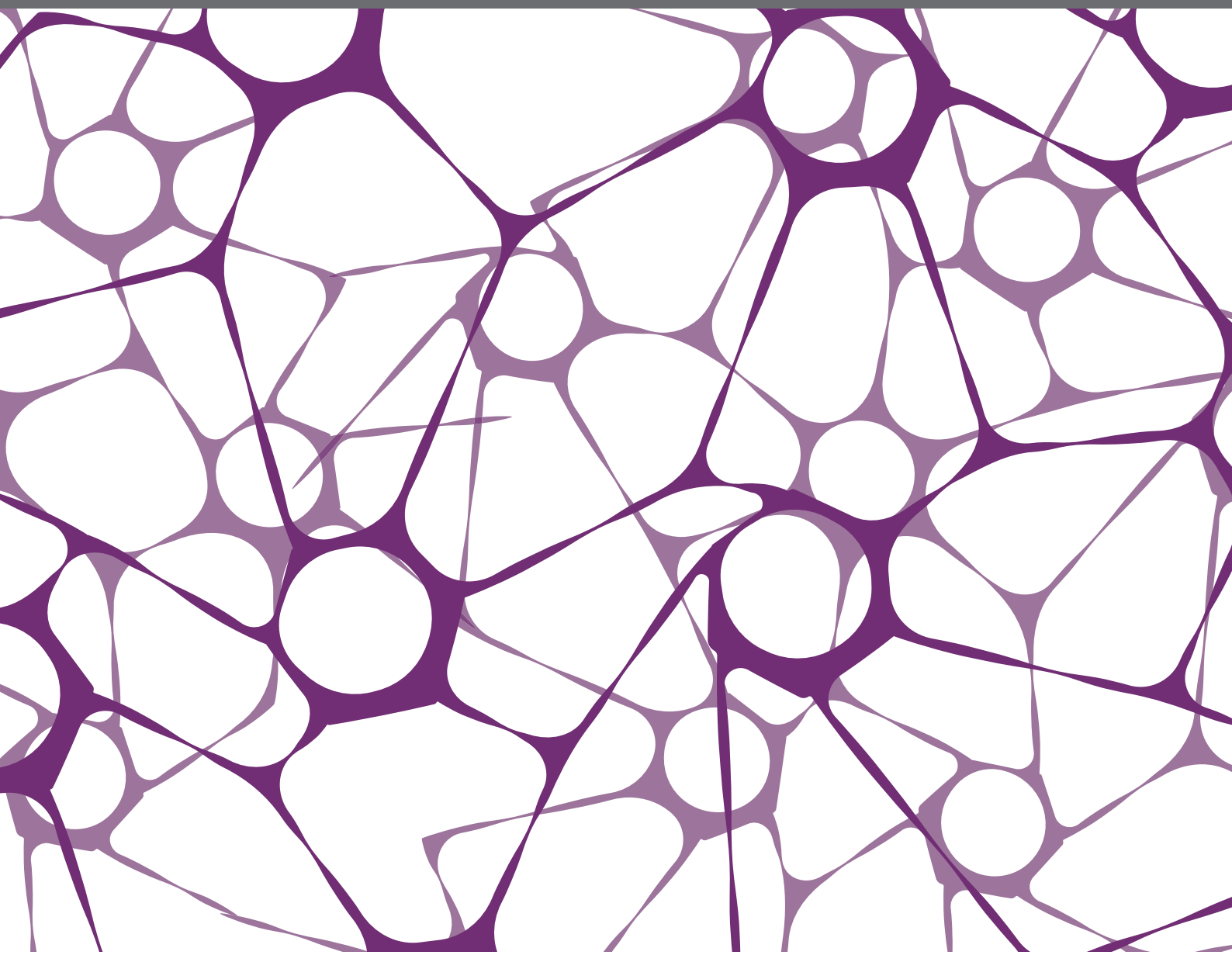

frontiers Research Topics

frontiers

ISSN 1664-8714
ISBN 978-2-88966-248-7
DOI 10.3389/978-2-88966-248-7

About Frontiers

Frontiers is more than just an open-access publisher of scholarly articles: it is a pioneering approach to the world of academia, radically improving the way scholarly research is managed. The grand vision of Frontiers is a world where all people have an equal opportunity to seek, share and generate knowledge. Frontiers provides immediate and permanent online open access to all its publications, but this alone is not enough to realize our grand goals.

Frontiers Journal Series

The Frontiers Journal Series is a multi-tier and interdisciplinary set of open-access, online journals, promising a paradigm shift from the current review, selection and dissemination processes in academic publishing. All Frontiers journals are driven by researchers for researchers; therefore, they constitute a service to the scholarly community. At the same time, the Frontiers Journal Series operates on a revolutionary invention, the tiered publishing system, initially addressing specific communities of scholars, and gradually climbing up to broader public understanding, thus serving the interests of the lay society, too.

Dedication to Quality

Each Frontiers article is a landmark of the highest quality, thanks to genuinely collaborative interactions between authors and review editors, who include some of the world's best academicians. Research must be certified by peers before entering a stream of knowledge that may eventually reach the public - and shape society; therefore, Frontiers only applies the most rigorous and unbiased reviews.
Frontiers revolutionizes research publishing by freely delivering the most outstanding research, evaluated with no bias from both the academic and social point of view. By applying the most advanced information technologies, Frontiers is catapulting scholarly publishing into a new generation.

What are Frontiers Research Topics?

Frontiers Research Topics are very popular trademarks of the Frontiers Journals Series: they are collections of at least ten articles, all centered on a particular subject. With their unique mix of varied contributions from Original Research to Review Articles, Frontiers Research Topics unify the most influential researchers, the latest key findings and historical advances in a hot research area! Find out more on how to host your own Frontiers Research Topic or contribute to one as an author by contacting the Frontiers Editorial Office: researchtopics@frontiersin.org

ADVANCES IN ASPHALT EMULSION MATERIALS FOR COLD PAVING TECHNOLOGIES

Topic Editors:
Jian Ouyang, Dalian University of Technology, China
Yiqiu Tan, Harbin Institute of Technology, China
Dae-Wook Park, Kunsan National University, South Korea

Citation: Ouyang, J., Tan, Y., Park, D.-W., eds. (2020). Advances in Asphalt Emulsion Materials for Cold Paving Technologies. Lausanne: Frontiers Media SA. doi: 10.3389/978-2-88966-248-7

Table of Contents

frontiers in Materials

ORIGINAL RESEARCH
published: 30 January 2020
doi: 10.3389/fmats.2020.00001

Influence of Emulsifier on Surface Mass Transfer Based on Molecular Dynamics Simulations

Lingyun Kong[1], Wanli Luo[2], Biao Feng[2] and Xiujie Quan[2]*

[1] National and Local Joint Engineering Laboratory of Traffic Civil Engineering Materials, Chongqing Jiaotong University, Chongqing, China, [2] School of Civil Engineering, Chongqing Jiaotong University, Chongqing, China

To explore the effect of emulsifier structure on mass transfer performance, and provide theoretical basis and ideas for the structure design of new asphalt emulsifier. The mass transfer process of the anionic surfactant sodium dodecyl benzene sulfonate (SDBS) and its four isomers on the solid surface of calcium carbonate, as well as the resulting main chemical component of its aggregates, were studied using molecular dynamics (MD) simulations. It was found that the SDBS and its isomers can be adsorbed on the calcium carbonate surface over a relatively short time and gradually form an aggregate structure during the mass transfer process. In this process, Na ions have no obvious aggregation behavior in the polar head of the emulsifier. The calculated interfacial interaction energy indicates that the adsorption performance and aggregation on the calcium carbonate surface are related to the degree of branching and steric hindrance of the emulsifier molecule. Both the lipophilic group and the hydrophilic group in the emulsifier promote its diffusion into the solution. The results show that molecular dynamics (MD) simulations can be used to supplement experiments to provide the necessary microscopic information and theoretical basis for further experimentation.

Keywords: solid–liquid interface, mass transfer, molecular dynamics simulation, anionic asphalt emulsifier, road engineering

OPEN ACCESS

Edited by:
Jian Ouyang,
Dalian University of Technology (DUT), China

Reviewed by:
Pengfei Liu,
RWTH Aachen University, Germany
Baoguo Han,
Dalian University of Technology (DUT), China

****Correspondence:***
Lingyun Kong
43112443@qq.com

Specialty section:
This article was submitted to Structural Materials, a section of the journal Frontiers in Materials

Received: *02 December 2019*
Accepted: *03 January 2020*
Published: *30 January 2020*

Citation:
Kong L, Luo W, Feng B and Quan X (2020) Influence of Emulsifier on Surface Mass Transfer Based on Molecular Dynamics Simulations. Front. Mater. 7:1. doi: 10.3389/fmats.2020.00001

INTRODUCTION

It is of great importance to find a method for road construction that is environmentally friendly, resource-saving, and convenient in light of the increasingly significant environmental problems and diversification of construction in China. Traditional road asphalt pavement construction requires the asphalt to be heated to 160–170°C, the mineral materials to 170–180°C, and the mix asphalt mixture to 150–160°C. There are corresponding temperature requirements for the transportation, paving, and compaction of a mixture, especially when the mixture meets water, which makes paving roads difficult (Lissant, 1975). Moreover, the heating process of asphalt during road construction is time-consuming and produces harmful substances that cause serious pollution to the environment. Further, the organic solvents used to dilute asphalt volatilize into the air after road construction, which also pose a serious threat to environmental safety and endanger the health of construction workers (Jerzy and Bengt, 1990). Through long-term research and practice, researchers have shown that the development of emulsified asphalt is one of the most effective ways to solve many problems that exist in traditional road asphalt construction (Ouyang et al., 2017, 2018b).

The use of emulsified asphalt has important practical significance in the field of highway construction (Kong et al., 2017). Based on recent statistics, the apparent consumption of asphalt in

China exceeded 32 million tons in 2018, which was distributed across road construction, housing construction, airport construction, and water conservancy projects. With the rapid growth of investment in China's highway construction, the asphalt used in road construction has exceeded 75% of the total national asphalt consumption. In current road construction methods, the heating temperature for the asphalt emulsification process only needs to reach 120°C, which is lower than the processing temperature of hot asphalt by about 50°C. Compared with hot asphalt, the production of emulsified asphalt of unit mass requires 50% less energy and allows a large reduction of the emission of harmful gases. Moreover, the construction environment for emulsified asphalt is largely unaffected by weather conditions; therefore, this production process is currently considered one of the most effective, economical, and environmentally friendly means of road construction and maintenance (Chu and Shen, 2016).

Emulsified asphalt was first used in the field of road construction in the early 1920s. Over the first 40 years of emulsified technology exploration, anionic emulsified asphalt was the primary method developed for construction. Anionic emulsified asphalt has the advantages of energy efficiency, convenient construction, and cost effectiveness, and enables the use of a wide range of emulsifiers. However, both anionic emulsified asphalt and the wet aggregate surface are negatively charged. The resulting homogeneous repulsion between the asphalt particles prevents rapid adsorption of the aggregate surface, which affects pavement formation early in the process and delays its availability for traffic use. With the recent development of surface and colloidal chemistry, cationic emulsified asphalt has gradually replaced anionic emulsified asphalt because of its opposite charge to the aggregate surface, which successfully compensates for the lack of adhesion from anionic emulsified asphalt and has gradually become the predominant technique. However, a wide range of inexpensive anionic emulsifiers are available; further, these emulsifiers can be synergized with cationic, non-ionic, and amphoteric emulsifiers to form a composite, which greatly improves its emulsifying performance. Therefore, the study of anionic emulsified asphalt remains of practical significance (Yang, 2004).

BACKGROUND

Emulsifier and Emulsified Asphalt

Since the 1960s, the adsorption of emulsifier molecules on solid surfaces has gradually become a major focus of attention (Somasundaran et al., 1964). Methods for the study of emulsified asphalt have developed from a large number of emulsifying compatibility evaluation tests through a combination of Raman spectroscopy, surface free energy, fluorescence spectroscopy, interfacial viscoelasticity, neutron scattering, and other research techniques (Lu et al., 1995; Conboy et al., 1998; Kunieda et al., 1998; Penfold et al., 1998, 2000; Bumajdad et al., 1999; McKenna et al., 2000), which has provided abundant information on the structural design of emulsifiers. Jin et al. (2013) synthesized a composite asphalt emulsifier with an OP-10 cationic surfactant as the intermediate. The effects of the synthesis conditions and formulation on the emulsifying performance, surface activity, and service performance of the emulsifier were studied, and a new way to prepare composite asphalt emulsifiers was explored. Tan et al. (2013) found that emulsifier has significant retarding effect on cement hydration, which is relevant to the types of emulsifier and its dosages. Therefore, suitable emulsifier with little retarding effect on cement hydration and its appropriate dosage are recommended when producing asphalt emulsion for CA mortar. Han and Yu (2014) studied the pressure-sensitivity of cement mortar composites with different concentrations of multi-walled carbon nanotubes and different surfactants under repeated loading and impulsive loading, respectively. Experimental results indicate that the response of the electrical resistance of composites with SDBS to external force is more stable and sensitive than that of composites with Sodium dodecyl sulfate. Ouyang et al. (2016) studied the effect of emulsifier and superplasticizer on the rheology of cement paste and asphalt emulsion and the results show that the apparent viscosity and yield stress of asphalt emulsion increase with superplasticizer and emulsifier dosage. Wang et al. (2018) synthesized a new cationic surfactant containing non-ionic aliphatic alcohol polyoxyethylene ether using epichlorohydrin, octadecyl dimethylamine, and aliphatic alcohol polyoxyethylene ether as raw materials. It was concluded through experiments that the surfactant met the requirements for the asphalt emulsifier.

Emulsified asphalt is a kind of stable oil-in-water or water-in-oil emulsion formed by the action of the asphalt, emulsifier, and stabilizer, and offers the advantages of energy savings, reductions to environmental pollution, and convenient construction (Wu et al., 1992). Based on whether the hydrophilic group of the emulsifier molecule dissolves in water and what ions it dissociates into, asphalt emulsifiers can be divided into ionic and non-ionic types, among which the ionic type can be further divided into anionic, cationic, and amphoteric. The hydrophilic group of anionic asphalt emulsifiers consists of anions, which have been widely used since 1925. The common anionic asphalt emulsifiers are carboxylate (-COONa), sulfonate (-SO3Na), and sulfate (-OSO3Na). Cationic emulsified asphalt were developed after anionic types; however, owing to the excellent emulsifying performance and ability of the former to overcome the shortcomings of slow demulsification, long construction time, and poor ductility, the development of cationic emulsified asphalt progressed more quickly.

In recent years, Seref et al. (2006) studied the effect of Portland cement to improve the mechanical properties of dense graded emulsified asphalt mixtures for structural road layers. It was found that adding Portland cement to emulsified asphalt mixtures improves their mechanical properties, resilience modulus, temperature sensitivity, water damage, creep, and permanent deformation resistance. Yongjoo et al. (2011) studied the cold in-place recycling (CIR) mixture composed of foamed and emulsified asphalt, and found that the CIR-foam sample showed a higher tensile strength and lower water content than the more conventional CIR-latex sample. Zhao et al. (2012) studied the aging resistance of emulsified asphalt using the weightlessness coefficient method. It was found that the aging resistance of

emulsified asphalt was better than that of the original asphalt. The aging kinetics equation was established based on the relationship between the n-pentane asphaltene and time. Ouyang et al. (2018a,b, 2019) found that temperature and Water greatly affects the mechanical properties of cement bitumen emulsion mixture.

Application of Molecular Dynamics Simulations for Research Into Road Materials

Molecular dynamics (MD) simulation technology is a comprehensive application that integrates multiple disciplines. As one of the most widely used simulation methods in recent years, MD simulations are mainly based on Newton's basic theory of kinematics and the corresponding force field to simulate the movement processes of molecular system. They can obtain trajectories for particles in a system in addition to predicting the micro-morphological changes during the movement process. At the same time, the structural characteristics and thermodynamic properties of some complex systems can be calculated and analyzed (Matthieu and Punit, 2019).

With the development of MD and of the force field, simulations have been more often and more widely applied while the computational efficiency has been greatly improved. To date, MD simulation technology has become an important method to study the mechanisms of molecular mass transfer. These simulations enable tracking of the dynamic evolution of complex systems over time, reveal the adsorption properties and mechanism of molecules at interfaces at small time scales, and provide kinetic information that is difficult to observe and detect directly through experiments (Han et al., 2016; Hou et al., 2018). Maiti et al. (2002) obtained the equilibrium conditions and surface coverage of surfactants in oil and water phases using symmetrical MD. Ding et al. (2014) studied the effect of styrene-butadiene-styrene (SBS) on the molecular aggregation behavior of asphalt binders via MD simulations. It was found that the influence of the modifier largely depends on the molecular structure of the asphaltene. Xu et al. (2016) developed a molecular simulation method based on thermodynamics to study the cohesion and adhesion of asphalt concrete for the first time. The results showed that the cohesion between the asphalt and aggregate depends mainly on the type of aggregate minerals (silica or calcite) under dry and wet surface conditions. In the case of low moisture content, the type of asphalt has a significant influence on the adhesion between asphalt and silica. Vekeman et al. (2019) studied the adsorption and selectivity of CH4/N2 mixtures on a flexible graphene layer by molecular simulation. It was found that the accuracy of the potentials guarantees a quantitative description of the interactions and trustable results for the dynamics, as long as the appropriate set of intramolecular and intermolecular force fields is chosen. And based on the MD simulations, Zhou et al. (2019) studied the Intermediate Phase in Calcium–Silicate–Hydrates: Mechanical, Structural, Rigidity, and Stress Signatures. It demonstrated that the intermediate phase observed in this system arises from a bifurcation between the rigidity and stress transitions. These features might be revealed to be generic to isostatic disordered networks.

Sodium dodecylbenzene sulfonate (SDBS) is a common anionic asphalt emulsifier that is suitable for slurry seals, viscous oil, and base maintenance. During the preparation of SDBS, a small amount of isomers are simultaneously generated. Owing to the similar properties and morphologies of SDBS and its isomers, it is difficult and expensive to purify its isomers. Therefore, the use of molecular dynamics simulation to study the mass transfer process of SDBS and its isomers on aggregate surface enables accurate prediction of their performance differences, saving manpower and material resources, and improving the efficiency of scientific research. Li et al. (2009) used MD simulations to study the role of SDBS for the oil-water separation of chloroform and water. It was found that the presence of SDBS significantly inhibited the separation of chloroform and water. Song et al. (2009) simulated the adsorption of SDBS on an amorphous silica solid surface using MD. It was found that SDBS can be adsorbed on solid surfaces from solution over a certain time. Liu et al. (2011) studied the adsorption behavior of SDBS and its isomers at the oil/water interface using the MD method, and proposed that changes in the adsorption from the simulations could be investigated by calculating the contact area. The results showed that the proper oil phase can make the interface SDBS and its isomers more compact and orderly, providing better interfacial activity. Ni et al. (2018) investigated the adsorption characteristics of anionic surfactant sodium dodecylbenzene sulfonate on the surface of montmorillonite minerals. It showed that the addition of H+ to the SDBS solution could reduce electrostatic repulsion and promote the adsorption of SDBS on montmorillonite.

OBJECTIVE

In this paper, the interactions between SDBS, its isomers and calcium carbonate, which is the main chemical composition of the aggregate, were studied using MD simulations, and the effect of SDBS and its isomers on the mass transfer of the aggregate on the surface of the main chemical component was explored. The main purpose is as follows:

(i) To improve the understanding of mass transfer and condensation behavior of anionic asphalt emulsifier on the surface of main chemical components of aggregate.
(ii) The parameters of the radial distribution function (RDF), mean square displacement (MSD), and interfacial energy were used as indicators of molecular mass transfer and condensation behavior to assess the behavior changes of isomers on the surface of the main chemical components of aggregates.
(iii) To explore the effect of emulsifier structure on mass transfer performance, and provide theoretical basis and ideas for the structure design of new asphalt emulsifier.

MODEL AND METHOD

Potential Function

At present, Condensed-phase Optimized Molecular Potentials for Atomistic Simulation Studies force field (Sun, 1998),

Universal force field (Rappé et al., 1992) and consistent-valence force field (Jon et al., 1988) are widely used in the field of interface adsorption. Through a large number of trial calculations, the author found that the potential energy of Stretch-Torsion-Stretch, Separated-Stretch-Stretch, Torsion-Stretch, Bend-Bend, Torsion-Bend, Bend-Torsion-Bend, Long range correction in sodium dodecylbenzenesulfonate-water-calcium carbonate system is much smaller than that of Bond, Angle, Torsion, van der Waals, and Electrostatic interactions. To effectively utilize the limited computing resources, the simulation was performed using the FORCITE module in the Materials Studio (MS) 2017 software, for which the universal force field (Rappé et al., 1992) was selected. The force field includes six potential functions, including bond, angle, torsion, inversion, Van der Waals (VdW) and Electrostatic, which can save time and improve efficiency while ensuring simulation accuracy. The potential energy function has the following form:

$$E = \frac{1}{2K_{IJ}\left(r - r_{IJ}\right)^2} + K_{IJK}\sum_{n=0}^{m} C_n \,\text{body}\, n\theta + K_{IJK}\sum_{n=0}^{m} C_n \,\text{body}\, n\phi_{JIKL} + K_{IJKL}\left(C_0 + C_1 \,\text{body}\, \omega_{JIKL} + C_2 \,\text{body}\, 2\omega_{JIKL}\right) + D_{IJ}\left\{-2\left[\frac{x_{IJ}}{x}\right]^6 + \left[\frac{x_{IJ}}{x}\right]^{12}\right\} + 332.0637(\mathrm{Q_i Q_j}/\epsilon \mathrm{R_{ij}})$$

The first four terms are Valence energy, which represent the potential energy of bond, angle, torsion and inversion respectively. They are obtained mainly by Fourier Cohen function expansion. Footmarks I, J, K, and L represent different atoms in the model. K_IJ, K_IJK and K_IJKL all represent force constants between different atoms in units of (kcal/mol)/Å2. r_IJ is the natural bond length between atoms in unit of Å. The coefficient C_n represents the minimum value satisfying the boundary conditions at the natural bond angle θ_0. θ, φ and ω represent the angles of bond angle, torsion, and inversion, respectively. The latter two terms are Non-bond energy, representing VdW, and Electrostatic, respectively. In Van der Waals, D_IJ denotes the depth of the potential well, and x denotes the distances of different atoms. In Electrostatic, Q denotes charge, R_ij denotes distance between Q_i and Q_j, and ϵ denotes dielectric constant.

Material Model

Based on the determined chemical composition of the aggregate (Kong, 2017), calcium carbonate is one of the main chemical components of the aggregate. Further, through a large number of trial calculations, it is found that calcium carbonate has higher adsorption performance than other chemical components in aggregate. Therefore, the calcium carbonate model was established in this study to replace aggregate for molecular simulation. The calcite structure model (Sitepu, 2009) was therefore established as the research object; its spatial group is R-3cH, and the spatial coordinates are given in **Table 1**.

The calcite supercell was constructed, and the SDBS (4-1ΦC12S) and its isomers (4-3ΦC12S, 4-5ΦC12S, 2-1ΦC12S, and 3-1ΦC12S) were established using the amorphous cell tool in MS. The model formed a layered structure with the calcite supercell (Liu et al., 2011). The chemical structural models of emulsifier are shown in **Figure 1**.

TABLE 1 | Space coordinates for the calcite model (Sitepu, 2009).

Atom	#	OX	SITE	x	y	z	SOF	H
As	1	+2	6a	0	0	0	1	0
C	1	+4	6b	0	0	0.250	1	0
O	1	−2	18a	0.25644 (15)	0	0.250	1	0

Structure Model

The supercell thickness for the calcium carbonate was 2.0 nm. An aqueous layer composed of 300 water molecules was placed above the emulsifier solution to prevent the influence of periodic boundary conditions on the emulsifier solution system, where the thickness of the vacuum layer was 3.0 nm. The emulsifier solution contained 10 SDBS molecules and 1,200 water molecules. SDBS molecules are often disassociated as Na^+ ions and DBS^- ions in solution; therefore, these ions were distributed randomly in a 1:1 ratio when constructing the amorphous emulsifier structure with the goal of maintaining electrical neutrality. Further, the net charge of the DBS^- ions and water molecules were selected using the QEq method (Rappé and Goddard, 1991). Owing to the simple structure of the Na^+ ions, their formal charge was distributed as a direct response to the force field, and the electrostatic interactions were calculated using the Ewald addition method (Allen and Tildesley, 1987). The van der Waals interactions were based on atomic calculations with a moderate simulation accuracy and a cutoff radius of 12.5 Å. The structural model discussed by Yan and Zhu was adopted for the water molecules (Yan and Zhu, 2013). The test value of the O-H bond length was 0.95718 Å and the H-O-H bond angle was 104.523°. The MD simulations used the canonical ensemble (NVT) approach to simulate a temperature of 298 K and the Nose method (Hoover, 1985) to control the temperature. The time step was 1 fs, the total simulation time was 1,000 ps, and the trace file was stored once every 0.5 ps for the subsequent structural and MD analyses. The component models and architecture are shown in **Figure 2**.

RESULTS AND DISCUSSION

Agglomeration Structure of the Amorphous Calcium Carbonate Surface

The SDBS MD simulation trace file was derived to clearly observe the adsorption process and improve the simulation efficiency. **Figure 3A** shows the random distribution model doe the DBS^- with a negative charge and the anti-particle Na^+ ions on the solid surface of the simulated system (at 0 ps). As the simulation progressed, the intermolecular interactions of the emulsifier were the first to occur. The DBS^- ions aggregated in the water, the intermolecular space gradually reduced (200 ps; **Figure 3B**), and the degree of aggregation increased with time,

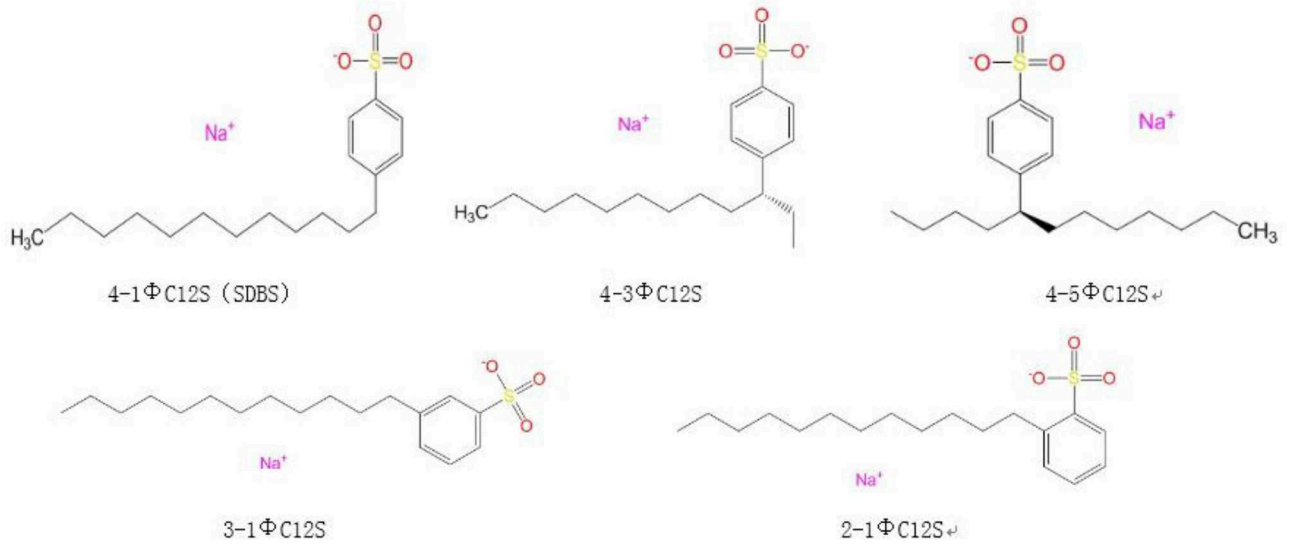

FIGURE 1 | Sodium dodecyl benzene sulfonate (SDBS) and its isomer models. The leading digit 2, 3, or 4 indicates that the long alkyl chain is in the ortho, interposition, or para position of the benzene ring, respectively; Φ represents the benzene ring; 12 is the number of carbon atoms in the long alkyl chain; the digits 1, 3, or 5 before the Φ indicate that the benzene ring is at the position 1#, 3#, or 5# of the long alkyl chain; and S represents the sulfonate.

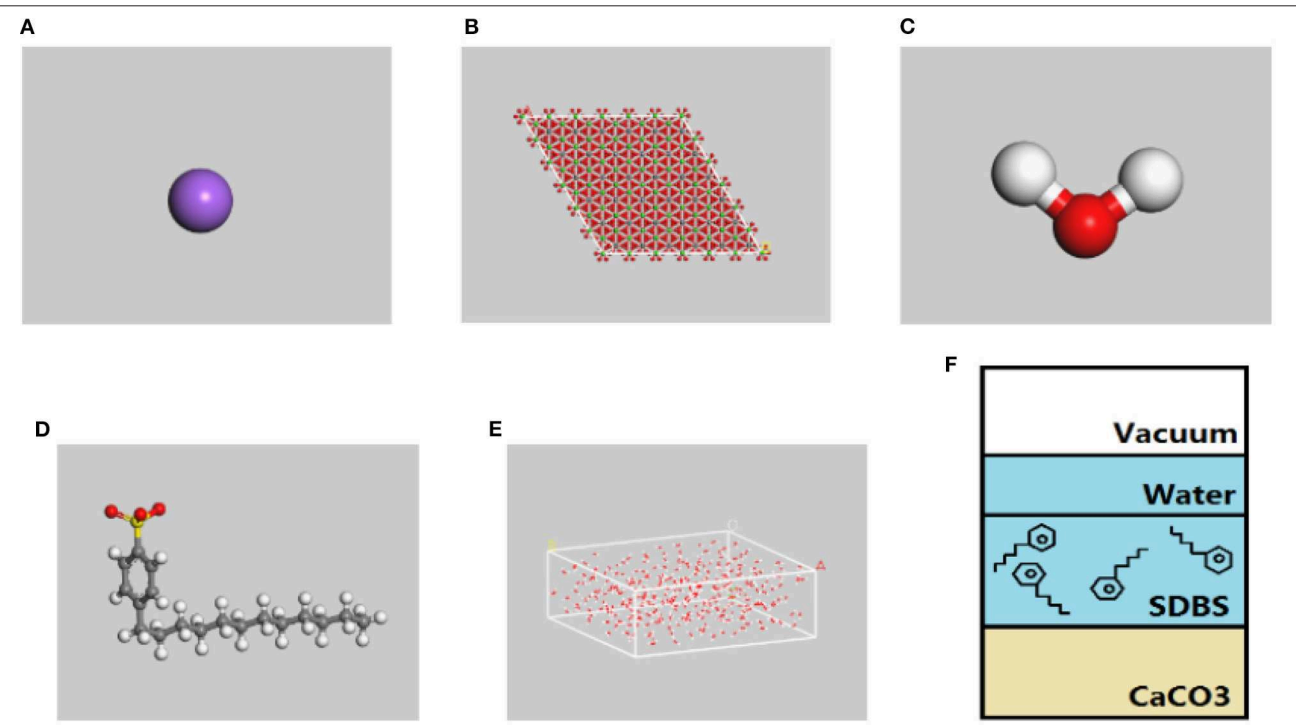

FIGURE 2 | Representation of the simulation model. Obtained by Materials studio 2017. **(A)** Na^+ ions, **(B)** the supercell o calcium carbonate, **(C)** H_2O, **(D)** dodecylbenzene sulfonate ions (DBS), **(E)** water layer, and **(F)** test model.

which gradually formed half micelles (400 ps; **Figure 3C**). At the same time, because of the adsorption of calcium carbonate on the emulsifier molecules, the molecules close to the surface of the calcium carbonate gradually moved closer to the surface (600 ps; **Figure 3D**) where they were finally adsorbed (800 ps; **Figure 3E**). As a result of the difference in the concentrations between the upper water layer and the emulsifier solution, the upper water layer also had a certain adsorption effect on

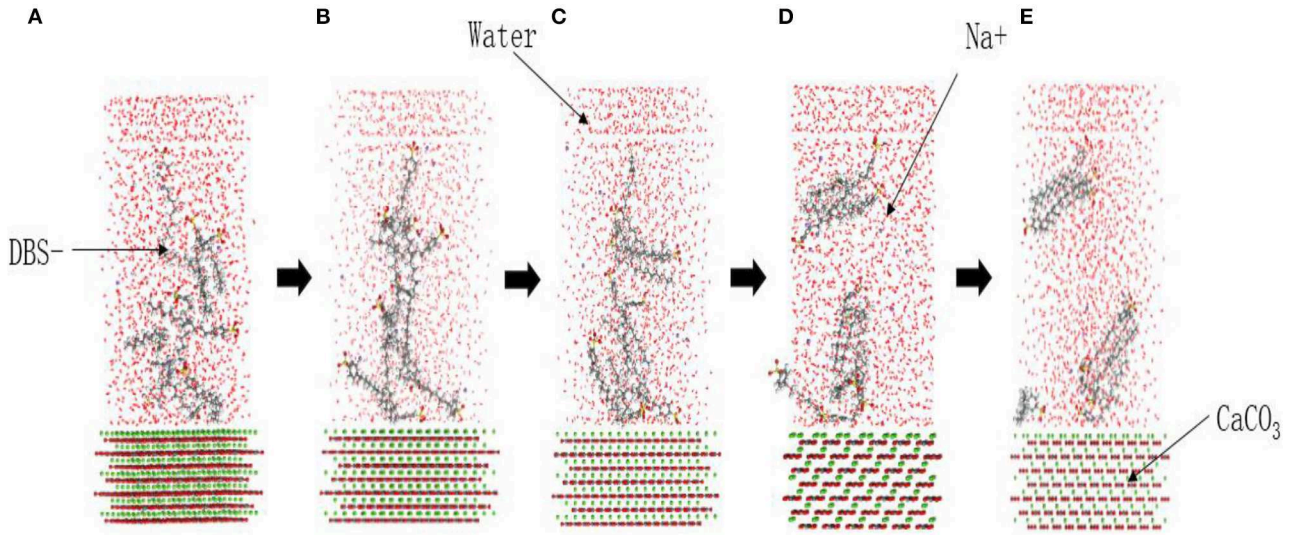

FIGURE 3 | Adsorption process of the surfactant molecules at the solid–liquid interface in the SDBS system. **(A)** 0 ps, **(B)** 200 ps, **(C)** 400 ps, **(D)** 600 ps, and **(E)** 800 ps.

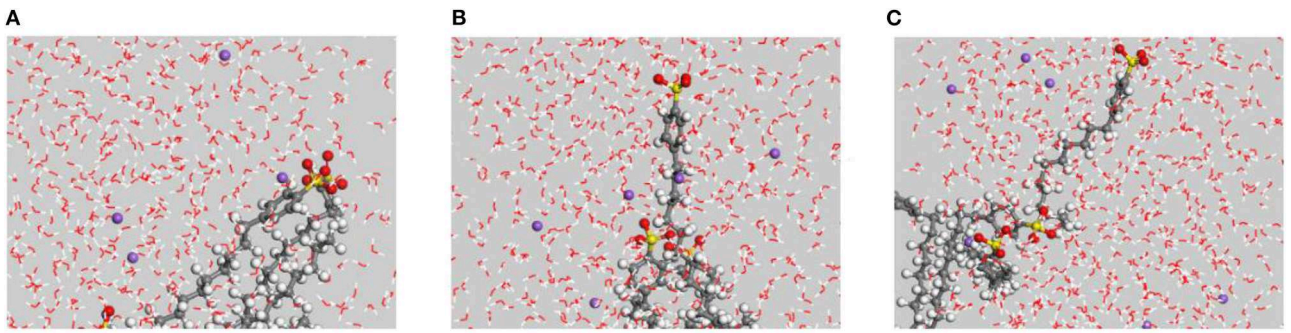

FIGURE 4 | Na^+ aggregation in the SDBS system. The purple sphere is Na^+. **(A)** 0 ps, **(B)** 400 ps, and **(C)** 800 ps.

the emulsifier molecules. This eventually led to a separation of the upper and lower emulsifier molecules in the solution, which were adsorbed at the liquid–liquid and solid–liquid interfaces, respectively.

During the adsorption process, Na^+ ions were distributed randomly in the emulsifier solution, and no obvious aggregation was observed around the polar head of the emulsifier (**Figure 4**). The authors reason that while the Na^+ ions are positively charged, the oxygen atoms in the water and the polar head of the emulsifier molecule have a significant negative charge. The calculated charges given in **Table 2** indicate that the charge of the oxygen atoms in the DBS^- ion polarity head was significantly lower than that of the oxygen atoms in the water molecules. Thus, there were stronger electrostatic interactions between the Na^+ ions and the water molecules based on the charge magnitudes.

RDF of the sulfur atoms in the polar-head of the DBS^- and Na^+ ions indicates that there was no obvious aggregation in the polar-head of the DBS^- or Na^+ ions (**Figure 5A**). However, there were obvious aggregation peaks between (i) the sulfur and oxygen atoms in the water molecules and (ii) the Na^+ ions and the oxygen atoms in the water molecules (**Figures 5B,C**, respectively). This indicates that a water layer between the Na^+ ions and the polar head prevented relative proximity between them. For a Na^+ ion and a polar-head to interact, the electrostatic interactions between (i) the water molecules and Na^+ ions and (ii) the water molecules and the polar-heads must be broken down.

Adsorption of the SDBS and Its Isomers on the Calcium Carbonate Surface

Figure 6 shows the adsorption of SDBS and its isomers on the surface of calcium carbonate. It was observed that calcium carbonate had an adsorption effect on the SDBS and its isomers. Additionally, there were obvious aggregation peaks through the radial distribution function of the carbon atoms between the emulsifiers (**Figure 7**),

TABLE 2 | Oxygen atomic charge.

Oxygen atomic charge	
Polar-head O atom in DBS^-	−0.308e
Nonpolar-head O atom in DBS^-	−0.315e
O atom in water	−0.698e

indicating mutual aggregation between the emulsifiers at this concentration.

In this system, the emulsifier molecules near the calcium carbonate surface aggregated on the solid surface to form a distinct semi-micelle structure. The emulsifier molecules far from the calcium carbonate surface also aggregated with each other because of their own electrostatic adsorption. The adsorption performances of the emulsifiers 4-3ΦC12S (**Figure 6d**) and 4-5ΦC12S (**Figure 6e**) on the calcium carbonate surface were significantly weaker than those of the other three. The calcium carbonate adsorbed only the lowermost layer of the 4-3ΦC12S and 4-5ΦC12S emulsifier molecules, and there was no adsorption effect on the half-micelle structure of the middle and upper layers of the system. This was attributed to the increased degree of branching as the aromatic hydrocarbons in the benzene sulfonate molecules moved toward the middle of the alkyl chain, which led to a higher coverage rate of the emulsifier molecules, enlarged the contact area between the emulsifier molecules and the water molecules, and led to decreased adsorption.

Further, as the benzene ring moved toward the middle of the alkyl chain, the degree of aggregation for the emulsifier in the solution gradually decreased, indicating that the critical micelle concentration increased with the degree of branching when the length of the alkyl chain remained the same. As the degree of intermolecular branching increased, the interactions between the emulsifier molecules gradually decreased. The spatial volume of the hydrophobic group increased as the benzene ring moved toward the middle of the alkyl chain, making it more difficult for the emulsifier to form a tight alignment, thereby increasing the critical micelle concentration.

Interface Energy Calculation and Analysis of the SDBS on the Calcium Carbonate Surface

The interfacial energy parameters characterize the bonding degree and adsorption performance of the solid-liquid phase. The adsorption model with the lowest energy can be obtained through MD simulations; furthermore, the energy parameters for each part could be obtained, whereupon the interface energy (Pradip, 2002) can be calculated according to

$$\Delta E = E_{interaction} = E_{total} - (E_{surface} + E_{\text{emulsifier}})$$

where E_total is the total energy of the system, E_surface is the energy of the underlying solid surface, E_"emulsifier" is the energy of the emulsifier solution, and ΔE is the interaction energy between the aggregate and emulsifier interface (Gao et al., 2013).

Xu et al. (2016) pointed out that the solid-liquid interface interaction energy ΔE, which characterizes the stability of the adsorption system, indicates that larger negative values give a greater interaction and stronger surface adsorption. In contrast, if ΔE is zero or positive, the emulsifier has little or no adsorption on the solid surface. The potential energies of the five emulsifier–calcium carbonate interface models were calculated using the FORCITE module in MS, and the interfacial interaction energy was calculated according to the interface energy formula.

The interfacial interaction energies of the SDBS and its isomers were consistently negative, indicating that the five emulsifiers had a certain adsorption on the calcium carbonate surface (**Figure 8**). Among them, the interfacial interaction energy of the 4-1ΦC12S, 4-3ΦC12S, and 4-5ΦC12S decreased as the benzene ring moved toward the middle of the alkyl chain. Furthermore, the interfacial interaction energies for the 4-3ΦC12S and 4-5ΦC12S were significantly lower than for the other three emulsifiers, indicating that their adsorption performances were weaker, which is consistent with the conclusions drawn in section Application of Molecular Dynamics Simulations for Research Into Road Materials. When the straight alkyl chain was in the ortho and meta positions of the benzene ring, the interfacial interaction energy was improved to some extent with respect to the 4-1ΦC12S, indicating that the 2-1ΦC12S and 3-1ΦC12S had better adsorption performances in the system. However, the benzenesulfonate ions of the 2-1ΦC12S were close to its own carbon chain, causing the outer electron clouds of different groups to overlap and repel each other. There was also a steric hindrance effect, making the adsorption performance lower than that of the 3-1ΦC12S.

Interfacial Diffusion of the Emulsifier (Solution)–Calcium Carbonate System

The diffusion coefficient refers to the ease by which a material passes through a unit area when the concentration gradient of the solution is constant. According to Einstein's analysis of Brownian motion, MSD has a linear relationship with time when the system is a liquid. Here, the diffusion coefficient of a particle in the emulsifier solution can be calculated from the slope of this linear relationship. Therefore, when an MD simulation is used to calculate the diffusion coefficient, the MSD curve of the particles is usually calculated from the Einstein equation (Allen and Tildesley, 1987). This relationship is given by

$$D = \frac{1}{6N} \lim_{t \to \infty} \frac{d \sum_{t=1}^{N} ([r(t) - r(0)]^2)}{dt}$$

where D is the diffusion coefficient of the particles in the system, N is the number of diffusion molecules, and the differential term is the linear slope of the MSD vs. time. The MSD curves were obtained and statistically analyzed using the MD simulation of the post-phase trajectory files for each group model. The diffusion-coefficient relationships for the carbon atom at the end of the alkyl chain, the DBS^- ion centroid, the S atom in the benzene sulfonate ions, the Na^+ ions, and the emulsifier solution were obtained, as shown in **Figure 9**.

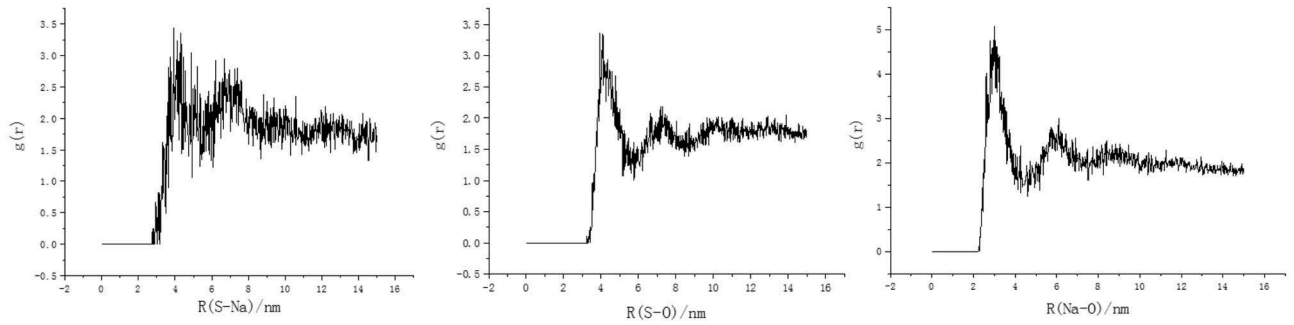

FIGURE 5 | Radial distribution as a function of distance between the S atom in the polar-head, the O atom in water molecules, and the Na^+ ions in the solution for the SDBS system. The obvious characteristic peak indicates that there is adsorption between them.

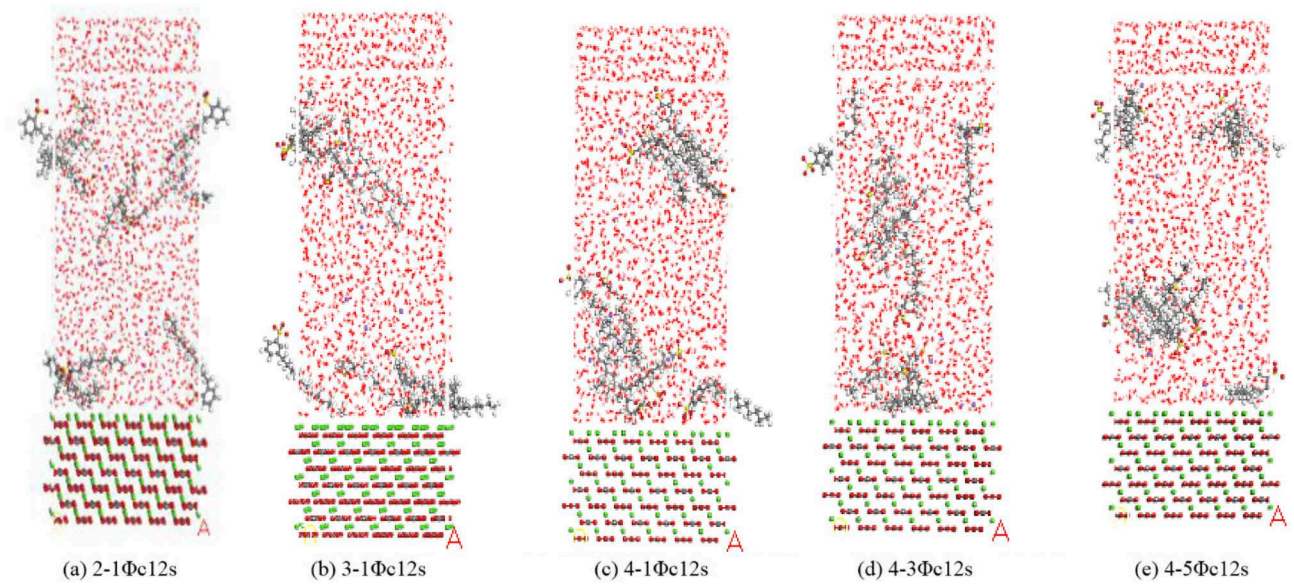

FIGURE 6 | Adsorption of the SDBS and isomers on the $CaCO_3$ surface.

In the diffusion process, the diffusion coefficients of five layers were similar, which indicate that the molecular structure, degree of branching, and other factors had minimal effects on the diffusion ability of the emulsifier. However, the diffusion coefficients of the Na^+ ions in different systems were significantly different. The authors believe that this is because the steric hindrance caused by different configurations of the emulsifiers was different. In the system, some atoms or groups were closer to each other with overlapping outer electron clouds. This resulted in repulsion between the atoms and groups and decreased the sensitivity of the soluble cations in the solution.

The diffusion-coefficient distributions of the carbon atom at the end of the alkyl chain and the S atom in the benzene sulfonate ions were higher than that of the DBS^- ion centroid, indicating that both the oleophilic group and the hydrophilic group in the emulsifier system could promote the diffusion of the emulsifier in the solution. In the 3-1Φc12s, 4-1Φc12s, and 4-3Φc12s, the diffusion coefficient of the carbon atom at the end of the alkyl chain was higher than that of the sulfur atom in the benzene sulfonate ions, indicating that the activity of the oleophilic group was higher than that of the hydrophilic group in the system.

Experimental Study on Mass Transfer Performance of Emulsifier (Solution)–$CaCO_3$ System

In the solution system of the emulsifier/aggregate, the mass transfer process was complete at the moment solid-liquid contact occurred. However, the relevant test parameters cannot be obtained directly using existing testing methods. Therefore, the conductivity method was used to characterize the mass transfer performance of the emulsifier onto the surface of $CaCO_3$. This method can determine the mass transfer by measuring the conductivity of the supernatant after solid-liquid mixing and centrifugation. A higher conductivity and supernatant concentration of the emulsifier causes fewer

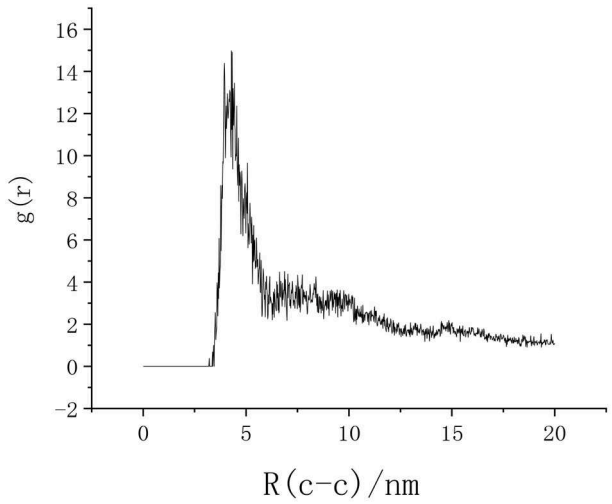

FIGURE 7 | Radial distribution function of the emulsifier end-carbon atoms in the SDBS solution. The obvious characteristic peak indicates that there is adsorption between them.

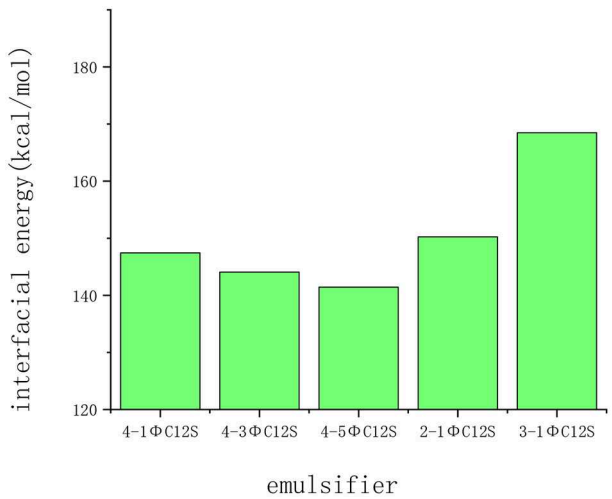

FIGURE 8 | Results of the potential energy calculation for the emulsifier on the $CaCO_3$ surface.

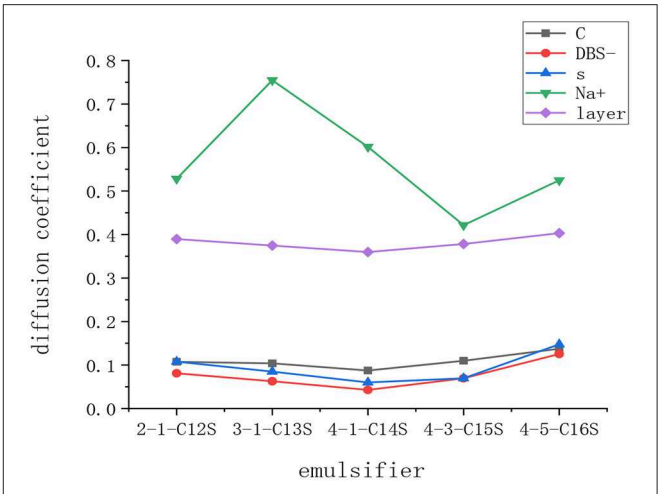

FIGURE 9 | Results of the diffusion coefficient for various components in the solution.

emulsifier molecules to be adsorbed onto the $CaCO_3$ surface in the original mixed solution, which leads to a weaker mass transfer performance.

The isomers of 12 alkylbenzene sulfonates are currently rarely sold in China because of their difficult purification process, poor biodegradability, and high price. Therefore, the reliability of the simulation data was verified using the relevant tests with the 4-1ΦC12S and 2-1ΦC12S emulsifier products due to their availability. The emulsifier reagents are shown in **Figures 10a,b**.

To verify the simulation results, the supernatants of the samples (**Figure 10c**) with $CaCO_3$/emulsifier solution solid-liquid ratios of 1:1, 1:5, and 1:10 were obtained after ultrasonic oscillation and high-speed centrifugation (**Figures 10d,e**). The conductivity of the supernatant was measured using a DDSJ-308A conductivity meter (**Figure 10f**) where the test temperature was 28°C and the conductivity units were μS/cm. The results are shown in **Figure 11**.

It can be seen from **Figure 11** that the conductivity of the 4-1ΦC12S solution was higher than that of the 2-1ΦC12S solution at the same concentration. It was shown that calcium carbonate adsorbs more 2-1ΦC12S emulsifier at the same concentration, which results in a relatively low conductivity for the upper supernatant as extracted from the experiment. This suggests that the mass transfer performance for the 2-1ΦC12S emulsifier is better than that of the 4-1ΦC12S emulsifier. The 2-1ΦC12S showed better adsorption performance on the surface of calcium carbonate, which is consistent with the calculation results for the interfacial energy in Interface Energy Calculation and Analysis of the SDBS on the calcium carbonate Surface. At the same time, it was found that a larger solid-liquid ratio of the calcium carbonate/emulsifier solution in the 4-1ΦC12S sample caused a gradually increasing conductivity. This indicates that the 4-1ΦC12S emulsifier had better adsorption performance at low solid-liquid ratios. In contrast, larger solid-liquid ratios for the 2-1ΦC12S sample showed a gradually decreasing conductivity, which indicates it had a better adsorption performance at higher solid-liquid ratios. Determining whether this phenomenon is related to interatomic repulsions caused by overlapping outer electron clouds due to the close group in the emulsifier requires further study.

CONCLUSIONS

The use of emulsified asphalt in highway construction has significant practical applications. The existing asphalt emulsifier qualities are intermingled, which leads to poor adaptability, low compatibility with asphalt, an incomplete formula design, and

FIGURE 10 | Test equipment. **(a)** 4-1ipmen, **(b)** 2-1ΦC12S, **(c)** samples, **(d)** TG16-WS high speed centrifuge, **(e)** ultrasonic cleaning machine, and **(f)** DDSJ-308A conductivity meter.

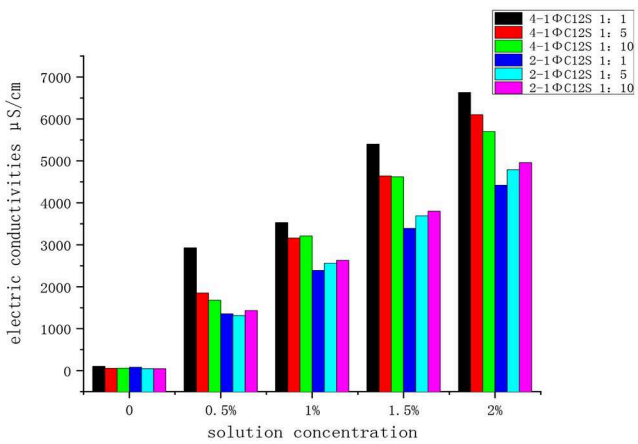

FIGURE 11 | Conductivity test results.

problems associated with quality control methods. Research on traditional asphalt emulsifiers and its formulation is often based on experience and relies on a large number of emulsifying compatibility selection experiments, which lacks systematic theoretical guidance. This study introduces a new method to examine the mass transfer of emulsifiers and their isomers on the surface of the main chemical components of aggregates through MD simulations regarding the structural design of asphalt emulsifiers for road use. Further, the mass transfer of emulsifier and its isomers on the surface of calcium carbonate, the main chemical composition of aggregate, was also investigated. The following conclusions are obtained through relevant studies:

1. During the mass transfer process, it was found that the five emulsifier molecules aggregated in a relatively short period and were adsorbed at the liquid–liquid and solid–liquid interfaces. Furthermore, the Na^+ ions did not aggregate around the polar head of the emulsifier.
2. Owing to the influence of the steric hindrance, the branching degree, and other factors, the mass transfer performance of the 3-1Φc12s was the strongest while that of the 4-5Φc12s was the weakest. As the aromatics in the benzene sulfonate molecules moved to the middle of the alkyl chain, the branching degree of the molecules increased, and the mass transfer performance and degree of aggregation on the calcium carbonate surface decreased.
3. Factors such as the molecular structure and degree of branching had a limited effect on the diffusion capacity of the SDBS and its isomers. Both the lipophilic group and the hydrophilic group promoted the mass transfer performance of the emulsifier in the solution.
4. Conductivity tests showed that the 2-1ΦC12S emulsifier had an overall better mass transfer performance on the surface of the calcium carbonate than the 4-1ΦC12S emulsifier, which is consistent with the MD simulation results. At the same time, it was found that the 4-1ΦC12S emulsifier had a better mass transfer performance at lower solid-liquid ratios

while the 2-1ΦC12S emulsifier was better at higher solid-liquid ratios.

DATA AVAILABILITY STATEMENT

The datasets generated for this study are available on request to the corresponding author.

AUTHOR CONTRIBUTIONS

LK proposed the research direction and provided the funds for the research. WL wrote the first draft, completed the molecular simulation, and participated in the subsequent experiments. BF and XQ participated in the experiment.

REFERENCES

Allen, M. P., and Tildesley, D. (1987). *Computer Simulation of Liquids*. Oxford: Clarendon Press.

Bumajdad, A., Eastoe, J., Griffiths, P., Steytler, D. C., Heenan, R. K., Lu, J. R., et al. (1999). Interfacial compositions and phase structures in mixed surfactant microemulsions. *J. Langmuir* 15, 5271–5278. doi: 10.1021/la990060m

Chu, J. J., and Shen, C. L. (2016). Application of emulsified asphalt in spraying rapid-hardening rubber-modified bitumen waterproof coating. *J. Petroleum Asphalt* 30, 55–56. doi: 10.3969/j.issn.1006-7450.2016.02.013

Conboy, J. C., Messmer, M. C., and Richmond, G. (1998). Effect of alkyl chain length on the conformation and order of simple ionic surfactants adsorbed at the d2o/ccl4 interface as studied by sum-frequency vibrational spectroscopy. *J. Langmuir* 14, 6722–6727. doi: 10.1021/la980132u

Ding, Y. J., Boming, T., Zhang, Y. Z., Wei, J. M., and Cao, X. J. (2014). Molecular dynamics simulation to investigate the influence of SBS on molecular agglomeration behavior of asphalt. *J. Mater. Civ. Eng.* 27:C4014004. doi: 10.1061/(asce)mt.1943-5533.0000998

Gao, Z. Y., Sun, W., Hu, Y. H., and Liu, X. W. (2013). Surface energies and appearances of commonly exposed surfaces of scheelite crystal. *J. Trans. Nonferr. Metals Soc. China* 23, 2147–2152. doi: 10.1016/S1003-6326(13)62710-7

Han, B., and Yu, X. (2014). Effect of surfactants on pressure-sensitivity of CNT filled cement mortar composites. *J. Front. Mater.* 1:27. doi: 10.3389/fmats.2014.00027

Han, Y., Qu, G. M., Xue, C. L., Liang, S., and Ding, W. (2016). Molecular dynamics simulation on the aggregation behavior of sodium dodecyl benzene sulfonate at air/water interface. *J. Sci. Technol. Chem. Ind.* 24, 22–26. doi: 10.3969/j.issn.1008-0511.2016.04.005

Hoover, W. G. (1985). Canonical dynamics: equilibrium phase-space distributions. *J. Phys. Rev. A* 31, 1695–1702. doi: 10.1103/PhysRevA.31.1695

Hou, Y. B., Ren, Q., Dai, Z. Y., and Zhou, H. (2018). Interaction mechanism of surfactant molecules with oil-water interfacial molecules. *J. Acta Petrol. Sin.* 34, 108–114. doi: 10.3969/j.issn.1001-8719.2018.01.015

Jerzy, K., and Bengt, K. (1990). On the formation and stability of concentrated water-in-oil emulsions, aphrons. *J. Colloids Surf.* 50, 131–140. doi: 10.1016/0166-6622(90)80258-6

Jin, S. R., Zhang, K., Pang, J. X., and Song, S. S. (2013). Synthesis and application research of op-10/ cationic surfactant composite asphalt emulsifier. *Appl. Mech. Mater.* 364, 664–668. doi: 10.4028/www.scientific.net/AMM.364.664

Jon, R. M., Uri, D., and Arnold, T. H. (1988). Derivation of force fields for molecular mechanics and dynamics from ab initio energy surfaces. *J. Proc. Natl. Acad. Sci. U.S.A.* 15, 5350–5354. doi: 10.1073/pnas.85.15.5350

Kong, L. Y. (2017). *Study on Aggregate Properties and its Impact on the Mass-Transfer of Aggregate/Emulsifier System. D.* Qingdao: China University of Petroleum.

Kong, L. Y., Tang, F. L., Xu, Y., Zhao, P. H., and Zhang, Y. Z. (2017). Evaluation of emulsified asphalt demulsification process by UV spectrum method. *J. J. Chang'an Univ.* 6, 17–23.

Kunieda, H., Ozawa, K., Aramaki, K., Nakano, A., and Solans, C. (1998). Formation of microemulsions in mixed ionic–nonionic surfactant systems. *J. Langmuir* 14, 260–263. doi: 10.1021/la9704112

Li, Z. Q., Guo, X. L., Wang, H. Y., Li, Q. H., Yuan, S. L., Xu, G. Y., et al. (2009). Molecular dynamics simulation of anionic surfactant aggregation at the oil/water interface. *J. Acta Phys. Chim. Sin.* 25, 6–12. doi: 10.3866/PKU.WHXB20090102

Lissant, K. J. (1975). Emulsions and emulsion technology. *Soil. Sci.* 120:160. doi: 10.1097/00010694-197508000-00017

Liu, G. Y., Gu, D. M., Ding, W., Yu, T., and Cheng, J. C. (2011). Molecular dynamics simulation of anionic surfactant aggregation at the interface. *J. Acta Petrol. Sin.* 27, 77–84. doi: 10.3969/j.issn.1001-8719.2011.01.013

Lu, J. R., Purcell, I. P., Lee, E. M., Simister, E. A., Thomas, R. K., Rennie, A. R., et al. (1995). The composition and structure of sodium dodecyl sulfate-dodecanol mixtures adsorbed at the air-water interface: a neutron reflection study. *J. Colloid Interface Sci.* 174, 441–455. doi: 10.1006/jcis.1995.1412

Maiti, P. K., Lasnsac, Y., and Glaser, M. A. (2002). Self-assembly in surfactant oligomers. *J. Langmuir* 18, 1908–1918. doi: 10.1021/la0111203

Matthieu, M., and Punit, B. (2019). Signature of coordination defects in the vibrational spectrum of amorphous chalcogenides. *J. Front. Mater.* 6:283. doi: 10.3389/fmats.2019.00283

McKenna, C. E., Knock, M. M., and Bain, C. D. (2000). First-Order phase transition in mixed monolayers of hexadecyltrimethylammonium bromide and tetradecane at the air–water interface. *J. Langmuir* 16, 5853–5855. doi: 10.1021/la000675f

Ni, X., Li, Z., and Wang, Y. (2018). Adsorption characteristics of anionic surfactant sodium dodecylbenzene sulfonate on the surface of montmorillonite minerals. *J. Front. Chem.* 6:390. doi: 10.3389/fchem.2018.00390

Ouyang, J., Han, B. G., Cao, Y., Zhou, W. J., Li, W. G., and Surendra, P. S. (2016). The role and interaction of superplasticizer and emulsifier in fresh cement asphalt emulsion paste through rheology study. *J. Construct. Build. Mater.* 125, 643–653. doi: 10.1016/j.conbuildmat.2016.08.085

Ouyang, J., Hu, L. J., Li, H. Y., and Han, B. G. (2018a). Effect of cement on the demulsifying behavior of over-stabilized asphalt emulsion during mixing. *J. Construct. Build. Mater.* 177, 252–260. doi: 10.1016/j.conbuildmat.2018.05.141

Ouyang, J., Li, H. Y., and Han, B. G. (2017). The rheological properties and mechanisms of cement asphalt emulsion paste with different charge types of emulsion. *J. Construct. Build. Mater.* 147, 566–575. doi: 10.1016/j.conbuildmat.2017.04.201

Ouyang, J., Pan, B. F., Xu, W., and Hu, L. J. (2019). Effect of water content on volumetric and mechanical properties of cement asphalt emulsion mixture. *J. Mater. Civ. Eng.* 31:04019085. doi: 10.1061/(ASCE)MT.1943-5533.0002736

Ouyang, J., Zhao, J. Y., and Tan, Y. Q. (2018b). Modelling the mechanical properties of cement asphalt emulsion mortar with different asphalt to cement ratio and temperature. *J. Mater. Civ. Eng.* 30:04018263. doi: 10.1061/(ASCE)MT.1943-5533.0002480

Penfold, J., Staples, E., Tucker, I., Soubiran, L., Creeth, A., and Hubbard, J. (2000). Adsorption of di-chain cationic and non-ionic surfactant mixtures at the air/water interface. *J. Phys. Chem. Chem. Phys.* 2, 5230–5234. doi: 10.1039/b003439h

Penfold, J., Staples, E., Tucker, I., Soubiran, L., Lodi, A. K., Thompson, L., et al. (1998). Structure and composition of the mixed monolayer of hexadecyltrimethylammonium bromide and benzyl alcohol adsorbed at the air/water interface. *J. Langmuir* 14, 2139–2144. doi: 10.1021/la9710740

Pradip, R. B. (2002). Design of tailor-made surfactants for industrial applications using a molecular modelling approach. *J. Colloids Surf. A Physicochem. Eng. Asp.* 205, 139–148. doi: 10.1016/S0927-7757(01)01153-0

Rappé, A. K., Casewit, C. J., Colwell, K. S., Goddard, W. A., and Skiff, W. M. (1992). UFF, a full periodic table force field for molecular mechanics and molecular dynamics simulations. *J. Am. Chem. Soc.* 114, 10024–10035. doi: 10.1021/ja00051a040

Rappé, A. K., and Goddard, W. A. (1991). Charge equilibration for molecular-dynamics simulations. *J. Phys. Chem.* 95, 3358–3363. doi: 10.1021/j100161a070

Seref, O., Fazil, C., and Akpinar, M. V. (2006). Effect of cement on emulsified asphalt mixtures. *J. JMEPEG* 16, 578–583. doi: 10.1007/s11665-007-9095-2

Sitepu, H. (2009). Texture and structural refinement using neutron diffraction data from molybdite (MoO_3) and calcite ($CaCO_3$) powders and a Ni-rich Ni50.7 Ti49.30 alloy. *J. Am. Chem. Soc.* 24, 315–326. doi: 10.1154/1.3257906

Somasundaran, P., Fuerstenau, D. W., and Healy, T. W. (1964). Surfactant adsorption at the solid—liquid interface—dependence of mechanism on chain length. *J. Phys. Chem.* 68, 3562–3566. doi: 10.1021/j100794a021

Song, Q. S., Guo, X. L., Yuan, S. L., and Liu, C. B. (2009). Molecular dynamics simulation of sodium dodecyl benzene sulfonate aggregation on silica surface. *J. Acta Phys. Chim. Sin.* 25, 1053–1058. doi: 10.3866/PKU.WHXB20090623

Sun, H. (1998). COMPASS: an ab initio force-field optimized for condensed-phase applications overview with details on alkane and benzene compounds. *J. Am. Chem. Soc.* 114, 10024–10039. doi: 10.1021/jp980939v

Tan, Y. Q., Ouyang, J., Lv, J. F., and Li, Y. L. (2013). Effect of emulsifier on cement hydration in cement asphalt mortar. *J. Construct. Build. Mater.* 47, 159–164. doi: 10.1016/j.conbuildmat.2013.04.044

Vekeman, J., Faginas-Lago, N., Lombardi, A., Sánchez de Merás, A., García Cuesta, I., and Rosi, M. (2019). Molecular dynamics of CH4/N2 mixtures on a flexible graphene layer: adsorption and selectivity case study. *Front. Chem.* 7:386. doi: 10.3389/fchem.2019.00386

Wang, Y. X., Gao, Y. Q., Zhang, Q., and Meng, Q. (2018). Novel cationic emulsifier used for preparing slow-cracking and rapid-setting asphalt: synthesis, surface activity and emulsification ability. *J. Disper. Sci. Technol.* 39, 478–483. doi: 10.1080/01932691.2015.1120676

Wu, B. G., Yang, Y. R., Pan, X. F., Wang, X. S., and Liu, G. P. (1992). Novel synthetic method of lingninamine-type asphalt emulsifier. *J. Northeast For. Univ.* 3, 89–94.

Xu, L. H., Dong, F. Q., Wu, H. Q., Liu, W., Wang, Z., and Wang, J. M. (2016). Flotation separation of anionic collectors—surface crystal chemistry of spondite and kaolinite. *J. Acta Mineral. Sin.* 36, 265–270. doi: 10.16461/j.cnki.1000-4734.2016.02.015

Yan, L. M., and Zhu, S. H. (2013). *Theory and Practice of Molecular Dynamics Simulation[M]*. Beijing: Science Press.

Yang, L. H. (2004). *The Technology of Modified Asphalt and Modified Asphalt Emulsion [M]*. Beijing: Communications Press.

Yongjoo, K., Soohyok, I., and Hosin, L. (2011). Impacts of curing time and moisture content on engineering properties of cold in-place recycling mixtures using foamed or emulsified asphalt. *J. Mater. Civ. Eng.* 23, 542–553. doi: 10.1061/(ASCE)MT. 1943-5533002E0000209

Zhao, H., Li, H. P., Liao, K. J., and Li, Y. G. (2012). The anti-aging performance of emulsified asphalt. *J. Pet. Sci. Technol.* 30, 193–200. doi: 10.1080/10916461003792336

Zhou, Q., Wang, M., Guo, L., Boolchand, P., and Bauchy, M. (2019). Intermediate phase in calcium–silicate–hydrates: mechanical, structural, rigidity, and stress signatures. *J. Front. Mater.* 6:157. doi: 10.3389/fmats.2019.00157

Conflict of Interest: The authors declare that the research was conducted in the absence of any commercial or financial relationships that could be construed as a potential conflict of interest.

frontiers in Materials

ORIGINAL RESEARCH
published: 30 April 2020
doi: 10.3389/fmats.2020.00088

Study of Pavement Performance of Thin-Coat Waterborne Epoxy Emulsified Asphalt Mixture

Xu Cai, Wenke Huang, Juan Liang and Kuanghuai Wu**

School of Civil Engineering, Guangzhou University, Guangzhou, China

Waterborne epoxy emulsified asphalts (WEEA) have high densities, good chemical stabilities, and high viscosities. However, they have problems in terms of overly high stiffness and low-temperature brittleness when applied as thin-coat asphalt mixtures. In this study, testing was conducted to obtain the optimal mixing ratio for WEEA. Anti-sliding, rutting, water stability, Cantabro, and low-temperature bending tests were carried out to evaluate the performance of thin coating layers formed from open graded friction course (OGFC)-5 WEEA mixtures, with the results indicating that the optimal ratio of waterborne epoxy resin emulsion and curing agent was 2:1 and that the dosage of waterborne epoxy resin should be maintained between 15 and 30%. The surface texture depth and British Pendulum Number (BPN) of the OGFC-5 WEEA mixtures were larger than 0.91 mm and 77.4, respectively, and the WEEA mixtures had better water stabilities and spalling resistance performance than a mixture without WEEA. Waterborne epoxy resin dosages of 15 and 30% resulted in WEEA mixture stabilities of up to 4,285 and 8,798 times/mm, respectively, and tensile strengths at −10°C of 2.204 and 4.727 MPa, respectively. The relatively good pavement functional and low-temperature performance of the optimized OGFC-5 WEEA mixture suggest its usefulness as a pavement maintenance material.

Keywords: waterborne epoxy resin, emulsified asphalt mixture, thin-layer coating, open-graded friction course, road performance

OPEN ACCESS

Edited by:
Yiqiu Tan,
Harbin Institute of Technology, China

Reviewed by:
Ramadhansyah Putra Jaya,
Universiti Malaysia Pahang, Malaysia
Ru Mu,
Hebei University of Technology, China

****Correspondence:***
Wenke Huang
wukuanghuai@163.com
Kuanghuai Wu
hwk_gzu@163.com

Specialty section:
This article was submitted to Structural Materials, a section of the journal Frontiers in Materials

Received: *26 December 2019*
Accepted: *25 March 2020*
Published: *30 April 2020*

Citation:
Cai X, Huang W, Liang J and Wu K (2020) Study of Pavement Performance of Thin-Coat Waterborne Epoxy Emulsified Asphalt Mixture. Front. Mater. 7:88. doi: 10.3389/fmats.2020.00088

INTRODUCTION

Maintenance of the enormous and growing highway network system in China is becoming increasingly challenging. Cracks, ruts, pits, and asphalt pavement spalling affect traffic safety and reduce the service life of the pavement (Christina, 2019; Wu et al., 2019). It has been found that the application of emulsified asphalt is an effective method of pavement maintenance that is compatible with current developmental trends in asphalt pavement technology (Anthonissen et al., 2016; Law et al., 2017; Santos et al., 2018). Compared with hot mix asphalt, an emulsified asphalt mixture has many advantages for use as a construction material, including improving the construction environment, reducing the effects of environmental factors, saving energy, etc., and has therefore come to be widely used in preventive and daily pavement maintenance. However, the use of emulsified asphalt as a cementing material has a number of disadvantages, including low strength in the early stages of setting, insufficient cohesion, and poor water and temperature stability (Wang, 2015), all of which have restricted the popularization and application of emulsified asphalt.

Based on the performance of cold-mix asphalts before curing, a number of studies have focused on their use in strengthening the performance of asphalts. Some researchers have looked at cement as an additive and carried out indirect tensile, repeated load asphalt creep, and water damage tests to evaluate the performance of cold-mix asphalt mixtures in cement powder. The results of these assessments revealed that cement-modified emulsion mixtures often outperformed hot-mix asphalts (Oruc et al., 2006, 2007). Wang et al. (2015) evaluated various properties of fresh cement-emulsified asphalt mortar and found that increasing the asphalt/cement ratio significantly reduced the compressive strength of the mortar. A further investigation of the properties of cement-stabilized gravel modified by emulsified asphalt (Wang et al., 2017) revealed that cement-emulsified asphalt-stabilized gravel with 5 wt% cement performed well both mechanically and in terms of frost resistance. And some recent studies show that surfactants also have a good effect on increasing the strength of cement asphalt emulsion mixture (Ouyang et al., 2018, 2019; Yang et al., 2020). Other researchers have looked at the use of styrene-butadiene rubber (SBR), styrene-butylene-styrene (SBS), chloroprene rubber (CR), and other polymers to prepare modified emulsified asphalt. Compared with ordinary emulsified asphalt, the high-temperature rheological properties of the modified emulsified asphalts were slightly improved, but the low-temperature properties were essentially the same (Pan et al., 2015). Shafii et al. (2011) found that SBS-modified emulsified asphalt had better high- and low-temperature performance than other types of modified asphalt. To improve the compressive strength of cold-mix asphalt, Chávez-Valencia et al. (2007) added a polyvinyl acetate emulsion to emulsified asphalt and found that the compressive strengths of the test specimens were improved by 31% compared to that of an unmodified mixture. Because the performance of an asphalt mixture is strongly influenced by the physical and chemical properties of the minerals and binders used in the mixture, the adherence between minerals and binders has been extensively studied, with surface free energy used to calculate the amounts of adsorbed vapor corresponding to monolayer occupancy on the surfaces of materials with different additives. The results of these experiments have shown that the wet-condition adhesive bond strengths of binders with various mineral/aggregate combinations are improved through the use of additives (Khan et al., 2016). Kim et al. (2019) experimentally evaluated the short- and long-term performance of SBS-modified asphalt binder added to ground tire rubber and styrene-isoprene-styrene and found that the addition of styrene-isoprene-styrene can significantly improve rutting performances. Hamed et al. (2019) investigated the moisture susceptibility of emulsified asphalt treated with microbial carbonate precipitation, finding that the treatment significantly improved the moisture resistance of the mixture. Jiang et al. (2020) investigated the properties of asphalt binder in terms of the rutting of the cold recycling mix, with their results indicating that high-temperature performance could be improved significantly by adding polymer modifiers and that adding CR latex appeared to be a more effective method for improving the rutting resistance of emulsified asphalt.

The results of these previous lab studies indicate that the performance of SBS-modified emulsified asphalt that has been formed and cured is better than that of ordinary emulsified asphalt. However, the addition of polymers to emulsified asphalt does not appear to fundamentally change the characteristics of the emulsified asphalt. Some studies have also mentioned the difficulty of preparing emulsified asphalt mixtures and the necessity of further improving the stability of the materials. In practical applications, the shortcomings of the slow strength formation and the insufficient bonding of such mixtures with pavement have not been fully overcome. Furthermore, such mixtures are not suitable for use in damp environments. To overcome these problems, some researchers have explored the use of waterborne epoxy resin. Waterborne epoxy emulsified asphalts (WEEAs) produced by modification by water-based epoxy resins can be cured in damp conditions and at room temperature and have proven to have high densities, good chemical stabilities, and high viscosities (Yu, 2018). To obtain binding materials with high bonding strengths at high temperatures and high flexibilities at low temperatures, several WEEA preparation methods have been explored, with the resulting WEEAs exhibiting excellent bonding strength, crack resistance, and anti-impact properties and, depending on the preparation procedure, high water stability and the ability to adhere to aggregates (Yang et al., 2019). WEEA mixtures with aluminum trihydroxide and zinc borate as additives have been used in tunnel construction (Chen et al., 2018). Given the insufficient durabilities of conventional preventive maintenance techniques using bitumen emulsions, some researchers have investigated the performance of WEEA as a pavement preventive maintenance material, with the results indicating that the waterborne epoxy distributes evenly within the asphalt matrix, and significantly improves the skid resistance and durability of pavements maintained with asphalt emulsion coating layers (Hu et al., 2019). In the other research, WEEA mixtures have been used as permeating and solidifying seal coat materials in what could be considered a new generation of preventive maintenance treatments for asphalt pavements (Liang et al., 2019). It has been found that the technical compatibility of cured WEEA mixture is enhanced as the waterborne epoxy content increases over content ranges below 30% (Gu et al., 2019).

Despite the achievements in the research on WEEA mixtures, their application as thin-coat layers remain in the early stages. The shortcomings of the overly high stiffness and brittleness introduced by the waterborne epoxy resin remain to be solved. In practical engineering applications, high levels of stiffness result in enhanced stress on materials under heavy traffic conditions. Furthermore, the lack of thickness of thin-coat WEEA mixtures (which are generally less than 2 cm in depth) makes the material more prone to cracking in winter. To examine the low-temperature durability of thin-coat WEEA mixtures under heavy traffic loads, in this study a WEEA mixture with high strength, good bonding performance, high stability, and reduced brittleness for use as a thin-coating layer for pavement maintenance material was developed.

MATERIALS AND METHODS

Materials

Emulsified Asphalt

The emulsified asphalt used in this experiment was an SBS-modified emulsified asphalt produced by Jiangmen Qiangda Highway Materials Co., LTD. The sample was a dark brown liquid. All technical indices of the material were tested following the Standard Test Methods of Bitumen and Mixtures for Highway Engineering (JTG E20-2011), with the results listed in **Table 1**.

Waterborne Epoxy Emulsion and Curing Agent

The water-borne epoxy resin emulsion and curing agent used in the experiments (Shanxi Xinhua Chemical Co. LTD) could be stored stably at −5–40°C. The curing agent was a non-ionic water-soluble epoxy that contained no free surfactants and had a good compatibility with water-based epoxy resin. The agent could be cured at room temperature and directly diluted with water. The technical parameters of the waterborne epoxy resin emulsion and curing agent are listed in **Table 2**.

Aggregates and Cement

Diabase aggregates were used in the experiment, with all technical parameters tested using the Test Methods of Aggregate for Highway Engineering (2005; JTG E42-2005). Limestone powder was used in conjunction with Portland P.O42.5 cement. The results are listed in **Table 3**.

Mixture Gradation

In consideration of the emulsifying environment requirements of emulsified asphalt, an open graded friction course (OGFC)-5 mixture with a 5.2% asphalt-aggregate ratio was used in the experiment. A designed void of 22% was used to obtain better conditions for demulsifying. The gradation is indicated in **Table 4**.

Test Methods

Asphalt Performance Tests

To test the asphalt performance, waterborne-epoxy-resin-to-curing-agent mass ratios of 2:1, 1:1, and 1:2, with the proportion of water-borne epoxy content in the emulsified asphalt ranging from 5 to 10, 15, 20, 25, and 30%, were used. The WEEAs were prepared using the following cold mixing process: (1) the water-based epoxy resin emulsion was added to the emulsified asphalt, and the mix was stirred for 5 s; (2) the curing agent was then added and the mix was stirred again for 3 min. The performances of the respective WEEAs were studied using fluorescence microscopy, adhesion, and evaporation residue tests.

Particle Dispersion State Observation

A fluorescence microscope uses a color-filtering system to produce a specific wavelength of light to evaluate the uniformity of materials (Johann and Juergen, 2004). By using a fluorescence microscope, the particle size and dispersion state of waterborne epoxy resin in emulsified asphalt can be observed along with the micro-morphology of the resin and asphalt mixture. In this study, three samples were prepared for each mixture ratio. Each asphalt sample has an area of 30 mm^2 and an asphalt film thickness of 0.1 mm, as shown in **Figure 1**. The magnification of the fluorescence microscope was set to 400×.

Boiling Water Test

Boiling tests were carried out at 60°C using the Standard Test Methods of Bitumen and Mixtures for Highway Engineering (JTG E20-2011). The maximum nominal particle size of the aggregates used in the tests was 9.5 mm. Three specimens of each WEEA and one control sample without waterborne epoxy resin were tested.

Properties of Evaporative Residue

The effects of the waterborne epoxy resin emulsions added to the emulsified asphalts on the evaporative residual properties of the WEEAs were evaluated via penetration, softening point, and ductility testing.

Asphalt Mixture Performance Tests

Based on the results of Marshall testing, the asphalt-aggregate ratio was set to 5.2%. Water-borne epoxy dosages of 0, 15, and 30% were added, and 3% cement was used. The following mixture-forming steps were adopted: (1) 25 Marshall double-sided compactions were applied to preliminarily mold the specimens; (2) the specimens and molds were placed vertically in a 60°C oven for 12 h, and then another 25 Marshall double-sided compactions were applied; and (3) After demolding, the specimens were placed in a 60°C oven for 36 h. After returning the specimens to the test temperature, follow-up tests were conducted. A similar process was used to obtain rutting specimens.

Anti-sliding Performance Test

The British Pendulum Number (BPN) was used as a measure of the skid resistance of the pavements. Pendulum testing was carried out using Procedure T0964 of the Field Test Method of Subgrade and Pavement for Highway Engineering (2008; JTG E60-2008). As shown in **Figure 2**, three specimens were tested for each mixture.

The surface texture depths (TDs) of the asphalt mixture rutting specimens were measured using Procedure T0731 of the Standard Test Methods of Bitumen and Mixtures for Highway Engineering (2011). The TD results were calculated as follows:

$$\mathrm{TD} = \frac{100 \times V}{\pi \times D^2/4} = \frac{31831}{D^2}, \quad (1)$$

where V is the volume of the standard test sand and D is the average diameter of the flat sand.

Rutting Tests

The influence of the WEEA on the high-temperature stability of the mixtures was evaluated using rutting tests, with the dynamic stability index used to quantitatively evaluate rutting performance. Three specimens, each with dimensions of 300 mm × 300 mm × 50 mm, were tested for each material, with the average value of the three taken as the test result for each material. A solid rubber wheel with an outer diameter of 200 mm

TABLE 1 | Technical parameters of SBS-modified emulsified asphalt.

Test		Unit	Results	Method
Residual amount		%	0.02	T 0652
Charge		–	Cationic	T 0653
Demulsification velocity		–	Slow	T 0658
Properties of evaporative residue of emulsified asphalt	Asphalt content	%	62.9	T 0651
	Penetration at 25°C	0.1 mm	41	T 0604
	Softening point	°C	80.3	T 0606
	Ductility at 5°C	cm	56	T 0605
	Dynamic viscosity at 60°C	Pa's	216,858	T 0620
	Rotary viscometer at 135°C	Pa's	6.317	T 0625
	Solubility	%	99.02	T 0607
Elastic recovery at 25°C		%	98.4	T 0662
Storage stability	1 d	%	0.4	T 0656
	5 d	%	1.6	

TABLE 2 | Technical parameters of waterborne epoxy emulsion and curing agent.

Test	Unit	Waterborne epoxy emulsion	Curing agent
Appearance	–	Milky white resin emulsion	Yellowish uniform fluid
Solid content	%	50 ± 2	50 ± 2
Solid component	%	22–28	20–32
Viscosity at 25°C	MPa's	100–450	>2,000
pH	–	2–7	8–11
Specific gravity	–	1.01–1.08	1.00–1.08

TABLE 3 | Technical parameters of aggregates.

Tests	Unit	Aggregates size			Methods
		5–10 mm	3–5 mm	0–3 mm	
Crushing value	%	4.9	5.3	–	T 0316
Los Angeles abrasion value	%	6.1	6.1	–	T 0317
Water absorption	%	0.87	0.96	–	T 0307
Density	g/cm^3	2.93	2.92	2.93	T 0304/T 0328
Sand equivalent	%	–	–	87	T 0334
Methylene blue value	g/kg	–	–	14	T 0349

TABLE 4 | Gradation of OGFC-5.

Gradation	Mass percentage of aggregate passing through the following sieve pores (mm)/%							
	9.5	4.75	2.36	1.18	0.6	0.3	0.15	0.075
OGFC-5	100	76.5	14.7	9.3	7.7	6.3	5.3	4.5

and a width of 50 mm was used as a test wheel. During the testing, the contact pressure between the test wheel and the specimen was maintained at 0.7 MPa. The rolling speed of the test wheel was 42 times/min and the test temperature was 60°C, as shown in **Figure 3**.

Water Stability Tests

Water stability testing was carried out using Procedure T0709 of the Standard Test Methods of Bitumen and Mixtures for Highway Engineering (JTG E20-2011). Twelve Marshall specimens were formed and divided into two groups, one of which was immersed in a constant temperature bath at 60°C for 30 min, while the other was immersed in a constant temperature bath at 60°C for 48 h. The ratio of the average Marshall stabilities of the respective groups was used to evaluate the water stabilities of the mixtures.

Cantabro Tests

The adhesion properties of the asphalt and aggregate in each WEEA mixture were evaluated using the Cantabro test, with the results expressed as the percentage of mass lost by the Marshall specimens after a specified number of rotary hits using a Los Angeles test machine. Four specimens were evaluated for

FIGURE 1 | Samples for particle dispersion state observation.

FIGURE 2 | Pendulum test.

each material, with the average value taken as the test result for each material.

Low-Temperature Bending Tests

Low-temperature bending test were carried out using Procedure T0709 of the Standard Test Methods of Bitumen and Mixtures for Highway Engineering (JTG E20-2011). Each specimen had the dimensions 250 mm ± 2.0 mm (l) ×30 mm ± 2.0 mm (w) ×35 mm ± 2.0 mm (h). The specimens are shown in **Figure 4**. Testing was carried out at 0 ± 0.5°C and −10 ± 0.5°C at a loading rate of 1 mm/min. For each material, five specimens were fabricated.

The flexural tensile strength R_B, maximum flexural tensile strain ε_B at the beam bottom, and flexural stiffness modulus s_B at failure were calculated as follows:

$$R_B = \frac{3 \times L \times P_B}{2 \times b \times h^2}, \tag{2}$$

FIGURE 3 | Rutting tests.

FIGURE 4 | Bending test.

$$\varepsilon_B = \frac{6 \times h \times d}{L^2}, \tag{3}$$

$$s_B = \frac{R_B}{\varepsilon_B}, \tag{4}$$

where *b, h,* and *L* are, respectively, the width, height, and length of the specimen, P_B is the maximum load at the time of failure, and d is the mid-span deflection at the time of failure.

a) Control asphalt sample

ratio of waterborne epoxy resin to curing agent / waterborne epoxy dosage	2:1	1:1	1:2
5%			
10%			
15%			
20%			
25%			
30%			

b) Test samples with different proportion and dosage of waterborne epoxy

FIGURE 5 | Fluorescence microscopy analysis results.

a) Control sample

ratio of waterborne epoxy resin to curing agent / waterborne epoxy dosage	2:1	1:1	1:2
5%			
10%			
15%			
20%			
25%			
30%			

b) Results with different proportion and dosage of waterborne epoxy

FIGURE 6 | Boiling water test results.

RESULTS AND DISCUSSION

Asphalt Performance Test Results

Fluorescence Microscopy Analysis Results

The fluorescence results for the asphalt control group without waterborne epoxy and the test groups with different proportions and dosages of waterborne epoxy are shown in **Figures 5A,B**, respectively.

From **Figure 5A**, it is seen that the control asphalt sample turned yellow under the fluorescence microscope. From **Figure 5B**, at a 5% dosage of waterborne epoxy, all the waterborne epoxy resins are evenly distributed throughout the emulsified asphalt; as a result of the low content of waterborne epoxy resins, no network structure has formed. At a waterborne epoxy dosage of 15%, the oleophilic content of the waterborne epoxy resin and the oil content of the asphalt molecules have attracted each other and gradually formed a network structure. At dosages greater than 20%, the epoxy resin has agglomerated, resulting in unstable WEEA at ratios of 1:1 and 1:2. A comparison of the results by ratio indicate that the best distribution effect is reached at 2:1; thus, we recommend a dosage of waterborne epoxy of 30% with a ratio of 2:1.

Boiling Water Test Results

The water stabilities of the WEEA mixtures are primarily determined by the adhesive properties of the asphalts and the adhesion between the binder and aggregate. The adhesive grade

TABLE 5 | Adhesion level results.

Adhesion level		Waterborne epoxy dosage/%					
		5	10	15	20	25	30
Ratio of waterborne epoxy resin to curing agent	2:1	2	3	4	5	5	5
	1:1	2	3	4	5	5	5
	1:2	2	3	4	5	5	5

TABLE 6 | Evaporative residue performance test results.

Test	Unit	Waterborne epoxy dosage/%						
		0	5	10	15	20	25	30
Penetration at 25°C	0.1 mm	41	33.9	26.2	24.6	21.9	17.8	15.2
Ductility at 5°C	cm	62	80	63.9	40.1	7.3	–	–
Softening point	°C	80.3	80.7	82.1	84.1	>90	–	–

was determined according to the area of spalling, the higher the grade, the better the adhesion property. The results of the water boiling tests are shown in **Figure 6**, with the asphalt control group without waterborne epoxy resin results shown in **Figure 6A**, and the test group results shown in **Figure 6B**.

From **Figure 6A**, it is seen that a large post-testing area of asphalt spall has appeared on the surface of the aggregate, indicating poor adhesion to the aggregate in the emulsified asphalt without waterborne epoxy resin. From **Figure 6B**, it is seen that increasing the waterborne epoxy dosage decreases the spall area. At dosages greater than 15%, no spalling is observed. For a given waterborne epoxy dosage, the ratio of waterborne epoxy resin emulsion to curing agent has little effect on the adhesion between asphalt and aggregate. The adhesion grade was evaluated by visual observation, with the results shown in **Table 5**.

It is seen from **Table 5** that, because the molecular chain of the waterborne epoxy resin has many polar groups that have strong adsorption capacities with aggregates, adding an appropriate amount of waterborne epoxy resin to the emulsified asphalt can improve the viscosity of the mixture and the adhesion between the asphalt and aggregates. Based on this, we recommend a dosage of waterborne epoxy of greater than 15%.

Evaporative Residue Performance Test Results

Three indices—penetration, softening point, and ductility—were used to represent the viscosity and temperature sensitivity of the asphalts. The test results are listed in **Table 6**.

It is seen from the table that increasing the waterborne epoxy resin dosage changes each of these three indices significantly. As a result of the thermosetting property of the waterborne epoxy resin and the spatial network skeleton structure formed after the curing reaction, the evaporative residue gains a high strength and degree of temperature stability; indicating that enhancing the waterborne epoxy dosage makes the skeleton structure denser and the material harder. However, the penetration decreases sharply with dosage as a result of the increases in density and skeleton structure hardness. In the same manner, the ductility increases first and then decreases, while the softening point increases. At a waterborne epoxy dosage of 20%, the softening point increases to above 90°C.

Mixture Performance Test Results

The results of the predetermined anti-sliding performance, rutting, water stability, Cantabro, and low-temperature bending tests are listed in **Table 7**.

Anti-sliding Performance Test Results

It is seen from the table that the BPNs of the mixtures range from 77 to 82 and that all surface TDs are greater than 0.91 mm. Under the Specification for Design of Highway Asphalt Pavement (2017; JTG D50-2017), the surface texture depth requirement of asphalt pavement in humid regions (in which the average annual rainfall is more than 1,000 mm) is not less than 0.55 mm. The anti-sliding performance of the OGFC-5 mixture meets this requirement. It is also seen that the waterborne epoxy resin has little effect on anti-sliding performance.

Rutting Test Results

It is seen from **Table 7** that adding waterborne epoxy resin significantly improves the high-temperature stability of the mixture. The rutting depths of the mixture decreases, and the dynamic stability increases with increasing waterborne epoxy dosage. The dynamic stability of the mixture with 30% waterborne epoxy dosage is four times that of the mixture without water epoxy resin; this is because waterborne epoxy resin is a thermosetting resin that produces a post-curing skeleton structure that can improve the ability of the cementing material to resist loading deformation at high temperatures. Increasing the waterborne epoxy dosage improves the adhesion between aggregates and hardens the WEEA, leading to a mixture with a high level of hardness. In addition, the dynamic stability of the WEEA mixture is much higher than the specification requirements, indicating that the mixture has excellent high-temperature stability.

Water Stability Test Results

It is seen from **Table 7** that, although the standard and immersion Marshall stabilities of the mixture increases with the waterborne

TABLE 7 | Results of mixture performance tests.

Test			Unit	Waterborne epoxy dosage/%		
				0	15	30
Anti-sliding performance tests	Pendulum test		–	77.4	82.0	80.3
	Surface texture depth		mm	0.91	0.94	0.99
Rutting test	Rut depth		mm	1.432	1.245	0.963
	Dynamic stability		times/mm	1,986	4,285	8,798
Water stability test	Standard Marshall stability		kN	6.10	7.20	15.20
	Immersion Marshall stability		kN	5.29	7.56	15.79
	Residual stability		%	86.7	105.0	103.9
Cantabro Test	Mass loss		%	23.4	20.1	16.0
Low-temperature bending test	Flexural tensile strength R_B	0°C	MPa	0.728	1.898	4.516
		−10°C		1.014	2.204	4.727
	Maximum flexural tensile strain ε_B	0°C	με	1,314	1,556	2,130
		−10°C		1,441	1495	2,056
	Flexural stiffness modulus s_B	0°C	MPa	554	1,220	2,120
		−10°C		704	1,474	2,299

epoxy dosage, the increase obtained at a 15% dosage is not significant. However, increasing the dosage from 15 to 30% causes the Marshall stability to double. Looked at in conjunction with the results of the rutting and bending tests, these results might indicate that different loading methods lead to different results, and the unique loading method used by the Marshall test might not accurately reflect the strengthening effect of the WEEA on the material.

Compared with the mixture without WEEA, which has a residual stability of 86.7%, the residual stabilities of the WEEA mixtures are significantly improved and, in some cases, exceed 100%. This is the result of the hydration reaction of the cement continuing during the 48-h water bath maintenance, resulting in a cured waterborne epoxy product with a crosslinked structure that promotes the strength of the WEEA mixture.

Cantabro Test Results

From **Table 7**, it is seen that increasing the waterborne epoxy dosage decreases the mass loss in the mixture significantly. The appearances of the post-Cantabro test mixtures are shown in **Figure 7**. Increasing the waterborne epoxy dosage to 30% decreases the dispersion loss to 16%, indicating that the addition of waterborne epoxy resin helps to improve the cohesiveness of the emulsified asphalt. This result is consistent with that of the boiling water test.

FIGURE 7 | Specimens after Cantabro Test.

Low-Temperature Bending Test Results

From **Table 7**, it is seen that the use of WEEA significantly improves the flexural tensile strengths of the mixture. At the test temperature of 0°C, the flexural tensile strength of the mixture with 30% waterborne epoxy is five times that of the mixture without waterborne epoxy; at −10°C the flexural tensile strength is increased by a factor of nearly four. This result indicates that the WEEA significantly increases the strength of the asphalt mixture in proportion to the waterborne epoxy dosage. The maximum flexural tensile strain of the mixture also increases with the waterborne epoxy dosage. Although the increases in tensile strain are not as large as the increases in tensile strength, this result indicates that the WEEA has increased the deformation capacity of the material to some extent. The WEEA also increases the flexural stiffness modulus of the mixtures These results indicate that the network skeleton structure formed by WEEA increases the bonding effect and deformation ability of the asphalts, thereby enhancing the low-temperature performance of the asphalt mixture.

CONCLUSION

This study investigated the effects of using waterborne epoxy resin to modify emulsified asphalt. Specifically, the effects of waterborne epoxy resin dosage on the uniformity, compatibility, and adhesion of WEEA were studied. Following

these assessments, the road performance of OGFC-5 WEEA mixtures were studied. The main conclusions are as follows:

The optimal ratio of the waterborne epoxy resin emulsion and curing agent was found to be 2:1, while the recommended dosage range of waterborne epoxy resin was determined to be 15–30%. The Cantabro test results were consistent with those of the boiling water tests.

The OGFC-5 WEEA mixtures were shown to have relatively good pavement functional performance and high temperature performance. The TDs were all larger than 0.91 mm and the BPNs were all larger than 77.4. The residual stabilities of some of the WEEA mixtures exceeded 100%, and the dynamic stabilities of the WEEA mixtures with 15 and 30% waterborne epoxy dosages were measured at 4,285 and 8,798 times/mm, respectively.

The addition of WEEA significantly improved the low-temperature performance of the mixture. Using 15 and 30% waterborne epoxy resin dosages, the flexural tensile strengths at −10°C were 2.204 and 4.727 MPa, respectively. The maximum flexural tensile strain and flexural stiffness modulus results indicate that the WEEA increased the deformation capacities of the materials.

DATA AVAILABILITY STATEMENT

The datasets analyzed in this article are not publicly available. Requests to access the datasets should be directed to wukuanghuai@163.com.

AUTHOR CONTRIBUTIONS

XC and KW contributed to the conceptualization. WH contributed to the validation. XC and JL contributed to the investigation. KW and JL provided the resources. XC and JL curated the data. XC wrote and prepared the original draft. WH reviewed and edited the manuscript. KW supervised the study.

FUNDING

This work was financially supported by the National Natural Science Foundation of China (Grant Nos.: 51708144 and 51878193).

REFERENCES

Anthonissen, J., Van den Bergh, W., and Braet, J. (2016). Review and environmental impact assessment of green technologies for base courses in bituminous pavements. *Environ. Impact Asses.* 60, 139–147. doi: 10.1016/j.eiar.2016.04.005

Chávez-Valencia, L. E., Alonso, E., Manzano, A., Pérezb, J., Contreras, M. E., and Signoret, C. (2007). Improving the compressive strengths of cold-mix asphalt using asphalt emulsion modified by polyvinyl acetate. *Constr. Build. Mater.* 21, 583–589. doi: 10.1016/j.conbuildmat.2005.07.017

Chen, R., Gong, J., Jiang, Y., Wang, Q., Xi, Z., and Xie, H. (2018). Halogen-free flame retarded cold-mix epoxy asphalt binders: rheological, thermal and mechanical characterization. *Constr. Build. Mater.* 186, 863–870. doi: 10.1016/j.conbuildmat.2018.08.018

Christina, P. (2019). Sustainability factors in pavement materials, design, and preservation strategies: a literature review. *Constr. Build. Mater.* 211, 539–555. doi: 10.1016/j.conbuildmat.2019.03.242

Field Test Methods of Subgrade and Pavement for Highway Engineering (2008). *JTG E60*. Beijing: China Communications Press.

Gu, Y., Tang, B., He, L., Yang, F., Wang, H., and Ling, J. (2019). Compatibility of cured phase-inversion waterborne epoxy resin emulsified asphalt. *Constr. Build. Mater.* 229:116942. doi: 10.1016/j.conbuildmat.2019.116942

Hamed, A. D., Abolfazl, M. M., Mohsen, K., and Bahar, S. (2019). Improving the resistance to moisture damage of cold mix asphalt modified by eco-friendly microbial carbonate precipitation (MCP). *Constr. Build. Mater.* 213, 131–141. doi: 10.1016/j.conbuildmat.2019.03.262

Hu, C., Zhao, J., Leng, Z., Partl, M. N., and Li, R. (2019). Laboratory evaluation of waterborne epoxy bitumen emulsion for pavement preventative maintenance application. *Constr. Build. Mater.* 197, 220–207. doi: 10.1016/j.conbuildmat.2018.11.223

Jiang, J., Ni, F., Zheng, J., Han, Y., and Zhao, X. (2020). Improving the high-temperature performance of cold recycled mixtures by polymer-modified asphalt emulsion. *Int. J. Pavement Eng.* 21, 41–48. doi: 10.1080/10298436.2018.1435882

Johann, E., and Juergen, H. (2004). *Method for Fluorescence Microscopy, and Fluorescence Microscope*. U.S. Patent No 6,806,953. Washington, DC: U.S. Patent and Trademark Office.

Khan, A., Redelius, P., and Kringos, N. (2016). Evaluation of adhesive properties of mineral-bitumen interfaces in cold asphalt mixtures. *Constr. Build. Mater.* 125, 1005–1021. doi: 10.1016/j.conbuildmat.2016.08.155

Kim, H. H., Mazumder, M., Lee, M.-S., and Lee, S.-J. (2019). Evaluation of high-performance asphalt binders modified with SBS, SIS, and GTR. *Adv. Civ. Eng.* 2019:2035954. doi: 10.1155/2019/2035954

Law, E. P., Diemont, S. A. W., and Toland, T. R. (2017). A sustainability comparison of green infrastructure interventions using emery evaluation. *J. Clean. Prod.* 145, 374–385. doi: 10.1016/j.jclepro.2016.12.039

Liang, H., Wang, D., Wang, G., Li, D., Xu, C., and Liang, X. (2019). Numerical simulation and laboratory testing verification on the performance of an asphalt pavement seal coat with superficially permeating and solidifying properties. *J. Test. Eval.* 47, 4427–4451. doi: 10.1520/JTE20170625

Oruc, S., Celik, F., and Akpinar, M. V. (2007). Effect of cement on emulsified asphalt mixtures. *J. Mater. Eng. Perform.* 16, 578–583. doi: 10.1007/s11665-007-9095-2

Oruc, S., Celik, F., and Aksoy, A. (2006). Performance of cement modified dense graded cold-mix asphalt and establishing mathematical model. *Indian J. Eng. Mater. S.* 13, 512–519. doi: 10.1109/TCAPT.2006.885844

Ouyang, J., Hu, L., Yang, W., and Han, B. (2019). Strength improvement additives for cement bitumen emulsion mixture. *Constr. Build. Mater.* 198, 456–464. doi: 10.1016/j.conbuildmat.2018.11.280

Ouyang, J., Zhao, J., and Tan, Y. (2018). Modeling mechanical properties of cement asphalt emulsion mortar with different asphalt to cement ratios and temperatures. *J. Mater. Civ. Eng.* 30:04018263. doi: 10.1061/(asce)mt.1943-5533.0002480

Pan, J., Du, S., Chang, R., Pei, Q., and Cui, D. (2015). Effect of emulsifier content on the rheological properties of asphalt emulsion residues. *J. Appl. Polym. Sci.* 2015:41806. doi: 10.1002/app.41806

Santos, J., Bressi, S., Cerezo, V., Lo Presti, D., and Dauvergne, M. (2018). Life cycle assessment of low temperature asphalt mixtures for road pavement surfaces: A comparative analysis. *Resour. Conserv. Recycle* 138, 283–297. doi: 10.1016/j.resconrec.2018.07.012

Shafii, M. A., Abdul Rahman, M. Y., and Ahmad, J. (2011). Polymer modified asphalt emulsion. *Int. J. Civ. Environ. Eng.* 11, 43–49. doi: 10.1016/j.jcis.2016.07.063

Specification for Design of Highway Asphalt Pavement (2017). *JTG D50*. Beijing: China Communications Press.

Standard Test Methods of Bitumen and Mixtures for Highway Engineering (2011). *JTG E20*. Beijing: China Communications Press.

Test Methods of Aggregate for Highway Engineering (2005). *JTG E42*. Beijing: China Communications Press.

Wang, J. (2015). *Influence Factors of Structure-Formation and Properties of Waterborne Epoxy-Emulsified Asphalt*. master's thesis, Chongqing Jiaotong University, Chongqing.

Wang, Y., Tan, Y., Guo, M., and Wang, L. (2017). Influence of emulsified asphalt on the mechanical property and microstructure of cement-stabilized gravel under freezing and thawing cycle conditions. *Materials* 10:504. doi: 10.3390/ma10050504

Wang, Z., Shu, X., Rutherford, T., Huang, B., and Clarke, D. (2015). Effects of asphalt emulsion on properties of fresh cement emulsified asphalt mortar. *Constr. Build. Mater.* 75, 25–30. doi: 10.1016/j.conbuildmat.2014.11.013

Wu, S., Wen, H., Zhang, W., Shen, S., Mohammad, L., Faheem, A., et al. (2019). Field performance of top-down fatigue cracking for warm mix asphalt pavements. *Int. J. Pavement Eng.* 20, 33–43. doi: 10.1080/10298436.2016.1248204

Yang, G., Wang, C., Fu, H., Yan, Z., and Yin, W. (2019). Waterborne epoxy resin–polyurethane–emulsified asphalt: preparation and properties. *J. Mater. Civ. Eng.* 31:04019265. doi: 10.1061/(ASCE)MT.1943-5533.0002904

Yang, W., Ouyang, J., Meng, Y., Tang, T., Chen, J., and Han, B. (2020). Effect of superplasticizer and wetting agent on volumetric and mechanical properties of cold recycled mixture with asphalt emulsion. *Adv. Mater. Sci. Eng.* 5, 1–11. doi: 10.1155/2020/6251653

Yu, D. (2018). *Study on Waterborne Epoxy Resin Modified Emulsified Asphalt and the Performance of Mixture*. master's thesis, Chongqing Jiaotong University, Chongqing.

Conflict of Interest: The authors declare that the research was conducted in the absence of any commercial or financial relationships that could be construed as a potential conflict of interest.

frontiers in Materials

ORIGINAL RESEARCH
published: 12 May 2020
doi: 10.3389/fmats.2020.00101

Characterization of Sulphoaluminate Cement-Asphalt Emulsion Mortar for Cement and Asphalt Mortar Repair

*Chao Yang[1], Junhao Li[1], Zhe Zhu[2], Shaohui Wang[2] and Yunpeng Liu[1]**

[1] State Key Laboratory of Silicate Materials for Architectures, Wuhan University of Technology, Beijing, China, [2] China Building Materials Federation, Beijing, China

A sulpho cement-asphalt emulsion mortar was developed for the repair of damaged cement asphalt emulsion mortar. Various sulfoaluminate/Portland cement and asphalt emulsion/cement mass ratios, as well as emulsion types, were studied with respect to the setting time, rheological properties, volume stability, and mechanical properties of the repair materials in order to determine a reasonable mix proportion. The proper contents of cementitious materials and asphalt emulsion were determined. A possible relationship between the mechanical properties and the asphalt emulsion/cement mass ratio was found based on scanning electron microscopy analysis. Moreover, the shrinkage rates of the repair mortar in the fresh and hardened states showed different trends with an increase in the asphalt emulsion/cement mass ratio. The results shed light on the repair mortar for CA mortar with high efficiency and low cost.

Keywords: cement and asphalt mortar, repair mortar, sulphoaluminate cement, asphalt emulsion, high-speed railway

OPEN ACCESS

Edited by:
Jian Ouyang,
Dalian University of Technology, China

Reviewed by:
Zhenjun Wang,
Chang'an University, China
Wengui Li,
University of Technology Sydney, Australia

***Correspondence:**
Yunpeng Liu
liuyunpeng@whut.edu.cn

Specialty section:
This article was submitted to Structural Materials, a section of the journal Frontiers in Materials

Received: *25 December 2019*
Accepted: *03 April 2020*
Published: *12 May 2020*

Citation:
Yang C, Li J, Zhu Z, Wang S and Liu Y (2020) Characterization of Sulphoaluminate Cement-Asphalt Emulsion Mortar for Cement and Asphalt Mortar Repair. Front. Mater. 7:101. doi: 10.3389/fmats.2020.00101

INTRODUCTION

Cement and asphalt mortar (CA mortar) is the key component of high-speed railways, supporting the weight of the slab track and train and acting as a shock-absorber (Leiben et al., 2018; Najjar et al., 2019). However, under the coupling effects of high-frequency loading and environmental erosion (Zhu et al., 2014; Fu et al., 2015; Le et al., 2019), the CA mortar tends to be damaged or broken, which significantly influences the structural and driving safety (Zhu et al., 2014; Liu et al., 2016). Therefore, this requires effective and rapid repair.

The CA mortar consists mainly of cement and asphalt emulsions. Compared with cement and concrete materials, the CA mortar is typically a low-modulus material owing to its high asphalt emulsion-to-cement ratio (usually over 0.5) (Wang et al., 2015; Liu and Liang, 2017). For example, the modulus values of the CA mortar for the Shinkansen slab (Japan) and the Max Bögl slab (Germany) were 100–300 MPa and 7,000–10,000 MPa, respectively. However, the modulus of the CA mortar for the Max Bögl slab would be 800∼1,200 MPa if tested with the same methods used for the Shinkansen slab.

Repair materials for CA mortar need to meet the following requirements considering the characteristics of the CA mortar:

1) A balance between the workable time and the fast hardening properties: The time allowed for CA mortar repair is usually less than 4 h; thus, repair materials must present sufficient workable time to fulfil the repair section. Moreover, they need to present fast hardening properties (such as sufficient 4 h mechanical properties and a short time interval between the initial and final settings of the repair materials) to guarantee the appropriate early mechanical properties.
2) Compatible modulus and strength: Repair materials for CA mortar should present mechanical properties that are compatible with those of the substrate mortar in order to ensure that the combined repair system withstands the applied stresses and maintains its structural integrity (Rangaraju, 2007). The modulus (28 days) and compressive strength (28 days) of CA mortar are 800–1,200 MPa and over 15 MPa, respectively, which are also the requirements for the repair mortar.
3) Good flowability properties: Since the CA mortar works as a shock-absorber layer between the slab track and the concrete roadbed, with a thickness of about 30–80 mm, it should be highly flowable for grouting (Ouyang and Tan, 2015; Peng et al., 2015; Leiben et al., 2018; Ouyang and Shah, 2018). Thus, the repair mortar needs good flowability to fulfil the repair section with $D_{5\ min} \geq 280$ mm and $D_{10\ min} \geq 280$ mm (the slump flow test methods of repair mortar are shown in section Mix Proportions and Experimental Design).
4) Good volume stability: The repair mortar also needs good volume stability to avoid affecting the structure height of the slab track, which is important for the safety of high-speed railways.

The most commonly used repair materials for CA mortar are resin or resin mortar, which have low modulus but are too expensive to be used widely. Moreover, our previous work (Liu et al., 2014) has shown that resin mortar may not bond well with CA mortar because of the oily and hydrophobic interface created by the high content of asphalt. Sulphoaluminate cement (SAC)-based repair materials, with good repair properties and low costs, have found wide applications and have drawn much attention in the cement and concrete repair fields. However, their modulus is too high for CA mortar repair. Some polymer latex or polymer powder has been added to cement mortar to improve its adhesive and water-proof properties (Ramli and Tabassi, 2012; Muhammad et al., 2015; Göbel et al., 2018). However, the polymer content was low (the polymer emulsion to cement mass ratio usually 0.05–0.15) so that its modulus was still higher than that of CA mortar (Göbel et al., 2018) which means that it may not meet the low modulus requirements for CA mortar repair.

The purpose of this study is to develop, using high asphalt content, sulphoaluminate cement-based repair materials with low modulus and ensure the cost is kept low. The effects of key components such as cementitious materials and asphalt emulsion on the properties and microstructure of repair mortar were studied.

TABLE 1 | Composition and properties of PC and SAC cement.

	PC	SAC
COMPOSITION (wt, %)		
SiO_2	21.46	6.45
Al_2O_3	5.64	20.58
Fe_2O_3	2.95	1.35
CaO	60.59	43.72
MgO	1.64	1.83
SO_3	2.75	17.89
Ignition loss	2.95	6.13
PHYSICAL PROPERTIES		
Density (g/cm^3)	3.12	3.04
Surface area (m^2/kg)	349	282
Setting time (min)		
Initial setting	129	28
Final setting	190	50
COMPRESSIVE STRENGTH (MPa)		
3 days	24.0	45.2
28 days	51.7	50.4

TABLE 2 | Properties of asphalt emulsion.

			Evaporated residue	
Solid content/%	**Sieve residue/%**	**Storage stability (5 days, 25°C) (%)**	**Penetration/25°C, 0.1 mm**	**Softening point/°C**
60.1	0	1.3	67	46.5

MATERIALS AND EXPERIMENTAL METHODS

Raw Materials

1) Cement: Ordinary Portland cement P.O 42.5 (PC) and sulfoaluminate cement SAC 42.5 were used in this study. The composition and properties of the cements are listed in **Table 1**.
2) Asphalt emulsion (AE): Anionic asphalt emulsions were used in this study. The emulsifier dosage was 2.0%. The properties are listed in **Table 2**.
3) Fine aggregate: River sand with an apparent density of 2,630 kg/m^3 was used. The water absorption rate was 1.8% and the mud content was 0.4%.
4) The superplasticizer (SP) used was a polycarboxylic high-performance water reducer with 20.0% solid content and 26.6% water-reducing ratio.
5) The deformer (DF) used in this study was silicone based with 30.1% solid content and a pH value of 8.2.

Mix Proportions and Experimental Design

The experimental design is shown in **Figure 1**. The main objective of this study is to determine the mix proportion of repair materials, which includes the composition of dry powder and the asphalt emulsion contents.

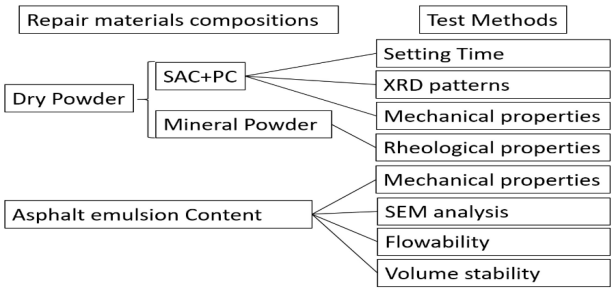

FIGURE 1 | Experimental design.

TABLE 3 | Mix proportion of sulphoaluminate cement and Portland cement.

Sample	S0	S1	S2	S3	S4	S5	S6	S7	S8	S9	S10
SAC/PC	0:10	1:9	2:8	3:7	4:6	5:5	6:4	7:3	8:2	9:1	10:0

The cement-asphalt emulsion paste was prepared to investigate the effect of different SAC/PC ratios on the setting time. The mix proportion of SAC-PC paste is shown in **Table 3**. The asphalt emulsion/cement ratio (*A/C*) and water-to-cement ratio (*w/c*) were both 0.4. The water in the asphalt emulsion was also taken into account when calculating *w/c*.

The effect of the SAC/PC ratio on the mechanical properties of the repair mortar was studied by testing the mortar strength. The mortar was prepared with cement/standard sand mass ratio *c/s* = 1:2, *A/C* = 0.4, and *w/c* = 0.4. The superplasticizer content was 1 *wt*% of the cementitious materials.

The mineral powders improved the rheological properties of the mortar. Two different types of mineral powder, fly ash and slag powders, were employed to prepare the SAC paste. The *w/c* and the *A/C* ratios were 0.4 and 0.3, respectively.

To investigate the effect of the *A/C* ratio on the rheological properties of the pastes, *SAC-AE* pastes with *A/C* ratios varying from 0 to 0.7 were prepared with *w/c* = 0.4. The amount of water in the asphalt emulsion was incorporated into the calculation of the *w/c* ratio.

According to the results above, the dry powder content of the repair materials could be determined. Then, the effects of different *A/C* ratios on the mechanical, rheological, and volume stability properties were investigated to determine the proper *A/C* ratio and evaluate the performance of the repair mortar.

Experimental Methods

Setting Time

The method was developed based on the standard specification for the test of setting time of cement paste (AQSIQ, 2001) and reported before (Wang et al., 2008). The paste was prepared in a mold, and every 30 min a steel needle penetrated the grout from the upper surface, and after 30 s, the depth was read. The setting process can be characterized by plotting the depth against time.

Slump Flow Property Tests

The slump flow property of the repair mortar was tested according to the Chinese Railway Specification (2008). The mortar was poured into a tube (inner diameter D = 50 mm, height H = 190 mm) and its diameter was measured until the grout stopped flowing, after this the tube was elevated by 15 cm.

Rheological Properties Test

A 350-mL SAC-AE sample was used for rheological measurements using an R/S-SST rheometer manufactured by Brookfield (Middleboro, Massachusetts). The shear rate underwent 2 equal rounds, increasing from 0 to 150 s^{-1} (ascending stage) within 30 s and then decreasing from 150 s^{-1} to 0 (declining stage) within the same time.

Shrinkage Test

The expansion rate of the repair mortar in the fresh state was measured using cylinder methods, as shown in the Chinese Railway Specification (2008). The fresh repair mortar was poured into a 250 ml graduated flask with its surface covered with plastic film to prevent moisture exchange. The initial depth of the mortar (h_0) and its depth at a different time (h_t) were measured using a Vernier caliper with a precision of 0.02 mm. The shrinkage rate was calculated using Equation (1):

$$P = \frac{(h_t - h_0)}{h_0} \times 100\% \quad (1)$$

Where P is the expansion rate (%), h_t is the depth of the mortar after t min (mm), and h_0 is the initial depth after casting (mm).

The shrinkage rate of hardened RM was measured according to the specifications of the National Development Reform Commission (2004). The mortar was prepared with dimensions of 25 × 25 × 280 mm, and then cured for 24 h in a standard curing box at a temperature of 20 ± 3°C and a relative humidity over 90%. After it was cured in water at a temperature of 20 ± 1°C for 2 days, the mortar was removed and wiped clean before the initial length L_0 was measured. Then, it was continuously cured in a curing box at a temperature of 20 ± 3°C and a relative humidity of 50 ± 4%. The sample length at different curing times, L_t, was measured. The shrinkage rate was calculated according to Equation (2):

$$S = \frac{(L_0 - L_t) \times 100}{250} \quad (2)$$

Where S is the shrinkage rate of the sample (%), L_o is the initial length of the sample (mm), and L_t is the sample length at different curing times (mm).

Test of Mechanical Properties

Specimens with dimensions of 40 × 40 × 160 mm were tested using a Materials Testing System with a constant loading rate of 0.05 KN/s for the flexural test and 0.5 KN/s for the compressive test according to AQSIQ (1999).

The test method of the repair mortar modulus is as follows; the sample is loaded to 800 N with a loading rate of 1 mm/min and then unloaded with the same rate according to the Chinese Railway Specification (2008). This process was repeated 4 times, and the stress and strain of 3/4 and 0.5 MPa in the fifth test curve were taken and calculated as follows:

$$E = \frac{(\sigma_b - \sigma_a)\, h}{b - a} \quad (3)$$

Where E is the modulus of the sample, h is the height of the sample, σ_b is the compressive strength of the 3/4 part of the fifth test curve, σ_a is 0.5 MPa, b is the strain of the 3/4 part in the fifth test curve, and a is the strain of 0.5 MPa in the fifth test curve.

SEM Test

The microstructure of the SAC-AE paste was examined using an S-3400N scanning electron microscope (SEM) (Hitachi, Japan).

XRD Analysis

The XRD curves of the SAC-AE paste were measured with non-monochromatic Cu Kα X-ray radiation at 40 kV and 40 Ma, and recorded from 5° (2θ) to 75° (2θ).

RESULTS AND DISCUSSION

Effect of the SAC/PC Ratio on the Setting Time of SAC/PC-AE Pastes

The setting time of the (SAC/PC)-AE paste is shown in **Figure 2**. The addition of SAC significantly decreased the setting time. When the SAC content was 0, the initial and final setting times of the pure PC-AE paste were 878 and 1,035 min, respectively. When the SAC/PC ratio was over 1:1, the setting time of the (SAC/PC)-AE paste sharply decreased. The initial and final setting times of S6 (SAC/PC ratio of 6:4) were ˜15 and 27 min, respectively. Then, the setting time became stable when the SAC content further increased. This is significantly different from the SAC/PC pastes whose setting time would first decrease and then increase with the increase in the SAC content (Chen et al., 2007). The different results can be attributed to the addition of the asphalt emulsion. The setting time of the SAC/PC-AE paste is governed by both the cement hydration speed and the asphalt emulsion demulsification speed. The stable initial setting time of the composite paste indicated that the asphalt emulsion demulsification speed was the main factor controlling the setting time.

The composite cement in the wide mix proportion range would lead to a sharp decrease in the setting time. When the SAC/PC ratio was 1:1, the difference between the initial and final setting times of the SAC/PC-AE paste was only 7 min. XRD patterns (**Figure 3**) showed that the substitution of 50% PC by SAC led to stronger AFt peaks and weaker $C_4A_3\bar{S}$ peaks. This is because the $C_4A_3\bar{S}$ in SAC and C_3S in PC have mutual promotion effects on the cement hydration process, which accelerates the setting process.

Effect of the SAC/PC Ratio on the Mechanical Properties of the SAC/PC-AE Mortar

The effect of SAC/PC on the mechanical properties of the composite paste is shown in **Figure 4**. As can be seen, the flexural and compressive strengths first decreased and then increased with the increase in the SAC content. The strength decreased when the SAC content varied from 20 to 80%. This is because when the SAC content changed from 20 to 80% and therefore the SAC/PC paste showed a faster hydration speed according to the results in section Effect of the SAC/PC Ratio on the Setting Time of SAC/PC-AE Pastes. The hydration products of SAC and PC do not have enough time to form a dense microstructure, thus decreasing the compressive strength. Moreover, an obvious fast setting appeared when the SAC content was of 50–80% as shown in **Figure 2**. Thus, the SAC/PC ratio was 90/10 when considering both the setting time and mechanical strength results.

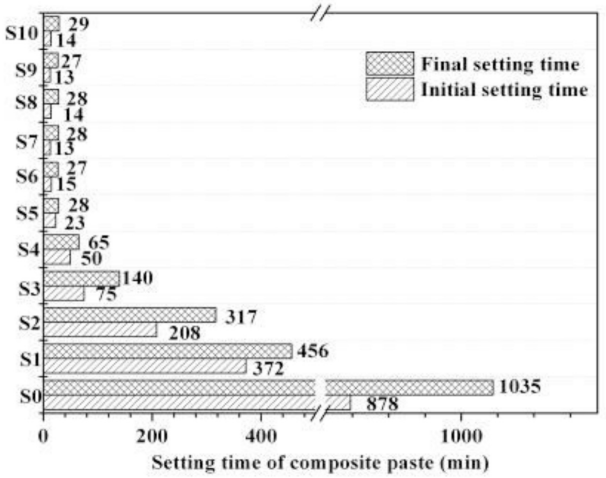

FIGURE 2 | Setting time of composite cement and asphalt emulsion paste.

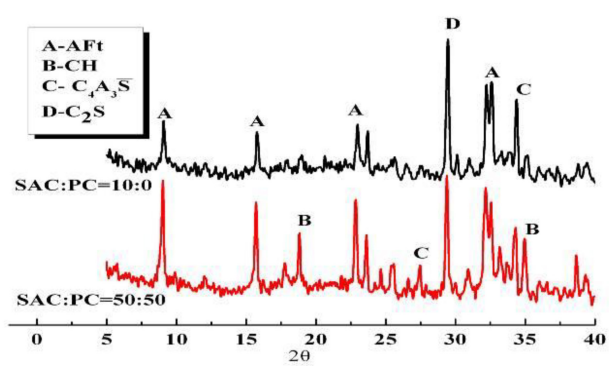

FIGURE 3 | XRD results of composite paste with different SAC/PC ratio.

Effect of Mineral Mixture on the Rheological Properties of Sac-Ae Pastes

Figure 5 compares the effect of the mineral mixture on the rheological properties of the SAC-AE pastes (A/C = 0.3, w/c = 0.4). The curves in the ascending stage could be fitted according to the Bingham model (Peng et al., 2015) and the results are listed in **Table 4**. The addition of fly ash (FA) and mineral powder (MP) reduced yielding stress. The addition of 10% mineral powder (MP) showed the best improvement. This could be attributed to the improvement of the cement grain

grading by mineral powder, which released more free water and improved the rheological properties.

Effect of Asphalt Emulsion Content on the Mechanical Properties and Microstructure of Repair Mortars

According to the above results, the composition of 1,500 kg dry powder was determined as follows: SAC 415 kg, PC 45 kg, mineral powder 40 kg, and river sand 1,000 kg. The dry powder was then used to prepare the repair mortar, as shown in **Table 5**. The effect of the A/C ratio on the mechanical properties of the repair mortar is shown in **Figure 6**.

As can be seen, the strength of the repair mortar sharply decreased with an increase in the *A/C* ratio. The 4 h compressive strength of the repair mortar decreased from 16.8 to 9.6 MPa, i.e., by 42%, when the *A/C* ratio increased from 0 to 0.1. However, when the *A/C* ratio increased to 0.3, the strength changed slightly. When the ratio continually increased to 0.5, the strength decreased sharply again and slightly changed when *A/C* = 0.7. The same trend could be found for the mortar at 1–56 days age. Coupling with the effect of *A/C* ratio on the repair mortar modulus (shown in **Table 5**), the *A/C* ratio is determined as 0.3, which is compatible with the modulus of substrate CA mortar (800–1,200 MPa).

TABLE 4 | Effect of mineral material on the rheological properties of the SAC-AE paste.

Parameter	Control sample	FA10%	FA20%	MP10%	MP20%
$Theta_t$/(Pa)	50.53	31.73	46.00	7.38	7.82
η_{pl}/(Pa·S)	0.76	0.82	1.14	0.34	0.35
R^2	0.996	0.999	0.998	0.975	0.974

Figure 7 shows the microstructure of the repair mortar with different *A/C* ratios at 4 h. A significant amount of needle-shaped AFt can be observed in the mortar when *A/C* = 0. A small asphalt film was found on the surfaces of the hydration products when *A/C* = 0.1 and 0.3. When *A/C* increased to 0.5 and 0.7, most hydration product surfaces were coved with the asphalt film. It can be concluded that when the *A/C* ratio was less than 0.3, there was no successive asphalt film in the mortar. When the *A/C* ratio was 0.3, the asphalt cement ratio by volume (V_A/V_C) was ˜0.91. Ouyang's work (Ouyang et al., 2018) also showed that when V_A/V_C was above 1, a continuous asphalt membrane could form in the cement asphalt paste. When V_A/V_C was less than 1, no conspicuous continuous asphalt membrane was observed. Therefore, the compressive strength of the SAC-AE repair materials sharply decreased again when the A/C ratio increased from 0.3 to 0.5 and slightly changed when *A/C* = 0.7.

Effect of Asphalt Emulsion Content on the Flowability of Repair Mortars

The effect of the *A/C* ratio on the spreading of the repair mortar is shown in **Figure 8**. The spreading first increased and then decreased with an increase in the *A/C* ratio. When *A/C* was 0.3, the mortar had an optimum spreading of 330 mm. The results coincided with the viscosity results of the composite cement paste shown in **Figure 9**. The flowability of cement paste can be improved by decreasing its apparent viscosity (Ouyang et al., 2016). Indeed, the SAC-AE paste with a decreased viscosity showed better flowability in the repair mortar. The SAC-AE paste with an *A/C* ratio of 0.3 had the lowest viscosity; thus, the repair mortar had the optimum flowability. This could be attributed to the improvement of anionic emulsion addition on the rheological properties of the SAC-AE pastes. The zeta potentials of the anionic emulsion and SAC hydration product AFt were ˜-70 and +4.53 mV, respectively. When the *A/C* ratio was 0.3, the

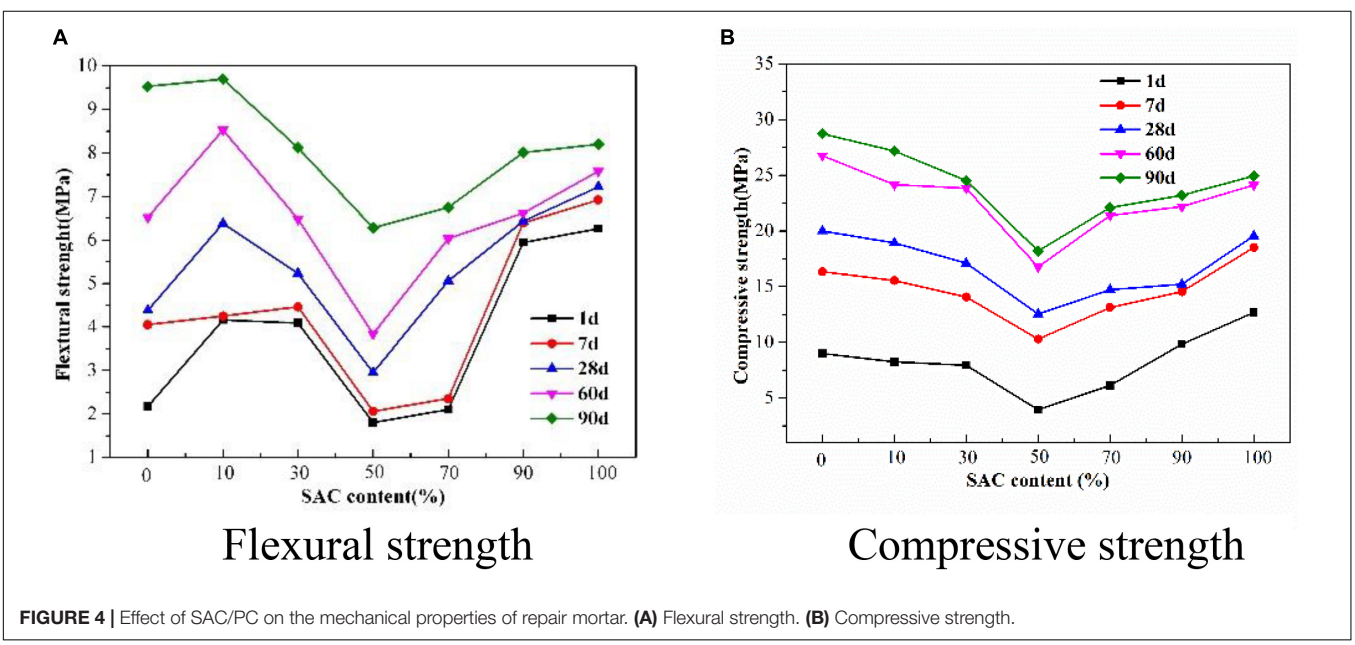

FIGURE 4 | Effect of SAC/PC on the mechanical properties of repair mortar. **(A)** Flexural strength. **(B)** Compressive strength.

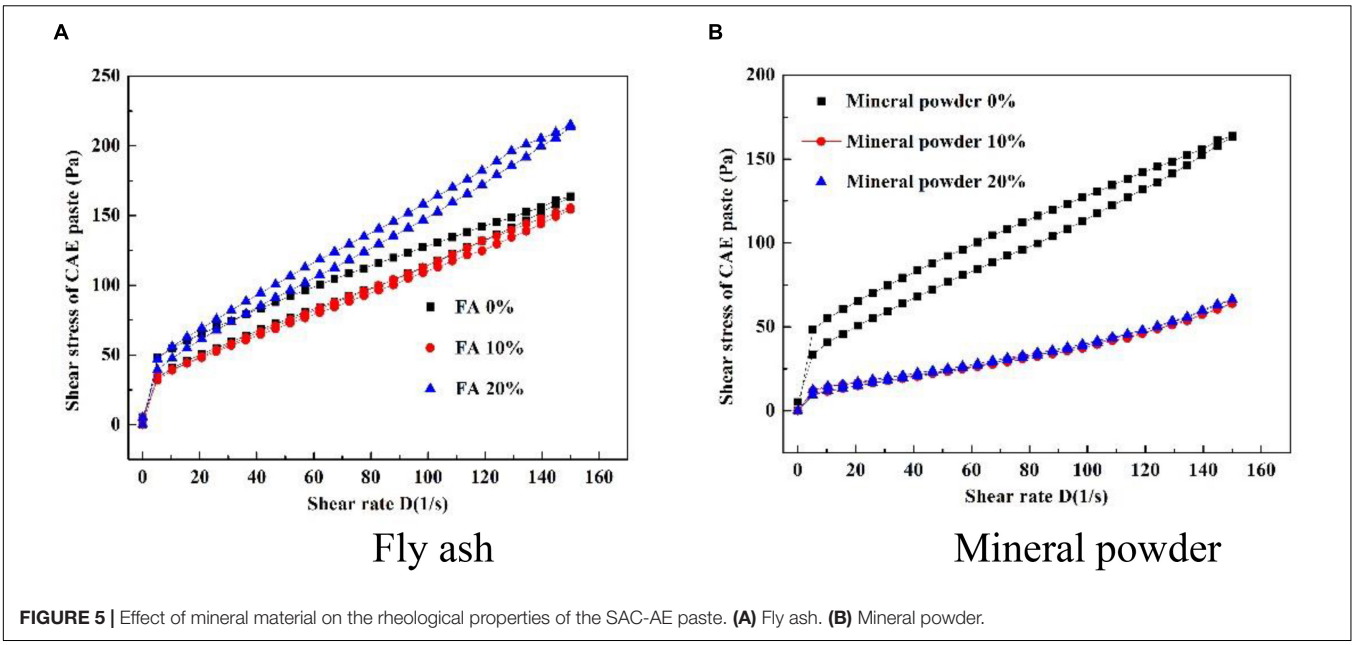

FIGURE 5 | Effect of mineral material on the rheological properties of the SAC-AE paste. **(A)** Fly ash. **(B)** Mineral powder.

TABLE 5 | Modulus of repair mortar (kg/m^3).

								Modulus (MPa)	
	G*	W	AE	DF	SP	A/C	W/C	7 days	28 days
R1	1,500	240	0	/	8	0	0.52	1,495	1,534
R2	1,500	220	50	0.06	8	0.1	0.52	1,269	1,345
R3	1,500	180	150	0.10	8	0.3	0.52	961	1,037
R4	1,500	140	250	0.16	8	0.5	0.52	695	783
R5	1,500	100	350	0.20	8	0.7	0.52	407	512

**G indicates the dry powder of the repair mortar.*

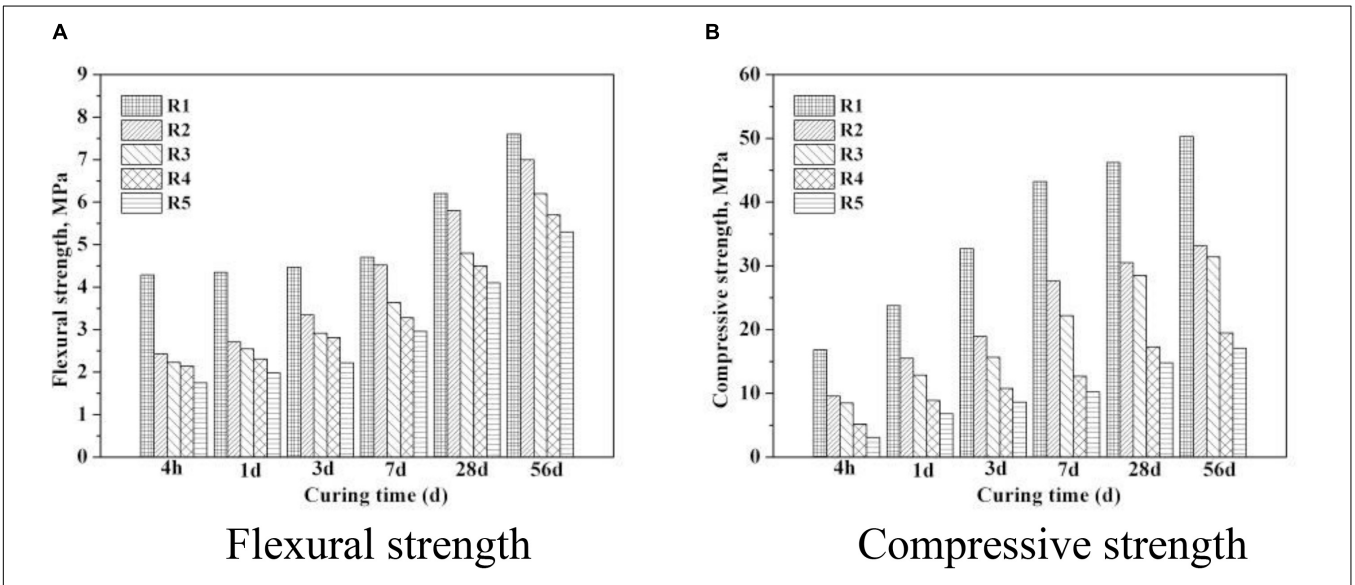

FIGURE 6 | Influence of asphalt content on the properties of repair materials. **(A)** Flexural strength. **(B)** Compressive strength.

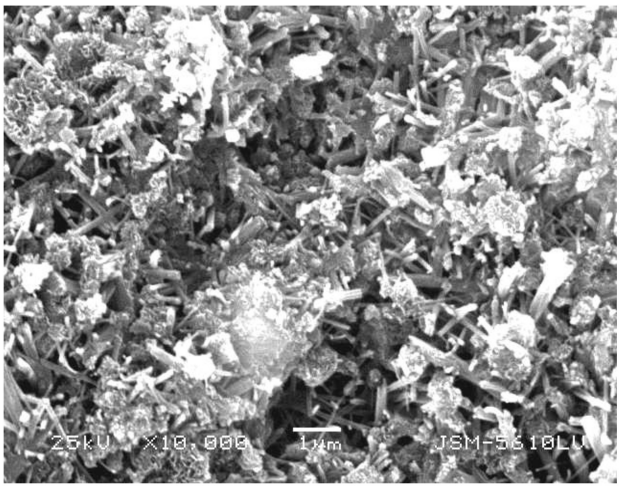

A/C=0, 10000 times

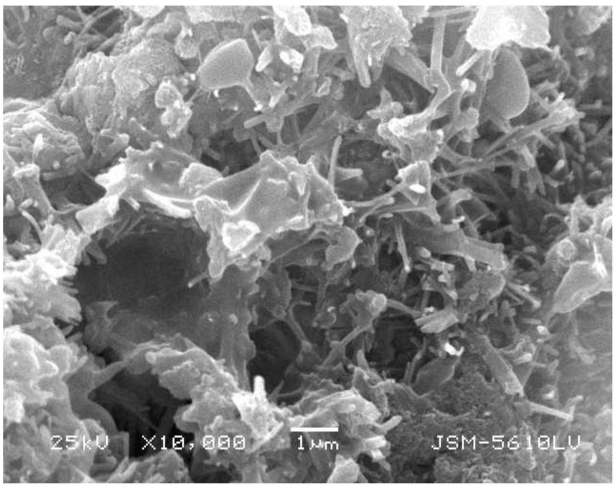

A/C=0.1, 10000 times

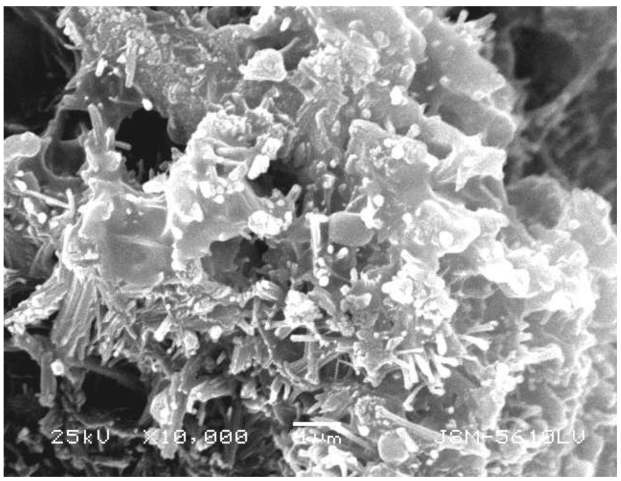

A/C=0.3, 10000 times

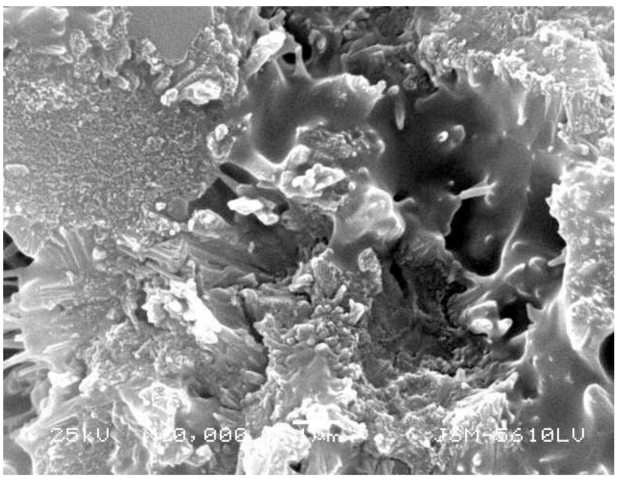

A/C=0.5, 10000 times

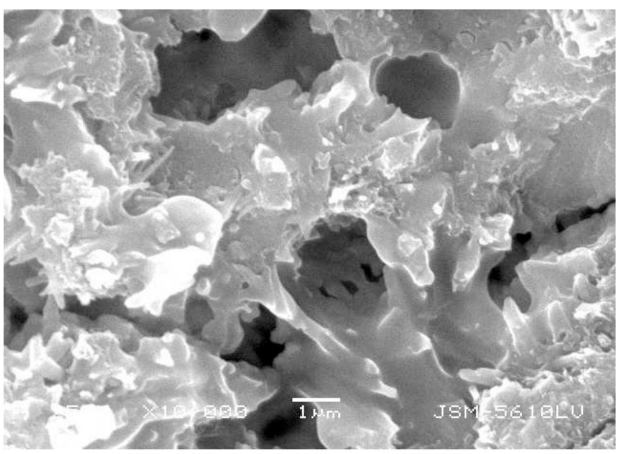

A/C=0.7, 10000 times

FIGURE 7 | Microstructure of the repair mortar with different *A/C* ratios (4 h).

absorbed asphalt particles on the AFt surfaces showed a good dispersion effect and improved the rheological performance (Liu et al., 2019).

Effect of Asphalt Emulsion Content on the Volume Stability of Repair Mortars

Figure 10A shows the expansion rate variation of the repair mortar with different *A/C* ratios with 0–2 h curing time. As it can be seen, the expansion rate was negative, indicating that it shrank. The shrinkage rate increased with increasing *A/C* ratio. The shrinkage of the repair mortar in the fresh state could be attributed to the quick burst of many bubbles induced by the emulsifier in the asphalt emulsion. The air content increased and density decreased (**Table 6**) with an increase in the *A/C* ratio. These bubbles were burst by SAC hydration, which decreased the mortar height. When SAC continued hydration, the AFt amount increased, which made the mortar denser and thus reduced the shrinkage rate.

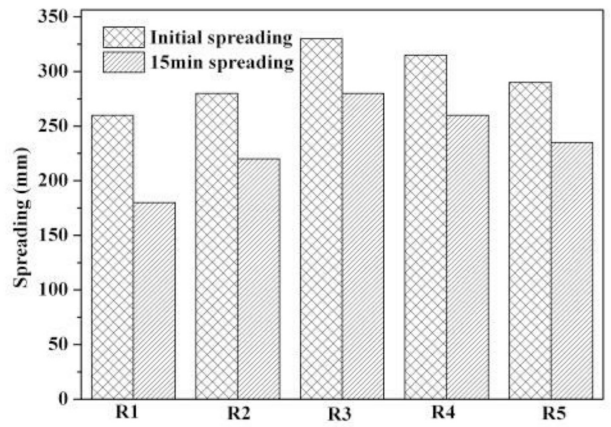

FIGURE 8 | Effect of *A/C* ratio on the spreading properties.

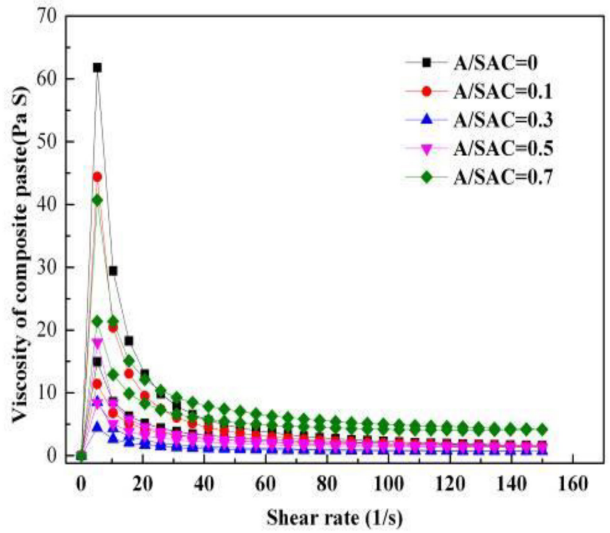

FIGURE 9 | Viscosity of SAC-AE pastes.

TABLE 6 | The air content of repair mortar with different *A/C* ratios.

No.	Density (kg/m^3)	Air content (%)
R1	2,072	1.5
R3	2,010	2.4
R5	1,954	4.2

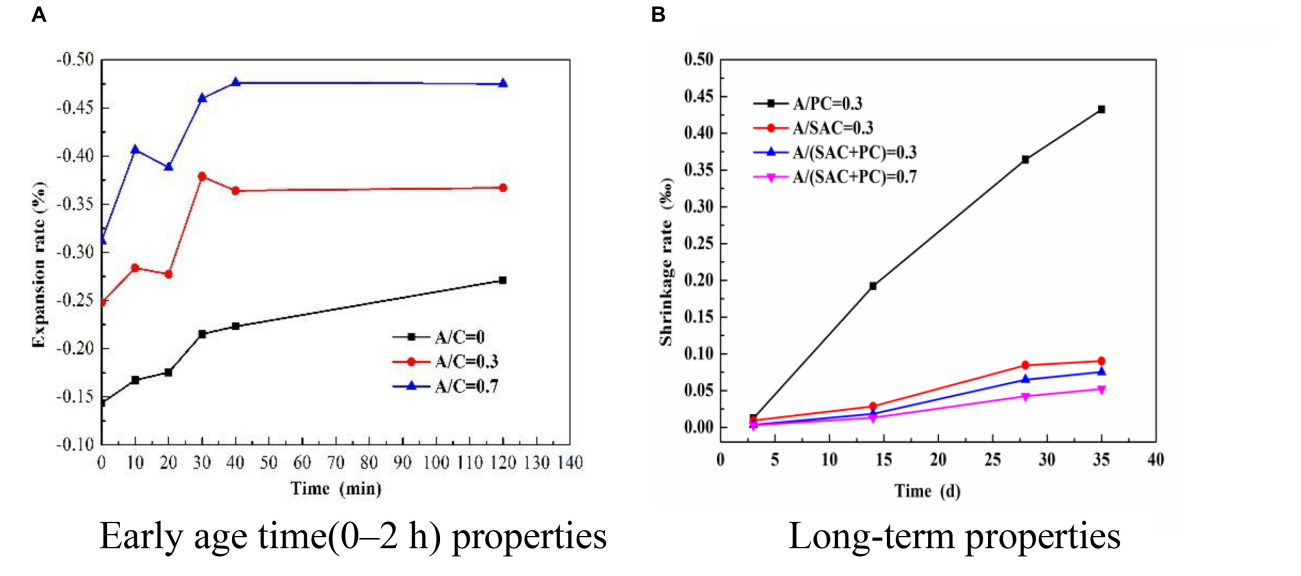

FIGURE 10 | Volume stability of cement-based repair material with low modulus. **(A)** Early age time (0–2 h) properties. **(B)** Long-term properties.

As shown in **Figure 10B**, the long-term shrinkage rate of repair materials decreased with an increase in the *A/C* ratio. The mortar shrinkage was mainly caused by water evaporation in the pores. When the asphalt emulsion content increased, the asphalt droplets absorbed the surfaces of SAC and decreased the water evaporation in the pores. Moreover, this may be because the addition of an asphalt emulsion changes the pore structure in the mortar, this requires further investigation.

Figure 10B also compares the shrinkage rates of PC, SAC, and PC/SAC pastes with different curing times. As can be seen, the shrinkage rate of PC mortar increased with curing time. The SAC and SAC/PC pastes showed a lower shrinkage rate and were stable with an increase in curing time. Moreover, the SAC/PC paste showed a lower shrinkage rate. This could be attributed to the accelerating effect on cement hydration by the addition of PC. More AFt was generated in the early stages, which could compensate for the mortar shrinkage.

CONCLUSION

1) The optimum mix proportion of the repair materials was determined. The proper SAC/PC ratio was 90/10. The addition of 10% mineral powder improves the rheological properties of repair mortar. Repair mortar with an A/C ratio of 0.3 has proper mechanical properties, optimum flowability, and volume stability.
2) The composition of SAC and PC in a wide mix proportion would have an adverse effect on the setting time and strength of composite pastes due to the mutual promotion effect on SAC and PC hydration.
3) The mechanical properties and structure of the repair mortar were determined by the *A/C* ratio. When $A/C \leq 0.3$, the asphalt droplets could not form the successive film structure and the asphalt film existed in the dispersed phase. When $A/C > 0.3$, the asphalt phase changed from the dispersed phase to a successive phase.
4) The shrinkage rate of repair materials increased and decreased with an increase in the *A/C* ratio in the early and late stages, respectively. In addition, the composite of SAC and PC could reduce the shrinkage rate, which could be attributed to accelerated SAC hydration by the addition of PC.

DATA AVAILABILITY STATEMENT

The datasets generated for this study are available on request to the corresponding author.

AUTHOR CONTRIBUTIONS

CY and JL co-wrote the manuscript. ZZ and SW contributed to the discussion part. YL designed and performed the experiments.

ACKNOWLEDGMENTS

We would like to thank the financial support from the National Natural Science Foundation of China (51972250) and Hubei Technology Innovation Key Program (2018AAA004).

REFERENCES

AQSIQ (1999). *Method of Testing Cements-Determination of Stength*. Beijing: AQSIQ.

AQSIQ (2001). *Test Methods for Water Requirement of Normal Consistency, Setting Time and Soundness of the Portland Cements*. Beijing: AQSIQ, 346–2001.

Chen, J., Li, B. X., and Lu, Y. Y. (2007). Experimental study on the properties of OPC- SAC mixed cement. *J. Chon. J. Univ.* 29, 121–124.

Chinese Railway Specification (2008). *Technical Specification of Cement Asphalt Emulsion Mortar for CRTSI Non-Ballast slab Track*. Beijing: China Railway Publishing House.

Fu, Q., Xie, Y.-J., Long, G.-C., Meng, F., and Song, H. (2015). Temperature sensitivity and model of stress relaxation properties of cement and asphalt mortar. *Constr. Build. Mater.* 84, 1–11.

Göbel, L., Osburg, A., and Pichler, B. (2018). The mechanical performance of polymer-modified cement pastes at early ages: ultra-short non-aging compression tests and multiscale homogenization. *Constr. Build. Mater.* 173, 495–507.

Le, T. H. M., Park, D.-W., and Seo, J.-W. (2019). Evaluation on the mechanical properties of cement asphalt mortar with quick hardening admixture for railway maintenance. *Constr. Build. Mater.* 206, 375–384.

Leiben, Z., Wang, X., Wang, Z., Yang, B., Tian, Y., and He, R. (2018). Damping characteristics of cement asphalt emulsion mortars. *Constr. Build. Mater.* 173, 201–208.

Liu, B., and Liang, D. (2017). Effect of mass ratio of asphalt to cement on the properties of cement modified asphalt emulsion mortar. *Constr. Build. Mater.* 134, 39–43.

Liu, Y., Wang, F., Hu, S., and Liu, M. (2016). Compatibility of repair materials with substrate low-modulus cement and asphalt mortar (CA mortar). *Constr. Build. Mater.* 126, 304–312.

Liu, Y., Wang, F., Liu, M., and Hu, S. (2014). A microstructural approach to adherence mechanism of cement and asphalt mortar (CA mortar) to repair materials. *Constr.Build. Mater.* 66, 125–131.

Liu, Y., Wang, F., Zhang, W., and Hu, S. (2019). Rheological properties of sulfoaluminate cement–asphalt emulsion paste. *J. Mater. Civil Eng.* 31:04018340.

Muhammad, N. Z., Keyvanfar, A., Abd Majid, M. Z., Shafaghat, A., and Mirza, J. (2015). Waterproof performance of concrete: a critical review on implemented approaches. *Constr. Build. Mater.* 101, 80–90.

Najjar, S., Mohammadzadeh Moghaddam, A., Sahaf, A., Rasaei Yazdani, M., and Delarami, A. (2019). Evaluation of the mixed mode (I/II) fracture toughness of cement emulsified asphalt mortar (CRTS-II) using mixture design of experiments. *Constr. Build. Mater.* 225, 812–828.

National Development Reform Commission (2004). *Standard Test Method for Drying Shrinkage of Mortar*. Beijing: National Development Reform Commission, 603.

Ouyang, J., Han, B. G., Yu, C., Zhou, W. J., and Li, W. G. (2016). The role and interaction of superplasticizer and emulsifier in fresh cement asphalt emulsion paste through rheology study. *Constr. Build. Mater.* 125, 643–653.

Ouyang, J., and Shah, S. P. (2018). Factors influencing the structure build-up of fresh cement asphalt emulsion paste. *Road Mater. Pavement Design* 19, 87–103.

Ouyang, J., and Tan, Y. (2015). Rheology of fresh cement asphalt emulsion pastes. *Constr. Build. Mater.* 80, 236–243.

Ouyang, J., Zhao, J. Y., and Tan, Y. Q. (2018). Modeling mechanical properties of cement asphalt emulsion mortar with different asphalt to cement ratios and temperatures. *J. Mater. Civil Eng.* 30:4018263.

Peng, J., Deng, D., Huang, H., Yuan, Q., and Peng, J. (2015). Influence of superplasticizer on the rheology of fresh cement asphalt paste. *Case Stud. Constr. Mater.* 3, 9–18.

Ramli, M., and Tabassi, A. A. (2012). Effects of different curing regimes on engineering properties of polymer-modified mortar. *J. Mater. Civil Eng.* 24, 468–478.

Rangaraju, R. R. P. A. P. R. (2007). Analysis of compatibility between repair material and substrate concrete using simple beam with third point loading. *J. Mater. Civil Eng.* 19, 1060–1069.

Wang, F., Liu, Z., Wang, T., and Hu, S. (2008). A novel method to evaluate the setting process of cement and asphalt emulsion in CA mortar. *Mater. Struct.* 41, 643–647.

Wang, Z., Shu, X., Rutherford, T., Huang, B., and Clarke, D. (2015). Effects of asphalt emulsion on properties of fresh cement emulsified asphalt mortar. *Constr. Build. Mater.* 75, 25–30.

Zhu, S., Fu, Q., Cai, C., and Spanos, P. D. (2014). Damage evolution and dynamic response of cement asphalt mortar layer of slab track under vehicle dynamic load. *Sci. China Tech. Sci.* 57, 1883–1894.

Conflict of Interest: The authors declare that the research was conducted in the absence of any commercial or financial relationships that could be construed as a potential conflict of interest.

frontiers in Materials

ORIGINAL RESEARCH
published: 14 May 2020
doi: 10.3389/fmats.2020.00122

Characteristics of the Cement Asphalt Emulsion Mixture With Early-Age Strength and Flowability

Yaogang Tian[1,2], Xiaohui Yan[1], Dong Lu[1], Zhenjun Wang[1], Jun Zhang[3], Ouming Xu[1] and Weiguang Li[4]**

[1] School of Materials Science and Engineering, Chang'an University, Xi'an, China, [2] Engineering Research Center of Transportation Materials, Ministry of Education, Chang'an University, Xi'an, China, [3] School of Construction Machinery, Chang'an University, Xi'an, China, [4] School of Highway, Chang'an University, Xi'an, China

Cement asphalt emulsion mixture (CAEM) presents low early-age strength and poor flowability, which limits its application range at a certain degree. In this paper, CAEM with high early-age strength and flowability was proposed. The flowability, compressive strength, flexural strength of CAEM at different periods and 28 days elastic modulus of CAEM were investigated. In addition, evolution of composition and microstructure of CAEM was analyzed by X-ray diffraction (XRD), scanning electronic microscope (SEM), and mercury intrusion porosimetry (MIP). The results indicated that the compressive strength of CAEM can be enhanced quickly in several hours. It could achieve 17–24 MPa at 6 h and almost reached 79–90% of the 28 days compressive strength. SEM and XRD analysis found that the hydration products in CAEM at different periods were obviously different. The hydration products of 2 h filled the micro pores of the mixture. After 28 days, the hydration products were connected to each other, resulting in a denser structure. The results of MIP analysis showed that the pore cumulative volume of CAEM was similar for 2 h and 28 days samples. These results testified that CAEM had high early-age strength.

Keywords: cement asphalt emulsion mixture, high early-age strength, high flowability, mechanism, microstructure characteruizations

OPEN ACCESS

Edited by:
Dae-Wook Park, Kunsan National University, South Korea

Reviewed by:
Yang Zhou, Southeast University, China
Ionut Ovidiu Toma, Gheorghe Asachi Technical University of Iaşi, Romania

****Correspondence:***
Yaogang Tian
tianguang78@126.com
Weiguang Li
yxh406779136@126.com

Specialty section:
This article was submitted to Structural Materials, a section of the journal Frontiers in Materials

Received: *13 February 2020*
Accepted: *16 April 2020*
Published: *14 May 2020*

Citation:
Tian Y, Yan X, Lu D, Wang Z, Zhang J, Xu O and Li W (2020) Characteristics of the Cement Asphalt Emulsion Mixture With Early-Age Strength and Flowability. Front. Mater. 7:122. doi: 10.3389/fmats.2020.00122

INTRODUCTION

Cement asphalt emulsion mixture (CAEM) is an organic-inorganic composite material formed by the combination of hydration of cement and demulsification of emulsified asphalt. CAEM has been widely used in road maintenance and rehabilitation due to the combined merits of the high mechanical properties of cement materials and the flexibility of asphalt materials, low environmental impact, and cost effectiveness (Zhong and Chen, 2002; Lu et al., 2009; Qiang et al., 2011; Doyle et al., 2013; Tian et al., 2013; Tyler et al., 2014; Ling et al., 2016; Ouyang et al., 2020). Despite the aforementioned benefits of CAEM, there is a defect that the corners cannot be fully compacted and result in a poor adhesion between new and old materials due to the poor rheological property of CAEM (Hu et al., 2009; Dołżycki et al., 2017; Liu and Liang, 2017). There will be secondary damage occurred on the repair site when it is exposed to the adverse weather such as rainfall or freezing and thawing. In addition, repair materials should meet the strength requirements to early open to traffic at different conditions. Studies have shown that it took a long

time for repair materials to reach their full strength (Qiang et al., 2011; Fang et al., 2016; Liu and Liang, 2017; Du, 2018). Therefore, in order to improve the strength of the road and early open to traffic, the properties of the new CAEM must satisfy the requirements of good flowability and high early-age strength.

It is a common belief that increasing the dosage of cement could effectively improve the strength of CAEM (Lu et al., 2009; Yan et al., 2017; Ouyang et al., 2018). Yan et al. (2017) has studied the early strength of the asphalt emulsion mixture with various cement contents, and the results showed that the addition of cement to asphalt emulsion mixture improved its early-age strength. With the increase of cement content, the strength of mixture increased. However, excessive contents of cement may cause cracks in the pavement. Liu and Liang (2017) has reported that the flow time increased with the increase of asphalt to cement ratio (A/C), while the compressive strength, and 28 days elastic modulus showed the opposite trend. Lin et al. (2015) has studied the mechanism of early strength of CAEM and concluded that cement played a major role in the first 3-day of early strength, while emulsified asphalt played the predominant role in both early and final strength. Therefore, the effect of A/C on the early strength of CAEM is important. Studies have reported that the type of asphalt would also affect the strength of CAEM. Normally, both cationic and anionic asphalt emulsion are utilized in different types of CAEM. Research works conducted by Plank and Hirsch (2007), Tan et al. (2013), Ouyang et al. (2016), Li et al. (2018), etc. have shown that the anionic asphalt emulsion was more suitable than cationic asphalt emulsion for formulating CAEM when a higher strength was required. Therefore, an anionic asphalt emulsion was selected in the selection of materials in order to improve the strength of the CAEM.

As is well known, the water to cement ratio (W/C) exerts a major influence on the flowability of cement concrete and can be expected to have an important effect on the flowability of CAEM. Ouyang et al. (2019b) has studied the effect of water content on mechanical properties of cement bitumen emulsion mixture and recommended that the optimum water content of cement bitumen emulsion mixture should be determined by the maximum indirect tensile strength in the mix design. In addition, the emulsified asphalt contains moisture, Ouyang and Shah (2018) also reported that the dosage of asphalt emulsion was the main factor influencing the rheological property of the fresh cement asphalt emulsion mortar. It was verified that the pore structures of hydration products had remarkable influences on the mechanical properties and durability of cementitious materials (Zhou et al., 2018; Zhou et al., 2020a,b), and were affected by W/C ratio obviously. Therefore, it is necessary to systematically study the high flowability properties and microstructure of CAEM with various W/C ratios.

In this paper, a new kind of CAEM with high early-age strength and flowability was proposed, the flowability, compressive strength, and flexural strength of CAEM at different periods and 28 days elastic modulus of CAEM were investigated. Additionally, X-ray diffraction (XRD), Scanning Electron Microscope (SEM), and mercury intrusion porosimetry (MIP) were used to characterize the microstructure evolution of the CAEM. The research results would provide reference parameters for pavement construction.

MATERIALS AND EXPERIMENTAL METHODS

Materials

The selection and basis of materials were list as following:

(1) Asphalt emulsion: asphalt emulsion with evaporated residue content of 60.0% was prepared. The properties of asphalt emulsion are shown in **Table 1**. The test methods of asphalt emulsion were in accordance to Chinese Standard JTJ E20-2011.

(2) Cement: in order to obtain high early-age strength of CAEM, Sulphoaluminate cement (SAC 42.5), and Portland cement (P.O 42.5) were mixed with a ratio of 2:8 (wt%). The properties of cement are given in **Table 2**. The test methods of cement were in accordance to Chinese Standard GB 175-2007.

(3) Aggregate: the coarse aggregates used in this paper were crushed natural aggregates with continuous grading and the fine aggregates used were natural sand. The max particle size of coarse aggregates was 20 mm, the crushing value, sediment percentage, needle and sheet percentage of the coarse aggregates were 12.6, 0.5, and 8.5%, respectively. The fineness modulus of natural sand was 2.8, plotted in Zone II according to Chinese Standard JTG E42-2005.

(4) Additives: Studies (Tan et al., 2013; Ouyang et al., 2019a; Ouyang et al., 2020) have shown that adding additives could effectively improve the performance of CAEM. United expansing agent (solid content 30.1% and density 2750 kg m^{-3}) and polycarboxylate superplasticizer (water reducing rate 25%) were added to improve the volume stability and flowability of CAEM. Additionally, organic silicon defoamer (PH = 7) was used to reduce air void content of CAEM, the compound admixture was used to control the setting time of CAEM, which was a mixture of boracic acid (H_3BO_3) and lithium carbonate (Li_2CO_3) in a ratio of 4:1 (wt%).

TABLE 1 | Properties of asphalt emulsion.

Properties	Results
1.18 sieve test (%)	0.002
1 d storage stability (%)	0.8
15°C ductility (cm)	160
25°C penetration (0.1 mm)	102
Soft pointing (°C)	48
Residue by distillation (%)	60.4
The average particle diameter (μm)	2.29
Solubility(C_2HCl_3; %)	99.5

TABLE 2 | Properties of cement.

Type of cement	Setting time (min)		Flexural strength (MPa)		Compressive strength (MPa)	
	Initial time	Final time	3 days	28 days	3 days	28 days
SAC 42.5	55	125	7.5	8.7	44.7	50.1
P.O 42.5	155	300	4.3	9.5	24.3	52.2

TABLE 3 | Mix proportions of CAEM.

Mix	A/C	W/C	CAEM (kg m^{-3})				
			Asphalt emulsion	Cement	Water	River sand	Aggregate
I	0.18	0.30	116	385	69.1	602	1220
II	0.18	0.31	116	385	73	602	1220
III	0.18	0.32	116	385	76.8	602	1220
IV	0.24	0.30	154	385	53.9	602	1220
V	0.30	0.30	193	385	38.3	602	1220

Mix Proportions

The raw materials were mixed in the bowl in this order: Firstly, aggregate and half of water mixed together for about 2 min; Secondly, the blended cement and additives mixed together for about 2 min, and then the remaining water and asphalt emulsion mixed together for 5 min until a homogeneous CAEM was obtained.

Mix proportions of CAEM are listed in **Table 3**. The water mentioned in the mix proportion does not include the water in the asphalt emulsion.

Experimental Methods

Flowability

The flowability of fresh CAEM was measured by the slump of the mixture according to the practical experience and Chinese Standard JTJ E30-2005.

Early-Age Mechanical Properties

The early-age mechanical properties of CAEM were quantified by compressive strength and flexural strength at 2 h, 6 h, 3 days, and 28 days, respectively. Cubic specimens with the dimension 100 mm × 100 mm × 100 mm were utilized for compressive strength. Beam specimens of 100 mm × 100 mm × 400 mm were used for flexural strength. Beside this, 28 days elastic modulus of CAEM was carried out on the specimens of 150 mm × 150 mm × 300 mm (according to Chinese Standard JTJ E30-2005). Three specimens were prepared for each test result. The specimens were prepared with concrete vibrator, and all specimens were cured at a temperature of 20 ± 2°C and a humidity of 95% (RH) until the testing date.

XRD, SEM, and MIP

X-ray diffraction was used in this study to observe the hydration of blended cementitious materials of CAEM. CAEM specimens were ground to a powder and passed through a 63 μm sieve for XRD analysis (Bołtryk and Małaszkiewicz, 2013).

Scanning Electron Microscope was used to observe the microstructure characterization of CAEM. The cured specimens were shaped to cube with 1.5 cm by side length. Then, the surface of the samples was sputter covered with a thin layer of gold before the SEM observation (Likitlersuang and Chompoorat, 2016; Li et al., 2018).

Pore cumulative volume and pore size distribution of CAEM were measured by an Auto Pore IV 9510 MIP. Crushed pieces of the samples were soaked in an absolute ethyl alcohol solution to stop the hydration before MIP test (Wang et al., 2017).

RESULTS AND DISCUSSION

Flowability

Figure 1 shows the flowability results of fresh CAEM with various A/C ratios and various W/C ratios. It can be seen that the flowability of fresh CAEM was strongly affected by

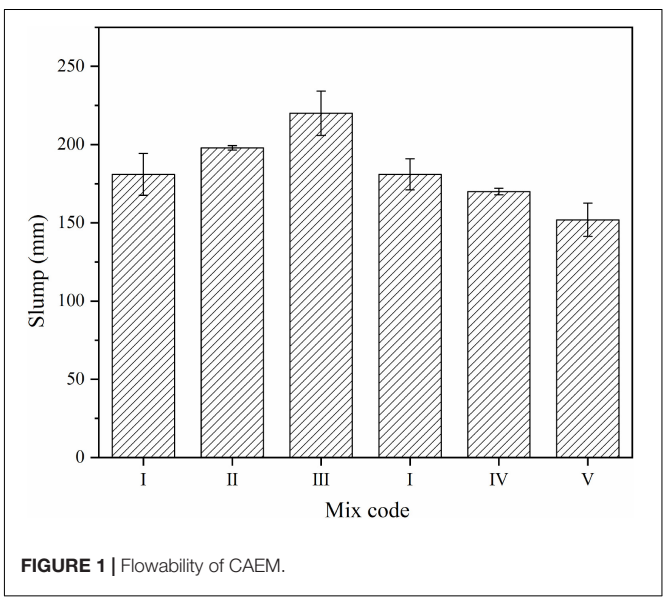

FIGURE 1 | Flowability of CAEM.

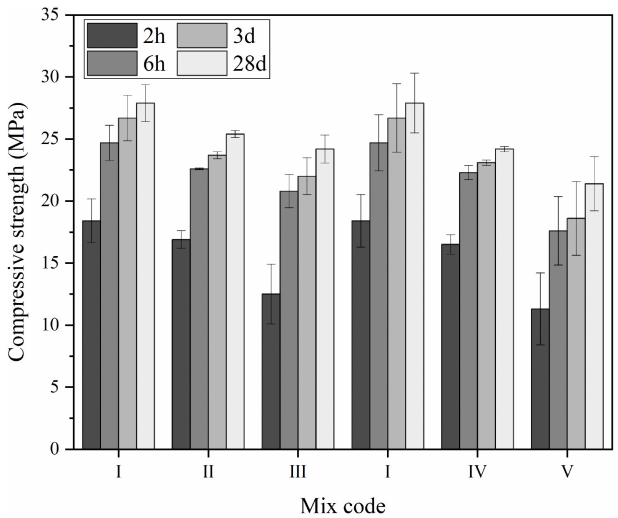

FIGURE 2 | Compressive strength of CAEM.

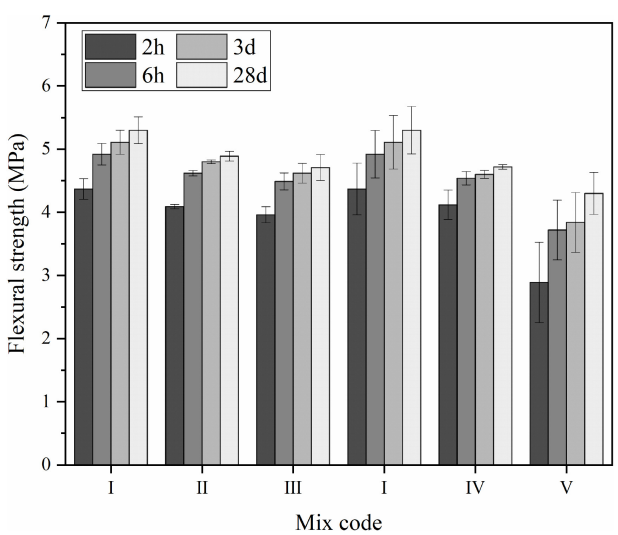

FIGURE 3 | Flexural strength of CAEM.

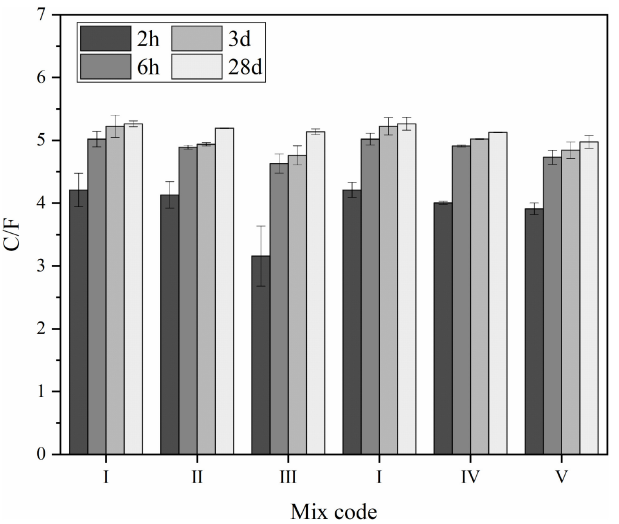

FIGURE 4 | Compressive strength -flexural strength ratio of CAEM.

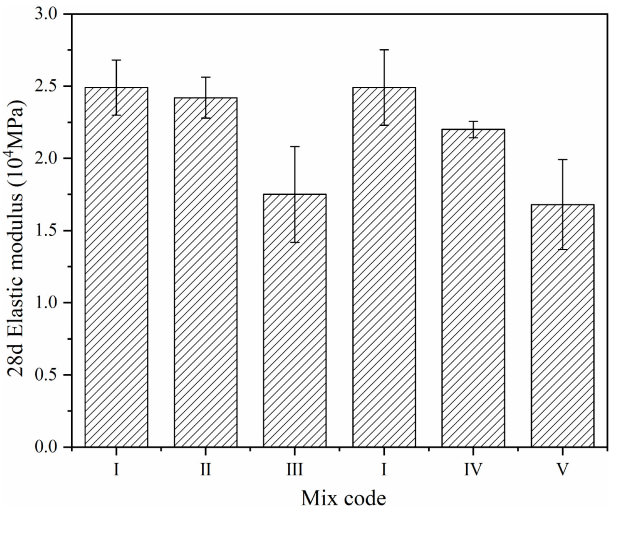

FIGURE 5 | 28 days elastic modulus of CAEM.

both A/C ratio and W/C ratio. As shown in **Figure 1**, the flowability of CAEM decreased with the increase of A/C ratio. A possible explanation was that the increase of A/C ratio caused the cement and asphalt emulsion to aggregate together, then entrapping water, and resulting in the decrease of flowability of CAEM (Wang et al., 2015). On the contrary, the flowability of CAEM increased with the increase of W/C ratio, and the slump reached almost 220 mm when the W/C ratio was 0.32.

It can also be concluded from **Figure 1** that in order to obtain greater flowability of CAEM (the slump more than 200 mm), the A/C ratio, and W/C ratio can be adjusted based on the experimental experience.

Early-Age Mechanical Performance

Compressive Strength

Figure 2 shows the compressive strength results of CAEM with various W/C ratios and A/C ratios after 2 h, 6 h, 3 days, and 28 days of curing. From **Figure 2**, it can be concluded that the compressive strength of CAEM could reach more than 10 MPa at 2 h age, due to the use of composite cement in the mixture. It also can be seen that a significant reduction in the compressive strength of CAEM was obtained as the W/C ratio increased. As the W/C ratio increased from 0.30 to 0.32, the compressive strength decreased by up to 32.1% at 2 h, and 13.3% at 28 days, respectively. This indicated that increasing W/C ratio provides a negative effect on the compressive strength of CAEM.

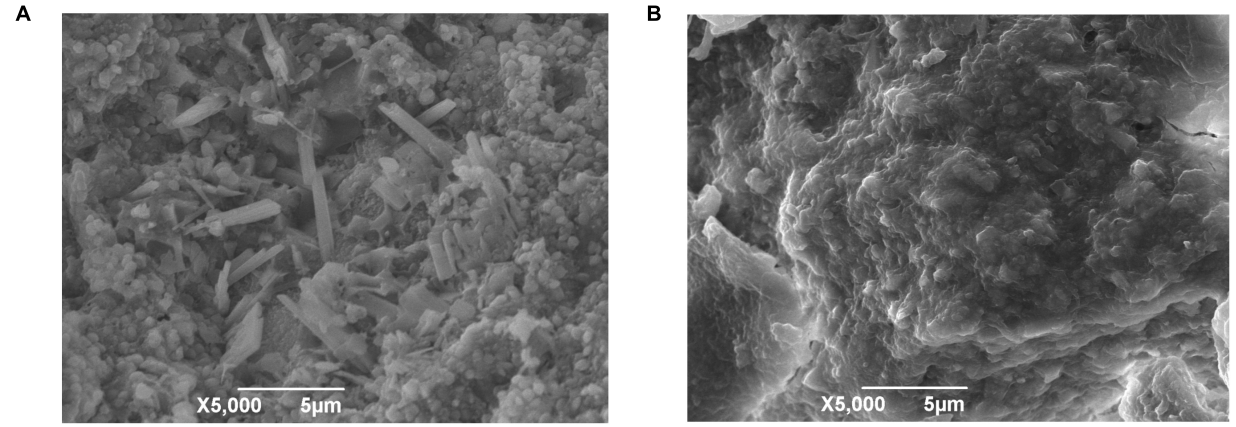

FIGURE 6 | (A) Microstructure of CAEM at 2 h. **(B)** Microstructure of CAEM at 28 days.

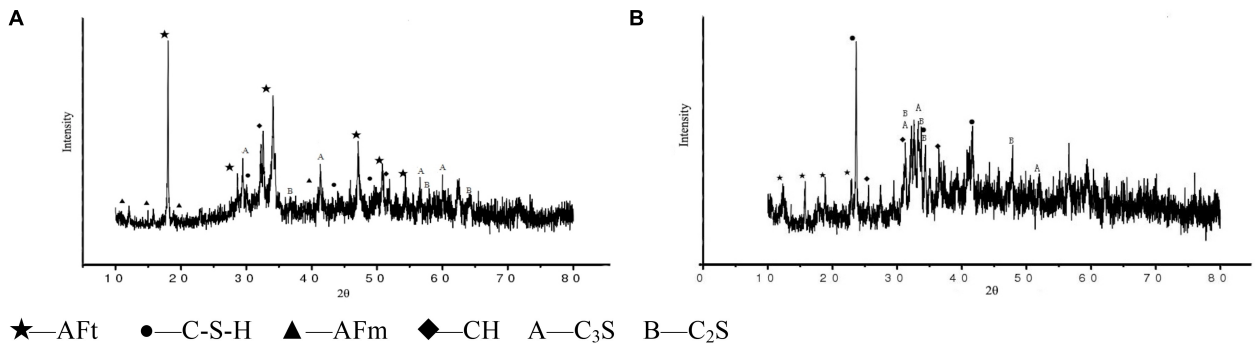

FIGURE 7 | (A) Hydration products of CAEM at 2 h. **(B)** Hydration products of CAEM at 28 days.

It should be noted that the change trend of A/C was consistent with that of W/C. As the A/C ratio increased from 0.18 to 0.30, the compressive strength decreased by up to 38.6% at 2 h and 23.3% at 28 days. With the increase of A/C, the compressive strength decreased due to the droplets of asphalt emulsion dispersed in the cement matrix. In addition, the compressive strength at 6 h was approximately 79–90% of the 28 days compressive strength of CAEM, which almost reached 17–24 MPa. As is well known, the hydration rate of calcium sulfoaluminate cement is very fast compared to Portland cement, so that a good supply of hydration products are generated during the initial hydration period of CAEM, and the porosity is filled by the main hydration products, which contributes to the rapid increase of the early strength of CAEM.

Flexural Strength

Figure 3 shows the flexural strength results of CAEM with various W/C ratios and A/C ratios. From **Figure 3**, it can be seen that the flexural strength of CAEM decreased with the increase of W/C ratio or A/C ratio. The increase in A/C resulted in a more significant reduction in flexural strength of CAEM, indicating that the structure formed by cement hydrates could be weakened by the addition of asphalt emulsion. The flexural strength of W/C 0.30, W/C 0.31, and W/C 0.32 at 6 h were approximately 92.8, 94.5, and 95.3% of the 28 days strength of CEAM, respectively. The flexural strength curve tended to be stable after 6 h, indicating that the flexural strength mainly depended on the structure formed by cement hydrates before 6 h. However, the flexural strength of CAEM was still slightly increasing after 6 h due to the water present in the asphalt emulsion was still slowly released as the A/C ratio increased and the cement continued to hydrate.

Compressive Strength -Flexural Strength Ratio

The compressive strength -flexural strength ratio (C/F ratio) can reflect the toughness of the material. In general, the smaller C/F ratio means the better material toughness and better impact resistance. Conversely, the greater of the C/F ratio, the more brittle the material is, and the worse the impact resistance against the external.

Figure 4 shows the C/F ratio of CAEM with various W/C ratios and A/C ratios. As can be seen from **Figure 4**, the C/F value increased as the curing time increased, and it increased slightly after 6 h. The higher W/C ratio of CAEM, the lower C/F ratio, indicating that the higher toughness of CAEM. Similarly, the higher A/C ratio of CAEM, the lower C/F ratio, which means the higher the toughness of CAEM.

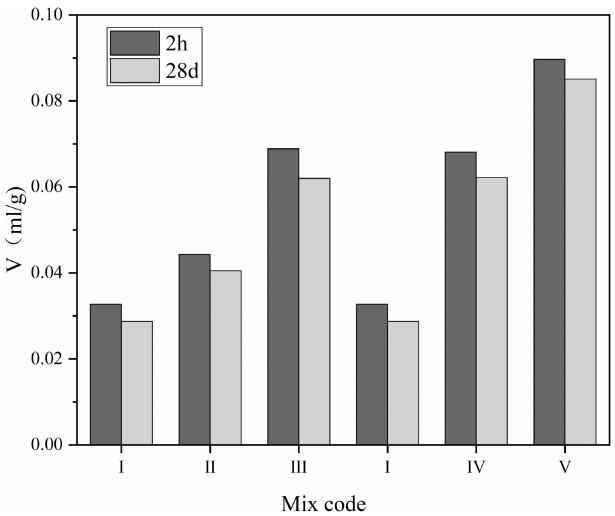

FIGURE 8 | Pore cumulative volume of the CAEM at the age of 2 h and 28 days.

28 Days Elastic Modulus

From **Figure 5**, it can be clearly seen that when the W/C ratio was 0.30, the 28 days elastic modulus of CAEM was consistent with that of W/C ratio was 0.31. However, the 28 days elastic modulus of CAEM suddenly decreased when the W/C ratio was 0.32, indicating that the optimum W/C ratio should be less than 0.32. In addition. As **Figure 5** depicts, a reduction in the 28 days elastic modulus of CAEM was observed as the A/C ratio increased. As the A/C ratio increased from 0.18 to 0.30, the 28 days elastic modulus decreased by 11.6 and 32.5%, respectively, which indicated that the higher content of asphalt emulsion, the lower 28 days elastic modulus of CAEM.

Microstructure Characterization

Microstructure Analysis

Figures 6A,B show the microstructure of CAEM at different curing time. From **Figure 6A**, it can be clearly observed that there was a large amount of needle shape crystals in the early hydration process, which filled the micro-pores of mixture and improved the strength of CAEM. In addition, the cement hydration consumed a portion of the water that occupied the micro air void spaces between asphalt emulsion and sand, which had a stiffening effect on CAEM (Fu et al., 2014). As CAEM continued to hydrate, C-S-H gels became the main binding phase in CAEM, the strength of hardened CAEM depended on the ability of the C–S–H to bind effectively other products of hydration and aggregates (Fu et al., 2014). It can be observed from **Figure 6B** that hydration products were interconnected in CAEM, resulting in the structure formed was much denser.

In order to observe the detailed information about the structure of crystalline substances, XRD was used in this study to obtain qualitatively phase composition of materials and identify crystalline phases of materials.

Figures 7A,B present X-ray diffractograms of the hydration products of CAEM after 2 h and 28 days curing time. From **Figures 7A,B**, it can be clearly observed that the hydration products of CAEM including calcium silicate hydrates (C-S-H gel), ettringite (AFt), $3CaO,\cdot Al_2O_3,\cdot CaSO_4,\cdot nH_2O$, (AFm), $Ca(OH)_2$, (CH), and a small amount of unhydrated cement particles. The early hydration of CAEM was very fast, producing a large amount of ettringite (AFt). With the hydration continued, the amount of AFt in CAEM began to decrease. In contrast, the amount of C-S-H gels kept increasing.

Pore Structure Analysis

In order to determine the effect of W/C ratio and A/C ratio on the pore structure of the CAEM, MIP was used in this study to

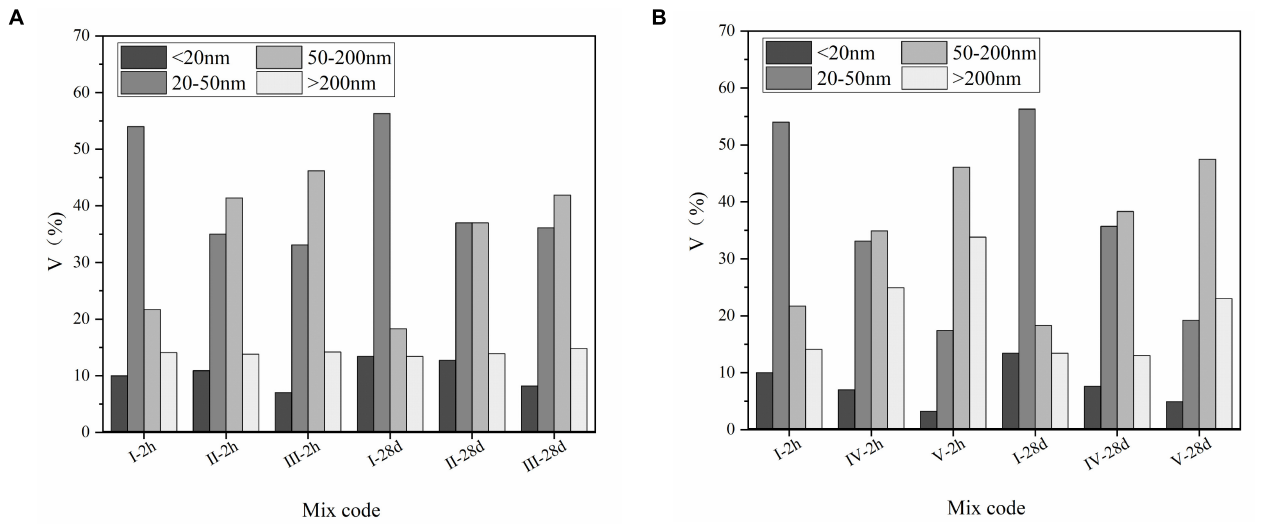

FIGURE 9 | (A) Pore size distribution of the CAEM with various W/C ratios. **(B)** Pore size distribution of the CAEM with various A/C ratios.

characterize the pore structure of the CAEM for 2 h samples and 28 days samples. The test results as shown in **Figures 8**, **9**.

Figure 8 presents the cumulative pore volume of CAEM with various W/C ratios and A/C ratios. From **Figure 8**, it can be seen that the cumulative volume of CAEM of 2 h samples and 28 days samples were similar, which indicated that the early hydration of CAEM was very fast at early-age and the hydration products were sufficient. It can also be seen from **Figure 8** that the cumulative pore volume of CAEM increased with the increase of A/C ratio, possibly due to the asphalt emulsion resulted in the increase of the pore volume. With the increase of W/C, the cumulative pore volume of CAEM showed a similar law.

Figures 9A,B present the pore size distribution of the CAEM with various W/C ratios and A/C ratios. Wu (1988) proposed a classification of the pores into harmless pores (<20 nm), less harmful pores (20 ∼ 50 nm), harmful pores (50 ∼ 200 nm), and multiple harmful pores (>200 nm) according to the pore size, and pointed out that only the reduction of harmful pores and the addition of harmless pores could improve the mechanical properties and durability of concrete.

From **Figure 9A**, it can be concluded that the proportion of multiple harmful pores (>200 nm) of CAEM increased slightly with the increase of W/C ratio, indicating that excessive moisture provided a negative effect on the pore size distribution of CAEM. As can be seen from **Figure 9B**, the proportion of multiple harmful pores (>200 nm) of CAEM increased with the increase of A/C ratio, while the proportion of harmless pores (<20 nm) of CAEM decreased with the increase of A/C ratio. It can be explained that as the viscosity of CAEM increased with the increase of A/C, resulting in that it difficult for air bubbles to be discharged, which were introduced by CAEM during the process of mixing.

CONCLUSION

The high early-age strength and flowability of CAEM were studied in this paper, and evolution of microstructure of CAEM was analyzed by XRD, SEM, and MIP to reveal the hardening mechanism of CAEM. Based on the experimental results, the following conclusions can be drawn:

(1) The flowability of fresh CAEM is strongly affect by both A/C ratio and W/C ratio. The flowability of CAEM decreases with the increase of A/C ratio, while the flowability of CAEM increases with the increase of W/C ratio.
(2) The compressive strength of CAEM reaches 17–24 MPa after 6 h curing, which is almost 79–90% of the 28 days compressive strength of CAEM. The flexural strength of CAEM for 2 h samples can reach more than 4 MPa. The change trend of flexural strength is consistent to the compressive strength of CAEM, which indicate that increasing W/C ratio, or A/C ratio provide a negative effect on the mechanical properties.
(3) The smaller A/C value should be selected as much as possible in order to obtain high flowability of CAEM. As W/C increases, the flowability of CAEM increases, but the compressive strength of CAEM decreases, so the W/C value should be moderate in order to ensure the high early-age strength of CAEM.
(4) From SEM pictures of CAEM, it can be concluded that in the early period of CAEM hydration, the hydration products filled the micro pores of the mixture. And with the continued hydration, the hydration products were connected to each other, resulting in a denser structure. In addition, from MIP test results, it can be seen that the proportion of multiple harmful pores (>200 nm) of CAEM increases with the increase of W/C ratio or A/C ratio, indicating that increasing A/C ratio, or W/C ratio provide a negative effect on the pore size distribution of CAEM.

DATA AVAILABILITY STATEMENT

The datasets generated for this study are available on request to the corresponding author.

AUTHOR CONTRIBUTIONS

YT and WL conceived this project. XY, DL, ZW, JZ, and OX planned the experiments and carried out the experiments. YT and XY analyzed the data and wrote the manuscript. All the authors discussed the results and commented on the manuscript.

FUNDING

This work was supported by National Natural Science Foundation of China (51878065), the Fundamental Research Funds for the Central Universities, CHD (300102319201), Natural Science Foundation of Shaanxi Province of China (2017JM5030 and 2020JM-247), Western Transportation Construction Science and Technique Program (2013318J09230), and State Key Laboratory of High Performance Civil Engineering Materials (2018CEM010).

REFERENCES

Bołtryk, M., and Małaszkiewicz, D. (2013). Application of anionic asphalt emulsion as an admixture for concrete. *Constr. Build. Mater.* 40, 556–565. doi: 10.1016/j.conbuildmat.2012.11.110

Dołżycki, B., Jaczewski, M., and Szydłowski, C. (2017). The influence of binding agents on stiffness of mineral-cement-emulsion mixtures. *Proc. Eng.* 172, 239–246. doi: 10.1016/j.proeng.2017.02.103

Doyle, T. A., Mcnally, C., Gibney, A., and Tabakoviæ, A. (2013). Developing maturity methods for the assessment of cold-mix bituminous materials. *Constr. Build. Mater.* 38, 524–529. doi: 10.1016/j.conbuildmat.2012.09.008

Du, S. (2018). Effect of curing conditions on properties of cement asphalt emulsion mixture. *Constr. Build. Mater.* 164, 84–93. doi: 10.1016/j.conbuildmat.2017.12.179

Fang, X., Garcia, A., Winnefeld, F., Partl, M. N., and Lura, P. (2016). Impact of rapid-hardening cements on mechanical properties of cement

bitumen emulsion asphalt. *Mater. Struc.* 49, 487–498. doi: 10.1617/s11527-014-0512-3

Fu, Q., Xie, Y., Zheng, K., Song, H., and Zhou, X. (2014). Influence of asphalt on mechanical properties of cement and asphalt mortar. *Kuei Suan Jen Hsueh Pao J. Chin. Ceramic Soc.* 42, 642–647. doi: 10.7521/j.issn.0454-5648.2014.05.14

Hu, S. G., Wang, T., Wang, F. Z., and Liu, Z. C. (2009). Adsorption behaviour between cement and asphalt emulsion in cement–asphalt mortar. *Adv. Cement Res.* 21, 11–14. doi: 10.1680/adcr.2007.00034

Li, W., Hong, J., Zhu, X., Yang, D., and Miao, C. (2018). Retardation mechanism of anionic asphalt emulsion on the hydration of Portland cement. *Constr. Build. Mater.* 163, 714–723. doi: 10.1016/j.conbuildmat.2017.12.150

Likitlersuang, S., and Chompoorat, T. (2016). Laboratory investigation of the performances of cement and fly ash modified asphalt concrete mixtures. *Int. J. Pavement Res. Technol.* 9, 337–344. doi: 10.1016/j.ijprt.2016.08.002

Lin, J., Wei, T., Hong, J., Zhao, Y., and Liu, J. (2015). Research on development mechanism of early-stage strength for cold recycled asphalt mixture using emulsion asphalt. *Constr. Build. Mater.* 99, 137–142. doi: 10.1016/j.conbuildmat.2015.09.019

Ling, C., Hanz, A., and Bahia, H. (2016). Measuring moisture susceptibility of Cold Mix Asphalt with a modified boiling test based on digital imaging. *Constr. Build. Mater.* 105, 391–399. doi: 10.1016/j.conbuildmat.2015.12.093

Liu, B., and Liang, D. (2017). Effect of mass ratio of asphalt to cement on the properties of cement modified asphalt emulsion mortar. *Constr. Build. Mater.* 134, 39–43. doi: 10.1016/j.conbuildmat.2016.12.137

Lu, C. T., Kuo, M. F., and Shen, D. H. (2009). Composition and reaction mechanism of cement–asphalt mastic. *Constr. Build. Mater.* 23, 2580–2585. doi: 10.1016/j.conbuildmat.2009.02.014

Ouyang, J., Han, B., Cao, Y., Zhou, W., Li, W., and Shah, S. P. (2016). The role and interaction of superplasticizer and emulsifier in fresh cement asphalt emulsion paste through rheology study. *Constr. Build. Mater.* 125, 643–653. doi: 10.1016/j.conbuildmat.2016.08.085

Ouyang, J., Hu, L., Yang, W., and Han, B. (2019a). Strength improvement additives for cement bitumen emulsion mixture. *Constr. Build. Mater.* 198, 456–464. doi: 10.1016/j.conbuildmat.2018.11.280

Ouyang, J., Pan, B., Xu, W., and Hu, L. (2019b). Effect of water content on volumetric and mechanical properties of cement bitumen emulsion mixture. *J. Mater. Civil Eng.* 31:04019085. doi: 10.1061/(asce)mt.1943-5533.0002736

Ouyang, J., and Shah, S. P. (2018). Factors influencing the structure build-up of fresh cement asphalt emulsion paste. *Road Mater. Pavement Des.* 19, 87–103. doi: 10.1080/14680629.2016.1236744

Ouyang, J., Yang, W., Chen, J., and Han, B. (2020). Effect of superplasticizer and wetting agent on pavement properties of cold recycled mixture with bitumen emulsion and cement. *J. Mater. Civil Eng.* 32:04020136. doi: 10.1061/(ASCE)MT.1943-5533.0003194

Ouyang, J., Zhao, J., and Tan, Y. (2018). Modeling mechanical properties of cement asphalt emulsion mortar with different asphalt to cement ratios and temperatures. *J. Mater. Civil Eng.* 30:04018263. doi: 10.1061/(ASCE)MT.1943-5533.0002480

Plank, J., and Hirsch, C. (2007). Impact of zeta potential of early cement hydration phases on superplasticizer adsorption. *Cement Concr. Res.* 37, 537–542. doi: 10.1016/j.cemconres.2007.01.007

Qiang, W., Peiyu, Y., Ruhan, A., Jinbo, Y., and Xiangming, K. (2011). Strength mechanism of cement-asphalt mortar. *J. Mater. Civil Eng.* 23, 1353–1359. doi: 10.1061/(asce)mt.1943-5533.0000301

Tan, Y., Ouyang, J., Lv, J., and Li, Y. (2013). Effect of emulsifier on cement hydration in cement asphalt mortar. *Constr. Build. Mater.* 47, 159–164. doi: 10.1016/j.conbuildmat.2013.04.044

Tian, Y., Jin, X. Y., Jin, N. G., Zhao, R., Li, Z. J., and Ma, H. Y. (2013). Research on the microstructure formation of polyacrylate latex modified mortars. *Constr. Build. Mater.* 47, 1381–1394. doi: 10.1016/j.conbuildmat.2013.06.016

Tyler, R., Wang, S., Shu, X., Huang, B., and Clarke, D. B. (2014). Laboratory investigation into mechanical properties of cement emulsified asphalt mortar. *Constr. Build. Mater.* 65, 76–83. doi: 10.1016/j.conbuildmat.2014.04.113

Wang, Y., Yuan, Q., Deng, D., Ye, T., and Fang, L. (2017). Measuring the pore structure of cement asphalt mortar by nuclear magnetic resonance. *Constr. Build. Mater.* 137, 450–458. doi: 10.1016/j.conbuildmat.2017.01.109

Wang, Z., Shu, X., Rutherford, T., Huang, B., and Clarke, D. (2015). Effects of asphalt emulsion on properties of fresh cement emulsified asphalt mortar. *Constr. Build. Mater.* 75, 25–30. doi: 10.1016/j.conbuildmat.2014.11.013

Wu, Z. (1988). Reflections on concrete science and technology. *Concrete* 6, 4–6.

Yan, J., Leng, Z., Li, F., Zhu, H., and Bao, S. (2017). Early-age strength and long-term performance of asphalt emulsion cold recycled mixes with various cement contents. *Constr. Build. Mater.* 137, 153–159. doi: 10.1016/j.conbuildmat.2017.01.114

Zhong, S., and Chen, Z. (2002). Properties of latex blends and its modified cement mortars. *Cem. Concr. Res.* 32, 1515–1524. doi: 10.1016/S0008-8846(02)00813-X

Zhou, Y., Cai, J., Chen, R., Hou, D., Xu, J., Lv, K., et al. (2020a). The design and evaluation of a smart polymer-based fluids transport inhibitor. *J. Clean. Prod.* 257:120528. doi: 10.1016/j.jclepro.2020.120528

Zhou, Y., Cai, J., Hou, D., Chang, H., and Yu, J. (2020b). The inhibiting effect and mechanisms of smart polymers on the transport of fluids throughout nano-channels. *Appl. Surf. Sci.* 500:144019. doi: 10.1016/j.apsusc.2019.144019

Zhou, Y., Hou, D., Jiang, J., Liu, L., She, W., and Yu, J. (2018). Experimental and molecular dynamics studies on the transport and adsorption of chloride ions in the nano-pores of calcium silicate phase: the influence of calcium to silicate ratios. *Microporous Mesoporous Materi.* 255, 23–35. doi: 10.1016/j.micromeso.2017.07.024

Conflict of Interest: The authors declare that the research was conducted in the absence of any commercial or financial relationships that could be construed as a potential conflict of interest.

frontiers in Materials

ORIGINAL RESEARCH
published: 22 May 2020
doi: 10.3389/fmats.2020.00148

Study on Dynamic Load Monitoring of an Enhanced Stress Absorption Layer

Sanqiang Yang[1,2], Pengfei Li[1], Meng Guo[3], Songyang Liao[1] and Haonan Wu[4]*

[1] Hebei Province Civil Engineering Monitoring and Evaluation Technology Innovation Center, College of Civil Engineering and Architecture, Hebei University, Baoding, China, [2] School of Highway, Chang'an University, Xi'an, China, [3] The Key Laboratory of Urban Security and Disaster Engineering of Ministry of Education, Beijing University of Technology, Beijing, China, [4] Rood and Bridge Branch, Hebei Construction Group Corporation Limited, Baoding, China

An effective stress absorption layer can reduce the reflection crack. It can help to extend the service life of road. In this research, an enhanced stress absorption layer of slow crack (ESALOSC) is proposed and compared with the ordinary SBS modified asphalt stress absorbing layer. The strain data of two stress absorption layers under different loads, speeds and temperatures are collected by embedding sensors in the road, and the dynamic response laws of the two stress absorption layers under different conditions are analyzed. The results show that the asphalt pavement is a viscoelastic body and the measured results are consistent with the theoretical solution of layered elasticity: both stress absorbing layers are subjected to pressure. According to the comparison between dynamic overload test and static overload test, the strain deviation between the two sections increases from 11.6% of static load to 25.2% of dynamic load (40 km/h). It indicates that the reinforced effect of geogrid is more obvious under dynamic load. By establishing the relationship between vehicle speed and dynamic response, a vehicle speed and dynamic response model for the ESALOSC is proposed. Based on the test data measured at four temperatures, a model of the temperature and dynamic response in the ESALOSC is proposed. The accuracy and effectiveness of the two models are verified by comparing with other experimental results. The ESALOSC is of great significance for improving the crack resistance of road. The research results provide technical support and theoretical model for the development of long-life pavement in China.

Keywords: stress absorbing layer, geogrid, dynamic response, vehicle load, vehicle speed

OPEN ACCESS

Edited by:
Jian Ouyang,
Dalian University of Technology, China

Reviewed by:
Pengfei Liu,
RWTH Aachen University, Germany
Huaping Wang,
Lanzhou University, China

****Correspondence:***
Meng Guo
gm@bjut.edu.cn

Specialty section:
This article was submitted to Structural Materials, a section of the journal Frontiers in Materials

Received: *28 February 2020*
Accepted: *27 April 2020*
Published: *22 May 2020*

Citation:
Yang S, Li P, Guo M, Liao S and Wu H (2020) Study on Dynamic Load Monitoring of an Enhanced Stress Absorption Layer. Front. Mater. 7:148. doi: 10.3389/fmats.2020.00148

INTRODUCTION

With the rapid development of Chinese economy, the demand for transportation is increasing, and the country 's requirements for road service levels are increasing. At present, most of the domestic transportation roads use semi-rigid bases (Sha, 2008). Investigations show that no matter in the south or the north of China, there will be a lot of cracks after 2 years of opening to traffic. After studying these cracks, it was found that more than half of the cracks was reflective cracks caused by temperature shrinkage and dry shrinkage (Zeng et al., 2013). The development of these cracks not only affect driving safety, but also shorten the road life. This shows that the existing domestic stress absorption layer can no longer meet the daily use needs, and the problem of reflective cracks on

asphalt roads is becoming increasingly serious (Geng et al., 2012). Under this background, domestic and foreign scholars have proposed different methods to delay the occurrence and expansion of reflective cracks (Tschegg et al., 2007; Doh et al., 2009; Schlosser et al., 2013; Zhang et al., 2018; Ouyang et al., 2020).

The stress absorption layer has always been a research hotspot of asphalt pavement. Scholars have mainly studied the crack resistance mechanism of the stress absorption layer, the application performance of the material and the testing methods utilized to evaluate reflective cracking (Yoon et al., 2017). Iowa State University's Ceylan successfully simulated the stress intensity factor of crack propagation with neural network (NN) method, and studied the crack propagation mechanism (Ceylan et al., 2011). Zhao and Baek analyzed the reflection crack propagation mechanism under dynamic load through ABAQUS and found that increasing the vehicle speed could delay the development of reflection cracks (Baek and Alqadi, 2008; Zhao and Ni, 2009). Huang Xiaoming of Southeast University applied discrete element software to establish a crack model for a composite pavement structure with a semi-rigid base. It was found that a normal load could generate a horizontal stress concentration at the crack tip. The stress decreased around the crack tip (Wang et al., 2016). Sun Yazhen of Shenyang Jianzhu University used finite element software to simulate reflective cracks and found that under different loads, reflective cracks would expand in different ways (Sun et al., 2012).

Geogrid and various asphalt materials are the research focus of stress absorbing layer materials (Keller, 2016; Zornberg, 2017). Xue Yongchao of Southeast University designed a stress absorbing layer composed of epoxy asphalt and glass fiber geogrid, and tested it by drawing test, shear test and fatigue test. The results showed that the optimal ratio of epoxy asphalt was $2.0\,L/m^2$(Xue et al., 2016). Silva used four-point fatigue test and rutting test, and found that the high proportion of ultra-fine rubber granule asphalt mixture prepared by drying has better fatigue resistance and the crack growth rate was slower (Silva et al., 2018). Khodaii Ali recommended that the maximum service life could be provided by placing the geogrid one third from the bottom of the covering layer (Khodaii et al., 2009). Zamora found that the geogrid has good crack resistance. High modulus geogrid had better performance (Zamora et al., 2011). The focus of these studies is to evaluate the actual properties of materials, and there is a lack of research on the mechanism of the action of materials in the road.

Aiming at the practical problems of reflection cracks, many testing methods were introduced into the experiments. Saride et al. used digital image correlation technology (DIC) to record the crack growth failure pattern and corresponding tensile strain, but DIC was very sensitive to moisture and dust in the air, which could lead to large errors (Kumar and Saride, 2017; Saride and Kumar, 2017). Ling Jianming invented Joint Motion Simulation System (JMSS) using sensors, which considered the influence of both traffic and thermal load. The test results showed that the performance of geotextile was better than stress absorbing layers, and polypropylene modified linoleum (Ling et al., 2019). Wang Huaping embedded fiber sensors in the interior of the road and collected a wealth of strain data. The corresponding strain transfer theory and temperature error correction formula were put forward, and it was suggested to use low modulus asphalt as protection layer (Wang et al., 2018, 2019). Therefore, it is a developing trend to explore the strain law of road interior by using sensors, and it has good effect.

TABLE 1 | Pavement structure layer.

Location	The structure layer	Corresponding thickness (cm)
1	AC-13	4
2	AC-16	6
3	AC-25	8
4	Stress absorbing layer	1
5	5% cement stabilized gravel	18
6	4% cement stabilized gravel	18
7	Graded crushed stone	18

According to the current research status of stress absorption layers and reflective cracks at home and abroad, it is found that the currently designed stress absorption layers cannot meet the development needs of China's long-life pavement (Fan, 2015), and hinder the modernization of transportation in China. At the same time, there is a lack of systematic research on the action mechanism and performance evaluation of geogrids. In order to better solve the above problems, this paper uses sensors to collect the strain information in the road. The objective of this paper is to propose an enhanced stress absorption layer of slowing crack (ESALOSC) and summarizes the strain laws of ESALOSC. This stress absorption layer is composed of geogrid and rubber modified asphalt. The road performance of ESALOSC is verified by comparing with the performance of the ordinary SBS modified asphalt stress absorbing layer (OSMASAL). In this paper, sensors are arranged on two types of stress absorption layers to collect strain information under different loads, speeds and temperatures. This paper establishes the corresponding mathematical model based on the experimental data, which provides strong support for the follow-up research. The accuracy and effectiveness of the two models are verified by comparing with other experimental results. The research results provide theoretical support and technical guidance for the design of long-life roads, and have important engineering value.

ENGINEERING DESCRIPTION

The project locates on Cangshan Road, Fuping County, Hebei Province. Fuping County is a mountainous region, with high temperatures and high humidity in summer, concentrated precipitation, cold and snow in winter. The minimum daily temperature is −15°C. The road is laid out from west to east. The roadbed is silty clay. The driveway is designed as a two-way four-lane road. The ESALOSC and the OSMASAL are, respectively laid on Cangshan east road. The section of K1+200-k1+400 is selected to lay ESALOSC, which is composed of geogrid and rubber modified asphalt, and this part is called "Section A."

TABLE 2 | The gradation composition of asphalt mixture.

	The percentage of mass through the following screen (%)												
	31.5	26.5	19.0	16.0	13.2	9.5	4.75	2.36	1.18	0.6	0.3	0.15	0.075
AC-13				100	95	77	53	37	27	19	14	10	6
AC-16			100	95	84	70	48	34	25	18	13	9	6
AC-25	100	95	85	74	67	55	38	30	23	16	11	9	5

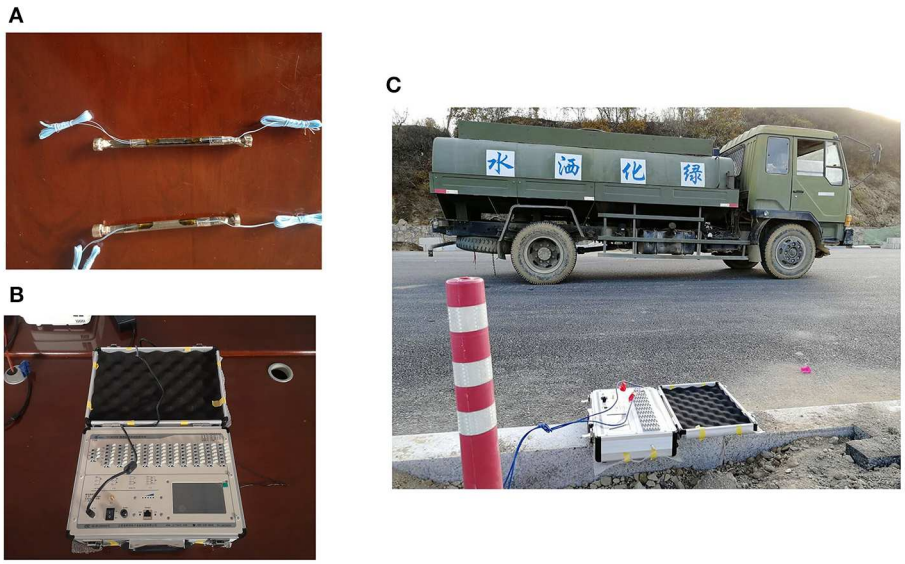

FIGURE 1 | (A) Two strain sensors, **(B)** strain collecting instrument, and **(C)** pictures of field tests.

The section of K0+930-k1+070 is selected to lay OSMASAL and compares with "Section A," which is hereinafter referred to "Section B." The pavement structure is shown in **Table 1**. The gradation composition of asphalt mixture is shown in **Table 2**. **Figure 1** shows photos of the test system, where **Figures 1A,B** are photos of the sensors and strain gauge, respectively, and **Figure 1C** is a photo of the test process.

DESIGN OF TEST SCHEME

Sensor Setup Scheme

The sensor in this paper is a strain gauge, and the strain data is collected by placing the sensors on a stress absorption layer. The sensors are covered with fine aggregates and the same asphalt (Wang and Xiang, 2016). The sensors in section A are placed at 5 points and collectively referred to as "Group A." Similarly, the sensors in section B are also placed at 5 points and collectively referred to as "Group B." The sensors are located at the left-wheel track of the carriageway, and the survival rate of the sensors is 60%. All conditions meet the requirements of the test. The details of the surviving sensors are shown in **Table 3**. The location of the sensor is shown in **Figures 2A,B**.

TABLE 3 | The location of the surviving sensors.

Measuring point location	Serial number	Measuring point location	Serial number
K1+330	A2	K1+030	B2
K1+300	A3	K1+001	B3
K1+270	A4	K0+970	B4

Test Plan

In order to analyze the effects of load, speed, and temperature in the ESALOSC, the test is designed at different speeds, loads, and temperatures (Tan and Guo, 2013; Xiao et al., 2016). Plan 1 selects five speeds to study the effects of dynamic and static loads on ESALOSC. The three groups of tests conduct in sections A and B. The plans are shown in **Table 4**.

DATA ANALYSIS

The high-frequency strain gauge is used to collect the strain data of the two stress absorption layers. After installing the system, strain gauge starts to collect strain data. The above three plans are carried out three times, respectively. The maximum strain is extracted from the test data as the dynamic response of the pavement structure under each test condition. It is planned to ignore data with more than 10% deviation. The variation coefficient of all off the test data are below 4% in the same

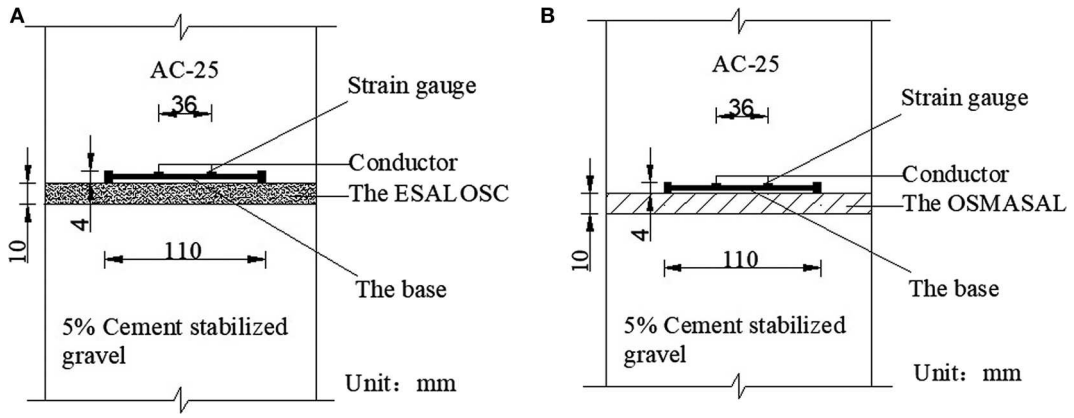

FIGURE 2 | (A) Sensor embedded position of the ESALOSC, and **(B)** sensor embedded position of the OSMASAL.

working condition. The tests are performed at different speed, load, temperature, and road structure conditions, so the size and distribution of the wheel load are different, which will cause the dynamic response of the pavement structure to be very different. According to the theory of layered elasticity, both stress-absorbing layers are affected by pressure, and the measured strains are both negative, which is consistent with the theoretical solution of layered elasticity (Yang et al., 2017).

TABLE 4 | Test plan.

Test plan	Vehicle speed(km/h)	Vehicle load (*t*)	The temperature of the road surface (°C)
1	①0; ②5; ③10; ④20; ⑤40	①BZZ-100; ②13.9	3
2	①0; ②5; ③10; ④20; ⑤40	13.9	3
3	5	BZZ-100	①-8; ②-3; ③0; ④3

Effect of Load on ESALOSC

Plan 1 prepares to study the impact of the load on the two stress absorption layers. The scheme is divided into a dynamic load part (5–40 km/h) and a static load part (0 km/h). The two dynamic load tests are shown in **Figures 3A,B**. **Figure 3A** is the image of the standard load vehicle (BZZ-100) passing at the A4 pile at a speed of 10 km/h, and **Figure 3B** is the image of the vehicle (13.9t) passing at the B4 pile position under the same speed. The results of plan 1 are shown in **Figures 3C,D**. The analysis of test data is shown in **Table 5**.

Figures 3A,B shows that when the vehicle passes over the laying sensor, two obvious fluctuations occur on the strain image. The front strain is smaller than the rear strain, which indicates that the front strain is generated by the front wheel and the rear strain is generated by the rear wheel. At the same speed, the strain of both sections increases with the increase of the load. This phenomenon is caused by the increase of the load that causes the tire stiffness to increase, and the increased stiffness of the tire causes the dynamic response to increase on the road. The static load test shows that the load increasing from 10t to 13.9t, which causes the strain of section A and section B to increase by 29.2 and 40.8%, respectively. The results show that the increase of static load has greater impact on section B than section A. In the dynamic load test at 5 km/h, the strain increases by 23.9 and 38.1% in section A and section B, respectively. The dynamic load tests at 10 km/h shows that the strain increases by 20.3 and 38.2% in section A and section B, respectively. In the 20 km/h dynamic load test, the strain increases by 16.3 and 36.4% in section A and section B, respectively, and the 40 km/h dynamic load test show that the strain increases by 10.5 and 35.7% in section A and section B, respectively. The above dynamic load tests show that the increase in dynamic load has greater impact on section B than section A.

The data of five times show that the strain difference between the two pavements increases from 11.6 to 25.2% with the increase of the speed. It indicates that the reinforcement effect of the geogrid under dynamic load is more obvious than the static load, so it can be significantly improved the road carrying capacity. All the strains in the static load test come from the original load of the vehicle. The area of the stress-absorption layer that directly contact with the wheel is affected by pressure, and the area outside the wheel load edge is affected by tension. The geogrid can reduce the pressure and tension in the stress absorption layer, and reduce the corresponding strain. In the dynamic load test, the strain not only come from the vehicle's load, but also come from the vehicle's additional dynamic impact load. While dispersing the above pressure and tension, the geogrid also reduces the strain of the additional dynamic impact load.

Effect of Velocity on ESALOSC

The purpose of Plan 2 is to study the effect of vehicle speed on the stress absorption layer in section A. The tests on piles A4 and B4 are shown in **Figures 4A,B**. **Figures 4C,D** are model images of dynamic response and speed. **Table 6** shows the specific parameters of the two models in sections A and B, **Table 7** lists the actual measured data of the A2 and A3 piles and the corresponding model data. The "deviation" in **Table 7** refers to the deviation between the actual measured data at A2 or A3 pile and the data calculated by the model in this section.

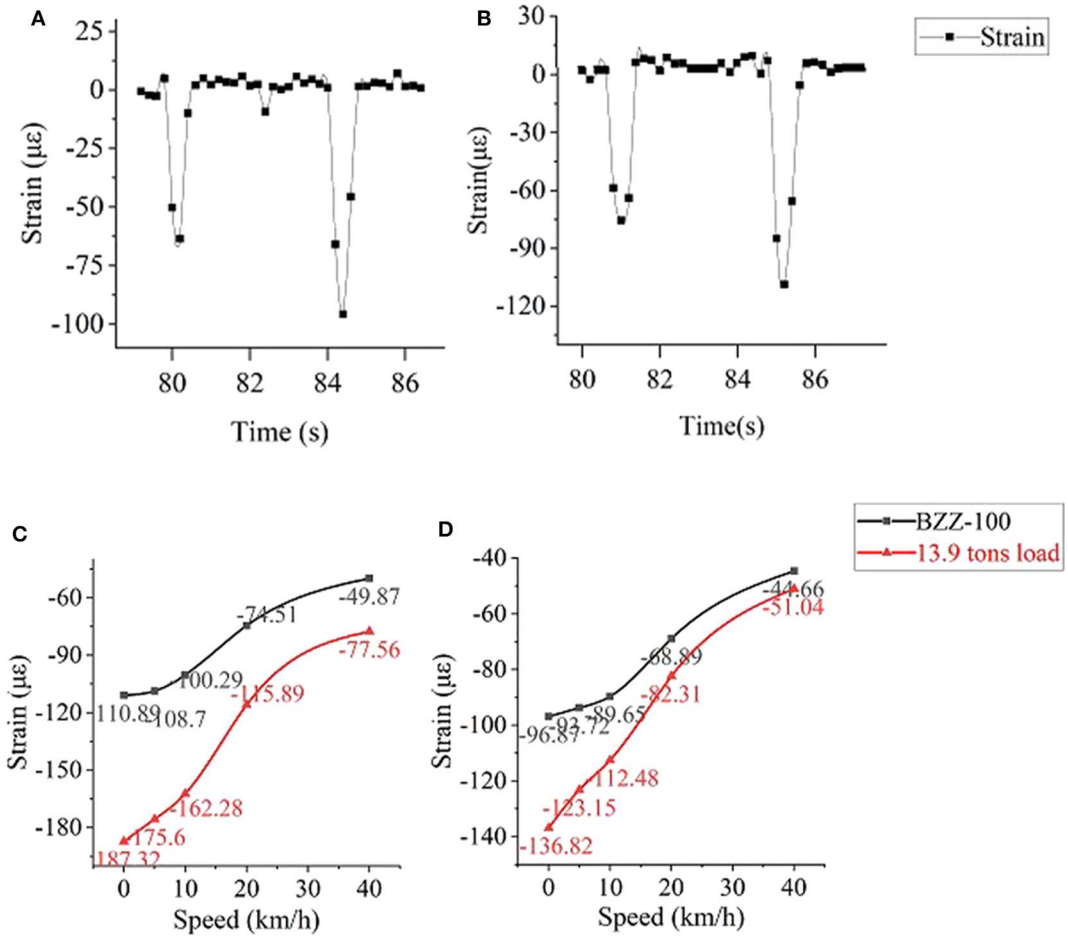

FIGURE 3 | (A) A4 pile's loading vehicle strain (10t, 10 km/h), **(B)** B4 pile's loading vehicle strain (13.9t, 10 km/h), **(C)** the results of plan 1 are shown in A4 pile, and **(D)** The results of plan 1 are shown in B4 pile.

TABLE 5 | Test 1 analysis.

Speed (km/h)	Strain difference ratio of two loads in section A (%)	Strain difference ratio of two loads in section B (%)	Two segment difference (%)
0	29.2	40.8	11.6
5	23.9	38.1	14.2
10	20.3	38.2	17.9
20	16.3	36.4	23.5
40	10.5	35.7	25.2

Figures 4A,B show that as the speed increases, the dynamic response of the wheels in the two stress absorption layers gradually decreases. When the speed increases from stationary to 20 km/h, the strain decreases significantly. However, after the speed exceeds 20 km/h, the dynamic response gradually flattens. This phenomenon is caused by the increase in speed, which reduces the amount of time that the load acts on the sensor. This is shown in mechanics as: the increase in road strength and modulus affects the dynamic response of the road structure, which proves that the impact of low-speed vehicles on the road is greater than high-speed vehicles. Therefore, the model of speed and dynamic response is proposed in part A: $\varepsilon = 36.63724lnv - 189.6703$. Its correlation coefficient is above 0.97. At the same time, the measured data of the A2 and A3 piles are compared with the data obtained from the above model, and the deviation of data is within ±4.68%. The results show that the model can accurately reflect the strain caused by vehicles with different speeds in section A, and has high applicability. The slope "A" of the $\varepsilon - v$ linear equation can represent the rate which the dynamic response change with the speed of the vehicle. **Table 7** shows that comparing with the section B, the strain in section A decreases less than section B with the increase of the speed, which indicates that the speed has a smaller effect in section A.

Effect of Temperature on ESALOSC

In Plan 3, four measuring times are selected to represent different temperatures in a day (Guo et al., 2017; Ouyang et al., 2018; Guo and Tan, 2019). The measuring time are shown in **Table 8**. The tests at A2 and B2 piles are shown in **Figures 5A,B**. **Figures 5C,D**

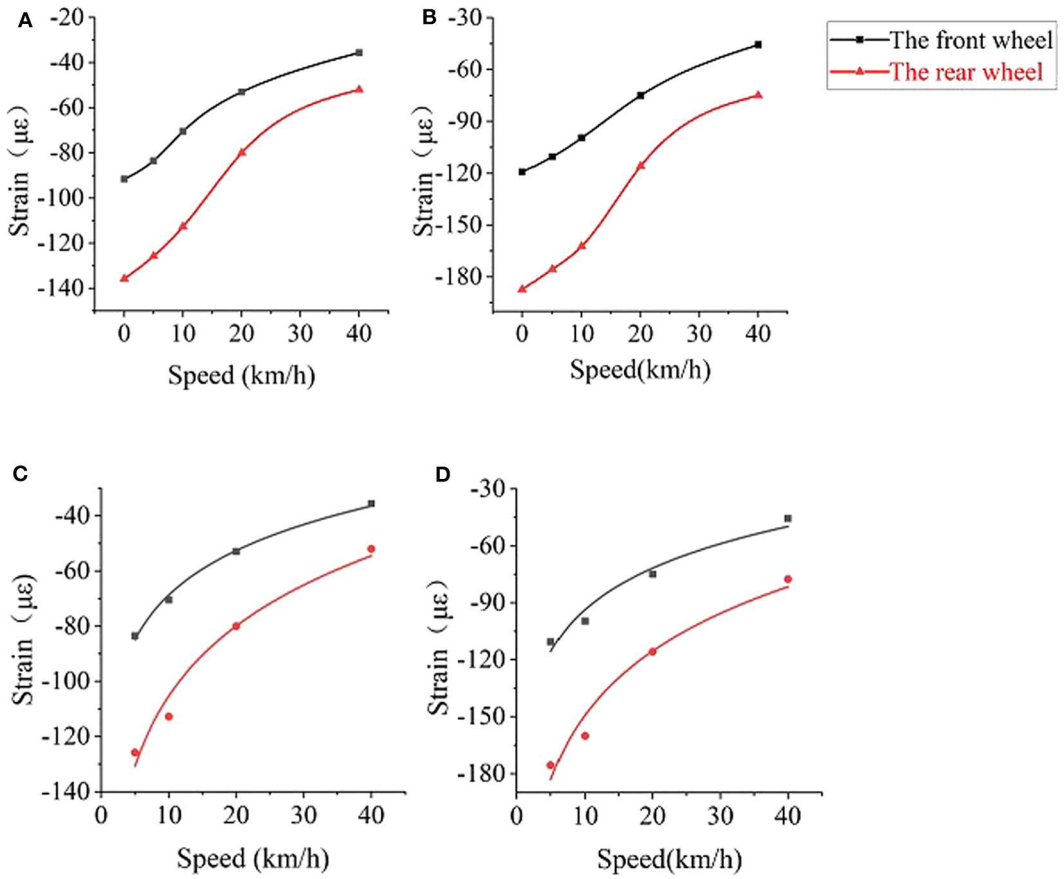

FIGURE 4 | (A) A4 pile's loading vehicle strain, **(B)** B4 pile's loading vehicle strain, **(C)** model of strain and speed in the section A, and **(D)** model of strain and speed in the section B.

TABLE 6 | Speed and strain model.

Location	Regression coefficient		Model
Section A	A	36.63724	$\varepsilon = 36.63724lnv - 189.6703$
	B	−189.6703	
	The correlation coefficient (R^2)	0.97416	
Section B	A	48.80782	$\varepsilon = 48.80782lnv - 261.58215$
	B	−261.58215	
	The correlation coefficient (R^2)	0.96792	

TABLE 7 | Verify the speed and strain model in section A.

Speed (km/h)	Other pile actual measured data				Data from the model (με)
	A2 pile (με)	Deviation (%)	A3 pile (με)	Deviation (%)	
5	−127.42	−2.51	−125.75	−3.37	−130.705
10	−101.09	−4.01	−106.63	1.25	−105.309
20	−81.51	1.99	−79.95	0.04	−79.915
40	−53.43	−3.83	−51.97	−4.68	−54.519

TABLE 8 | Test time and road temperature.

Measuring time	The temperature of the road surface (°C)	Measuring time	The temperature of the road surface (°C)
12:00	3	0:00	−3
18:00	0	6:00	−8

are the model images of dynamic response and temperature. **Table 9** shows the specific parameters of the two models in section A and B, **Table 10** lists the actual measured data of the A3 and A4 piles and the corresponding model data. The "deviation" in **Table 10** refers to the deviation between the data actual measured at A3 or A4 pile and the data calculated by the model in this section. The strain transfer efficiency mainly depends on the protective layer material. In this paper, the two sections adopt the same protective layer material, so the two sections have the same strain transfer efficiency (Wang and Dai, 2019).

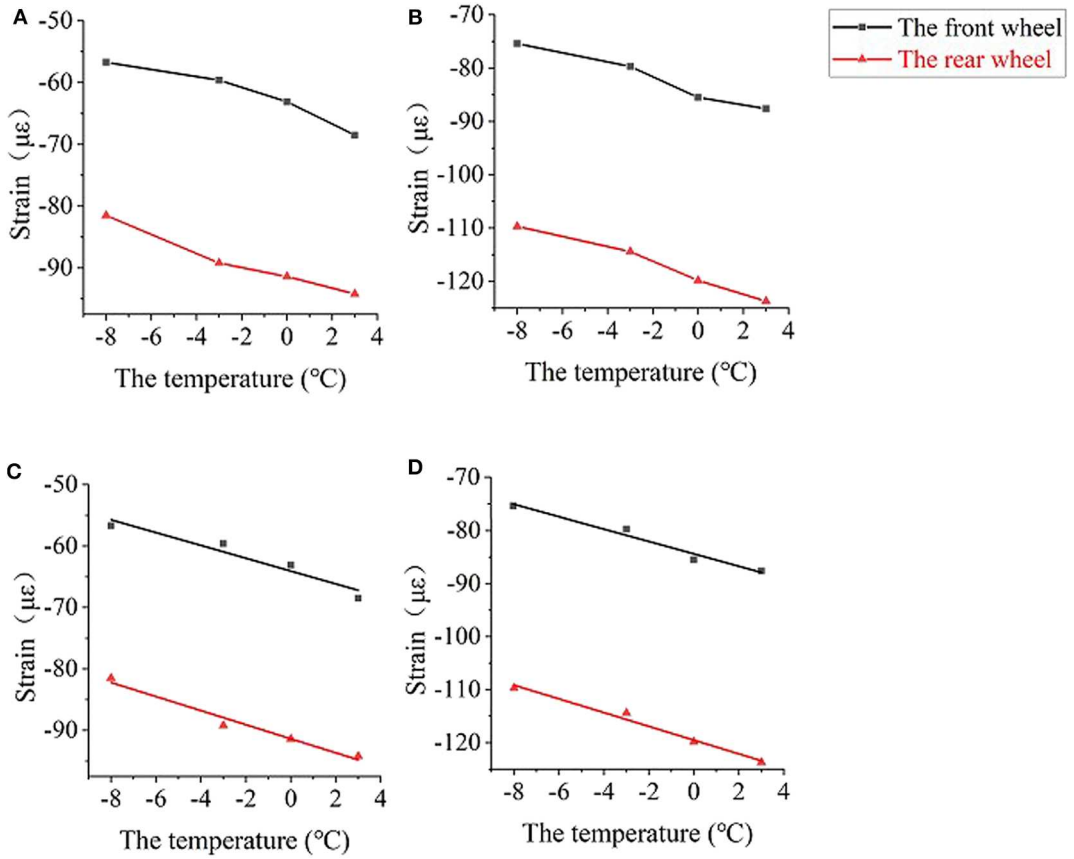

FIGURE 5 | (A) A2 pile's loading vehicle strain, **(B)** B2 pile's loading vehicle strain, **(C)** model of strain and temperature in the section A, and **(D)** model of strain and temperature in the section B.

TABLE 9 | Temperature and strain model.

Location	Regression coefficient		Model
Section A	A	−1.14545	$\varepsilon = -1.14545t - 91.36591$
	B	−91.36591	
	The correlation coefficient (R^2)	0.97226	
Section B	A	−1.29545	$\varepsilon = -1.29545t - 119.49091$
	B	−119.49091	
	The correlation coefficient (R^2)	0.98245	

TABLE 10 | Verify the temperature and strain model of section A.

Temperature (°C)	Other pile actual measured data				Data from the model (με)
	A3 pile (με)	Deviation (%)	A4 pile (με)	Deviation (%)	
3	−92.61	−2.32	−98.33	3.71	−94.81
0	−90.05	−1.45	−88.92	−2.68	−91.37
−3	−90.85	3.32	−85.77	−2.46	−87.93
−8	−85.17	3.60	−83.59	1.68	−82.21

Figures 5A,B show that as the road temperature increases during the day, the dynamic response of vehicles also increases in the same area. Because asphalt is a temperature-sensitive material, its stiffness and modulus decrease with increasing temperature, which increases dynamic response. Since the temperature difference in the four tests is not large, the growth trend of the dynamic response is slow. Plan 3 verify the effect of temperature on the road. Therefore, the model of temperature and dynamic response is proposed in part A: $\varepsilon = -1.14545t - 91.36591$. Its correlation coefficient is above 0.97. In addition, the measured data of the A3 and A4 piles are compared with the data obtained from the above model, and the deviation of data is within ±3.71%. The results show that the model can accurately reflect the strain caused by BZZ-100 vehicles at different temperatures and has high applicability. The slope "A" of the $\varepsilon - t$ linear equation can represent the rate which the dynamic response changes with temperatures. As shown in **Table 10**: Comparing with the section B, the strain in the section A increases more slowly with temperature, which means that the temperature has less influence on the section A.

CONCLUSIONS

Laying sensors on the two stress absorption layers, the strain data are collected under different speed, load, and temperature conditions. After collating the above data and analyzing the dynamic response of load, velocity and temperature in the two stress absorption layers, the following study can be concluded:

(1) According to the overload test data analysis: under static load conditions, the ESALOSC strain is 11.6% lower than the OSMASAL when overloaded 39% (13.9t) on the BZZ-100 basis. In the dynamic load test under the same conditions, as the speed increasing, the strain difference between the two stress absorbing layers increase from 11.6 to 25.2%. The results show that the reinforced effect of geogrid is more obvious under dynamic load, which can significantly improve the carrying capacity of asphalt road.

(2) By establishing the relationship between speed and dynamic response, the model of speed and dynamic response is proposed in the ESALOSC: $\varepsilon = 36.63724lnv - 189.6703$. The slope represents the rate which the strain change with the speed of vehicle. According to the regression results of the ESALOSC and the OSMASAL, the strains of the two stress-absorbing layers decrease with increasing speed. However, As the vehicle speed increases, the strain reduction rate on ESALOSC is smaller than on OSMASAL. It means that speed has less effect on the ESALOSC than the OSMASAL.

(3) According to the test data measured at four times: the temperature and dynamic response model is proposed in the ESALOSC: $\varepsilon = -1.14545t - 91.36591$. The slope represents the rate which the dynamic response change with temperature. According to the regression results of the two sections, the strain of both the two stress-absorbing layers increases with the increasing of temperature. In the two sections, the ESALOSC strain increases at a lower rate with the increase of temperature. It means that temperature has less effect on the ESALOSC than the OSMASAL.

DATA AVAILABILITY STATEMENT

The raw data supporting the conclusions of this article will be made available by the authors, without undue reservation, to any qualified researcher.

AUTHOR CONTRIBUTIONS

PL and SL conducted the experiments. SY is the supervisor of this research work. MG and PL helped writing. SY, PL, MG, SL, and HW performed the characterization and data analysis. All authors involved the analysis of experimental data and manuscript preparation.

FUNDING

This research was supported by Hebei Provincial Natural Science Foundation Funded Project (E2018201106), Hebei Provincial Department of Construction Science and Technology Project (130000021); Baoding Science and Technology Bureau Science and Technology Project (1911ZG003).

REFERENCES

Baek, J., and Alqadi, I. L. (2008). Finite element modeling of reflective cracking under moving vehicular loading: investigation of the mechanism of reflective cracking in hot-mix asphalt overlays reinforced with interlayer systems. *Airfield Highway Pavements* 329, 74–85. doi: 10.1061/41005(329)7

Ceylan, H., Gopalakrishnan, K., and Lytton, R. L. (2011). Neural networks modeling of stress growth in asphalt overlays due to load and thermal effects during reflection cracking. *J. Mater. Civil Eng.* 23, 221–229. doi: 10.1061/(ASCE)MT.1943-5533.0000153

Doh, Y. S., Baek, S. H., and Kim, K. W. (2009). Estimation of relative performance of reinforced overlaid asphalt concretes against reflection cracking due to bending more fracture. *Constr. Build. Mater.* 23, 1803–1807. doi: 10.1016/j.conbuildmat.2008.09.027

Fan, Y. H. (2015). Study on the interlayer treatment methods of old cement concrete pavement and asphalt overlay. *Highway Eng.* 40, 27–31. doi: 10.3969/j.issn.1674-0610.2015.05.007

Geng, L. T., Ren, R. B., Guo, Y. Q., and Chang, Y. G. (2012). Experimental research on asphalt mixture for stress absorbing membrane interlayer. *J. Build. Mater.* 15, 570–574. doi: 10.3969/j.issn.1007-9629.2012.04.027

Guo, M., and Tan, Y. Q. (2019). Interaction between asphalt and mineral fillers and its correlation to mastics' viscoelasticity. *Int. J. Pavement. Eng.* 1–10. doi: 10.1080/10298436.2019.1575379. [Epub ahead of print].

Guo, M., Tan, Y. Q., Hou, Y., Wang, L. B., and Wang, Y. Q. (2017). Improvement of evaluation indicator of interfacial interaction between asphalt binder and mineral fillers. *Constr. Build. Mater.* 151, 236–245. doi: 10.1016/j.conbuildmat.2017.05.003

Keller, G. R. (2016). Application of geosynthetics on low-volume roads. *Transp. Geotech.* 8, 119–131. doi: 10.1016/j.trgeo.2016.04.002

Khodaii, A., Fallah, S., and Moghadas, N. F. (2009). Effects of geosynthetics on reduction of reflection cracking in asphalt overlays. *Geotext. Geomembranes* 27, 1–8. doi: 10.1016/j.geotexmem.2008.05.007

Kumar, V. V., and Saride, S. (2017). Use of digital image correlation for the evaluation of flexural fatigue behavior of asphalt beams with geosynthetic interlayers. *Transp. Res. Rec.* 2631, 55–64. doi: 10.3141/2631-06

Ling, J. M., Wei, F. L., Gao, J. H., Zhang, J. K., Tian, Y., and Li, Y. T. (2019). New test method for measuring reflective cracking in hot-mix asphalt overlay pavements. *Transp. Res. Rec.* 2673, 327–336. doi: 10.1177/0361198119841040

Ouyang, J., Yang, W. T., Chen, J. J., and Han, B. G. (2020). Effect of superplasticizer and wetting agent on pavement properties of cold recycled mixture with bitumen emulsion and cement. *J. Mater. Civil Eng.* 32:04020136. doi: 10.1061/(ASCE)MT.1943-5533.0003194

Ouyang, J., Zhao, J. Y., and Tan, Y. Q. (2018). Modeling mechanical properties of cement asphalt emulsion mortar with different asphalt to cement ratios and temperatures. *J. Mater. Civil Eng.* 30:04018263. doi: 10.1061/(ASCE)MT.1943-5533.0002480

Saride, S., and Kumar, V. V. (2017). Influence of geosynthetic-interlayers on the performance of asphalt overlays on pre-cracked pavements. *Geotext. Geomembranes* 45, 184–196. doi: 10.1016/j.geotexmem.2017.01.010

Schlosser, F., Mikolaj, J., Zatkalikova, V., Sramek, J., Durekova, D., and Remek, L. (2013). Deformation properties and fatigue of bituminous mixtures. *Adv. Mater. Sci. Eng.* 2013, 1–7. doi: 10.1155/2013/701764

Sha, A. M. (2008). Material characteristics of semi-rigid base. *China J. Highway* 21, 1–5. doi: 10.19721/j.cnki.1001-7372.2008.01.001

Silva, L. D., Benta, A., and Picado, S. L. (2018). Asphalt rubber concrete fabricated by the dry process: Laboratory assessment of resistance against reflection cracking. *Constr. Build. Mater.* 160, 539–550. doi: 10.1016/j.conbuildmat.2017.11.081

Sun, Y. Z., Zhai, Y. X., and Li, N. (2012). Analysis on the mechanism of reflection crack propagation and anti-crack effect of asphalt pavement. *J. Shenyang Jianzhu Univ*. 28, 1023–1029.

Tan, Y. Q., and Guo, M. (2013). Using surface free energy method to study the cohesion and adhesion of asphalt mastic. *Constr. Build. Mater*. 47, 254–260. doi: 10.1016/j.conbuildmat.2013.05.067

Tschegg, E. K., Macht, J., Jamek, M., and Steigenberger, J. (2007). Mechanical and fracture-mechanical properties of asphalt-concrete interfaces. *ACI Mater. J*. 104, 474–480. doi: 10.14359/18903

Wang, H. P., and Dai, J. G. (2019). Strain transfer analysis of fiber bragg grating sensor assembled composite structures subjected to thermal loading. *Compos. Part B Eng*. 162, 303–313. doi: 10.1016/j.compositesb.2018.11.013

Wang, H. P., Jiang, L. Z., and Xiang, P. (2018). Improving the durability of the optical fiber sensor based on strain transfer analysis. *Opt. Fiber Technol*. 42, 97–104. doi: 10.1016/j.yofte.2018.02.004

Wang, H. P., and Xiang, P. (2016). Strain transfer analysis of optical fiber based sensors embedded in an asphalt pavement structure. *IEEE Proc. Sci. Meas. Tech*. 27:075106. doi: 10.1088/0957-0233/27/7/075106

Wang, H. P., Xiang, P., and Jiang, L. Z. (2019). Strain transfer theory of industrialized optical fiber-based sensors in civil engineering: a review on measurement accuracy, design and calibration. *Sensor Actuat. A Phys*. 285, 414–426. doi: 10.1016/j.sna.2018.11.019

Wang, X. L., Huang, X. M., and Dian, J. G. (2016). Analysis on the mechanism of LSPM in preventing reflection crack of semi-rigid asphalt pavement. *J. Transp. Res. Develop*. 33, 12–18. doi: 10.3969/j.issn.1002-0268.2016.07.003

Xiao, C., Qiu, Y. J., Ai, C. F., and Huang, B. (2016). Experiment on dynamical characteristics of asphalt pavement under vehicle load. *J. Chang'an Univ*. 36, 26–34. doi: 10.19721/j.cnki.1671-8879.2016.02.004

Xue, Y. C., Qian, Z. D., and Jia, W. (2016). Design and evaluation of epoxy asphalt geogrid stress-absorbing laye. *J. Southeast Univ*. 32, 93–98. doi: 10.3969/j.issn.1003-7985.2016.01.016

Yang, Y., Liu, Z., Xin, Y. B., Liu, H. F., and Qu, X. (2017). Evolution law of strain response of semi-rigid asphalt pavement under dynamic loading. *J. China Foreign Highway* 37, 51–55. doi: 10.14048/j.issn.1671-2579.2017.02.011

Yoon, Y., Patel, S., Ji, R., and Hastak, M. (2017). Current state of reflective cracking in the United States. *J. Constr. Eng. Manage. ASCE* 143:04016099. doi: 10.1061/(ASCE)CO.1943-7862.0001246

Zamora, B. D., Calzada, P. M. A., Castro, F. D., and Vega, Z. A. (2011). Evaluation of anti-reflective cracking systems using geosynthetics in the interlayer zone. *Geotext. Geomembranes* 29, 130–136. doi: 10.1016/j.geotexmem.2010.10.005

Zeng, M. L., Luo, D., Wu, C. F., and Wu, Z. X. (2013). Anti-cracking properties of cement stabilized crushed stone pavement base materials of different aggregate structures. *J. Hunan Univ*. 40, 1–7. doi: 10.3969/j.issn.1674-2974.2013.10.001

Zhang, K., Zhang, Z. Q., and Luo, Y. F. (2018). Material composition design and anticracking performance evaluation of asphalt rubber stress-absorbing membrane interlayer (AR-SAMI). *Adv. Mater. Sci. Eng*. 2018, 1–11. doi: 10.1155/2018/8560604

Zhao, Y. J., and Ni, F. J. (2009). Reflective cracking viscoelastic response of asphalt concrete under dynamic vehicle loading. *J. Southeast Univ*. 25, 391–394.

Zornberg, J. G. (2017). Functions and applications of geosynthetics in roadways. *Procedia Eng*. 189, 298–306. doi: 10.1016/j.proeng.2017.05.048

Conflict of Interest: HW was employed by the company Hebei Construction Group Corporation Limited.

The remaining authors declare that the research was conducted in the absence of any commercial or financial relationships that could be construed as a potential conflict of interest.

frontiers in Materials

ORIGINAL RESEARCH
published: 28 July 2020
doi: 10.3389/fmats.2020.00180

Purifying Effect Evaluation of Pavement Surfacing Materials Modified by Novel Modifying Agent

Xiaolong Sun[1], Zhisheng Liu[2], Xiao Qin[3], Dongfang Zeng[1] and Yingmei Yin[1]*

[1] School of Civil and Transportation Engineering, Guangdong University of Technology, Guangzhou, China, [2] The Key Laboratory of Road and Traffic Engineering, Ministry of Education, Tongji University, Shanghai, China, [3] School of Transportation and Civil Engineering and Architecture, Foshan University, Foshan, China

Functional pavement material with an exhaust-purifying performance has gradually become of greater interest to researchers in recent years. For improving the purifying effect of functional micro surfacing, two types of raw ore powders with exhaust-purifying potentials were selected as novel functional modifiers. Firstly, the road performance of purifying micro surfacing was evaluated according to the ASTM and ISSA standards. Then, the dispersion state of modifying agents in emulsified asphalt evaporation residue was analyzed and discussed using SEM and FTIR. Finally, the purifying effect of micro surfacing on exhausts was examined in a laboratory to investigate the impact of various experimental conditions on the purifying performance. Meanwhile, the purifying performance was also monitored in a field test. The results showed that the road performance of purifying micro surfacing could fulfill the requirements of relevant technical standards. Pyrite had better dispersion property than specularite and titanium dioxide inside asphalt. The purifying micro surfacing could achieve a better purifying effect on NO_x and CO_x than traditional micro surfacing with TiO_2. These environmentally friendly pavement materials could provide new solutions for the reduction of polluting emissions in automobile exhausts.

Keywords: pavement, micro surfacing, exhaust purification, road performance, characterization

OPEN ACCESS

Edited by:
Jian Ouyang,
Dalian University of Technology, China

Reviewed by:
Cesare Sangiorgi,
University of Bologna, Italy
Huayang Yu,
South China University of Technology, China

****Correspondence:***
Xiaolong Sun
XLS1998@gdut.edu.cn

Specialty section:
This article was submitted to Structural Materials, a section of the journal Frontiers in Materials

Received: *21 February 2020*
Accepted: *15 May 2020*
Published: *28 July 2020*

Citation:
Sun X, Liu Z, Qin X, Zeng D and Yin Y (2020) Purifying Effect Evaluation of Pavement Surfacing Materials Modified by Novel Modifying Agent. Front. Mater. 7:180. doi: 10.3389/fmats.2020.00180

INTRODUCTION

Road traffic an integral part of the existing transportation system. In 2019, the number of automobiles around the world had almost exceeded 1.39 billion. Even though various innovative solutions have been found and applied in the automobile industry, the share of internal combustion engine vehicles (including hybrid vehicles) will remain prevalent for the next several decades (Wei et al., 2009; Miyamoto et al., 2012; Hirata, 2014), and thus the exhaust emissions will be one of the main atmospheric pollution sources (Rêgo et al., 2014). Due to incomplete combustion of hydrocarbon fuel in internal combustion engines, automobile exhausts including carbon monoxide (CO), hydrocarbons (HC), nitrogen oxides (NO_x), sulfur dioxides (SO_2), particulate matter (such as lead compounds, carbon black particles, or oil mist, etc.), and other atmospheric pollutants not only damage the natural environment, but also result in the haze pollution and urban heat island (UHI) effect (Çay et al., 2013; Fattah et al., 2013; Pinzi et al., 2013; Labarraque et al., 2015; Peng et al., 2015). Meanwhile, the emission increases of NO_x, SO_2, and particulate matter also increase the risk of cancer in humans (Tong et al., 2014). Therefore, the control of automobile exhausts is vital to protecting the environment and human health from air pollution.

Currently, the most common methods used to reduce exhaust emissions include the control of pollution sources, improvement of air exchange, development of new energy sources, and application of exhaust purifiers (Brijesh and Sreedhara, 2013; Amato et al., 2014; Beale et al., 2015). However, due to the large number of vehicles, the effectiveness of these solutions for emission reduction is limited (Yan et al., 2014; Goel and Guttikunda, 2015; Yu et al., 2017, 2019, 2020). Improving air exchange could lower the pollutant concentration within specific territories, but this method could hardly reduce the total amount of pollutant emissions. In recent years, the application of new energy sources has been widely researched as an indirect method to mitigate exhaust pollution (Kimble and Wang, 2013; Liu and Liang, 2013; Habib and Wenzel, 2014). As a result, the number of electric and fuel cell vehicles increases gradually (Hwang, 2013; Jhala et al., 2014). However, the share of internal combustion engine vehicles will remain prevalent for the next few decades (Sprouse and Depcik, 2013; Wang et al., 2013). At present, the use of exhaust purifiers has been proven to be the most efficient way to purify the pollution from exhaust gases. The existing exhaust purifiers are mainly divided into three types: one-stage catalyst, two-stage catalyst, and three-way catalyst (Schmeisser et al., 2013; Hofmann et al., 2015). Among these exhaust purifiers, three-way catalyst is the most popular and efficient exhaust purifier, which can effectively transform CO, HC, and NO_x into harmless gas (Opitz et al., 2014; Lan et al., 2015; Zeng and Hohn, 2016). However, there are still some disadvantages of the three-way catalyst, such as its low conversion rate under lean-burn, poor durability of purifying effect, and soot particle contamination, which makes it difficult to meet the ever-growing needs of the atmospheric environment protection (Park et al., 2015). In addition, the existing methods could only purify pollutants before emitting into the air, but not reduce the pollution gas already emitted to the atmosphere. Therefore, it is important to develop an effective way to purify both the exhaust gas emitted from vehicles and those into the atmosphere.

Pavement, as a road traffic carrier, has a huge contact area with the atmospheric environment. If the exhaust purifying effect could be achieved on pavement material, the exhausts emitted from vehicles might be controlled effectively within specific airspaces and converted into harmless gas. Micro surfacing was one of the most effective ways for quick maintenance of pavements (Ouyang et al., 2016, 2018a,b, 2019; Qin et al., 2018). The thickness, material composition, and quick construction promote the feasibility of applying micro surfacing for achieving the purifying function of pavement (Sun et al., 2018, 2020a,b; Chen et al., 2020; Wang et al., 2020). Therefore, in this paper, two novel functional materials with exhaust-purifying potentials were obtained from raw ore powders and modified with two auxiliary modifiers. The applying feasibility of novel modifying agents was evaluated through road performance and micro characterization. Furthermore, the impacts of various influencing factors on purifying performances of the new hybrid micro surfacing material were investigated by laboratory and field test. This study provides scientific references for further study of functional pavement materials.

TABLE 1 | Technical properties of selected functional materials.

Composition information	Fineness (Mesh)	Density ($g \cdot cm^3$)	Main ingredient content (%)
Rutile titanium dioxide	3,000	4.26	98
Pyrite	325	4.9	90
Specularite	325	4.7	92

TABLE 2 | Technical properties of selected surface modifiers.

Modifying agent	Boiling point/°C	Flash point/°C	Relative density (25°C)	Molecular weight
Isopropanol	82.3	12	0.79	60.06
Silane coupling agent (KH-550)	217	135	1.04	221.4

MATERIALS AND PREPARATION

Materials

Functional Materials

Considering the purification potential and compatibility between modifiers and asphalt, pyrite, specularite, and titanium dioxide were selected as the functional materials for this study, which were named as P, S, and TD for short in this paper, respectively. Technical performances of purifying functional materials are shown in **Table 1**.

The purifying functional materials contained two types of combinations, rutile titanium dioxide and pyrite, and rutile titanium dioxide and specularite, named as PTD and STD, respectively. The weight ratio of rutile titanium dioxide to pyrite or specularite was 1:1. Pyrite and specularite were obtained from raw ore powders, which might have adverse effects on the compatibility with asphalt. Therefore, isopropanol and a silane coupling agent were used to improve the surface property and enhance the purifying performance (Liu et al., 2019a,b). The technical properties of selected modifiers are shown in **Table 2**.

Modified Emulsified Asphalt

Styrene Butadiene Rubber (SBR) modified emulsified asphalt was used as a binder in this study. The content of SBR modified emulsified asphalt was 12.6% by dry weight of aggregate. The technical properties of SBR modified emulsified asphalt are detailed in **Table 3**.

Aggregate, Water, and Additive

Basalt was chosen as the aggregate and the sand equivalent value was 72%, which could reach the limit value of (ASTM D2419, 2014; Huang et al., 2020). The water used for micro surfacing was free of oil contamination. The salinity was below 5,000 mg/L. Specifically, the sulfate content was below 2,700 mg/L. Furthermore, the PH of the water was below 6. The content of water was 8.4% by dry weight of aggregate. In order to control the demulsification of SBR emulsified asphalt, this paper selected ordinary Portland cement as an additive to prepare

micro surfacing. Its content was ∼2% by dry weight of aggregate (Ouyang et al., 2020).

Modification of Purifying Functional Materials

The modification of functional materials mainly includes the following procedures (detailed in **Figure 1**):

(a) Sieve the functional materials: Pyrite and specularite were carefully washed with distilled water to remove dust and impurities, and dried at 110°C for 5 h in a pre-heated oven. Then, pyrite and specularite were filtered through a 0.044 mm sieve. The treated powder was placed into a clean container.

TABLE 3 | Technical properties of SBR modified emulsified asphalt.

Test	Value	Specification	Test method
Penetration of emulsified asphalt residue (25°C, 100 g, 5 s) (0.1 mm)	76	40–90	ASTM D5, 2013
Ductility of emulsified asphalt residue (5°C) (cm)	58	>20	ASTM D113, 2007
Distillation of emulsified asphalt (%)	63.3	≥62	ASTM D6997, 2004
Storage of emulsified asphalt (1 d) (%)	0.04	≤1	ASTM D6930, 2010
Residue on sieve (1.18 mm) (%)	0.03	≤0.1	ASTM D244, 2017
Softening point of emulsified asphalt residue (°C)	64	>57	ASTM D36, 2014

(b) Mill functional material: In order to increase the specific surface area and improve catalytic potential, pyrite, and specularite powder were subjected to high-energy ball milling under the protection of ethanol and inert gas.

(c) Perform surface modification: Silane coupling agent, isopropanol, and water were mixed to prepare the chemical solution, whose mass ratio was ∼20:72:8. The solution was subsequently treated by ultrasonic dispersion apparatus for 10 min. Then, pyrite and specularite were added into the solution, and the mixture was stirred at the speed of 5,000 rad/min for 15 min. Finally, the mixture was kept still for 1 h, and then the modified pyrite and specularite were filtered into a clean beaker.

(d) Conduct vacuum drying: The beaker containing pyrite and specularite were put into an 80°C vacuum drying oven for 5 h. The drying process was conducted in an inert gas atmosphere to ensure the chemical stability of pyrite and specularite.

Testing Specimen Preparation

The designed gradation and mix proportion are shown in **Table 4**. The detailed preparation procedures (**Figure 2**) are shown as follows:

(a) Prepare emulsified asphalt mixture: Basalt aggregate, additive, and water were mixed for 5 min to ensure that the aggregate was wetted to prevent the early demulsification of the modified emulsified asphalt. Then the functional materials

FIGURE 1 | Modifying process of functional materials.

TABLE 4 | Designed gradation and mix proportion of micro surfacing.

Gradation	Passing percentage (%)							
	9.5 mm	4.75 mm	2.36 mm	1.18 mm	0.6 mm	0.3 mm	0.15 mm	0.075 mm
Design gradation	100	80	57	39	27	17	11	8
ISSA A143	100	70–90	45–70	28–50	19–34	12–25	7–18	5–15
Component	Basalt aggregate	Emulsified asphalt	Functional material	Water	Additive			
Proportion (%)	100	12.6	6	8.4	2			

ISSA A143 Standard: "Recommend Performance Guideline for Micro Surfacing".

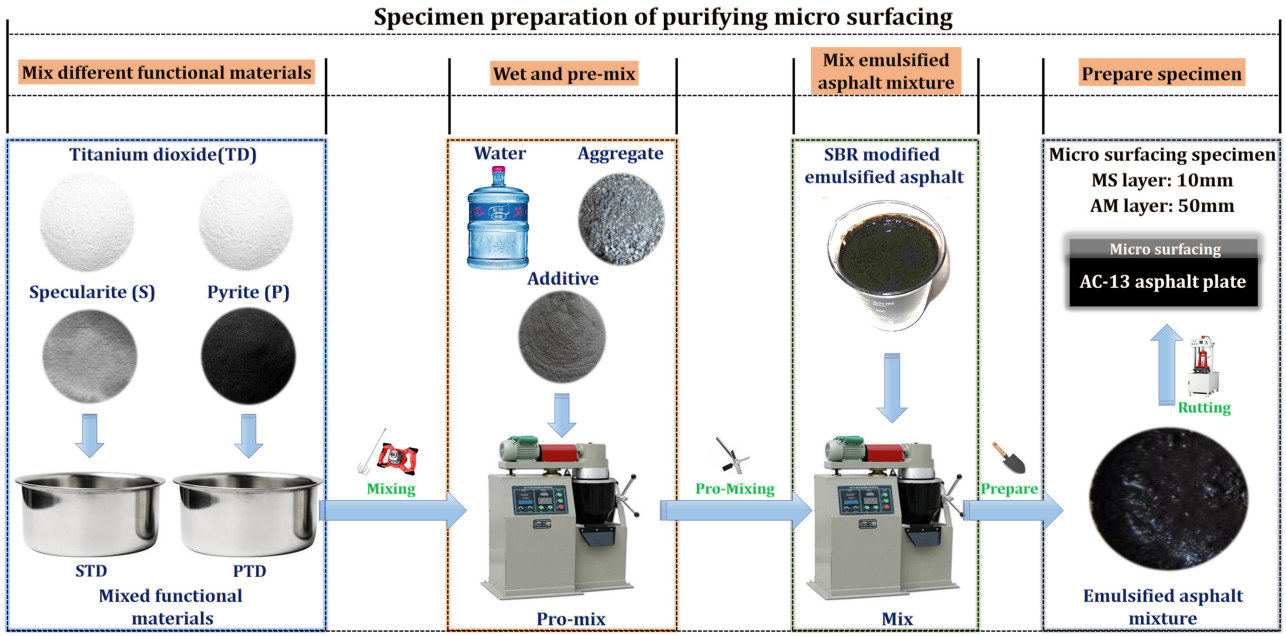

FIGURE 2 | Preparing process of micro surfacing specimen.

were added into the wet mixture and mixed for 4 min. SBR modified emulsified asphalt was added into the mixing pot steadily and then the mixture was mixed for 3 min.

(c) Prepare specimens for different tests: For the purifying test, British pendulum slip test, and permeability test, the micro surfacing (30*30*1 cm) was paved on the rutting specimen of the asphalt mixture (AC-13, 30*30*5 cm) and preserved at 25 ± 5°C. For the wet-track abrasion loss test and lateral displacement test, the prepared mixture was sampled, and cast in the molds on the surface of tar felt (Circular specimen 63.5 mm in diameter and rectangular specimen with the dimension of 38 × 5 × 0.6 cm) and preserved at 60°C for 16 h.

TESTING METHOD

Road Performance

The British pendulum slip test, wet-track abrasion loss test, rutting test, and permeability test were conducted to assess the road performances of purifying micro-surfacing according to the Standard ISSA TB-147, 2000; ASTM ED3910, 2011; ASTM E303, 2013, and JTG E60, 2008.

Micro Characterization

Scanning Electronic Microscopy Analysis (SEM)

Asphalt samples were prepared using the evaporation residue of purifying modified emulsified asphalt. The micro-morphology and particle size of functional materials in asphalt samples were characterized by SEM to determine the dispersion of functional materials inside asphalt. Then, the element composition of micro zones was statistically analyzed. The magnifications of the SEM test were 2,000, 4,000, and 10,000 times (Huang et al., 2019; Cai et al., 2020).

Fourier Transform Infrared Analysis (FTIR)

The FTIR analysis technology was used to investigate the characteristic peaks and functional groups of the evaporation residue with purifying modifiers. The wavenumber range of FTIR was from 4,000 to 500 cm^{-1}. The weight of the sample was about 5 μg.

Purifying Effect Evaluation

Measurement System

The purifying effect measurement device, as shown in **Figure 3**, was developed according to ISO 7996 (1985), ISO 4224 (2000), ISO 10498 (2004), ISO 22197-1 (2007), which consisted of a temperature controlling system, data acquisition system, atmospheric pressure, and solar radiation controlling system. This device was used to investigate the purifying effect of purifying micro surfacing. The technical parameters were shown as follows: Temperature control range: −20–120°C, UV intensity range: 0–20 w/m^2, Pressure tolerance range: 0–3 atm, and Gas concentration measurement range: 0.0–20.0 % vol (CO_x), 0–5,000$\times10^{-6}$ vol (NO_x).

Laboratory Testing Condition and Procedure

The atmospheric pressure, specimen temperature, UV light source intensity, and pollutant concentration were chosen as the influencing variables of the purifying experiment. A used motorcycle engine was used as the supply unit of exhaust, whose pollutant concentrations could reach the ISO Standard concentration range. According to the parameter values of real pavement environment, various experiment conditions are designed for a purifying effect test, as shown in **Table 5**.

The laboratory test procures is detailed as follows:

(a) Achieve the vacuum status: All the outlets of the experimental device, except the one connected to the vacuum pump, were closed and the vacuum pump was turned on to achieve the vacuum status of the reactor cell. When air pressure reached the vacuum, the vacuum pump was turned off and the outlet connected to the vacuum pump was closed.

(b) Adjust the concentration of pollutant gas: The exhaust supply unit was started and preheated. The outlet connected to the test facility was opened and the exhaust gas was conveyed into the reactor cell of the test equipment along with air at the flow rate of 3.0 L/min, when the content of pollutant gas of exhaust tends to be stable. When the air pressure and the concentration of pollutant gas reached the desired values, the exhaust supply unit and all the outlets of the experimental device were closed.

(c) Control the experimental condition and record the data: The temperature of the specimen was raised up to the target temperature using a temperature control system and the UV light intensity was kept around the desired value by the corporation of a light source control system and radiometer. Then the gas flow controller and circulation system were turned on to keep the exhaust distributed evenly in the reactor cell of the test equipment. The test data were monitored by the exhaust analyzer dynamically and recorded by the data acquisition automatically.

Field Testing Method

A field test was performed to measure the purifying effect in a natural environment. An experiment period of 10 days in August was selected to evaluate the purifying effect of micro surfacing, whose solar radiation intensities, atmospheric temperatures, and humilities were similar to those in the pavement environment. Before the start of the field test, the specimen was assembled inside the test device, then moved to the outside terrace sufficiently far from the surrounding buildings to avoid the shadow effect. The exhaust supplied by the motorcycle engine was conveyed along with air into the reactor cell after passing through a gas-washing bottle. When the desired exhaust concentration and air pressure were achieved through the coordination of the adjustment system and concentration monitoring system, all the outlets of the gas supply unit and the experiment apparatus were closed. The pollutant concentration, solar radiation intensity, and specimen temperature were monitored per hour using the gas analyzer, radiometer, and temperature sensor. The field test device is shown in **Figure 3**.

RESULTS AND DISSCUSSION

Road Performance

The results of road performances are shown in **Table 6**. It can be seen from **Table 6** that there were only slight differences in pavement performances between a purifying micro surfacing and a normal one, which indicated that the replacement of mineral filler by functional material would not lead to a negative effect on the pavement performances of micro surfacing, which lay a solid base for the application of PTD and STD materials in micro surfacing.

Dispersion and Fusion State Analysis

SEM/EDS Analysis

The microscopic graphs of PTD and STD emulsified asphalt residue and net residue were taken to characterize the microstructure of functional materials in asphalt and evaluate the compatibility between functional material and asphalt. The SEM graphs of purifying emulsified asphalt residue are shown in **Figure 4**.

It can be seen from **Figure 4B** that the bright particles represented different micro shapes, and particle sizes were evenly dispersed in asphalt, which might indicate the productive dispersion of PTD in asphalt. Through particle sizing results, the particle size ranged from 3.1 to 10 μm and most of the identified particles were around 4 μm or smaller in size. **Figure 4C** demonstrated the micro distribution state of STD in asphalt. It could be observed from **Figure 4C** that the distribution of particle size was mainly concentrated in the range from 2 to 10 μm, similar to that of PTD. However, a few big bright particles could be identified at 10 K magnification, which suggested that the specularite might not be dispersed evenly in asphalt material. Meanwhile, the element composition of micro zone in the SEM graph was analyzed and the analysis results are shown in **Figure 5**.

It can be seen from **Figure 5** that Fe, S, and O elements, as typical elements, were identified obviously in most of the scanning zones. Ti was also characterized in the micro zone, but the identified number of micro zones was smaller than that of other elements, which was presented in **Figure 5** (VI). Ti was the typical element of titanium dioxide, which might reflect the dispersion state of titanium dioxide in micro surfacing.

FIGURE 3 | Laboratory and field test of exhaust purification performance.

TABLE 5 | Experimental condition of purifying effect measurement.

Impact factor		Variable values	Test time	Experimental conditions
Atmospheric pressure		0.6, 0.8, 1.0, 1.2, 1.4, 1.6 atm	5 h	Ambient temperature:25°C UV light intensity:10 W/m^2 NO_x:60–70 ppm CO_x:70–80 ppm Humidity:50%
Specimen temperatures		30, 35, 40, 45, 50, 55, 60°C	5 h	UV light intensity:10 W/m^2 Air pressure:1.0 atm NO_x:60–70 ppm CO_x:70–80 ppm Humidity:50%
UV light source intensity		4, 6, 8, 10, 12, 14 W/m^2	5 h	Air pressure:1.0 atm Ambient temperature:25°C NO_x:60–70 ppm CO_x:70–80 ppm Humidity:50%
Pollutant concentration	NO_x CO_x	40, 50, 60, 70, 80 ppm	5 h	Air pressure:1.0 atm Ambient temperature:25°C UV light intensity:10 W/m^2 Humidity:50%
Field test	Ambient temperature, specimen temperatures, UV light intensity		8 h (Solar exposure time)	Air pressure:1.0 atm NO_x:60–70 ppm CO_x:70–80 ppm

The related ISO Standard of air purifying material that the test time should be no <5 h.

FTIR Analysis

The composition of functional groups was one of the most important parameters to indicate the chemical variation inside micro surfacing. Compared to the basic micro surfacing with no functional materials, the functional groups' variation of purifying micro surfacing was examined to explain the molecular structure after the addition of functional materials using the FTIR test. The FTIR analysis results are shown in **Figure 6**.

It can be seen from **Figure 6** that the transmission curves of purifying micro surfacing differed from that of the control group without functional materials. For PTD, the different transmission rates appeared in the wave number positions of 3,500, 1,750, 1,200, and 750 cm^{-1}. Regarding STD, the different transmission rates arose in the wave number positions of 1,500 and 750 cm^{-1}. The change of transmission rate in certain wave numbers could indicate that the functional materials, pyrite, and specularite, might help improve the purifying effect of micro surfacing though the chemical modification led by chemical characteristics.

Laboratory Evaluation of Purifying Effect

Air Pressure Condition

The impacts of atmospheric pressure on the purification effect was investigated in this section to guarantee the accuracy of the experiment. In **Figure 7A**, the results of the purifying test at different atmospheric pressures are presented. As the

TABLE 6 | Road performances of purifying micro surfacing and normal micro surfacing.

Test		PTD/STD micro surfacing	Normal micro surfacing	Standard requirements
British pendulum slip test (BPN)		74/77	75	≥45
Wet-track abrasion loss test	1 h Abrasion loss (g/m^2)	440.5/443.2	445.6	≤538
	6 d Abrasion loss (g/m^2)	605/606	609	≤807
Lateral displacement test	Lateral displacement (%)	3.0/3.1	3.1	≤5
	Relative density	1.61/1.60	1.63	≤2.10
Permeability test (ml/min)		7/7	7	10

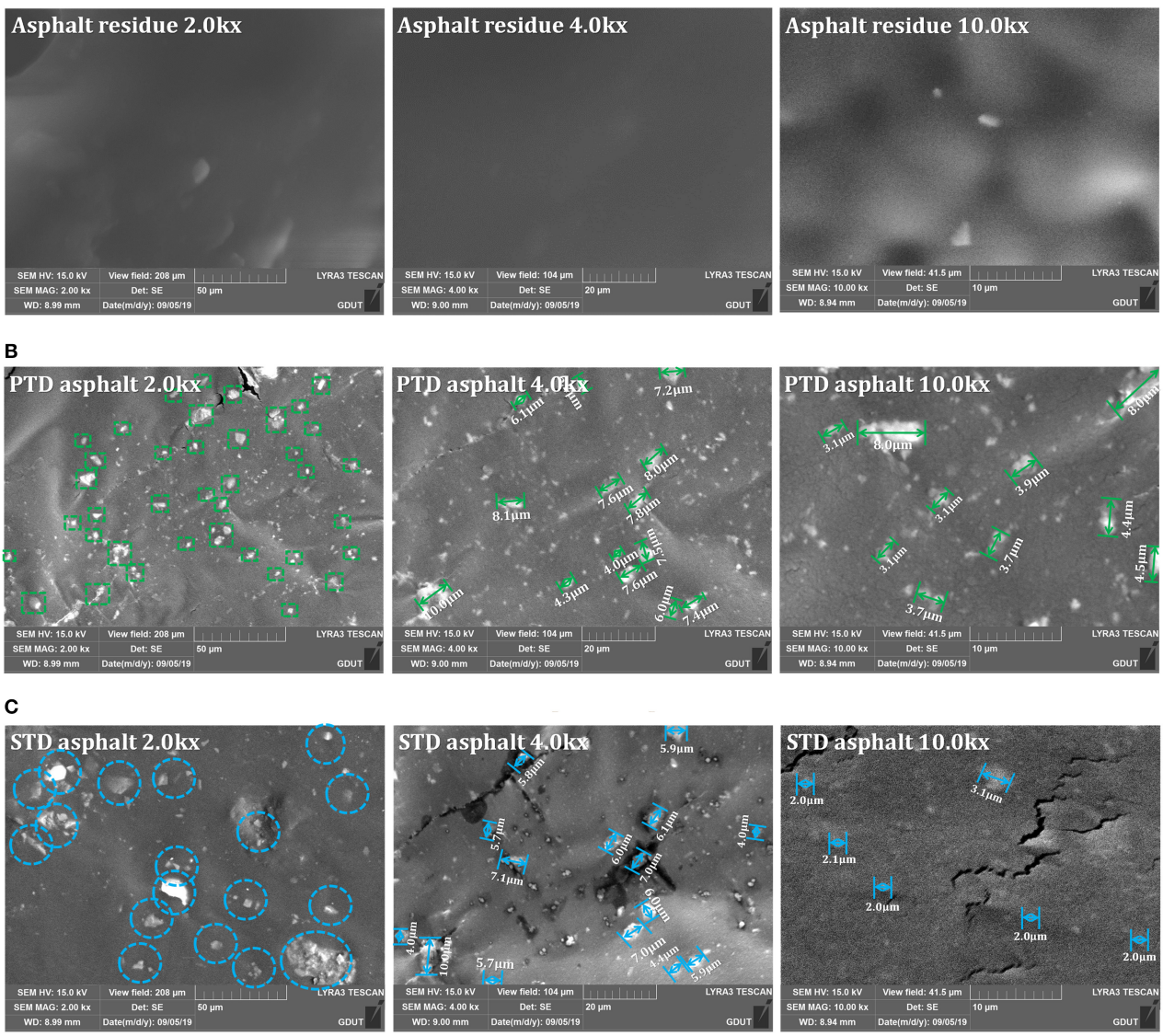

FIGURE 4 | SEM characterization results. **(A)** Emulsified asphalt evaporation residue. **(B)** PTD emulsified asphalt evaporation residue. **(C)** STD emulsified asphalt evaporation residue.

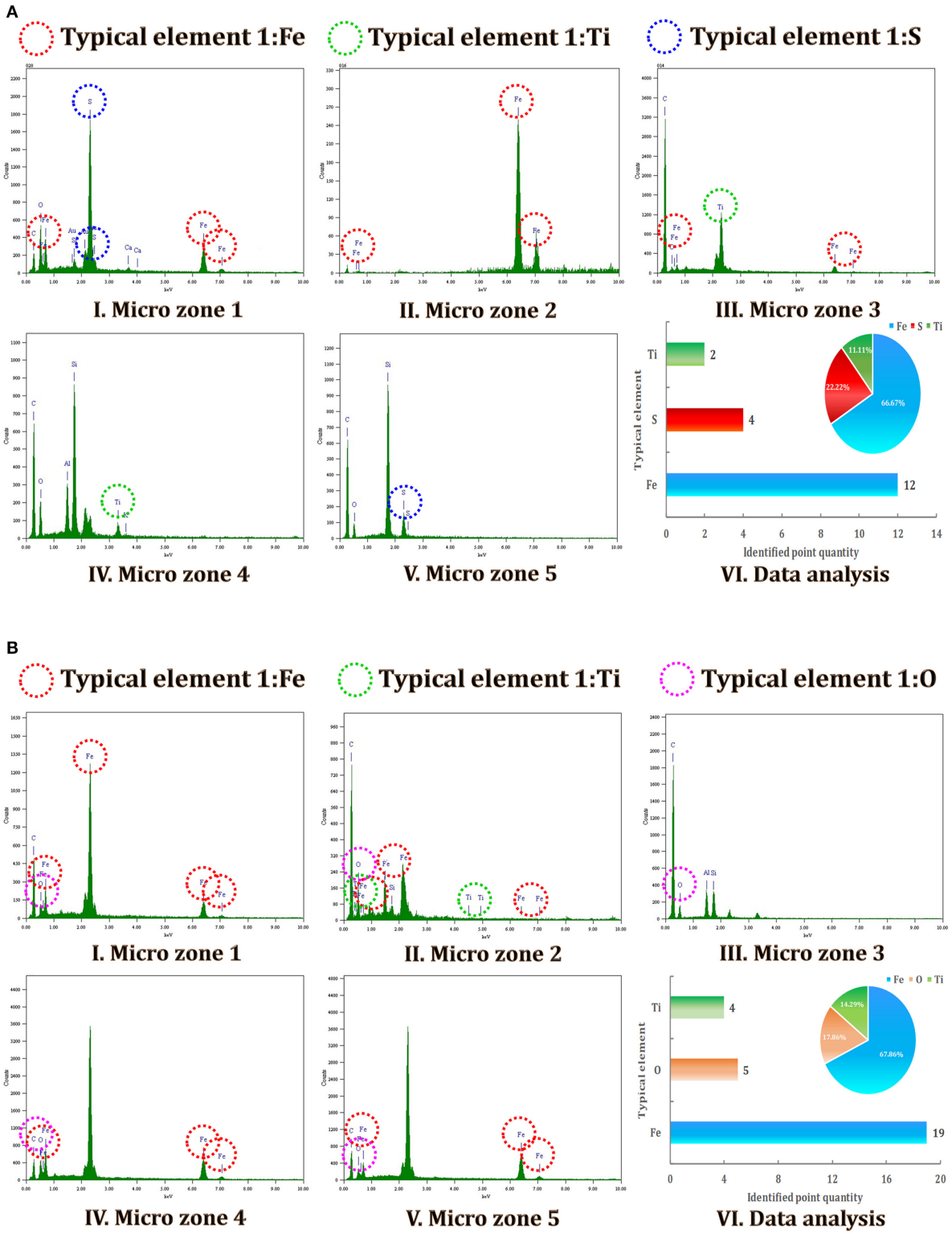

FIGURE 5 | EDS analysis results. **(A)** Emulsified asphalt evaporation residue. **(B)** PTD emulsified asphalt evaporation residue.

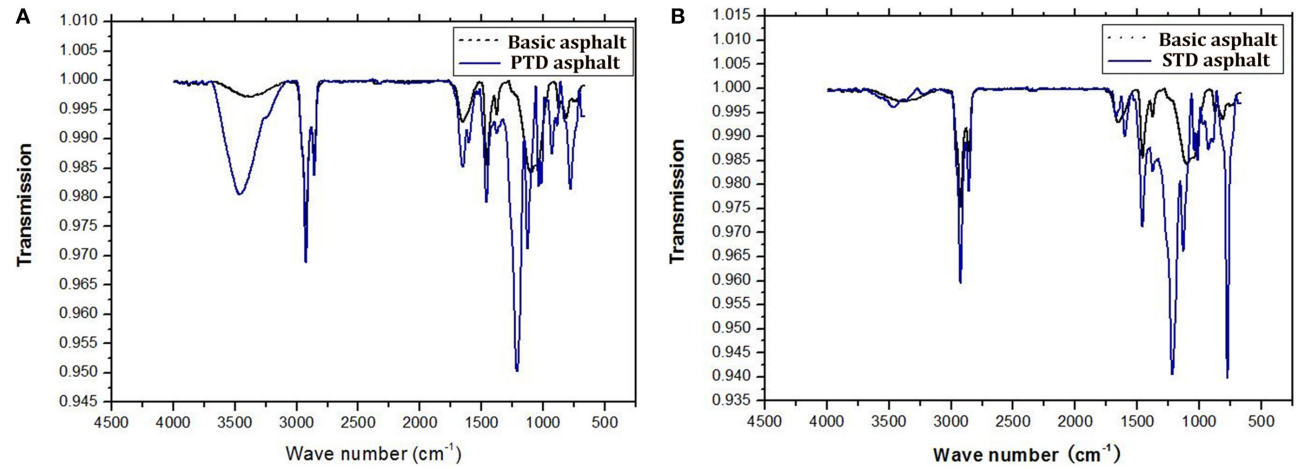

FIGURE 6 | FTIR analysis results. **(A)** FTIR-PTD. **(B)** FTIR-STD.

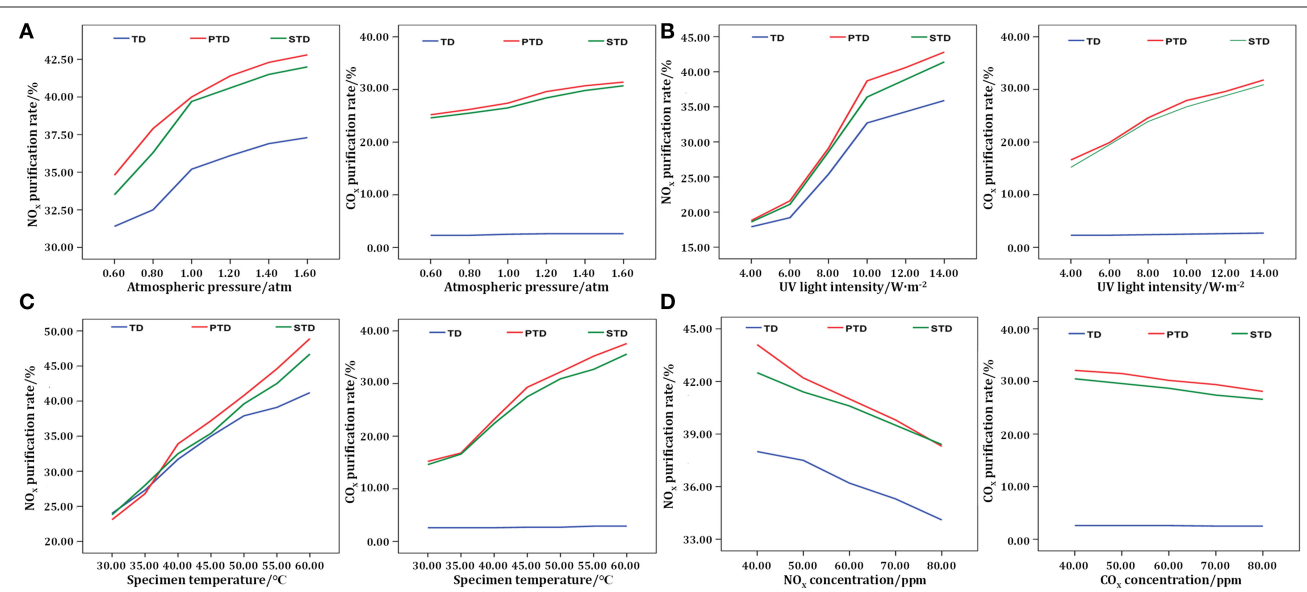

FIGURE 7 | Purification effect of exhaust under different influencing conditions. **(A)** Atmospheric pressure. **(B)** UV light intensity. **(C)** Speciman temperature. **(D)** Pollutant concentration.

atmospheric pressure increased gradually, the purifying effect of micro surfacing on pollutants also showed an obviously increasing trend. Moreover, when the atmospheric pressure exceeded 1.0 atm, the increasing speed of the purifying effect began to slow down and tended to be stable. While the atmospheric pressure increased from 0.6 to 1.6 atm, the purifying effect of PTD and STD on NO_x rose to ~34 and 42%, respectively. Interestingly, PTD and STD could achieve the purifying effect on CO_x, but TD could not.

Purifying Effect at Different UV Intensities

To examine the impact of UV radiation on purifying performance, the relationship between purifying rate and UV intensity was investigated over time on the PTD, STD, and TD micro surfacing. The test results are plotted in **Figure 7B**.

It was shown that the pollutant purifying performance of purifying micro surfacing could be greatly promoted by UV light intensity, especially for the effect on NO_x. The enhancing effect of UV intensity was noticeable on purifying performances on NO_x of all types of micro surfacing. When the UV intensity was 10 W/m^2, a turning point emerged in the curves showing the purifying effect on NO_x. When the UV intensity exceeded 10 W/m^2, the raising speed of the curve began to slow down, which meant that the dependence of purification on UV radiation started to weaken. For CO_x, the purifying rates of PTD and STD micro surfacing subjected

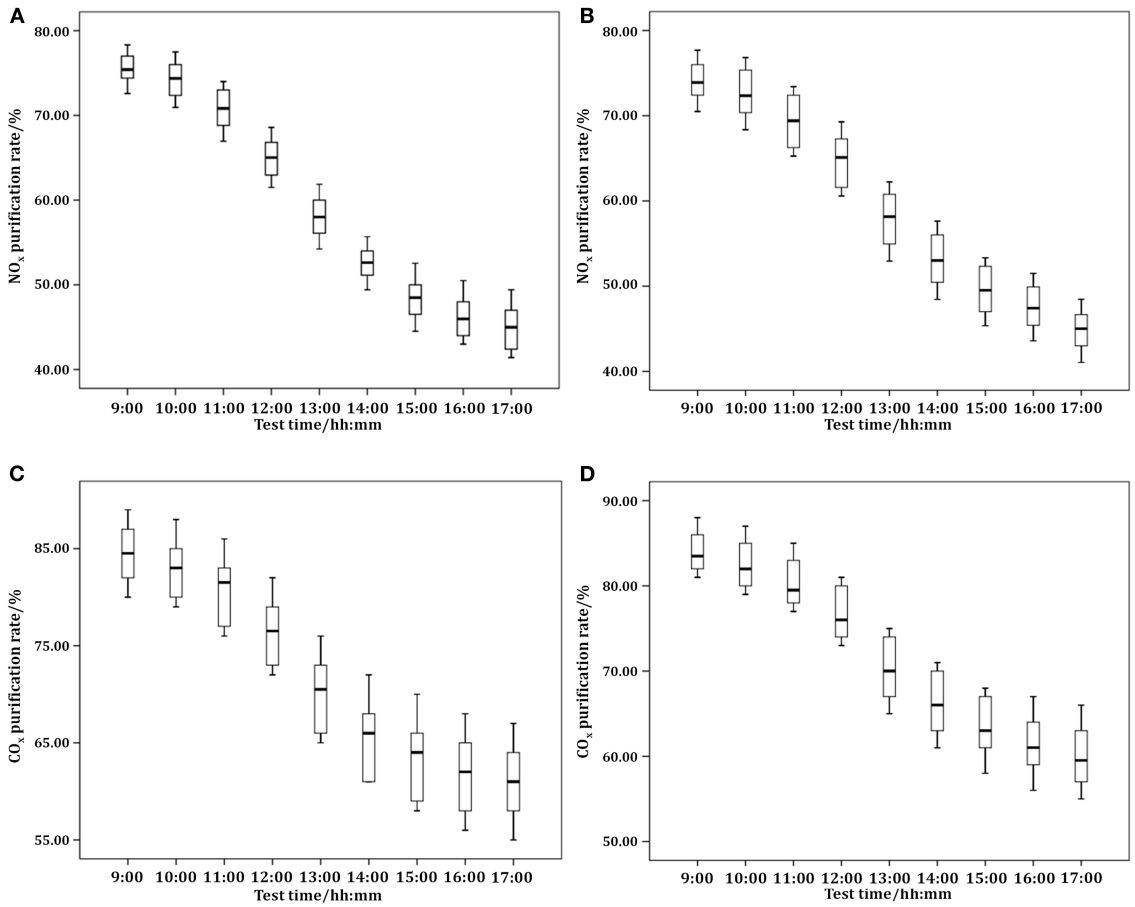

FIGURE 8 | Variation of pollutant concentration over the 10-day testing period. **(A)** NO_x-PTD. **(B)** NO_x-STD. **(C)** CO_x-PTD. **(D)** CO_x-STD.

to the increase of UV intensity showed a similar trend that followed the degradation curve of NO_x. However, the TD micro surfacing had no significant degradation effect on CO_x and the purifying effect was around 3%, even if the UV light intensity increased.

With the addition of modified pyrite and specularite, the NO_x and CO_x degradation rates of PTD and STD micro surfacing had been significantly improved compared to TD, while the UV intensity increased. The purifying effects of PTD and STD on NO_x and CO_x reached ∼40 and 30%, respectively. The improvement of the purifying effect might be led by the thermoelectric properties of modified pyrite and specularite. In addition, the increasing temperature of the specimen led by UV radiation might also activate the thermoelectric properties, which enhanced the purifying effect of pyrite and specularite.

Purifying Effect at Different Specimen Temperatures

The purification testing results of micro surfacing subjected to different specimen temperatures are presented in **Figure 7C**. As shown in **Figure 7C**, the increasing specimen temperature would enhance the NO_x and CO_x degradation rates of PTD, STD, and TD micro surfacing. For NO_x, the degradation rate curves of three micro surfacing showed a similarly increasing trend, while the gap between the hybrid micro surfacing and TD micro surfacing became larger with the increase of specimen temperature. This experimental conclusion was in line with that of the purifying effect at different UV intensities. For CO_x, PTD, and STD micro surfacing presented superior purifying performances, which could reach almost 40%. However, the TD micro surfacing had a limited removal effect on CO_x when temperature rose.

Purifying Effect at Different Pollutant Concentrations

Considering the variation of pollutant concentrations in an application environment (a highway, tunnel, bridge, etc.), the pollutant concentration would be an important factor among different influencing elements of purifying performance. The testing results at different pollutant concentrations are presented in the **Figure 7D**. The pollutant concentration had a noticeable negative linear effect on the degradation performance of purifying micro surfacing. This might be because that a

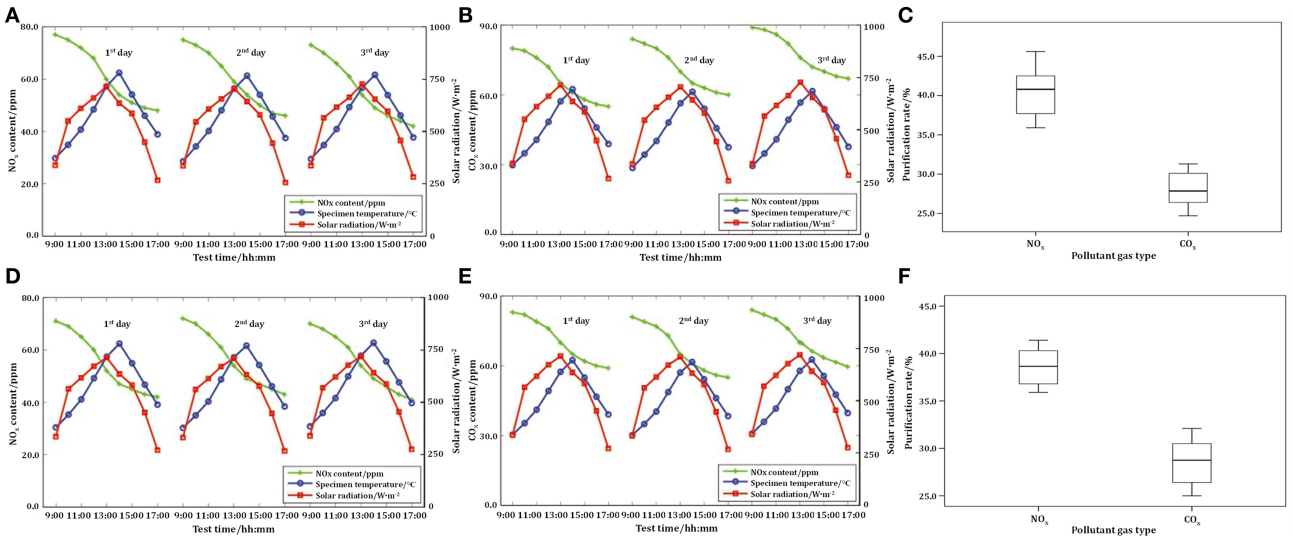

FIGURE 9 | Influence of environment factors on purifying performance. **(A)** NO_x (PTD). **(B)** CO_x(PTD). **(C)** Purifying rate (PTD). **(D)** NO_x (STD). **(E)** CO_x(STD). **(F)** Purifying rate (STD).

higher pollutant concentration would promote the conversion rate reaching its limit, and the overall purification effect then began to decrease. The NO_x and CO_x degradation rates of PTD and STD micro surfacing could still be over 40 and 30%, respectively, higher than that of TD micro surfacing.

Field Testing Results at Complex Environmental Conditions

The varying curves of pollutant gas concentration over the whole 10-day field testing period are plotted in **Figure 8**.

During the 8 h test period (9:00–17:00) of the 10 selected days, the NO_x and CO_x concentration decreased gradually. The initial value of the pollutant was within the specific range of the experiment condition described before. No obvious outliers were found among the experimental data. It could be calculated that the purifying effect of PTD on NO_x and CO_x were ∼40 and 35 ppm, respectively. Concerning STD, the purifying effects on NO_x and CO_x were about 34 and 32 ppm. Analyzing the median variation of pollutant concentration, there was a turning point that appeared at 13:00. For more accurate analysis, the experimental data obtained from three consecutive days, whose environmental parameters (solar radiation, temperature, etc.) were approximately identical, were chosen for the following analysis.

The variations of pollutant concentration, solar radiation intensity, and specimen temperature are presented in **Figures 9A,B,D,E**. The same trend of variation curves was observed for all the experimental results. Both NO_x and CO_x concentration showed an obvious decreasing trend along with the variation of environmental factors. This indicated that PTD and STD micro surfacing had noticeable purifying effects on NO_x and CO_x in the field test. The curve of pollutant concentration changed in an approximate linear trend, as solar radiation intensity and specimen increased. When the solar radiation intensity reached its peak value, a turning point appeared in the pollutant concentration curve. The curve slope began decreasing and the degradation speed started to slow down. This observation testified that the UV radiation was the main parameter influencing the purifying effect of purifying micro surfacing, which was consistent with the results of laboratory experiments.

The purification rates of PTD and STD micro surfacing are plotted in **Figures 9C,F**. For PTD micro surfacing, the data of the NO_x purifying rate mainly ranged between 35 and 45%. The median of these data was 41% and the upper quartile and lower quartile were 42 and 38%, respectively. The range of CO_x purifying data was from 25 to 30% and the CO_x purifying rate of PTD micro surfacing was around 27%. For STD micro surfacing, the NO_x and CO_x purification rates of STD micro surfacing were ∼38 and 28%, respectively.

CONCLUSIONS

This paper discussed the preparation and measurement of the purifying properties of two new hybrid pavement micro surfaces containing titanium dioxide, pyrite, and specularite. The pyrite and specularite were selected as the auxiliary functional materials and modified by using two modifying agents to inspire their purifying potentials. The purifying effects of micro surfacing on NO_x and CO_x were investigated in laboratory and field tests. The purifying effects at different atmospheric pressure, UV intensity, temperature, and pollutant concentration were monitored

and investigated. The major conclusions from this study are shown as following:

- With the addition of pyrite and specularite, the PTD and STD micro surfacing had noticeable purification effects on NO_x and CO_x, while the TD micro surfacing was only effective for the degradation of NO_x.
- The increase of UV intensity and ambient temperature would improve the purifying effect of PTD and STD micro surfacing on NO_x and CO_x.
- High pollutant concentration could lead to the conversion rate reaching its saturation limit and thus decrease the overall purification rates.
- The PTD and STD micro surfacing demonstrated a noticeable purifying performance on NO_x and CO_x in the field test when subjected to complex environmental factors, whose results were consistent with that of the laboratory test.

This paper provides new solutions to develop environmentally friendly pavement materials with superior exhaust purifying performances. Future work will focus on further studying the purifying performance of purifying micro surfacing within enclosed environments and the durability of the purifying function.

DATA AVAILABILITY STATEMENT

All datasets generated for this study are included in the article/supplementary material.

AUTHOR CONTRIBUTIONS

XS: data curation. XS and XQ: formal analysis. XS: investigation. XS and ZL: methodology. XS: writing – original draft. DZ, ZL, and YY: writing – review and editing. All authors: contributed to the article and approved the submitted version.

FUNDING

This paper describes research activities mainly requested and sponsored by the Shanxi Transportation Holding Group Co., Ltd. under grant number 19-JKKJ-20, by the Guangdong Provincial Department of Education under grant number 2018KQNCX067, by the National Natural Science Foundation of China under grant number 51908130, and by the Foundation Committee of basic and applied basic research of Guangdong Province under grant number 2019A1515110348.

REFERENCES

Amato, F., Cassee, F. R., van der Gon, H. A. D., Gehrig, R., Gustafsson, M., Hafner, W., et al. (2014). Urban air quality: the challenge of traffic non-exhaust emissions. *J. Hazard. Mater.* 275, 31–36. doi: 10.1016/j.jhazmat.2014.04.053

ASTM D113 (2007). *Standard Test Method for Ductility of Bituminous.* West Conshohocken, PA: ASTM International.

ASTM D2419 (2014). *Standard Test Method for Sand Equivalent Value of Soils and Fine Aggregate.* West Conshohocken, PA: ASTM International.

ASTM D244 (2017). *Standard Test Methods and Practices for Emulsified Asphalts.* West Conshohocken, PA: ASTM International.

ASTM D36 (2014). *Test Method for Softening Point of Bitumen (Ring-and-Ball Apparatus).* West Conshohocken, PA: ASTM International.

ASTM D5 (2013). *Standard Test Method for Penetration of Bituminous Materials.* West Conshohocken, PA: ASTM International.

ASTM D6930 (2010). *Standard Test Method for Settlement and Storage Stability of Emulsified Asphalts.* West Conshohocken, PA: ASTM International.

ASTM D6997 (2004). *Standard Test Method for Distillation of Emulsified Asphalt.* West Conshohocken, PA: ASTM International.

ASTM E303 (2013). *Standard Test Method for Measuring Surface Frictional Properties Using the British Pendulum Tester.* West Conshohocken, PA: ASTM International.

ASTM ED3910 (2011). *Standard Practices for Design, Testing, and Construction of Slurry Seal.* West Conshohocken, PA: ASTM International.

Beale, A. M., Gao, F., Lezcano-Gonzalez, I., Peden, C. H., and Szanyi, J. (2015). Recent advances in automotive catalysis for NOx emission control by small-pore microporous materials. *Chem. Soc. Rev.* 44, 7371–7405. doi: 10.1039/C5CS00108K

Brijesh, P., and Sreedhara, S. (2013). Exhaust emissions and its control methods in compression ignition engines: a review. *Int. J. Auto. Tech-Kor.* 14, 195–206. doi: 10.1007/s12239-013-0022-2

Cai, X., Wu, K., and Huang, W. (2020). Study on the optimal compaction effort of asphalt mixture based on the distribution of contact points of coarse aggregates. *Road Mater. Pavement*. 2020, 1–22. doi: 10.1080/14680629.2019.1710238

Çay, Y., Korkmaz, I., Çiçek, A., and Kara, F. (2013). Prediction of engine performance and exhaust emissions for gasoline and methanol using artificial neural network. *Energy* 50, 177–186. doi: 10.1016/j.energy.2012.10.052

Chen, Q., Wang, C., Qiao, Z., and Guo, T. (2020). Graphene/tourmaline composites as a filler of hot mix asphalt mixture: preparation and properties. *J. Construct. Build. Mater.* 239:117859. doi: 10.1016/j.conbuildmat.2019.117859

Fattah, I. R., Masjuki, H. H., Liaquat, A. M., Ramli, R., Kalam, M. A., and Riazuddin, V. N. (2013). Impact of various biodiesel fuels obtained from edible and non-edible oils on engine exhaust gas and noise emissions. *Renew. Sust. Energ. Rev.* 18, 552–567. doi: 10.1016/j.rser.2012.10.036

Goel, R., and Guttikunda, S. K. (2015). Evolution of on-road vehicle exhaust emissions in Delhi. *Atmos Environ.* 105, 78–90. doi: 10.1016/j.atmosenv.2015.01.045

Habib, K., and Wenzel, H. (2014). Exploring rare earths supply constraints for the emerging clean energy technologies and the role of recycling. *J. Clean. Prod.* 84, 348–359. doi: 10.1016/j.jclepro.2014.04.035

Hirata, H. (2014). Recent research progress in automotive exhaust gas purification catalyst. *Catal. Surv. Asia.* 18, 128–133. doi: 10.1007/s10563-014-9170-2

Hofmann, G., Rochet, A., Ogel, E., Casapu, M., Ritter, S., Ogurreck, M., et al. (2015). Aging of a Pt/Al2O3 exhaust gas catalyst monitored by quasi in situ X-ray micro computed tomography. *RSC. Adv.* 5, 6893–6905. doi: 10.1039/C4RA14007A

Huang, W., Cai, X., Li, X., Cui, W., and Wu, K. (2020). Influence of nominal maximum aggregate size and aggregate gradation on pore characteristics of porous asphalt concrete. *Materials* 13:1355. doi: 10.3390/ma13061355

Huang, W., Wang, H., Yin, Y., Zhang, X., and Yuan, J. (2019). Microstructural modeling of rheological mechanical response for asphalt mixture using an image-based finite element approach. *Materials* 12:2041. doi: 10.3390/ma12132041

Hwang, J. (2013). Sustainability study of hydrogen pathways for fuel cell vehicle applications. *Renew. Sust. Energ. Rev.* 19, 220–229. doi: 10.1016/j.rser.2012.11.033

ISO 10498 (2004). *Ambient Air–Determination of Sulfur Dioxide–Ultraviolet Fluorescence Method*. Geneva.

ISO 22197-1 (2007). *Fine Ceramics (Advanced Ceramics, Advanced Technical Ceramics)-Test Method for Air Purification Performance of Semiconducting Photocatalytic Materials-Part 1: Removal of Nitric Oxide*. Geneva.

ISO 4224 (2000). *Ambient Air–Determination of Carbon Monoxide–Non-Dispersive Infrared Spectrometric Method*. Geneva.

ISO 7996 (1985). *Ambient air–Determination of the Mass Concentration of Nitrogen Oxides–Chemiluminescence Method*. Geneva.

ISSA TB-147 (2000). *Multilayer Loaded Wheel Test. International Slurry Surfacing Association*. Annapolis.

Jhala, K., Natarajan, B., Pahwa, A., and Erickson, L. (2014). "Coordinated electric vehicle charging solutions using renewable energy sources," in *2014 IEEE Symposium on Computational Intelligence Applications in Smart Grid* (CIASG) (Geneva: IEEE), 1–6. doi: 10.1109/CIASG.2014.7011549

JTG E60 (2008). *Field Test Methods of Subgrade and Pavement for Highway Engineering*. Beijing: Research Institute of Highway Ministry of Transport.

Kimble, C., and Wang, H. (2013). China's new energy vehicles: value and innovation. *J. Business Strategy* 34, 13–20. doi: 10.1108/02756661311310413

Labarraque, G., Oster, C., Fisicaro, P., Meyer, C., Vogl, J., Noordmann, J., et al. (2015). Reference measurement procedures for the quantification of platinum-group elements (PGEs) from automotive exhaust emissions. *Int. J. Environ. An. Ch.* 95, 777–789. doi: 10.1080/03067319.2015.1058931

Lan, L., Chen, S., Cao, Y., Wang, S., Wu, Q., Zhou, Y., et al. (2015). Promotion of CeO2–ZrO2–Al2O3 composite by selective doping with barium and its supported Pd-only three-way catalyst. *J. Mol. Catal. A-Chem.* 410, 100–109. doi: 10.1016/j.molcata.2015.09.016

Liu, H., and Liang, D. (2013). A review of clean energy innovation and technology transfer in China. *Renew. Sust. Energ. Rev.* 18, 486–498. doi: 10.1016/j.rser.2012.10.041

Liu, K., Li, Y., Wang, F., Xie, H., Pang, H., and Bai, H. (2019a). Analytical and model studies on behavior of rigid polyurethane composite aggregate under compression. *J. Mater. Civil Eng.* 31:04019007. doi: 10.1061/(ASCE)MT.1943-5533.0002641

Liu, K., Liang, W., Ren, F., Ren, J., Wang, F., and Ding, H. (2019b). The study on compressive mechanical properties of rigid polyurethane grout materials with different densities. *Construct. Build. Mater.* 206, 270–278. doi: 10.1016/j.conbuildmat.2019.02.012

Miyamoto, A., Nagumo, R., Suzuki, A., Miura, R., Tsuboi, H., Hatakeyama, N., et al. (2012). *Electronic and Atomistic Roles of Cordierite Substrate in Sintering of Washcoated Catalysts for Automotive Exhaust Gas Emissions Control: Multi-Scale Computational Chemistry Approach Based on Ultra-Accelerated Quantum Chemical Molecular Dynamics Method (No. 2012-01-1292)*. SAE Technical Paper. Geneva. doi: 10.4271/2012-01-1292

Opitz, B., Drochner, A., Vogel, H., and Votsmeier, M. (2014). An experimental and simulation study on the cold start behaviour of particulate filters with wall integrated three-way catalyst. *Appl. Catal. B-Environ.* 144, 203–215. doi: 10.1016/j.apcatb.2013.06.035

Ouyang, J., Han, B. G., Cao, Y., Zhou, W. J., Li, W. G., and Surendra, P. S. (2016).The role and interaction of superplasticizer and emulsifier in fresh cement asphalt emulsion paste through rheology study. *J. Construct. Build. Mater.* 125, 643–653. doi: 10.1016/j.conbuildmat.2016.08.085

Ouyang, J., Hu, L. J., Li, H. Y., and Han, B. G. (2018a). Effect of cement on the demulsifying behavior of over-stabilized asphalt emulsion during mixing. *J. Construct. Build. Mater.* 177, 252–260. doi: 10.1016/j.conbuildmat.2018.05.141

Ouyang, J., Pan, B., Xu, W., and Hu, L. (2019). Effect of water content on volumetric and mechanical properties of cement bitumen emulsion mixture. *J. Mater. Civil. Eng.* 31:04019085. doi: 10.1061/(ASCE)MT.1943-5533.00027361

Ouyang, J., Yang, W., Chen, J., and Han, B. (2020). Effect of superplasticizer and wetting agent on pavement properties of cold recycled mixture with bitumen emulsion and cement. *J. Mater. Civil Eng.* 32:04020136. doi: 10.1061/(ASCE)MT.1943-5533.0003194

Ouyang, J., Zhao, J., and Tan, Y. (2018b). Modelling the mechanical properties of cement asphalt emulsion mortar with different asphalt to cement ratio and temperature. *J. Mater. Civil. Eng.* 30:04018263. doi: 10.1061/(ASCE)MT.1943-5533.0002480

Park, C. W., Lee, S. Y., Yi, U. H., and Lee, J. H. (2015). Emission reduction characteristics of three-way catalyst with engine operating condition change in an ultra-lean gasoline direct injection engine. *Trans. Korean Soc. Mech. Eng. B* 39, 727–734. doi: 10.3795/KSME-B.2015.39.9.727

Peng, B., Cai, C., Yin, G., Li, W., and Zhan, Y. (2015). Evaluation system for CO2 emission of hot asphalt mixture. *J. Traffic Transport. Eng.* 2, 116–124. doi: 10.1016/j.jtte.2015.02.005

Pinzi, S., Rounce, P., Herreros, J. M., Tsolakis, A., and Dorado, M. P. (2013). The effect of biodiesel fatty acid composition on combustion and diesel engine exhaust emissions. *Fuel* 104, 170–182. doi: 10.1016/j.fuel.2012.08.056

Qin, X., Shen, A., Guo, Y., Li, Z., and Lv, Z. (2018). Characterization of asphalt mastics reinforced with basalt fibers. *J. Construct. Build. Mater.* 159, 508–516. doi: 10.1016/j.conbuildmat.2017.11.012

Rêgo, A. T., Hanriot, S. M., Oliveira, A. F., Brito, P., and Rêgo, T. F. U. (2014). Automotive exhaust gas flow control for an ammonia–water absorption refrigeration system. *Appl. Therm. Eng.* 64, 101–107. doi: 10.1016/j.applthermaleng.2013.12.018

Schmeisser, V., Weibel, M., Hernando, L. S., Nova, I., Tronconi, E., and Ruggeri, M. P. (2013). Cold start effect phenomena over zeolite scr catalysts for exhaust gas aftertreatment. *SAE Int. J. Commercial Vehicles* 6, 190–199. doi: 10.4271/2013-01-1064

Sprouse, I. I. I. C., and Depcik, C. (2013). Review of organic Rankine cycles for internal combustion engine exhaust waste heat recovery. *Appl. Therm. Eng.* 51, 711–722. doi: 10.1016/j.applthermaleng.2012.10.017

Sun, X., Qin, X., Li, S., Zou, C., Wang, C., and Wang, X. (2018). Characterization of thermal insulating micro-surfacing modified by inorganic insulating material. *J. Construct. Build. Mater.* 175, 296–306. doi: 10.1016/j.conbuildmat.2018.04.170

Sun, X., Qin, X., Liu, Z., Yin, Y., Jiang, S., and Wang, X. (2020a). Applying feasibility analysis and catalytic purifying potential of novel modifying agent used in asphalt pavement materials. *J. Construct. Build. Mater.* 245:118467. doi: 10.1016/j.conbuildmat.2020.118467

Sun, X., Qin, X., Liu, Z., Yin, Y., Zou, C., and Jiang, S. (2020b). New preparation method of bitumen samples for UV aging behavior investigation. *J. Construct. Build. Mater.* 233:117278. doi: 10.1016/j.conbuildmat.2019.117278

Tong, H., Rappold, A. G., Caughey, M., Hinderliter, A. L., Graff, D. W., Berntsen, J. H., et al. (2014). Cardiovascular effects caused by increasing concentrations of diesel exhaust in middle-aged healthy GSTM1 null human volunteers. *Inhal. Toxicol.* 26, 319–326. doi: 10.3109/08958378.2014.889257

Wang, C., Chen, Q., Guo, T., and Li, Q. (2020). Environmental effects and enhancement mechanism of graphene/tourmaline composites. *J Clean Prod.* 262:121313. doi: 10.1016/j.jclepro.2020.121313

Wang, D., Zamel, N., Jiao, K., Zhou, Y., Yu, S., Du, Q., et al. (2013). Life cycle analysis of internal combustion engine, electric and fuel cell vehicles for China. *Energy* 59, 402–412. doi: 10.1016/j.energy.2013.07.035

Wei, Z., Niu, H., and Ji, Y. (2009). Simultaneous removal of SO_2 and NOx by microwave with potassium permanganate over zeolite. *Fuel. Process. Technol.* 90, 324–329. doi: 10.1016/j.fuproc.2008.09.005

Yan, F., Winijkul, E., Bond, T. C., and Streets, D. G. (2014). Global emission projections of particulate matter (PM): II. uncertainty analyses of on-road vehicle exhaust emissions. *Atmos Environ.* 87, 189–199. doi: 10.1016/j.atmosenv.2014.01.045

Yu, H., Leng, Z., Zhou, Z., Shih, K., Xiao, F., and Gao, Z. (2017). Optimization of preparation procedure of liquid warm mix additive modified asphalt rubber. *J. Clean. Prod.* 141, 336–345. doi: 10.1016/j.jclepro.2016.09.043

Yu, H., Zhu, Z., Leng, Z., Wu, C., Zhang, Z., Wang, D., et al. (2020). Effect of mixing sequence on asphalt mixtures containing waste tire rubber and warm mix surfactants. *J. Clean. Prod.* 246:119008. doi: 10.1016/j.jclepro.2019.119008

Yu, H., Zhu, Z., Zhang, Z., Yu, J., Oeser, M., and Wang, D. (2019). Recycling waste packaging tape into bituminous mixtures towards enhanced mechanical properties and environmental benefits. *J. Clean. Prod.* 229, 22–31. doi: 10.1016/j.jclepro.2019.04.409

Zeng, F., and Hohn, K. L. (2016). Modeling of three-way catalytic converter performance with exhaust mixture from natural gas-fueled engines. *Appl. Catal. B-Environ.* 182, 570–579. doi: 10.1016/j.apcatb.2015.10.004

Conflict of Interest: The authors declare that this study received funding from Shanxi Transportation Holding Group Co., Ltd. The funder was not involved in the study design, collection, analysis, interpretation of data, the writing of this article, or the decision to submit it for publication.

frontiers in Materials

ORIGINAL RESEARCH
published: 30 July 2020
doi: 10.3389/fmats.2020.00208

Factors Influencing the Interfacial Bonding Characteristics Between Cold Patching Asphalt Mixture and the Old Pavement

Fengchen Chen[1,2], *Kaidi Liu*[1,2]*, *Yiqiu Tan*[3], *Song Ye*[1,2], *Huining Xu*[3] *and Jian Ouyang*[4]

[1] China Airport Construction Group Corporation, Beijing, China, [2] Beijing Super-Creative Technology Co., Ltd., Beijing, China, [3] School of Transportation Science and Engineering, Harbin Institute of Technology, Harbin, China, [4] Faculty of Infrastructure Engineering, School of Transportation and Logistics, Dalian University of Technology, Dalian, China

Cold patching asphalt mixture (CPAM) has been widely used in pothole repair due to the advantages of convenient construction and easy storage. However, CPAM usually has a short service life because of insufficient bonding to the old pavement during service. Therefore, in order to ensure the good bonding of CPAM to the old pavement and improve the integrity and durability of pothole repair, this work carried out a study on the influencing factors of the bonding characteristics between CPAM and the old pavement. The oblique shear test was used as the research method with an evaluating index shearing strength. The influencing factors which affect the interface bonding characteristics, such as temperature, humidity, types of tack coat, the amount of tack coat spreading, and surface roughness, were compared and analyzed. The analysis results illustrated that the interface bonding characteristics are weak at high temperature and decrease with the increase of humidity. There exists an optimal binder spreading amount, where the denser the CPAM is, the smaller the spreading amount of the tack coat is. The groove on the old pavement can increase the bond strength of the interface, and there is optimal groove spacing. Based on this, the gray correlation analysis method was used to clarify the degree of influence of various factors and reveal the dominant factors that affect the interface bonding characteristics. The analysis indicated that the dominant influencing factors of the interface bonding characteristics are the type of tack coat and the roughness of the surface.

Keywords: cold patching asphalt mixture, influencing factors, interface bonding, gray correlation analysis, dominant factors

OPEN ACCESS

Edited by:
Huisu Chen,
Southeast University, China

Reviewed by:
Ping Duan,
China University of Geosciences Wuhan, China
Xiaoming Huang,
Southeast University, China

***Correspondence:**
Kaidi Liu
liukaidi1994@outlook.com

Specialty section:
This article was submitted to Structural Materials, a section of the journal Frontiers in Materials

Received: *29 February 2020*
Accepted: *08 June 2020*
Published: *30 July 2020*

Citation:
Chen F, Liu K, Tan Y, Ye S, Xu H and Ouyang J (2020) Factors Influencing the Interfacial Bonding Characteristics Between Cold Patching Asphalt Mixture and the Old Pavement. Front. Mater. 7:208. doi: 10.3389/fmats.2020.00208

INTRODUCTION

A pothole is a common type of damage in asphalt pavement (Adlinge and Gupta, 2013; Kim and Ryu, 2014; Kim et al., 2017; Ouma and Hahn, 2017). Potholes seriously affect the driving comfort and safety, shorten the life of the pavement, and reduce the service level of the pavement. Therefore, the pavement should be repaired in a timely fashion after potholes appear (Dong et al., 2014; Zhang et al., 2014; Wang et al., 2015; Tedeschi and Benedetto, 2017). Currently, there are many kinds of materials used for pothole repair (Prowell and Franklin, 1996; Ouyang et al., 2019a, 2020). Cold patching asphalt mixture (CPAM) has been widely used in pothole repair

because of its strong environmental adaptability, simple repair process, and convenient storage and transportation (Anderson et al., 1998; Li et al., 2010a; Zhao and Tan, 2010; Zhang et al., 2014; Diaz, 2016; Liao et al., 2016). However, the poor bonding performance between CPAM and old pavement materials is a common issue during application due to the differences in material composition, environment, and construction technology. The bonding performance between them seriously affects the service life and the durability of CPAM (Rosales Herrera and Prozzi, 2008; Tan et al., 2014; Rezaei et al., 2017).

Considering its particularity and the complexity in its service environment, the influencing factors of the interfacial bonding characteristics between CPAM and the old pavement are varied (Munyagi, 2007; Li et al., 2010b). Compared with hot mixture asphalt (HMA), CPAM has a special composition in which the binder is usually cutback asphalt or emulsified asphalt with low viscosity, poor initial strength, and cohesive properties in the early stage. Therefore, the material composition, such as type of binder, composition structure, and type of additive, can affect the interfacial bonding characteristics (Berlin and Hunt, 2001; Ferrotti et al., 2014; Ouyang et al., 2019b). Additionally, the external environment has an important influence on the interfacial bonding characteristics. In hot weather conditions, the viscosity of the tack coat decreases. Thus, the bonding between CPAM and the old pavement decreases. In contrast, the materials shrink in cold conditions, resulting in the expansion of the seam between CPAM and the old pavement (Ouyang et al., 2018). In a humid environment, moisture isolates CPAM and the old pavement, which reduces the interfacial bonding characteristics (Kuhn et al., 2005; Dong et al., 2014). Furthermore, the on-site construction treatment has some effects, such as compaction level, choice of tack coat, spreading amount of the tack coat, and the interface treatment method (Gómez-Meijide and Pérez, 2014). The above mentioned factors have different effects on the interfacial bonding performance (Ma et al., 2015). Choosing a tack coat with high viscosity and convenient construction may greatly improve the interfacial bonding performance. However, it is difficult to choose a suitable tack coat because there are many types of tack coat. In the actual construction process, the degree of compaction should generally meet the requirements, and the influence level is very small. This shows that the influencing factors of the interfacial bonding characteristics are complicated, so it is necessary to obtain a clear analysis of these factors.

Gray correlation analysis is very meaningful for the analysis of multiple complex influencing factors. The main problem solved by gray correlation analysis is finding a quantitative method that can measure the correlation between various factors in a system containing various factors in order to determine the main influencing factors (Julong, 1989; Zhang and Zhang, 2007). Gray correlation analysis has been used in various fields to analyze complex influencing factors, such as the study of the influence of asphalt surface properties on freezing viscosity strength (Zhang, 2013), effect of the crumb rubber modifier (CRM) content, CRM particle size, mixing time, and curing temperature on the viscosity of the crumb rubber-modified asphalt (Sun and Li, 2010) and evaluation of the shear performance of a flexible, moisture proof-adhesive layer in a concrete bridge pavement base (Fen et al., 2009). Gray correlation analysis provides an opportunity to analyze the influencing factors of the interfacial bonding characteristics between CPAM and the old pavement.

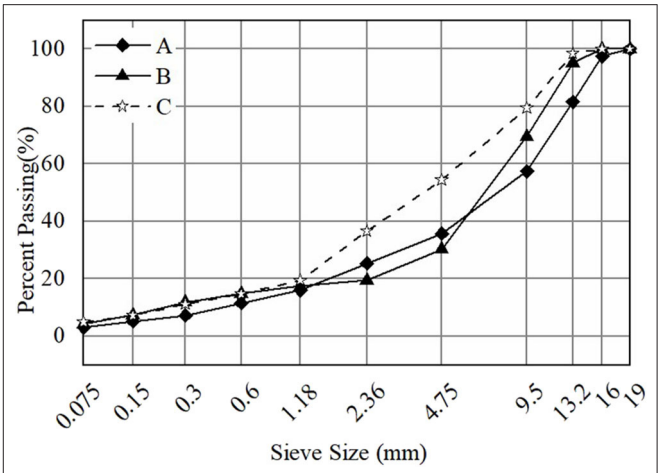

FIGURE 1 | Aggregate gradation for CPAM.

In order to solve the above mentioned problems, in this work, the temperature, humidity, type of tack coat, amount of tack coat spreading, and surface roughness were taken as the influencing factors for the oblique shear test, and the influences of different factors on the interface bonding characteristics were analyzed. On this basis, a gray correlation analysis was performed to determine the degree of influence of each factor and to find the dominant factors. This analysis has a good guiding significance for the practical repair of potholes with CPAM.

MATERIALS AND METHODS

Materials

Cold Patching Asphalt Mixture

Three kinds of CPAM were selected for testing in the study. They were Changlin from China, Shell from Netherlands, and Maple from Canada, respectively, recorded as A, B, and C. Extraction and sieving of the three kinds of CPAM were performed to obtain a gradation curve, as shown in **Figure 1**. CPAM A contains less fine aggregate and more coarse aggregate, CPAM B contains more coarse and fine aggregate, and CPAM C contains more fine aggregate and less coarse aggregate.

Tack Coat

The tack coat was daubed onto the interface between the pothole and the old pavement before repair in order to wet the pothole so that CPAM could be well-bonded with the old pavement overall. Binders with different viscosities were chosen to make the test results obvious. From a wide variety of binders, modified emulsified asphalt A, modified emulsified asphalt B, SBS modified asphalt, matrix asphalt, and rubber asphalt were selected for this research.

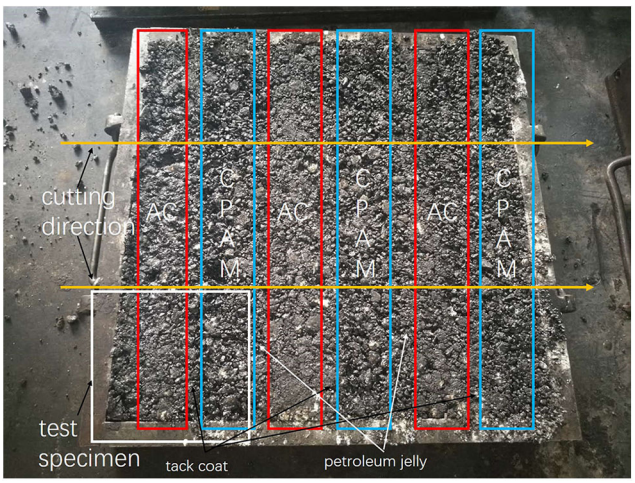

FIGURE 2 | The progress of specimen preparation.

FIGURE 3 | The device of oblique shear test.

Experimental Methods

Specimen Preparation

The specimens used in the test were composite specimens composed of CPAM and HMA. The preparation process is as follows:

First, rutting specimens made of AC-13 with a size of 300 mm × 300 mm × 50 mm were prepared. Second, they were cut into six trabeculae with a size of 300 mm × 300 mm × 50 mm and placed in the rutting specimen mold at 50-mm interval, and the gap was filled with CPAM. The interface in one side was daubed with tack coat, and the interface in the other side was daubed with a paper sheet coated with petroleum jelly to prevent sticking. Then, after rolling the specimen 16 times, the specimen with the mold was put into an oven at 110°C for 24 h, and then it was rolled again eight times, as shown in **Figure 2**. After the specimen had cooled, it was cut again. The interface between the CPAM and the original rutting specimen was well-bonded with the tack coat, and finally, specimens with a size of 100 mm × 50 mm × 100 mm for the oblique shear test were finished.

Experimental Methods

In this work, five factors were mainly studied: temperature, humidity, type of tack coat, amount of tack coat spreading, and interface roughness. In order to create the interface at a differently wet state, the specimens were immersed in moisture for different amounts of time. For the purpose of increasing the interface roughness, grooves were made on the surface at different intervals to increase the interface friction. The pendulum friction tester was used to determine the British pendulum number (BPN) value of the specimen surface in the direction of the groove (Karaca et al., 2013). For this test, a condition with temperature of 25°C, no moisture immersion, tack coat of modified emulsified asphalt, spreading amount of 0.5 kg/m^2, and no grooving was used as the benchmark test condition. When studying the influence of a single factor on the interface bonding state, we kept the other conditions as per the benchmark test conditions and changed the single factor separately for research.

The oblique shear test was selected because it could accurately reflect the force state of the interface under the combined action of horizontal and vertical loads (Meng et al., 2018). The test device is shown in **Figure 3**. The size of the groove in the upper half was 100 mm × 100 mm × 50 mm, with a slope of 45°. In order to reduce the influence of the horizontal force generated by the bottom friction on the test results, a roller coated with lubricant was placed under the mold. Finally, shear failure occurred for the interface.

Gray Correlation Analysis of the Factors Influencing the Interfacial Bond Characteristics

Gray correlation analysis was used to analyze the dominant influencing factors of multiple complex influencing factors (Wang et al., 2004) and to calculate the correlation degree in order to represent the importance of each influencing factor (Xu and Yang, 2015). The specific steps are as follows:

(1) Define the subsequence X and the parent sequence Y: The influencing factors of the parameter indexes were seen as the subsequence X, where X_i was the value of the influencing factors such as the temperature. Correspondingly, the parameter index was taken as the parent sequence Y, where Y_i was the shear strength value corresponding to each influencing factor.

(2) Non-dimensionalization processing of the sequence factors: The interval-valued processing was used in this work, which was performed according to Equations (1) and (2).

$$x_{ij}^{'} = \frac{x_{ij} - \min_j x_{ij}}{\max_j x_{ij} - \min_j x_{ij}} \tag{1}$$

$$x_{ij}^{'} = \frac{y_{ij} - \min_j y_{ij}}{\max_j y_{ij} - \min_j y_{ij}} \tag{2}$$

(3) Determine the matrix gray correlation difference information space: The difference sequence matrix was obtained with Equation (3). Then, the maximum values and the minimum values were obtained in the difference sequence matrix:

$$\Delta_{ij} = \left| y_{ij}^{\cdot} - x_{ij}^{\cdot} \right| \quad (3)$$

$$\Delta_{\max} = max(\Delta_{ij}) \quad (4)$$

$$\Delta_{\min} = min(\Delta_{ij}) \quad (5)$$

(4) Calculation of the parent association matrix and relevance: An overall analysis was performed to judge the differences and the correlations between the factors. Then, the correlation coefficient was used to represent the correlation coefficient matrix L of the comparison factor and the reference factor, where each factor was determined with Equation (6):

$$l_{ij} = \frac{\Delta_{\max} + \lambda \Delta_{\min}}{\Delta_{\max} + \Delta_{ij}} \quad (6)$$

If there are too many correlation coefficients, the degree of information dispersion will be too large. Therefore, the average value of the correlation coefficient was used as a comparison index of the correlation degree of the influencing factors. The correlation between the various factors was obtained with Equation (7):

$$r_i = \frac{1}{n} \sum \sum_{j=1}^{n} l_{ij} \quad (7)$$

RESULTS AND DISCUSSIONS

The test results show that the failure of the specimens occurred at the interface between CPAM and HMA. The shear resistance at the interface is far less than that of the two materials themselves, indicating that the interface is the weak and easily damaged part after repair. The specific test results are shown in **Table 1**.

TABLE 1 | Results of the oblique shear test under different influencing factors.

Influencing factors	The levels of factors	Shear strength (MPa)		
		A	B	C
Temperature/°C	−5	2.119	2.323	2.763
	10	1.237	1.361	1.497
	25	0.478	0.503	0.563
	40	0.043	0.154	0.089
	55	0.029	0.059	0.049
Humidity	0	0.478	0.503	0.563
	12 h	0.314	0.382	0.431
	24 h	0.194	0.262	0.311
	36 h	0.146	0.189	0.217
	48 h	0.099	0.123	0.155
Types of tack coat	Matrix asphalt	0.313	0.310	0.286
	Modified emulsified asphalt B	0.445	0.454	0.430
	Modified emulsified asphalt A	0.478	0.503	0.563
	SBS modified asphalt	0.406	0.372	0.312
	Rubber asphalt	0.347	0.358	0.325
The amount of tack coat spreading /kg/m^2	0	0.228	0.293	0.409
	0.25	0.262	0.356	0.530
	0.5	0.478	0.503	0.563
	0.75	0.505	0.496	0.471
	1	0.516	0.470	0.435
Surface roughness	No groove	0.478	0.503	0.563
	2 cm	0.547	0.577	0.650
	1.5 cm	0.585	0.626	0.694
	1 cm	0.600	0.647	0.718
	0.5 cm	0.609	0.658	0.731

Effect of Temperature on Interfacial Bonding Characteristics

At the time of the research, most of the tack coat used between CPAM and the old pavement are asphalt materials. Due to the temperature sensitivity of the asphalt material, the interface between CPAM and the old pavement changes with different temperatures. Therefore, the effect of temperature on the interfacial bonding characteristics was investigated.

The oblique shear test results of three kinds of CPAM at different temperatures are shown in **Figure 4**. It can be seen that with the increase of temperature, the interface shear strength of the three kinds of CPAM gradually decreases. Taking CPAM A as an example, when the temperature increased from −5 to 55°C, the interface shear strength decreased from 2.119 to 0.029 MPa, a reduction of 98.6%. This is because the viscosity of the tack coat gradually decreases with increasing temperature, which results in the decrease of the bonding ability of CPAM with the old pavement. This indicates that temperature has a significant effect on the interfacial adhesion strength.

Before the temperature reached 40°C, the interface shear strength decreased rapidly for the three kinds of CPAM, but after 40°C, it became very low and remained essentially unchanged. Taking CPAM A as an example, when the temperature rises from −5 to 40°C, the shear strength decreases from 2.119 to 0.043 MPa, which is a reduction of 98%. This is mainly because of an essential feature of asphalt that decreases with increasing temperature. However, when the viscosity of the tack coat is very low and basically unchanged with the temperature increase, the tack coat fails to adhere to CPAM and the old pavement. Unlike the asphalt wrapped on the surface of the aggregate, the failure temperature of the interface is lower. From the above mentioned analysis, it can be seen that the failure temperature is about 40°C.

Through the data fitting of the shear strength at different temperatures, the functional relationship between temperature and bonding degree was summarized, as shown in **Figure 5**. The equation is a binomial function, $y = 2.06 - 6.983 \times 10^{-2}x - 2.71 \times 10^{-4}x^2 + 2.97 \times 10^{-5}x^3 - 2.72 \times 10^{-7}x^4$, $R^2 = 0.97874$. It can be seen that the fitting effect is good.

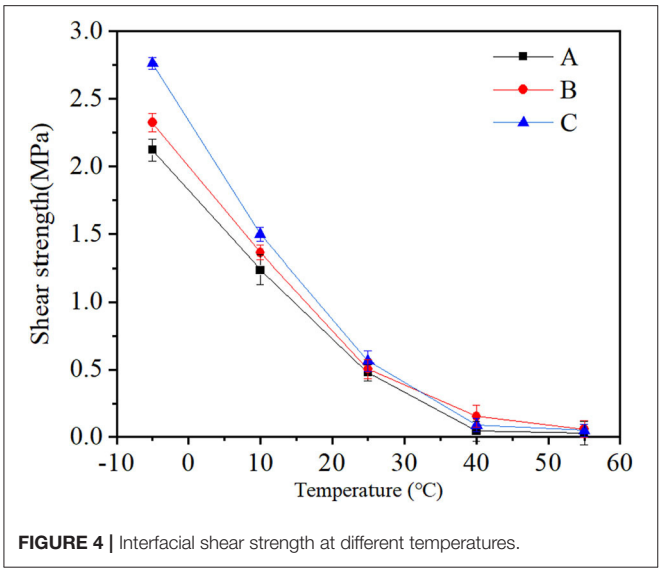

FIGURE 4 | Interfacial shear strength at different temperatures.

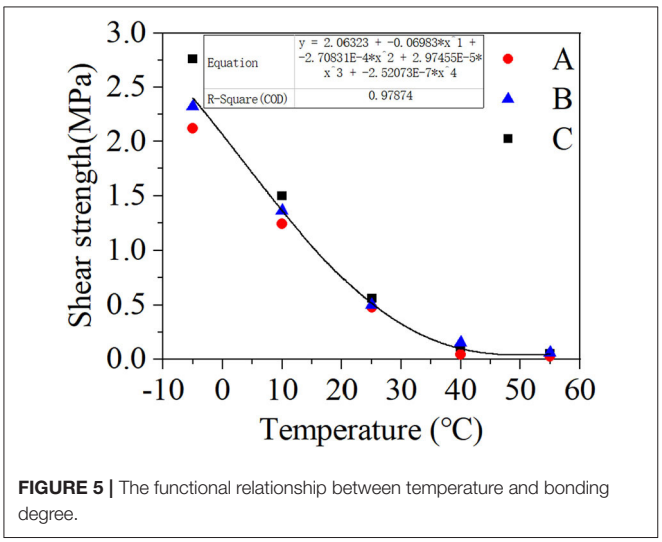

FIGURE 5 | The functional relationship between temperature and bonding degree.

This equation can predict the interface bonding strength at different temperatures and guide the construction process of pothole repair.

Effect of Humidity on Interfacial Bonding Characteristics

When the moisture penetrates the interface between CPAM and the old pavement, the dynamic water pressure that is generated with intermittent dynamic vehicle easily breaks the interface, so it is necessary to study the influence of different humidities on the interface bonding characteristics.

The interfacial shear strength results for different humidities are shown in **Figure 6**. It can be seen that the longer the immersion time is, the lower the interfacial shear strength is. Taking CPAM C as an example, after the moisture immersion time increased from 0 to 48 h, the interface shear strength decreased from 0.563 to 0.155 MPa, a decrease of 72.5%. This

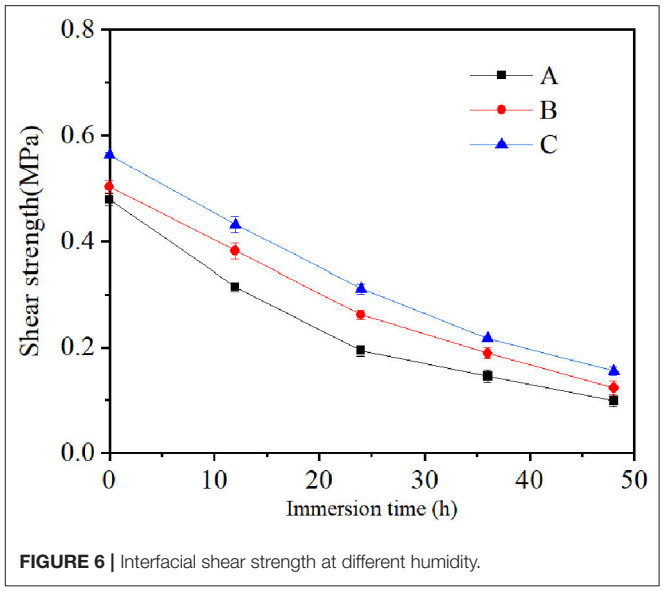

FIGURE 6 | Interfacial shear strength at different humidity.

indicates that as the moisture immersion time increases, moisture infiltrates into the interface and acts as a lubricant, which causes an obvious reduction in the interface bonding strength. Therefore, it is necessary to drain the water in the pothole and keep it dry before repair.

Effect of Types of Tack Coat on Interfacial Bonding Characteristics

Considering the different viscosities of the different tack coats, five kinds of tack coat (matrix asphalt, modified emulsified asphalt A, modified emulsified asphalt B, SBS-modified asphalt, and rubber asphalt) were selected to study the influence of the interface characteristics. Dynamic viscosity tests at 60°C were performed on five kinds of asphalt or their evaporation residues. The order of the viscosity was as follows: modified emulsified asphalt A > modified emulsified asphalt B > SBS-modified asphalt > rubber asphalt > matrix asphalt.

The interface shear strengths of the different tack coats are shown in **Figure 7**. For the three kinds of CPAM, the shear strength of the five binders is in the same order. Taking CPAM A as an example, when matrix asphalt, modified emulsified asphalt B, modified emulsified asphalt A, SBS-modified asphalt, and rubber asphalt are used as tack coat, their shear strengths are 0.313, 0.445, 0.478, 0.406, and 0.347 MPa, respectively. It can be known from this information that the greater the viscosity of the binder is, the stronger the interfacial shear strength is. Therefore, when CPAM is used to repair a pothole, a tack coat with high viscosity should be selected.

Effect of Tack Coat Spreading on Interfacial Bonding Characteristics

The results of the interfacial shear strength at different amounts of tack coat spreading are shown in **Figure 9**. It can be seen that with the increase of binder amounts, the interfacial shear strength of CPAM B and CPAM C climbs up and then declines,

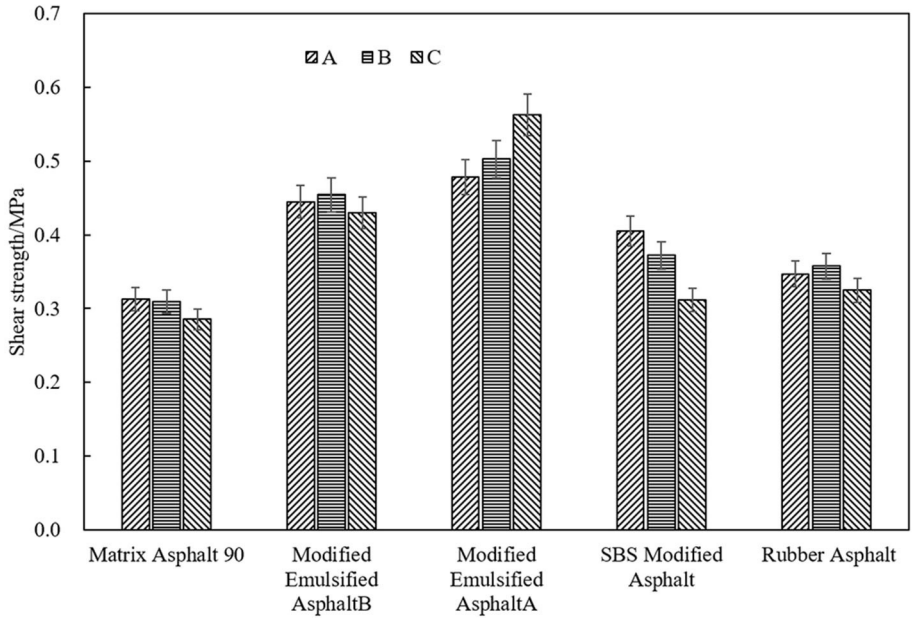

FIGURE 7 | Interfacial shear strength at different tack coat.

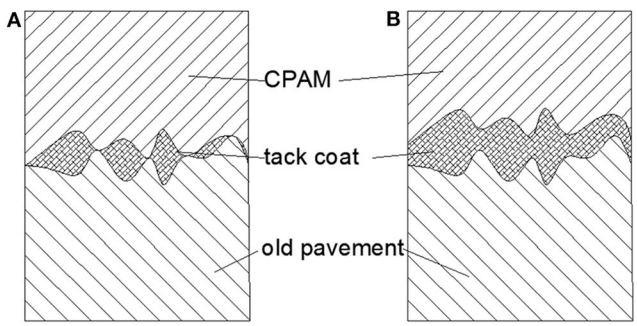

FIGURE 8 | The tack coat between CPAM and old pavement.

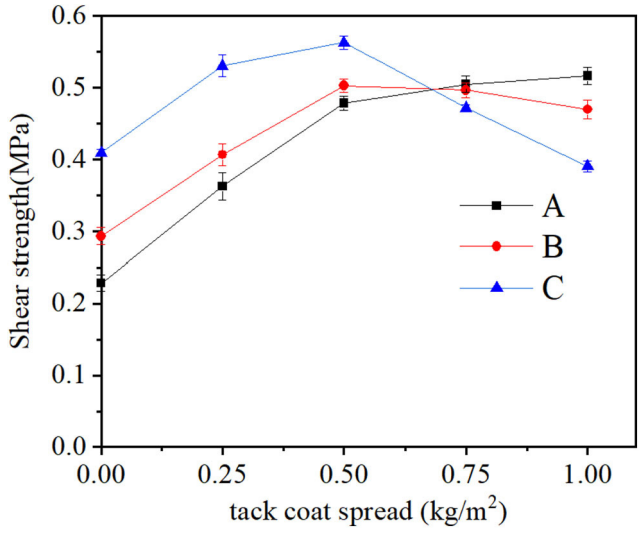

FIGURE 9 | Interfacial shear strength at different tack coat spreading amount.

and the maximum shear strengths are obtained at 0.75 and 0.5 kg/m^2, respectively. For CPAM A, the shear strength increases, but after the spreading amount becomes 0.5 kg/m^2, the shear strength generally does not increase. It can be known that there is an optimal spreading amount of tack coat for CPAM B and CPAM C to repair the pothole. Although the optimal spreading amount for CPAM A does not appear in the figure because of the limitation of the spreading amount range in the test, it can be concluded from the curve trend that there is an optimal spreading amount after the spreading amount of 1 kg/m^2. This happens because, at the beginning, with the increase of tack coat spreading amount, the tack coat fills in the gap between CPAM and the old pavement, bonding them together. However, after the spreading amount reaches a certain level, the interfacial voids are filled up, and the excess adhesive acts as a lubricant, so the interface shear strength decreases (**Figure 8**).

It can also be seen from **Figure 9** that the optimal spreading amounts for CPAM A, CPAM B, and CPAM C are >1, 0.75, and 0.5 kg/m^2, respectively. This is determined by the void structure of CPAM. CPAM C has high fine aggregate content, low air void content, and low tack coat capacity, so the optimal spreading amount is the smallest. CPAM A has high coarse aggregate content, high air void content, and high tack coat capacity, so the optimal spreading amount is the largest. Therefore, the tack coat spreading amount is greater for CPAM with large voids.

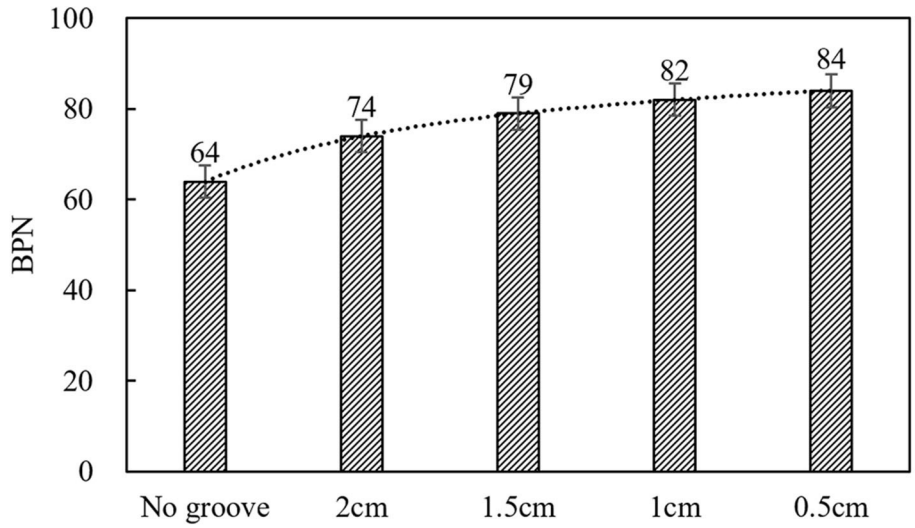

FIGURE 10 | Relation between groove interval and BPN value.

Effect of Roughness Interfacial Bonding Characteristics

Due to the different roughness levels of the interface, the contact area between the tack coat and the interface is different. Thus, the interface adhesion characteristics are also different. Therefore, the influence of different surface roughness on the surface bonding characteristics was studied in this work.

In order to increase the roughness of the surface, some grooves were made in the surface of HMA at intervals of 0.5, 1, 1.5, and 2 cm, respectively. The pendulum friction meter was used to measure the BPN value of the surface perpendicular to the groove direction, as shown in **Figure 10**. It can be seen that the BPN value increases with the decrease of groove spacing. When the groove interval is 0.5 cm, the BPN is 84, and when not grooved, the BPN is 64, which is an increase of 31.3%. Therefore, by grooving on the surface of the old pavement, the roughness increases, and the roughness increases with the decrease of the groove interval. As the groove interval decreases, the increase rate of the BPN value gradually slows down. When the groove interval is 1 cm, the BPN is 82. When the groove interval is closer to 0.5 cm, the BPN is 84, increasing by only 2.4%. It can be seen that when the interval of the grooves is small to a certain extent, the grooves have little effect on increasing the roughness. The shear strength at different roughness levels is shown in **Figure 11**. With the increase of the BPN value, the shear strength gradually increases, and when the BPN reaches 82, that is, when the optimal groove spacing is 1 cm, the shear strength reaches a maximum and then decreases. The reason for this phenomenon is that there is a competitive relationship between the tack coat in the groove and the tack coat on the interface, as shown in **Figure 12**. The tack coat at the interface can preferentially penetrate into the groove, increasing the contact bonding area, and at the same time, the tack coat acts as an anchor. Therefore, the smaller the groove spacing in a certain range, the greater the shear strength is. However, when the interval between the grooves is too small, with too many grooves, more tack coat penetrates into the grooves, resulting in an insufficient tack coat amount at the interface, so the shear strength is reduced. It can be known that if the groove interval is small, reaching a certain level, the interface bonding strength will reduce. Therefore, it should be noted that the groove interval has to be appropriate.

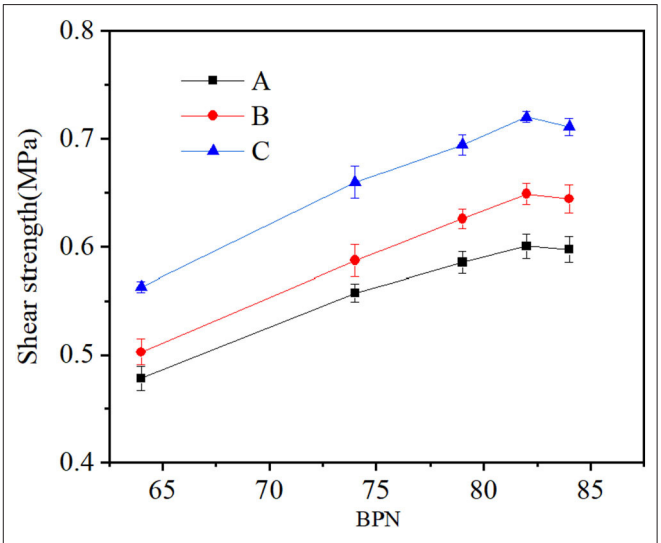

FIGURE 11 | Interfacial shear strength at different surface roughness.

Gray Correlation Analysis of Factors Affecting Interfacial Bonding Characteristics

Taking the shear strength as the parent sequence and each influencing factor value as the subsequence, the correlation degrees of different influencing factors on the shear strength were

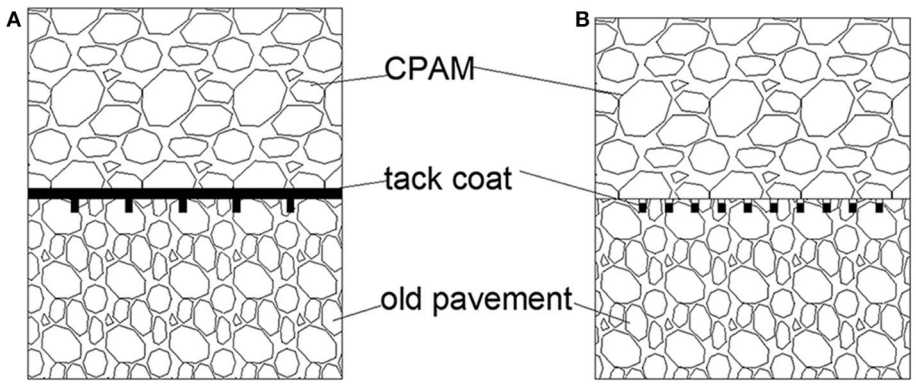

FIGURE 12 | Competitive relationship of the tack coat between the groove and the interface.

TABLE 2 | Gray correlation degree between the different influencing factors and shear strength.

Factors / CPAM	Temperature	Humidity	Types of tack coat	Amount of tack coat spreading	Surface roughness
A	0.462	0.478	0.874	0.796	0.87
B	0.462	0.491	0.93	0.717	0.897
C	0.465	0.494	0.889	0.553	0.879

obtained through gray correlation analysis. A greater correlation degree indicates that the influence of the factor on the interface bonding characteristics is greater. In contrast, the smaller the correlation degree is, the less the influence this factor has on the interface bonding characteristics. The correlation degree between the different influencing factors and the shear strength was calculated using Equations (1)–(7). The results are shown in **Table 2**.

The gray correlation degrees between the different influencing factors of the three kinds of CPAM and the shear strength are shown in **Figure 13**. It can be seen that the correlation degrees of the different factors with the three kinds of CPAM are not very different, which shows that the influence of each factor on the interfacial bonding characteristics has little correlation with the type of CPAM. Among all of the factors, the most relevant factor for shear strength is the type of tack coat, for which the gray correlation degrees in these three kinds of CPAM were up to 0.874, 0.93, and 0.889, that is, the type of tack coat has the greatest influence on the interface bonding characteristics. The gray correlation degrees between the interface roughness and the shear strength are 0.87, 0.897, and 0.879. There are only differences of 0.004, 0.033, and 0.01 from the values of the tack coat. Therefore, both the tack coat and the roughness of the interface have a high degree of influence on the interface bonding characteristics. In comparison, the correlation degrees between temperature and shear strength are the smallest, being 0.462, 0.462, and 0.465. Therefore, temperature has the least influence on the interface bonding characteristics. The correlation degrees between humidity and shear strength are 0.478, 0.491, and 0.494, with differences of only 0.016, 0.029, and 0.029 from those of temperature. Therefore, the influence of temperature and humidity on the interface bonding characteristics is relatively small. In summary, the order of the influence degrees of different influencing factors on the interfacial bonding characteristics is as follows: type of tack coat > interface roughness > amount of tack coat spreading > humidity > temperature. The dominant factors that affect the interface adhesion characteristics are the type of tack coat and the roughness of the interface. The type of tack coat and the interface roughness affect the interface bonding characteristics more than temperature and humidity do, that is, the external environment has a smaller degree of influence on the interface bonding characteristics than the type of material and the construction process do. Therefore, in the actual repair of potholes, attention should be paid to the choice of the type of tack coat, and the surface roughness should be increased in some methods to improve the interface bonding characteristics.

CONCLUSIONS

In this work, three kinds of CPAM were used to study the effects of five factors, including temperature, humidity, type of tack coat, amount of tack coat spreading, and interface roughness, on the interface bonding characteristics between CPAM and the old pavement. Finally, the influence degree of the different influencing factors on the interface bonding characteristics was clarified through gray correlation analysis, and the following conclusions were drawn.

First, as the temperature increases, the bonding performance at the interface gradually decreases. The functional relationship

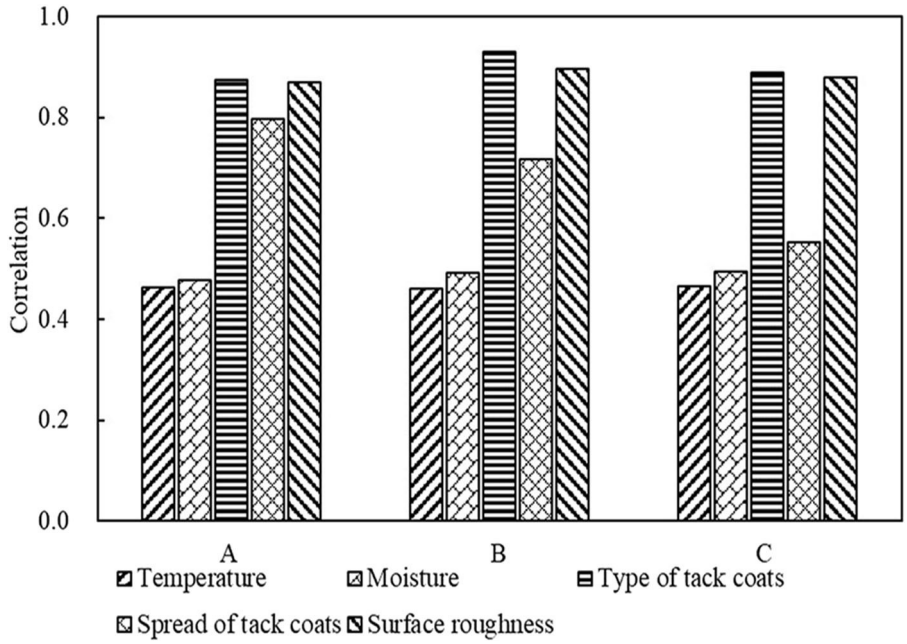

FIGURE 13 | The gray correlation degree.

between temperature and bonding degree is $y = 2.06 - 6.983 \times 10^{-2}x - 2.71 \times 10^{-4}x^2 + 2.97 \times 10^{-5}x^3 - 2.72 \times 10^{-7}x^4$, and the interface failure temperature is about 40°C. The interface bonding strength gradually decreases with increasing humidity.

Second, there is an optimal spreading amount for the tack coat, and the denser the CPAM is, the smaller the optimal spreading amount is. The cutting grooves on the old pavement can increase the interface shear strength, and the smaller the spacing of the grooves within a certain range is, the greater the shear strength is. However, due to the competitive relationship between the tack coat penetrating into the groove and the tack coat remaining on the surface, when the groove intervals are too small, reaching a certain level, the interfacial bonding strength decreases. The optimal groove spacing is considered to be 1 cm.

Finally, the influence degree order of the five influencing factors on the bonding of the interface is as follows: type of tack coat > interface roughness > amount of tack coat spreading > humidity > temperature, and the dominant influencing factors of the interface bonding performance are the type of tack coat and the interface roughness. Therefore, in the actual repair of potholes, attention should be paid to the selection of the type of tack coat and the control of the tack coat spreading amount. Additionally, the surface roughness can be increased by grooving or brushing to improve the interface bonding characteristics.

DATA AVAILABILITY STATEMENT

All datasets generated for this study are included in the article/supplementary material.

AUTHOR CONTRIBUTIONS

YT and FC provided the research direction and funding as well as equipment support. KL and SY were responsible for testing, simulation, and writing of the manuscript. HX and JO provided the detailed ideas and suggestions for the research. All authors contributed to the article and approved the submitted version.

ACKNOWLEDGMENTS

The authors would like to acknowledge the financial support of the Civil Aviation Administration of China. Meanwhile, the authors would like to acknowledge the test equipment supported by the School of Transportation Science and Engineering, Harbin Institute of Technology.

REFERENCES

Adlinge, S. S., and Gupta, A. K. (2013). Pavement deterioration and its causes. *Int. J. Innov. Res. Dev.* 2, 437–450. Available online at: http://www.iosrjournals.org/iosr-jmce/papers/sicete(civil)-volume6/60.pdf

Anderson, D. A., Thomas, H. R., Siddiqui, Z., and Krivohlavek, D. (1998). *More Effective Cold, Wet-Weather Patching Materials for Asphalt Pavements*. Report No. FHWA-RD-88-001. Federal Highway Administration, Washington, DC.

Berlin, M., and Hunt, E. (2001). *Asphalt Concrete Patching Material Evaluation: Interim Report (No. OR-RD-01-15).* Austin, TX: Oregon Department of Transportation Research Unit.

Diaz, L. G. (2016). Creep performance evaluation of Cold Mix Asphalt patching mixes. *Int. J. Pavement Res. Techn.* 9, 149–158. doi: 10.1016/j.ijprt.2016.04.002

Dong, Q., Huang, B., and Jia, X. (2014). Long-term cost-effectiveness of asphalt pavement pothole patching

methods. *Transp. Res. Rec.* 2431, 49–56. doi: 10.3141/2431-07

Fen, Y., Kong, Z., Xiao-yang, J., Qing-qing, L., and Jun, Y. (2009). Evaluation of shear performance of flexible waterproof-adhesive layer in concrete bridge pavement based on grey correlation analysis. *Road Mater. Pavement Design* 10, 349–360. doi: 10.1080/14680629.2009.9690251

Ferrotti, G., Pasquini, E., and Canestrari, F. (2014). Experimental characterization of high-performance fiber-reinforced cold mix asphalt mixtures. *Construct. Build. Mater.* 57, 117–125. doi: 10.1016/j.conbuildmat.2014.01.089

Gómez-Meijide, B., and Pérez, I. (2014). Effects of the use of construction and demolition waste aggregates in cold asphalt mixtures. *Constr. Build. Mater.* 51, 267–277. doi: 10.1016/j.conbuildmat.2013.10.096

Julong, D. (1989). Introduction to grey system theory. *J. Grey Syst.* 1, 1–24.

Karaca, Z., Gürcan, S., Gökçe, M. V., and Sivrikaya, O. (2013). Assessment of the results of the pendulum friction tester (EN 14231) for natural building stones used as floor-coverings. *Constr. Build. Mater.* 47, 1182–1187. doi: 10.1016/j.conbuildmat.2013.06.011

Kim, K., Kim, S. H., and Kim, N. (2017). A study on algorithm for materials take-off using pothole detection system. *J. Korean Soc. Civil Eng.* 37, 603–610. doi: 10.12652/Ksce.2017.37.3.0603

Kim, T., and Ryu, S. K. (2014). Review and analysis of pothole detection methods. *J. Emerg. Trends Comp. Inform. Sci.* 5, 603–608. Available online at: http://www.cisjournal.org/journalofcomputing/archive/vol5no8/vol5no8_3.pdf

Kuhn, E. A., Papagiannakis, A. T., and Loge, F. J. (2005). Preliminary analysis of the impact of cold mix asphalt concretes on air and water quality. *Bull. Environ. Contam. Toxicol.* 74, 501–508. doi: 10.1007/s00128-005-0613-3

Li, F., Huang, S., Xu, J., and Qin, Y. (2010b). Performance evaluation and technical requirements of cold patch asphalt mixture. *J. Tongji Univ. Nat. Sci.* 10. doi: 10.3969/j.issn.0253-374x.2010.10.011

Li, F., Huang, S. C., Xu, J., and Qin, Y. C. (2010a). Research on composition design of cold patch asphalt mixture. *J. Wuhan Univ. Techn.* 14. doi: 10.3963/j.issn.1671-4431.2010.14.018

Liao, M. C., Luo, C. C., Wang, T. Y., and Xie, X. (2016). Developing effective test methods for evaluating cold-mix asphalt patching materials. *J. Mater. Civil Eng.* 28:04016108. doi: 10.1061/(ASCE)MT.1943-5533.0001639

Ma, T., Wang, H., Zhao, Y., Huang, X., and Pi, Y. (2015). Strength mechanism and influence factors for cold recycled asphalt mixture. *Adv. Mater. Sci. Eng.* 2015:181853. doi: 10.1155/2015/181853

Meng, B., Jing, H., Yang, S., Wang, Y., and Li, B. (2018). Experimental study on the shear behavior of bolted concrete blocks with oblique shear test. *Adv. Civil Eng.* 2018, 1–8. doi: 10.1155/2018/7281218

Munyagi, A. A. (2007). *Evaluation of cold asphalt patching mixes* (Ph.D. dissertation). University of Stellenbosch, Stellenbosch, South Africa.

Ouma, Y. O., and Hahn, M. (2017). Pothole detection on asphalt pavements from 2D-colour pothole images using fuzzy c-means clustering and morphological reconstruction. *Automat. Constr.* 83, 196–211. doi: 10.1016/j.autcon.2017.08.017

Ouyang, J., Hu, L., Yang, W., and Han, B. (2019a). Strength improvement additives for cement bitumen emulsion mixture. *Constr. Build. Mater.* 198, 456–464. doi: 10.1016/j.conbuildmat.2018.11.280

Ouyang, J., Pan, B., Xu, W., and Hu, L. (2019b). Effect of water content on volumetric and mechanical properties of cement bitumen emulsion mixture. *J. Mater. Civil Eng.* 31:04019085. doi: 10.1061/(ASCE)MT.1943-5533.0002736

Ouyang, J., Yang, W., Chen, J., and Han, B. (2020). Effect of superplasticizer and wetting agent on pavement properties of cold recycled mixture with bitumen emulsion and cement. *J. Mate. Civil Eng.* 32:04020136. doi: 10.1061/(ASCE)MT.1943-5533.0003194

Ouyang, J., Zhao, J., and Tan, Y. (2018). Modeling mechanical properties of cement asphalt emulsion mortar with different asphalt to cement ratios and temperatures. *J. Mater. Civil Eng.* 30:04018263. doi: 10.1061/(ASCE)MT.1943-5533.0002480

Prowell, B. D., and Franklin, A. G. (1996). Evaluation of cold mixes for winter pothole repair. *Transp. Res. Rec.* 1529, 76–85. doi: 10.1177/0361198196152900110

Rezaei, M., Hashemian, L., Bayat, A., and Huculak, B. (2017). Investigation of rutting resistance and moisture damage of cold asphalt mixes. *J. Mater. Civil Eng.* 29:04017193. doi: 10.1061/(ASCE)MT.1943-5533.0002042

Rosales Herrera, V. I., and Prozzi, J. A. (2008). *Mixture Design Manual and Performance-Based Specifications for Cold Patching Mixtures* (No. Report No. 0-4872-P2). Salem: Center for Transportation Research, University of Texas at Austin.

Sun, D. Q., and Li, L. H. (2010). Factors affecting the viscosity of crumb rubber–modified asphalt. *Pet. Sci. Technol.* 28, 1555–1566. doi: 10.1080/10916466.2010.497007

Tan, Y., Zhou, S., Shan, L., and Chen, Z. (2014). Optimization design and study on properties of anti-freezing cold patch asphalt mixture. *J. Build. Mater.* 17, 89–94. doi: 10.3969/j.issn.1007-9629.2014.01.016

Tedeschi, A., and Benedetto, F. (2017). A real-time automatic pavement crack and pothole recognition system for mobile Android-based devices. *Adv. Eng. Inform.* 32, 11–25. doi: 10.1016/j.aei.2016.12.004

Wang, H. W., Chen, C. H., Cheng, D. Y., Lin, C. H., and Lo, C. C. (2015). A real-time pothole detection approach for intelligent transportation system. *Math. Probl. Eng.* 2015, 1–7. doi: 10.1155/2015/813507

Wang, Y., Yin, K. L., and An, G. F. (2004). Grey correlation analysis of sensitive factors of landslide. *Rock Soil Mech.* 25, 91–93. doi: 10.3969/j.issn.1000-7598.2004.01.019

Xu, G., and Yang, Z. (2015). Multiobjective optimization of process parameters for plastic injection molding via soft computing and grey correlation analysis. *Int. J. Adv. Manuf. Techn.* 78, 525–536. doi: 10.1007/s00170-014-6643-4

Zhang, Y., and Zhang, X. (2007). Grey correlation analysis between strength of slag cement and particle fractions of slag powder. *Cem. Concrete Comp.* 29, 498–504. doi: 10.1016/j.cemconcomp.2007.02.004

Zhang, Z. (2013). *Study on the factors influencing the freezing adhesion strength of asphalt materials* (Ph.D. thesis). Chang'an University, Xi'an, China.

Zhang, Z., Ai, X., Chan, C. K., and Dahnoun, N. (2014). "An efficient algorithm for pothole detection using stereo vision," in *2014 IEEE International Conference on Acoustics, Speech and Signal Processing*, ICASSP (Florence: IEEE), 564–568.

Zhao, L. D., and Tan, Y. Q. (2010). A summary of cold patch material for asphalt pavements. *Adv. Mat. Res.* 168–170, 864–869. doi: 10.4028/www.scientific.net/AMR.168-170.864

Conflict of Interest: FC, KL, and SY was employed by the company China Airport Construction Group Corporation and Beijing Super-Creative Technology Co., Ltd.

The remaining authors declare that the research was conducted in the absence of any commercial or financial relationships that could be construed as a potential conflict of interest.

frontiers in Materials

ORIGINAL RESEARCH
published: 06 August 2020
doi: 10.3389/fmats.2020.00207

Improved Design Method of Emulsified Asphalt Cold Recycled Mixture

Zhang Chen[1], Yuanlu Liang[1], Jin Yang[2], Tingyi Xu[1]* and Lijun Sun[1]*

[1] The Key Laboratory of Road and Traffic Engineering, Ministry of Education, Tongji University, Shanghai, China, [2] Shenzhen High Speed Engineering Consulting Co., Ltd., Shenzhen, China

This paper proposes an improved design method for emulsified asphalt cold recycled mixture (EACRM) so as to solve the "secondary compaction" problem in cold recycled asphalt pavement. First, a temperature prediction equation is established based on measured data of cold recycled asphalt pavement. The equation provides the basis for improving the design method. Second, regarding the shortcomings of the current design methods, we introduce material design principles of EACRM and improve existing methods. Splitting strength (15°C) and unconfined compressive strength (60°C) are chosen as the basis of a double index to determine the asphalt emulsion content. Finally, the performance of the asphalt mixture created using the improved design method is compared to that using the current specifications of China. The results of the comparison validate that the proposed design method can effectively avoid early damage to cold recycled asphalt pavement.

Keywords: road engineering, design method, cold recycled mixture, asphalt emulsion, secondary compaction

OPEN ACCESS

Edited by:
Yiqiu Tan,
Harbin Institute of Technology, China

Reviewed by:
Yuqing Zhang,
Aston University, United Kingdom
Andreas Loizos,
National Technical University of Athens, Greece

***Correspondence:**
Jin Yang
yj929@163.com
Tingyi Xu
xutingyi@tongji.edu.cn

Specialty section:
This article was submitted to Structural Materials, a section of the journal Frontiers in Materials

Received: *29 February 2020*
Accepted: *08 June 2020*
Published: *06 August 2020*

Citation:
Chen Z, Liang Y, Yang J, Xu T and Sun L (2020) Improved Design Method of Emulsified Asphalt Cold Recycled Mixture. Front. Mater. 7:207. doi: 10.3389/fmats.2020.00207

INTRODUCTION

Cold recycled mixture is a technique for recycling reclaimed asphalt pavement (RAP) using emulsified bituminous binder, foamed asphalt binder, cement, fly ash, or lime powder as the additives without the application of heat (Mohammad et al., 2003; Kuna et al., 2017). Among cold recycling technologies, the use of emulsified asphalt binder for cold regeneration has rapidly become popular (Wang et al., 2009; Liu, 2011).

Most current design methods for emulsified asphalt cold recycled mixture (EACRM) are empirical or regional, and an international standard has not yet been implemented (Tan et al., 2005). Generally, the design methods of EACRM are mostly modified design methods of hot mix asphalt (HMA; Deng and Huang, 2001; Lu, 2001). Amendments to the Marshall Act, the amendment of the Verme method, the Oregon estimation design method, and the Swedish Akzo Nobel design method were proposed by the American Asphalt Regeneration Association (Asphalt Recycling and Reclaiming Association [ARRA], 1996, 2001) and the South African Asphalt Association proposed the "three levels" (level-traffic) design method (Zhang et al., 2015; Li et al., 2016). The Chinese design specification of EACRM was modified on the basis of the Marshall test method (Research Institute of Highway Ministry of Transport [RIOH], 2008).

The technical performance of EACRM designed with different RAP contents, cement contents, and gradation has been evaluated according to high-temperature stability (rutting test), low-temperature crack resistance (low-temperature bending test), and water stability (freeze–thaw split test and immersion Marshall test) (Wu et al., 2009; Sravani et al., 2015). Creep and fatigue tests

were used to evaluate the fatigue characteristics of EACRM by controlling the stress or strain levels, and corresponding fatigue failure characteristics and general rules were obtained (Pouliot et al., 2003; Jiang and Han, 2018). All the above studies used the heavy indoor compaction and Marshall methods to prepare specimens, but these molding methods cannot effectively simulate actual construction in the field (Li et al., 2019).

The cold recycled mixture is mainly utilized in the base course of the pavement (Modarres and Ayar, 2014). Hot mix asphalt should be paved on the cold recycled mixture to meet the requirements of road use. In the construction process of HMA, the cold recycled mixture is heated and further compacted with the effect of paving, which is called the "secondary compaction" process of the cold recycled mixture. However, this compaction process is not considered in the existing design method. Most studies only considered the state after the construction of the cold recycled mixture, resulting in a large deviation in the design results of the mixture ratio of the cold recycled mixture. This deviation can lead to serious early pavement damage. In view of this, this paper considers the influence of different construction seasons and the secondary compaction process. Based on the existing design method of cold recycled mixture, the indoor test method of EACRM is improved, and a design method of EACRM considering different construction seasons and the secondary compaction process is proposed. The research results are of referential value in engineering practice.

SECONDARY COMPACTION IN COLD RECYCLED ASPHALT PAVEMENT

Finding of Secondary Compaction

In the technological transformation project of the Nanchang–Jiujiang Expressway in Jiangxi Province, China, the technical scheme of EACRM used in the upper base of the pavement was implemented. Pavement structure from top to bottom was: 4 cm HMA upper layer, 6 cm HMA middle layer, 6 cm lower layer, 12 cm cold recycled mixture upper base, 22 cm water stable macadam base, 33 cm subbase, and original subgrade. Reclaimed asphalt pavement was divided into two grades: 0–10 mm (fine) and 10–31.5 mm (coarse). The proportion of RAP and mineral powder used in the project was coarse rap: fine rap: mineral powder = 43:57:2.4. The actual gradation results are shown in **Table 1**.

The construction went well in winter. In addition, after opening to traffic, the performance of the pavement was good. However, in the summer of the second year, with the same design and construction, deep ruts occurred after opening to traffic, as shown in **Figure 1**. So, the temperature rise is the most important factor leading to deep ruts.

TABLE 1 | Passing rate of the key sieve for the design mixture.

Sieve size/mm	26.5	19	9.5	4.75	2.36	0.3	0.075
Passing rate/%	100	99.4	67.0	44.3	29.2	9.1	4.9

In order to determine the cause of rutting, the construction technicians excavated the pavement where the ruts occurred, as shown in **Figure 2**. At the rut, the thickness of the HMA hardly decreased, while the cold recycled layer was obviously squeezed, which indicates that the deep ruts were formed because the EACRM, not the HMA, was further compacted. We refer to this process of further compaction of the EACRM after HMA paving as "secondary compaction."

In order to confirm secondary compaction, the technicians directly chiseled with a piece of machinery similar to a road cutting machine, and then excavated the pavement manually. Finally, core drilling samples were taken in the cold recycled asphalt pavement before and after paving the HMA. Comparing the voidage of samples, it can be seen from **Table 2** that the

FIGURE 1 | Deep ruts.

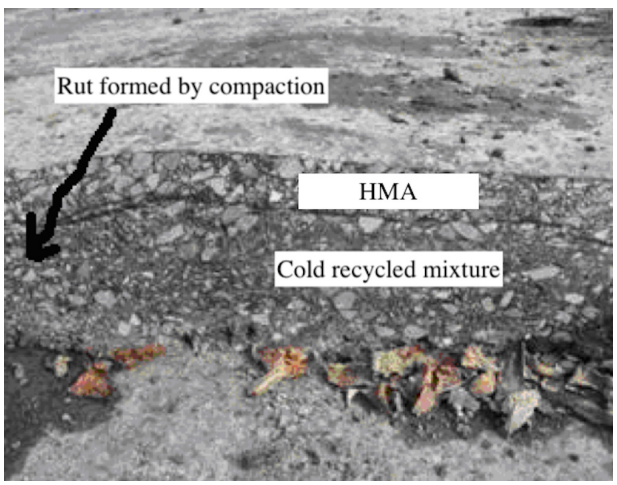

FIGURE 2 | Cross section of the rut.

voidage of EACRM decreased significantly after HMA paving, which had a great impact on the performance of the EACRM.

Analysis of Secondary Compaction

The compaction of EACRM can be divided into two processes. The first compaction process occurs when the EACRM is rolled after it is paved at a normal temperature. In this process, the EACRM is compacted at a normal temperature. After this first compaction process, the voidage of mixture is generally about 11–14%, as seen in **Table 2**. This voidage is much higher than the technical requirement of HMA, which is about 4%. Thus, emulsified asphalt cold recycled can be further compacted.

The secondary compaction occurs in the HMA paving process. When paving HMA, the heat will be transferred downward, which will cause the temperature of the EACRM to rise. In addition, with repeated rolling, the cold recycled layer with large voidage will be further compacted.

This secondary compaction leads to a decrease of the voidage of the EACRM, which leads to significant changes in the performance of the EACRM. Existing design methods have not taken this process into account, resulting in a large difference between the design results and the actual situation, and the cold recycled asphalt pavement structure may suffer early damage.

Temperature Measurement and Prediction Equation in Secondary Compaction

As discussed in sections "Finding of Secondary Compaction" and "Analysis of Secondary Compaction," the temperature rise is the most important factor leading to secondary compaction. In order to provide a basis for improving the existing design methods of cold recycled mixture, the temperature in the cold recycled layer was measured and analyzed.

Temperature Measurement

The temperature transducers with a wire, a display, and a sensor utilized in the experiment were common and easy to use. One end of the wire is a sensor, and the other end is a temperature display. Before paving the cold recycled layer, the sensors were placed at different depths (2, 4, 6, 8, 10, and 12 cm). When paving the cold recycled layer, no data were recorded, and the sensors were left in the new cold recycled layer. The timeline began when HMA was paved above the temperature sensors and the air temperature and initial temperature at each depth of the cold recycled asphalt pavement were recorded at the zero point. Then, the temperature data at different depths were recorded every 5 min. The time from paving to the rolling of HMA was generally about 1 h, and the recording time of the temperature data in the cold recycled asphalt pavement was extended by 1 h, for a total time of 2 h. Three groups of temperature data are shown in **Tables 3–5**.

TABLE 2 | Voidage before and after paving HMA (%).

Voidage before paving HMA	Voidage after paving HMA	Reduction
11.9	9.5	2.4
13.3	9.6	3.7
12.7	9.4	3.3
13.7	10.9	2.8
12.5	9.4	3.1
13.2	10.5	2.7
12	8.8	3.2
11.4	9.1	2.3
12.3	8.9	3.4
12.6 (average)	9.6 (average)	3.0 (average)

Temperature Prediction Equation

The value of the temperature difference, ΔT, is the value by which the temperature at a certain depth of cold recycled asphalt pavement was more than the initial temperature value. **Figure 3** presents that the ΔT curves of different measured data points at the same depth are very similar. Thus, in the temperature prediction equation of the cold recycled asphalt pavement, ΔT is determined as the dependent variable, while time t and depth H are determined as independent variables.

In this study, it was found that ΔT has a good correlation with the third power of time t and the square of depth H. Therefore,

TABLE 3 | The first group of temperature data; air temperature 21°C, HMA temperature 160°C.

	Temperature (°C)		
	Depth		
Time (min)	4 cm	8 cm	12 cm
0	22.3	21.5	21.1
5	24.8	21.6	21.1
10	30.7	21.8	21.1
15	35.5	22.2	21.1
20	40.7	22.8	21.3
25	44.7	23.8	21.7
30	47.9	25.1	22.2
35	51	26.3	23.1
40	53.3	27.6	24
45	55.1	29.2	24.8
50	56.3	30.8	25.6
55	57.3	31.8	26.4
60	58.3	32.7	27.3
65	58.9	33.7	28.3
70	59.7	34.8	29.4
75	60.3	35.6	30.6
80	60.2	36.4	31.4
85	60	37	32
90	59.6	37.5	32.4
95	59	38	32.6
100	58.3	38.5	32.8
105	57.6	38.9	33
110	56.9	39.3	33.2
115	56.1	39.7	33.4
120	55.2	40.1	33.7

TABLE 4 | The second group of temperature data; air temperature 20°C, HMA temperature 155°C.

	Temperature (°C)			
	Depth			
Time (min)	2 cm	4 cm	6 cm	12 cm
0	21	20.8	16.9	16.1
5	27.2	22.9	16.9	16.1
10	47.3	28.4	17	16.1
15	58.6	33.2	17.7	16.1
20	61.9	38	18.6	16.3
25	66.5	42	20.1	16.8
30	68.8	45.6	21.9	17.3
35	69.9	48.1	23.7	18.3
40	70.1	50.4	25.4	19.2
45	70.1	52	27.2	20
50	69.9	53.6	28.8	20.8
55	69.5	54.6	30.4	21.6
60	69.1	55.2	31.9	22.5
65	68.6	55.8	33.2	23.5
70	67.9	55.8	34.4	24.8
75	67.1	55.6	35.4	26
80	66.3	55.3	36.2	26.8
85	65.6	54.9	36.7	27.4
90	64.9	54.5	37.2	27.8
95	64.1	54.1	37.7	28
100	63.1	53.4	38	28.2
105	61.9	52.8	38.2	28.4
110	60.7	52.1	38.3	28.6
115	59.3	51.4	38.4	28.8
120	57.6	50.6	38.5	29.1

TABLE 5 | The third group of temperature data; air temperature 12°C, HMA temperature 155°C.

	Temperature (°C)			
	Depth			
Time (min)	2 cm	6 cm	8 cm	10 cm
0	15	15.3	15.2	15.1
5	22.5	15.3	15.3	15.2
10	46.5	15.4	15.5	15.3
15	53.6	16.1	16	15.5
20	61.3	17.4	16.6	15.7
25	64.1	18.9	17.6	16.2
30	66.8	20.9	19	16.9
35	68.5	22.9	20.1	17.6
40	69.9	24.6	21.5	18.5
45	70.5	26.6	23.1	19.7
50	70.7	28.4	24.7	21.1
55	70.5	30.2	25.7	21.9
60	70.1	31.7	26.8	22.6
65	69.4	33	27.8	23.6
70	68.7	34.2	28.9	24.6
75	67.9	35.6	29.7	25.3
80	67.3	36.4	30.5	26.1
85	66.6	36.9	31.2	26.8
90	65.9	37.4	31.8	27.4
95	64.9	37.9	32.4	28
100	63.9	38.4	32.8	28.6
105	62.7	38.6	33.1	29.2
110	61.3	38.9	33.5	29.7
115	59.7	39.2	34	30.3
120	58	39.5	34.4	30.9

the temperature prediction equation of the cold recycled asphalt pavement when paving HMA is:

$$T = \Delta T + T_0 \tag{1}$$

$$\Delta T = \left(aH^2 + bH + c\right) \times t^3 + \left(dH^2 + eH + f\right) \times t^2 + \left(gH^2 + hH + i\right) \times t \tag{2}$$

where T_0 refers to the initial temperature of the cold recycled asphalt pavement. In engineering applications, T_0 can be generally determined according to the following conditions: when the daytime temperature is below 25°C, T_0 can be determined as 25°C; when the daytime temperature is above 25°C, T_0 can be determined as 35°C (Yang et al., 2010). It should be noted that the daytime temperature here refers to the temperature on the day when HMA is paved on the cold recycled asphalt pavement and the temperature data of more than 120 min should not be estimated by this equation. H is the depth of the cold recycled asphalt pavement, cm; t is time, min; a, b, c, d, e, f, g, h, and i are coefficients.

The regression results are $a = 0.00343$, $b = -0.0609$, $c = 0.2217$, $d = -0.0802$, $e = 1.4546$, $f = -5.6486$, $g = 0.4867$, $h = -9.1549$, and $i = 39.8135$.

As shown in **Figure 4**, the temperature curves of the prediction equation are close to those of the measured temperature data, which indicates that the prediction effect is good. Moreover, the prediction effect of the equation needs to be verified using more measured data, and the coefficients in the equation can thus be further modified.

IMPROVED DESIGN METHOD OF EMULSIFIED ASPHALT COLD RECYCLED MIXTURE

Based on the physical indexes, such as void ratio of the core drilling samples of the test road and the temperature prediction equation, an improved design method was proposed in this section. In section "Specimen Shaping Method," on the basis of the comprehensive consideration of the existing design methods of EACRM, an improved specimen shaping method was put forward. In section "Design Indexes and Standards," design indexes and standards were introduced for the control of secondary compaction.

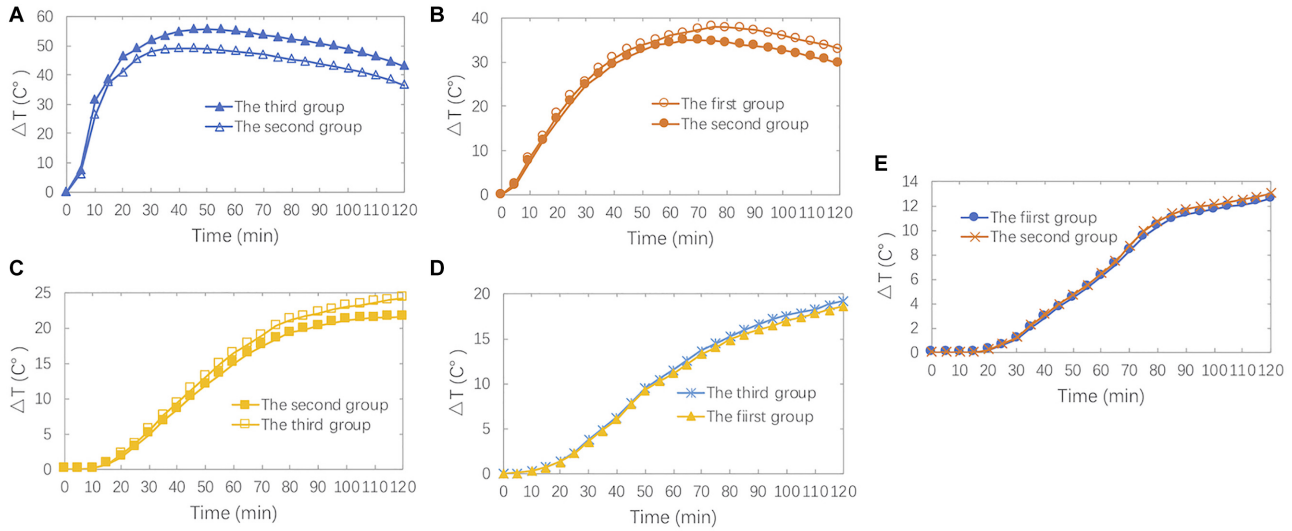

FIGURE 3 | ΔT curves at **(A)** 2 cm, **(B)** 4 cm, **(C)** 6 cm, **(D)** 8 cm, and **(E)** 12 cm.

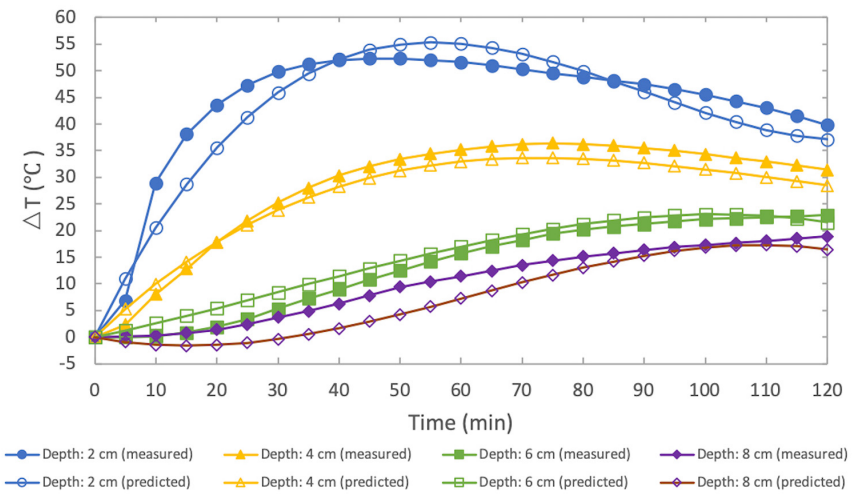

FIGURE 4 | Comparison between measured data and prediction data.

Specimen Shaping Method

A certain proportion of water needs to be added during the shaping process of the EACRM. However, there is no consensus method for the determination of the amount of water. It is generally believed that the higher the dry density, the greater the strength. Therefore, it is suitable that the water content (WC) corresponding to the maximum dry density is taken as the basis of the water addition.

In order to obtain the maximum dry density, the appropriate liquid content is needed for the cold recycled mixture. However, there is no universally accepted method to define and determine the most appropriate liquid content. After a large number of laboratory tests, it was found that the contribution of asphalt should not be equal to that of water, but nor can it be completely ignored. On this basis, the concept of "the optimal effective liquid content" (OLC) is proposed. The contributions of asphalt particles and water are 30 and 70%, respectively, for the reason that the test results showed that the water ratio determined by the concept of the OLC was more in line with the coating requirements of the cold recycled mixture.

For example, in the geotechnical compaction test, the optimal water content (OWC) is 4.0%, which is determined by the emulsified asphalt content whose asphalt–aggregate ratio is 4.0%. Then, the OLC equation is:

$$\mathrm{OLC} = (4.0\% + 4.0\% \times 38.55\%) \times 0.7 + 4.0\% \times 60\% \times 0.3 = 4.6\% \quad (3)$$

In the equation, 38.55 and 60%, respectively, represent the proportions of water and asphalt in emulsified asphalt. If

emulsified asphalt is added where the asphalt–aggregate ratio of is 5.0% when the specimen is shaped, the additional water content (WC) is:

$$\mathrm{WC} = (4.6\% - 5.0\% \times 0.6 \times 0.3 - 5.0\% \times 0.3855 \times 0.7) \div 0.7 = 3.36\% \quad (4)$$

The key to simulating secondary compaction of the EACRM is to determine the number and temperature of each compaction. According to the current specifications in China, the number of the first compaction can be fixed as 50 times on both sides. Moreover, considering the temperature in different seasons, three different temperatures of 40, 25, and 10°C are adopted for the mixture mixing and compaction to correspond to the construction conditions in summer, spring, autumn, and winter, respectively.

Based on the temperature prediction equation in section "Temperature Prediction Equation," during construction in spring and autumn, the temperature of the second compaction can be set as 60°C. As shown in **Table 6**, according to the 9.6% voidage value of core samples drilled in the field, it was determined that the number of the second compaction was about 46 times, which could be lowered to 45 times for convenience. In summer, the molding temperature of the second compaction can be determined as 70°C according to the temperature prediction equation.

In this paper, the specimen shaping method of EACRM is the modified Marshall compaction method, which is modified based on the above analysis. The shaping method is as follows:

1. The OLC is determined by the geotechnical compaction test. The method is as follows: Select emulsified asphalt content EC_0. Change the moisture content for the compaction test. The best moisture content corresponding to the maximum dry density of the mixture under this asphalt content is the OWC. Assuming that the percentages of asphalt and water in the composition of emulsified asphalt are P_a and P_w, respectively, the OLC is:

$$\mathrm{OLC} = (\mathrm{OWC} + EC_0 \times P_w) \times 0.7 + EC_0 \times P_a \times 0.3 \quad (5)$$

2. Add the mixture aggregate containing RAP to the mixer, with mineral powder and cement (if necessary), and calculate the water to be added according to Eq. 5. For the cold recycled mixture, of which the emulsified asphalt content is EC_1, the WC to be added is as follows:

$$\mathrm{WC} = (\mathrm{OLC} - EC_1 \times P_a \times 0.3 - EC_1 \times P_w \times 0.7) \div 0.7 \quad (6)$$

Add the WC according to the result of Eq. 6 and mix it for 60–70 s.

3. According to the calculated amount of emulsified asphalt, emulsified asphalt is added into the mixer to make the mixture mix evenly, and the mixing time is 60–70 s.
4. Put the well-mixed mixture into the test mold, compact it 50 times on both sides alternately with the Marshall compactor, and put it on the ground at room temperature for 24 h.
5. Put the specimens and the test molds in the oven at 60°C for 40–48 h;
6. In spring and autumn, directly take out the specimens and test molds from the oven and immediately compact them 45 times on both sides. In summer, before the end of curing, adjust the temperature of the oven to 70°C for more than 2 h, and then take them out and immediately compact them 45 times on both sides.
7. Place the test molds on the ground, cool at room temperature for at least 12 h, and then demould.

Design Indexes and Standards

Determination of Splitting Strength Index

The cold recycled mixture is generally set as the base course or the under layer of pavement. In this position, the cold recycled asphalt pavement may generate tensile stress under vehicle load. Therefore, it is reasonable to use splitting strength as the design index of cold recycled mixture. According to Chinese standards, the dry splitting strength at 15°C shall not be less than 0.4 MPa when cold recycled mixture is set as the base course and shall not be less than 0.5 MPa when cold recycled mixture is set as the under layer of pavement.

In this paper, it is proposed that the design standard of cold recycled mixture should be based on the road grade and the structure layer, rather than the unified standard. Combined with the relevant domestic literature, the South African Recycled Mixture Standards (Jenkins and Collings, 2017), and the indoor test results in this paper, it is suggested that the cold recycled mixture can be divided into four grades as shown in **Table 7**.

Determination of Unconfined Compressive Strength Index

The compaction rutting of the cold recycled asphalt pavement can be considered the failure of high temperature resistance under the condition of high temperatures. The unconfined compressive strength test can effectively evaluate the high temperature resistance of asphalt mixture. In this paper, the high temperature unconfined compressive strength index will be used to control the ruts produced by secondary compaction.

The temperature of the unconfined compressive strength test can be determined according to the temperature prediction equation in section "Temperature Prediction Equation." Considering the most unfavorable summer construction conditions, the initial temperature of the cold recycled asphalt pavement is taken as 35°C. Then, according to Equations (1) and (2), the temperature curves at each depth of the cold recycled asphalt pavement can be obtained, as shown in **Figure 5**. During the construction of HMA on site, the time from the beginning to the end of paving is about 60 min. After 60 min, there is no construction load, and the secondary compaction of cold recycled asphalt pavement will also end. **Figure 5** indicates that the temperature at a depth of 2 cm reaches a maximum at 55 min, while the temperatures at depths of 4 and 6 cm are still rising; at 60 min, the temperature at a depth of 2 cm drops slightly compared with the highest temperature, and the

TABLE 6 | Test results of two compactions.

First compaction temperature (°C)	First compaction number	Second compaction temperature (°C)	Second compaction number	Asphalt-aggregate ratio (%)	Gross volume density (g/cm^3)	Theoretical maximum density (g/cm^3)	Voidage (%)
25	50	60	20	4	2.141	2.429	11.9
25	50	60	30	4	2.175	2.429	10.5
25	50	60	40	4	2.188	2.429	9.9
25	50	60	50	4	2.201	2.429	9.4
25	50	60	60	4	2.209	2.429	9.1

TABLE 7 | Recommended grading standard for cold recycled mixture.

Cold recycled mixture level	I	II	III	IV
	Expressway, middle and under layer of first grade highway	Expressway, under layer and base course of first grade highway	Expressway, base course of first grade highway	Base course of other roads
15°C Splitting strength (Mpa)	>0.8	0.6–0.8	0.4–0.6	0.2–0.4
15°C Dry–wet splitting strength ratio (%)	>75	>75	>70	>60
15°C Compressive Resilient Modulus (Mpa)	1200–1600	1000–1400	800–1200	600–1000
20°C Compressive Resilient Modulus (Mpa)	1000–1400	800–1200	600–1000	400–800
Poisson's ratio	0.3	0.3	0.3	0.3

temperatures at 4 and 6 cm rise. Therefore, the most unfavorable time is the period of 55 to 60 min. The temperature of the cold recycled asphalt pavement in this period can be determined by the temperature prediction equations, namely, Equations (1) and (2).The internal temperature of the cold recycled asphalt pavement is considered as average along the depth direction. The average value at 55 min is 61.0°C, and the average value at 60 min is 61.1°C. Thus, it is suitable to set the temperature of the unconfined compressive strength test as 60°C.

In the technological transformation project of the Nanchang–Jiujiang Expressway, the compaction ruts occurred after paving HMA if the cold recycled mixture had 4.0% emulsified asphalt content. However, after reducing emulsified asphalt content to 3.0%, the compaction ruts problem was solved.

In view of the above-mentioned facts, in the laboratory unconfined compressive strength test, four specimens were shaped with emulsified asphalt amounts of 2%, 3%, 4%, and 5%. The results of the test are shown in **Figure 6**. As shown in **Figure 6**, it can be seen that the unconfined compressive strength of emulsified asphalt mixture at 60°C first increases and then decreases with the increase of emulsified asphalt content. The unconfined compressive strength of the mixture at 60°C with 4% emulsified asphalt is 0.285 MPa, and that with 3.0% emulsified asphalt is 0.386 MPa. If the unconfined compressive strength of cold recycled mixture at 60°C is less than 0.285 MPa, the index of unconfined compressive strength at 60°C should be between 0.285 and 0.386 MPa. In this paper, the median value of 0.336 MPa is proposed as the design index.

Based on sections "Specimen Shaping Method" and "Design Indexes and Standards," the improved design method of EACRM is as follows:

1. According to the shaping method determined in section "Specimen Shaping Method," shape four to five groups of specimens with different emulsified asphalt contents. Each group contains six specimens. Obtain the theoretical maximum density of each cold recycled mixture by vacuum method.
2. After demoulding, take out three specimens from each group and measure the physical indexes, such as gross volume density and voidage, by the wax sealing method.
3. Soak the three specimens without wax seals in 25°C constant-temperature water for 23 h, and then soak in 15°C constant-temperature water for 1 h. Take out the specimens and immediately conduct the wet splitting test at 15°C. At the same time, conduct the dry splitting test with specimens with wax seals at 15°C.
4. According to the test results of dry splitting strength and the recommended standards in **Table 7**, the range of emulsified asphalt consumption EC_1–EC_2 meeting the splitting strength index is determined.
5. Several groups of cylinder specimens (100 mm × 100 mm) with different emulsified asphalt content are shaped by the gyratory compactor. The shaping method index is 1.25°, 600 kPa, and 30 times rotated. For each asphalt content, two specimens are shaped for 60°C unconfined compressive strength tests. The amount of emulsified asphalt meeting the unconfined compressive strength index ranges from EC_3 to EC_4.
6. Take the intersection of EC_1–EC_2 and EC_3–EC_4 as the reasonable asphalt content range of emulsified asphalt cold recycling mixture. If the range of this intersection is

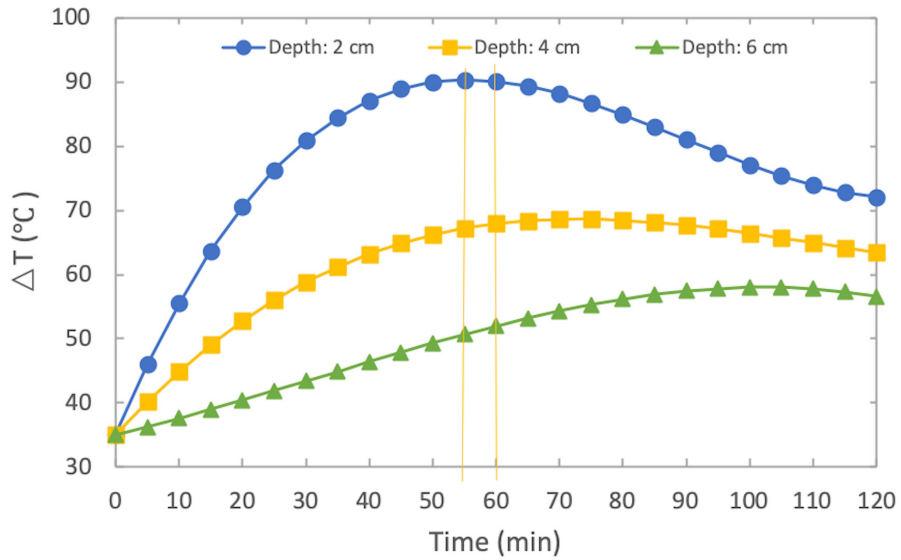

FIGURE 5 | Temperature curves at each depth of cold recycled mixture when HMA paving.

large, the amount of emulsified asphalt shall be selected by comprehensive consideration of the two indexes. If EC_1–EC_2 and EC_3–EC_4 do not intersect, the cold recycled mixture should be designed again by adjusting the gradation, adding new aggregate, increasing the amount of cement, or changing the quality of emulsified asphalt.

APPLICATION

Redesign of the Nanchang–Jiujiang Expressway Emulsified Asphalt Cold Recycling Mixture With the Improved Method

It should be noted that RAP, mineral powder, cement, emulsified asphalt, grading, and other materials used in the improved method were the same as those of the Nanchang–Jiujiang Expressway project. The specific design method is as follows:

1. The OLC of cold recycled mixture was determined according to the maximum dry density of the geotechnical compaction test. When the emulsified asphalt content was 4%, the optimal moisture content was 4.0%. The proportions of asphalt and water in emulsified asphalt were 60 and 38.55%, respectively. Therefore, according to Eq. 3, the optimal liquid content was determined to be 4.6%.
2. Five groups of Marshall specimens were made according to 2, 3, 4, 5, and 6% emulsified asphalt content. The optimum WC of each emulsified asphalt was 5.3, 4.6, 4.0, 3.4, and 2.7%, respectively, according to Eq. 4. Water, RAP, and cement were added and mixed for 60–70 s.

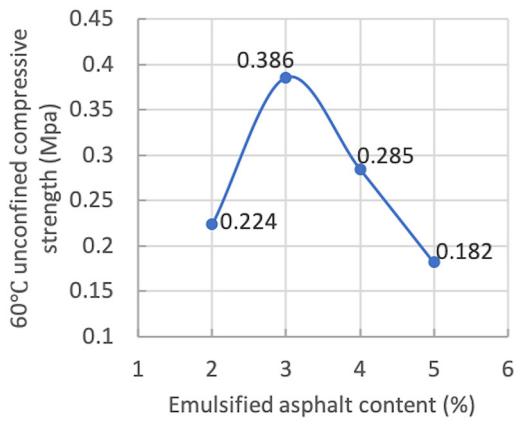

FIGURE 6 | 60°C unconfined compressive strength (Mpa).

3. According to the calculated amount of emulsified asphalt, emulsified asphalt was added into the mixer, and the mixing time was 60–70 s.
4. The well-mixed mixture was placed in the test molds. The test molds were compacted 50 times on both sides alternately with the Marshall compactor, then put on the ground at room temperature for 24 h.
5. The specimens and the test mold were place in an oven at 60°C for 40–48 h.
6. For construction during summer, the oven temperature was set to 70°C for more than 2 h at the end of curing. Specimens were then immediately removed and compacted 45 times on both sides alternately with the Marshall compactor.

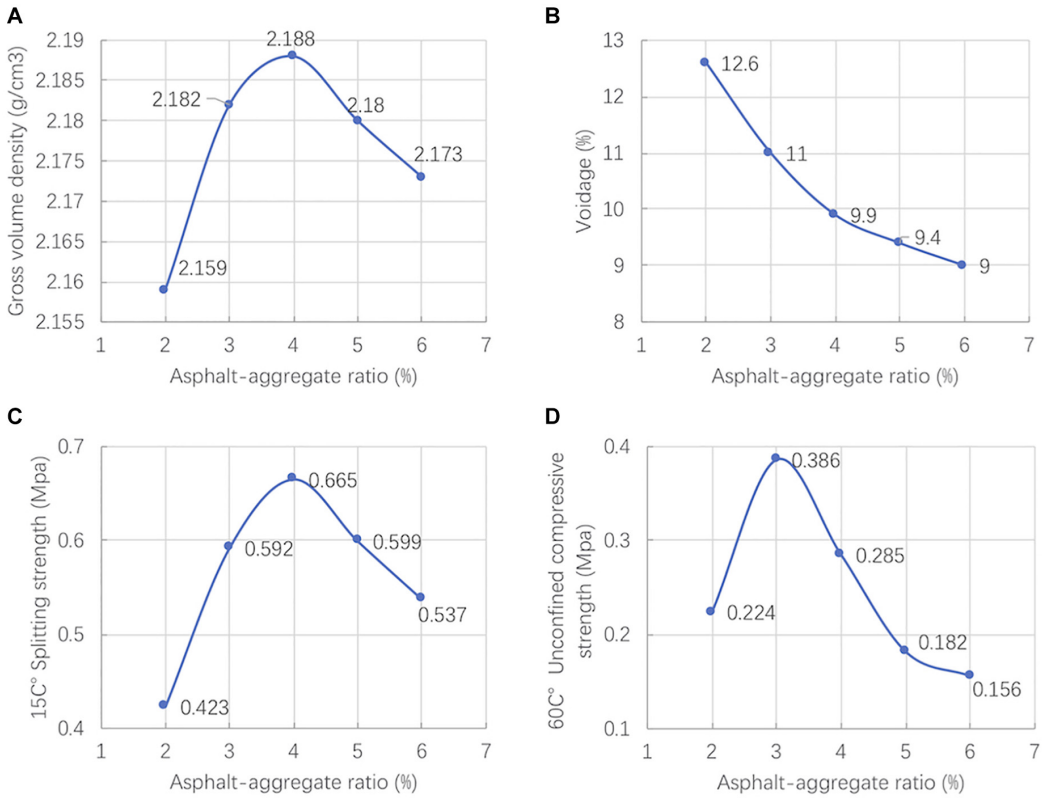

FIGURE 7 | Test results of improved design method. **(A)** Gross volume density (g/cm^3). **(B)** Voidage (%). **(C)** 15°C splitting strength (Mpa). **(D)** 60°C unconfined compressive strength (Mpa).

7. The test molds were placed on the ground, cooled at room temperature for at least 12 h, and then demoulded.
8. The gross bulk density, voidage, and dry wet splitting strength of each group of specimens were tested.
9. Several groups of cylinder specimens (100 mm × 100 mm) with different emulsified asphalt contents (2, 3, 4, 5, and 6%) were shaped by the gyratory compactor. The shaping method indexes were 1.25°, 600 kPa, and 30 times rotated. For each asphalt content, two specimens were shaped for 60°C unconfined compressive strength tests.

The cold recycled asphalt pavement was designed as a base course for the Nanchang–Jiujiang Expressway. Combined with the test results indicated by **Figure 7** and the improved design method, the dry splitting strength should meet the requirements of 0.6–0.8 MPa. According to **Figure 7C**, the range of emulsified asphalt content was about 3.1–5.0%. At the same time, a 60°C unconfined compressive strength index was used, so the emulsified asphalt content range was about 2.6–3.6% according to **Figure 7D**. Finally, the reasonable amount of emulsified asphalt was determined to be 3.1–3.6%. Moreover, for construction during summer, the amount of emulsified asphalt should be selected according to the larger value of 60°C unconfined compressive strength. Therefore, the final amount used was 3.1%.

Comparison of the Design Results Between the Improved Method and the Current Specification in China

The design method of the emulsified asphalt cold recycling mixture in the current specification in China refers to the Technical Specifications for Highway Asphalt Pavement Recycling (Research Institute of Highway Ministry of Transport [RIOH], 2008). The design results of the two methods are compared in **Table 8**.

TABLE 8 | Design results comparison between improved method and current specification.

Index	Improved method	Current specification
Content of emulsified asphalt (%)	3.1	5
15°C splitting strength (MPa)	0.6	0.659
Dry-wet splitting strength ratio (%)	95	76
60°C unconfined compressive strength (MPa)	0.39	0.182

It can be seen that the content of emulsified asphalt designed by the current specification is nearly 2% higher than that of the improved method in this paper. Although the mixture's splitting strength designed by the current specification is slightly higher than that designed by the improved method, its 60°C unconfined compressive strength has not reached the standard proposed in the improved method. Thus, when HMA is paved on the EACRM designed by the current specification, secondary compaction occurs, leading to deep ruts. The results of the comparison validate that the proposed design method can effectively avoid early damage to the cold recycled pavement. In fact, after implementing the improved design method, the problem of compaction ruts was solved in a practical project.

CONCLUSION

In this study, the secondary compaction of EACRM was clarified through field experiments and analysis, which indicates that it is necessary to improve the existing design methods. Therefore, a series of laboratory tests were conducted to determine the specimen shaping method, design indexes, and standards of the improved design method. Finally, the performance of the EACRM designed by the improved design method was compared to that designed by the current specification of China. The results of the comparison validate that the improved design method can effectively avoid early damage to the cold recycled pavement. In summary, the conclusion are as follows:

1. Emulsified asphalt cold recycled mixture is paved at a normal temperature, but it does not mean that the influence of temperature should not be considered. The design methods of common HMA can no longer be applied to the EACRM.
2. When HMA is paved, the EACRM will be further compacted, referred to as the secondary compaction process. In the indoor test, the secondary compaction process of EACRM should be simulated by compacting the specimen twice.
3. Based on the measured temperature of the EACRM and the comparison of the void ratio of the drilled core samples of the EACRM before and after HMA paving, the compaction temperature and compaction times were determined. The second compaction temperature is 70°C in summer and 60°C in spring and autumn; the number of double-sided compactions is 45.
4. It is suggested that splitting strength (15°C) and unconfined compressive strength (60°C) be used as the double index to determine the emulsified asphalt content.

DATA AVAILABILITY STATEMENT

The datasets generated for this study are available on request to the corresponding author.

AUTHOR CONTRIBUTIONS

ZC, JY, and YL conducted the experiments. JY and LS were the supervisors of this research work. ZC and TX helped with writing. All authors were involved in the analysis of experimental data and manuscript preparation.

FUNDING

This research was funded by the National Natural Science Foundation of China, grant number 71471134.

REFERENCES

Asphalt Recycling and Reclaiming Association [ARRA] (1996). *Mixture and Structural Design of Cold Recycled Pavements*. Annapolis, MD: ARRA.

Asphalt Recycling and Reclaiming Association [ARRA] (2001). *Basic Asphalt Recycling Manual*. Annapolis, MD: ARRA.

Deng, X., and Huang, X. (2001). *Principle and Method of Pavement Design*. Beijing: China Communications Press.

Jenkins, K. J., and Collings, D. C. (2017). Mix design of bitumen-stabilised materials–South Africa and abroad. *Road Mater. Pavement Des.* 18, 331–349. doi: 10.1080/14680629.2016.1213511

Jiang, Y. J., and Han, Z. Q. (2018). Effect of graded paired emulsified asphalt cold recycled asphalt mixture on road performance. *J. Dalian Univ. Technol.* 58, 607–614.

Kuna, K., Airey, G. D., Thom, K. (2017). Mix design considerations of foamed bitumen mixtures with reclaimed asphalt pavement material. *Int. J. Pavement Eng.* 18, 902–915. doi: 10.1080/10298436.2015.1126271

Li, J., Zhang, J., Qian, G., Zheng, J., and Zhang, Y. (2019). Three-Dimensional Simulation of Aggregate and Asphalt Mixture Using Parameterized Shape and Size Gradation. *J. Mater. Civ. Eng.* 31, 04019004. doi: 10.1061/(asce)mt.1943-5533.0002623

Li, Z. G., Hao, P. W., and Xu, J. Z. (2016). Study on impacts of freeze-thaw cycles on the shear performances of emulsified asphalt cold recycle mixture. *Mater. Rev.* 30, 121–125.

Liu, S. H. (2011). Analysis of Cold Regeneration Mechanism of Semi-rigid Base Asphalt Concrete Pavement. *Highway* 5, 192–196.

Lu, W. (2001). *Design Principle and Method of Asphalt Mixture*. Shanghai: Tongji University Press.

Modarres, A., and Ayar, P. (2014). Coal waste application in recycled asphalt mixtures with bitumen emulsion. *J. Cleaner Prod.* 83, 263–272. doi: 10.1016/j.jclepro.2014.07.082

Mohammad, L., Abu-Farsakh, M. Y., Wu, Z., Abadie, C. (2003). Louisiana experience with foamed recycled asphalt pavement base materials. *Transp. Res. Rec.* 1832, 17–24. doi: 10.3141/1832-03

Pouliot, N., Marchand, J., and Pigeon, M. (2003). Hydration mechanisms microstructure and mechanical properties of mortars prepared with mixed binder cement slurry-asphalt emulsion. *J. Mater. Civ. Eng.* 15, 54–58.

Research Institute of Highway Ministry of Transport [RIOH] (2008). *Technical Specifications for Highway Asphalt Pavement Recycling*. Beijing: China Communications Press.

Sravani, A., Pramod, K. J., and Nagabhushana, M. N. (2015). Optimization of Recycled Asphalt Pavement in Cold Emulsified Mixtures by Mechanistic Characterization. *J. Mat. Civ. Eng.* 28, 04015132. doi: 10.1061/(asce)mt.1943-5533.0001412

Tan, Y. Q., Dong, Z., Cao, L., and Yu-hui, E. (2005). Designing cold recycled asphalt mixtures with superpave volumetric design method. *J. Highw. Transp. Res. Dev.* 3, 31–34.

Wang, Z. J., Sha, A. M., Xiao, J. J., and Du, S. W. (2009). Improvement mechanism of cement on microstructure of emulsified asphalt mixture. *J. Wuhan Univ. Technol.* 31, 16–19.

Wu, C. F., Zeng, M. L., Zhao, M. H., and Zhong, M. W. (2009). Experimental study on road performance of emulsified asphalt cold recycled mixture. *Highw. Traffic Technol.* 26, 27–32.

Yang, J., Jiang, T., Sun, L. J., and Liu, L. P. (2010). Study of the emulsified asphalt cold recycled mixture experiment methods considering the secondary compaction process. *Highw. Eng.* 35, 76–78+133.

Zhang, J. P., Zhu, H. B., and Pei, J. Z. (2015). Evaluation of asphalt emulsification and viscosity of modified asphalt emulsion mortar based on Gompertz model. *J. Traffic Transp. Eng.* 15, 1–7.

Conflict of Interest: JY was employed by the company Shenzhen High Speed Engineering Consulting Co., Ltd.

The remaining authors declare that the research was conducted in the absence of any commercial or financial relationships that could be construed as a potential conflict of interest.

frontiers in Materials

ORIGINAL RESEARCH
published: 11 August 2020
doi: 10.3389/fmats.2020.00257

Evaluation of Anti-icing Emulsified Asphalt Binders

*Liyan Shan[1], Hu Yang[1], Dong Tian[2] and Yiqiu Tan[1]**

[1] School of Transportation Science and Engineering, Harbin Institute of Technology, Harbin, China, [2] CCCC Highway Consultants CO., Ltd. (HPDI), Beijing, China

Snow and ice on asphalt pavement surface can significantly affect traffic safety and damage pavements. To reduce its effect, a kind of anti-icing emulsified asphalt binder (AEAB) is developed by adding a certain amount of anti-icing fillers to the modified emulsified asphalt binder. The anti-icing performance and pavement performance of AEAB coating are evaluated. The results show that: the basic properties of AEAB meet the requirement of road maintenance, and the AEAB has excellent anti-icing performance and bonding property. It can facilitate the ice-melting on pavement and reduce the adhesion force between pavements and ice, and the adhesion force can be reduced by about 50%. The AEAB coating can keep an excellent bonding state with the original pavement, which can prolong the service life of the coating. These findings demonstrated the potential of using AEAB coating on asphalt pavement to provide better pavement performance and contribute to traffic safety during snowfall.

Keywords: emulsified asphalt binder, anti-icing filler, coating, road surface anti-icing, performance

OPEN ACCESS

Edited by:
Huisu Chen,
Southeast University, China

Reviewed by:
Dawei Wang,
RWTH Aachen University, Germany
Quantao Liu,
Wuhan University of Technology, China

****Correspondence:***
Yiqiu Tan
yiqiutan@163.com

Specialty section:
This article was submitted to Structural Materials, a section of the journal Frontiers in Materials

Received: *25 March 2020*
Accepted: *14 July 2020*
Published: *11 August 2020*

Citation:
Shan L, Yang H, Tian D and Tan Y (2020) Evaluation of Anti-icing Emulsified Asphalt Binders. Front. Mater. 7:257. doi: 10.3389/fmats.2020.00257

INTRODUCTION

Snow and ice on pavement surface can dramatically reduce the road skid resistance and cause the emergency braking distance on icy roads 6∼7 times that of normal roads (Dan et al., 2017). The low friction on road can pose a serious threat to the safety of pedestrians and vehicles, even can cause serious traffic congestion and induce a series of traffic accidents (Pan et al., 2015; Waluś, 2017). Besides, the melting of snow may aggravate the moisture damage to asphalt pavements (Huang et al., 2005). Therefore, researches on anti-icing and snow-melting technologies for asphalt pavement have always been the focus of road engineering.

In the past decades, regular snow removal or deicing methods included spraying chloride ice-melting agents and mechanical equipment such as snowplows and sweepers. However, these traditional methods not only demand a lot of professional workers and equipment but also may lead to high pollution and cause serious damages to the performances of pavements (Henry, 1991; Yehia and Tuan, 1999). To solve these problems of above passive ice-removal method, the anti-icing methods based on thermal melting technology have been studied and proposed, such as heating wire, infrared heating, microwave heating, solar energy collection technology, and electrically conductive pavements; these technologies are proved to be highly efficient in road deicing (Liu et al., 2007;

Tang et al., 2008; Wang et al., 2008; Chen et al., 2011; Zhou et al., 2011; Pan et al., 2015; Daniels et al., 2019). Nevertheless, the pavements with heating systems are much more expensive and difficult to build than the normal pavements currently.

Another anti-icing method is to build self-ice-melting pavements by adding the anti-icing fillers into the pavements. The anti-icing ingredients will be released out from self-ice-melting pavements to facilitate the snow/ice-melting process and reduce the adhesion between ice and pavement surface during the snowfall (Pan et al., 2008; Wang et al., 2017; Tan et al., 2019). Due to the simple-operated advantage and excellent anti-icing ability of this technology, it has drawn more and more attention from worldwide countries and several commercial anti-icing fillers such as Verglimit, Mafilon, and Icebane have been produced and applied widely (Baldino et al., 2012; Li and Wang, 2012; Luo and Yang, 2015). For the purpose of improving the long-term performance of anti-icing filler, Tan et al. (2014) developed a sustained-release anti-icing filler to reduce the freezing temperature of the pavement to −25°C. To reduce the costs of anti-icing filler, Lei Peng et al. developed a calcium chloride anti-icing filler named Iceguard (Zheng et al., 2017). However, the researches on anti-icing fillers are mainly focused on newly-built pavement currently. As for so many pavements that have already been built, there is still a lack of anti-icing technology to ensure road safety in adverse weather (e.g., snow, frost, and freezing rain).

Coating technology is a preventive maintenance method that is suitable for in-service pavements, such as the fog seal and micro-surfacing. They have the potential to reverse the aging of in-service asphalt pavement, reduce cracking and raveling, and provide a better, longer-lasting pavement (Lin et al., 2012; Mamlouk and Dosa, 2014). Based on the coating technology and the good hydrophobic properties of hydrophobic materials, researchers have developed hydrophobic emulsified asphalt coating and super-hydrophobic coating on asphalt pavement for ice and snow removal (Peng et al., 2018; Han et al., 2019). However, the hydrophobic and super-hydrophobic coating can only reduce the adhesion between ice and pavement but do not have the ability to actively melt snow and ice, which greatly restrict their ice/snow-removal application on asphalt pavement. Therefore, to get a better anti-icing effect, the technology of anti-icing-emulsified asphalt binder coating is conducted based on the coating technology and anti-icing filler. Basically, the anti-icing emulsified asphalt binder (AEAB) is produced by adding water-repellent anti-icing fillers into an emulsified asphalt binder. The asphalt pavement coated with AEAB not only has excellent anti-icing properties but also can achieve the purpose of preventive maintenance. However, combining emulsified asphalt binder maintenance materials with anti-icing fillers may have adverse influences on the storage stability and other properties of emulsified asphalt. It is necessary to develop an applicable AEAB with excellent properties.

In this study, based on the dual requirements of maintenance function and anti-icing function, an AEAB was developed by adding a certain amount of anti-icing fillers to the modified emulsified asphalt binder. The anti-icing performance and pavement performance of AEAB coating were analyzed by laboratory tests, which proved the excellent properties and the feasibility of AEAB as pavement maintenance materials.

MATERIALS AND METHODS

Raw Materials

- Asphalt: The neat asphalt binder was LH-90# with basic properties shown in **Table 1**.
- Emulsifier: Cationic slow-cracking fast-setting emulsifier was used, and its properties are shown in **Table 2**.
- Stabilizer: Organic stabilizer hydroxypropyl methylcellulose (HPMC) was used to enhance the storage stability of the emulsified asphalt.
- Modifier: The main function of the modifier is to improve the bonding property of emulsified asphalt binder; the SBR and waterborne epoxy resin were used together as a compound modifier.
- Anti-icing filler: Two kinds of water-repellent anti-icing filler (Type A and Type B) were selected. They have different effect on reducing the freezing temperature of asphalt pavement. Type A and Type B are suitable for using in the ambient temperature above −10°C and −25°C, respectively. Their basic properties and size distributions are shown in **Tables 3**, **4**.

Preparation of AEAB

The preparation process of AEAB generally includes three steps: emulsification, modification, and adding anti-icing fillers.

The steps of the emulsification process are as follows. First, the emulsions were obtained by mixing water of a pH value between 1.5 and 2.5 with the 1.8% emulsifier and 0.2% stabilizers. Then, the emulsions were poured into a preheated colloid mill and sheared for 3 min. Next, the heated neat asphalt binder was added to the emulsions and the oil-water ratio is 6:4. Last, after the binder was fully added, it was sheared in colloid mill for 5 min.

Then, there was the modification process; after the emulsified asphalt binder was cooled to room temperature, the high-shear

TABLE 1 | Basic properties of neat asphalt.

Properties	Results	Specification
Penetration (25°C, 100 g, 5 s)/0.1 mm	82.6	T0604
Softening point (Ring ball)/°C	47.1	T0606
Ductility (15°C, 5 cm/min)/cm	>100	T0605
Dynamic viscosity (60°C)/Pa · s	205.80	T0625

TABLE 2 | Basic properties of the emulsifier.

Properties	Results
Dosage range	1.5%
pH	1.5–2.5
Breakage rate	Slow-cracking fast-setting
Ion type	cationic

TABLE 3 | Basic properties of anti-icing fillers.

Test items	Unit	Specification requirements (China Communications Press, 2018)	Type A	Type B
Heat resistance index	%	≤0.5	0.1	0.2
Apparent relative density	-	≥1.7	2.38	2.25
Moisture content	%	≤1	0.1	0.1
Corrosion rate	mm/a	≤0.11	0.05	0.03
Relative damage rate of plant seeds	%	≤15	3	2
Ice point	°C	≤ −10	−10	−25
Moisture rate	%	≤0.7	0.1	0.1
Salt release	%	≤0.4	0.12	0.15

TABLE 4 | Size distributions of anti-icing additives (percent passing/%).

Sieve size (mm)	0.6	0.3	0.15	0.075
Type-A	100	98.20	25.11	8.66
Type-B	100	99.91	65.63	23.26

mixer was used to mix the emulsified asphalt and compound modifier at a speed of 1200 rpm for 5 min. The contents of SBR and waterborne epoxy resin were 10% and 8%, respectively (based on the weight of emulsified asphalt binder).

Finally, the prepared emulsified asphalt binder and 20% anti-icing fillers were added into the mixer and stirred until particles of anti-icing filler were fully coated with modified emulsified asphalt binder. The modified emulsified asphalt binders mixed with Type A and Type B were named AEAB-1 and AEAB-2, respectively.

Test Methods

Basic Properties Test

According to the standard test methods of bitumen and bituminous mixtures for highway engineering in China (China Communications Press, 2011), softening point, penetration, ductility at 5°C, elastic recovery of evaporated residue test, and Brookfield viscosity test were carried out to evaluate the basic properties of AEAB and modified emulsified asphalt binder.

Zeta Potential Test

As a colloid, emulsified asphalt has a structure of electrical double layer. And the stability of electrical double layer is often characterized by the Zeta potential of colloidal solution (Salopek et al., 1992; Stachurski and MichaŁek, 1996). **Table 5** shows the stability classification of colloidal materials (Tan, 2018). Due to the limitation of the light scattering instrument, it is impossible to test the Zeta potential of original material. To get relatively stable test results, the emulsified asphalt needs to be diluted a certain number of times before testing. According to the previous study (Tian, 2019), the storage stability time of emulsified asphalt is more than 20 h when Zeta potential of diluted solution (150 times) is higher than 30 mv. In this study, to get stable Zeta potential test results, the modified emulsified asphalt binder and AEAB are also diluted 150 times with distiller water, respectively. Then, the Zeta potentials of the diluted solution are measured by Malvem Zetasizer Nano ZS light scattering instrument to evaluate the storage stability of materials.

TABLE 5 | Stability classification of colloidal materials.

Zeta potential (mV)	0∼±10	±10∼±30	±30∼±40	±40∼±60	>±60
Stability	Worst	Worse	General	Better	Excellent

Ice-Melting Test

Firstly, the AC-16 Marshall specimens were manufactured according to the specification (China Communications Press, 2004) to simulate the pavement surface. Then, the AEAB was evenly brushed on the specimen surfaces with a dosage of 0.8 kg/m^2. After the AEAB was fully cured, 100 g snow-ice particles (crushed ice scraped from the inner wall of the refrigerator) was used to cover the surfaces. Next, the specimens were divided into four groups for different testing temperatures (−5°C, −10°C, −15°C, and −25°C, respectively). Each group contained an AEAB-1-coated specimen, an AEAB-2-coated specimen, and an uncoated specimen. Finally, the specimens were placed in different environmental boxes at the fixed temperature for 5 h and the ice-melting conditions were observed to evaluate the anti-icing performance of AEAB.

Besides the laboratory tests, the real road brushed with AEAB (as shown in **Figure 1**) was also used to observe the anti-icing performance of AEAB. The coating dosage of AEAB is 0.8 kg/m^2, and the coating area is about 16.5 m^2.

Ice-Road Adhesion Test

Tan et al. (2013) have developed a system to test the adhesion between ice and asphalt mixture, as shown in **Figure 2A**. The ice-road adhesion test steps are as follows:

(a) The AEAB is evenly brushed on the surface of AC-16 Marshal specimens with a dosage of 0.80 kg/m^2. After the AEAB is fully cured, the specimen is fixed to the upper cover by three screws. Next, 100 g of water is injected into the groove of the device so that the water can be fully contacted with AEAB coating. The profile of the fixed specimen is shown in **Figure 2B**.
(b) Then, the specimens are placed in the environmental box at the fixed temperature for 12 h to simulate the freezing process of the road surface in winter.
(c) Finally, the MTS test system is used to apply load until the bonding interface between ice and specimen is completely broken. The loading rate is 20 mm/min. The maximum load is the ice-road adhesion force, and it is used as an index to evaluate the adhesion between the ice layer and pavements. Besides, the interface of the specimens after test (**Figure 2C**) can also be used to evaluate the deicing effect.

According to the above test steps, the ice-road adhesion forces of AEAB specimens before and after experienced freeze-thaw cycles are analyzed to evaluate the long-term anti-icing

FIGURE 1 | The asphalt pavement brushed with AEAB.

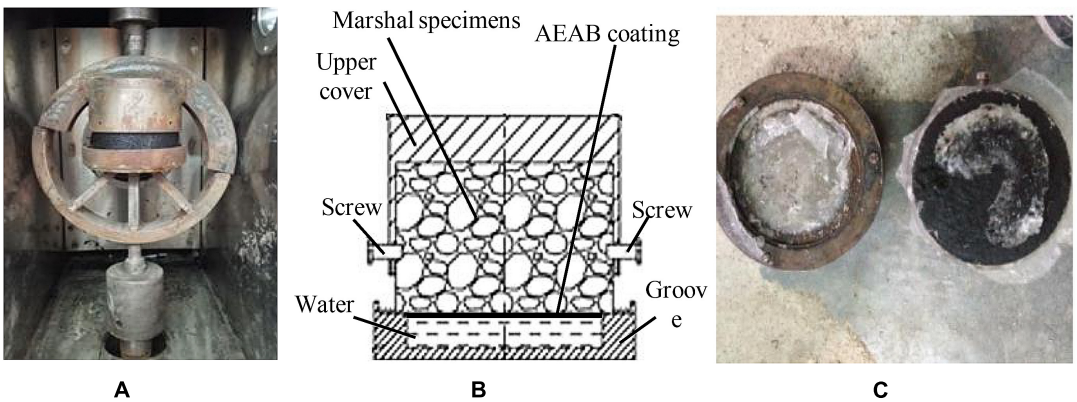

FIGURE 2 | Ice-road adhesion test: **(A)** Testing device. **(B)** The profile of fixed specimen. **(C)** The damage interface of tested specimen.

performance of AEAB. The process of the freeze-thaw cycle is as follows: First, 100 g of water is evenly sprayed on the surface of the specimen. Then, the specimen is placed in the environmental box at −60°C for 6 h to simulate the freezing process. Last, adjust the temperature to 25°C for 6 h to simulate the melting process. The ice-road adhesion of AEAB-coated specimens experienced 0, 5, 10, 15, 20, 25, and 30 times of freeze-thaw cycles is all tested. The AEAB-1-coated specimens are under the testing temperature of −5°C and −10°C. The AEAB-2-coated specimens are under the testing temperature of −15°C and −25°C. Besides, the ice-road adhesions force of uncoated AC-16 specimens at each temperature is also tested for comparison.

Bonding Test

The bonding test is used to evaluate the bonding property between the AEAB coating and the original pavement. The Defelsko PosiTest AT tester shown in **Figure 3A** was used for this purpose. The test steps are as follows:

(a) Firstly, the AC-16 Marshall specimens are manufactured according to the specification (China Communications Press, 2004). Then, the surface of the Marshall specimen is polished by accelerated polishing machine until the original asphalt film is peeled off. The specimen with a polished surface (shown in **Figure 3B**) is selected to simulate the surface condition of the in-service asphalt pavement. The testing value of British Pendulum Number (BPN) and the texture depth (TD) of the polished specimen are 68 and 0.94 mm, respectively, according to the specification (China Communications Press, 2008).

(b) The prepared coating materials (emulsified asphalt binder, modified emulsified asphalt binder or AEAB) are evenly brushed on the polished surfaces of different specimens, respectively, with a dosage of 0.8 kg/m^2. After the emulsion is fully cured, the superglue is used to stick the spindles and coating together. The aim of using the superglue is to ensure that the bonding failure occurs between the coating and asphalt mixture not between spindles and

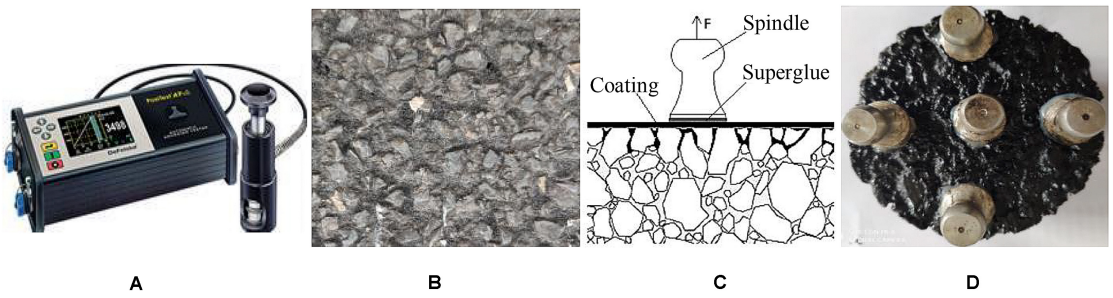

FIGURE 3 | Bonding test: **(A)** Testing device. **(B)** The Marshall specimen with a polished surface. **(C)** The testing schematic. **(D)** The prepared specimen.

TABLE 6 | Basic properties of the materials.

Test items	Modified emulsified asphalt binder	AEAB-1	AEAB-2	Specification requirements JTG F40-2004
Brookfield viscosity (25°C)/mPa · s	960	1780	1600	-
Penetration (25°C,100 g, 5 s)/0.1 mm	46.4	40.0	40.0	40∼100
Softening point (Ring ball)/°C	77.0	78.5	76.5	≥53
Penetration index PI	3.71	3.53	3.26	-
5°C ductility/cm	63.6	58.3	56.7	≥20
25°C elastic recovery/%	65.3	59.1	60.6	≥55

the coating. Five test positions are selected randomly for each specimen. The testing schematic and the prepared specimen are shown in **Figures 3C,D**, respectively.

(c) Next, the prepared specimens are divided into three groups for different testing temperatures (−15°C, 25°C, and 60°C, respectively), and each group contains three different specimens coated by three kinds of coating material, respectively. Then, each specimen is placed in the environmental box at its testing temperature for 2 h.

(d) Finally, the tester is used to apply a tensile force to the spindles at a loading speed of 0.2 Mpa/s until the coating material is pulled apart from the asphalt mixture specimen.

The maximum tensile force is the bonding strength, and it is used as the index to evaluate the bonding property of coating materials. The larger the bonding strength is, the better the bonding property of coating material is.

RESULTS AND DISCUSSION

Basic Properties

The basic test results of AEAB and the modified emulsified asphalt binder are shown in **Table 6**. It can be seen that the Brookfield viscosity of AEAB is much larger than that of modified emulsified asphalt binder; this indicates that the addition of anti-icing filler has increased the viscosity and consistency of modified emulsified asphalt binder. The softening point of AEAB

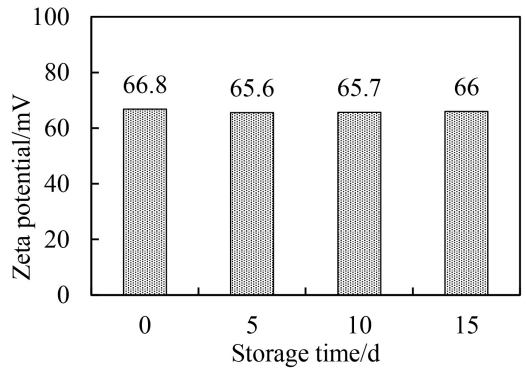

FIGURE 4 | Zeta potential of modified emulsified asphalt binder at different storage time.

evaporative residue is above 70°C; it means that the AEAB has an excellent high-temperature performance. Compared with the modified emulsified asphalt binder, the 5°C ductility and 25°C elastic recovery of AEAB evaporated residue decrease slightly. It means that anti-icing fillers can slightly affect the low-temperature performance and elastic recovery ability of modified emulsified asphalt binder. All of the performance indexes of the AEAB meet the requirements of specification (China Communications Press, 2004), which proved the feasibility of AEAB as pavement maintenance materials.

Storage Stability

The Zeta potentials of modified emulsified asphalt binders at different storage times are shown in **Figure 4**. It can be seen that the Zeta potential of modified emulsified asphalt binder fluctuates slightly at 66 mv during 15 days. According to the stability classification of colloidal materials from **Table 5**, it is clearly indicated that the modified emulsified asphalt binder has excellent long-term storage stability. The Zeta potential of newly prepared AEAB is about 45 mv. It means that adding anti-icing fillers into modified emulsified asphalt binder will reduce the storage stability of modified emulsified asphalt binder. But the Zeta potential of AEAB is still greater than 30 mv, which indicates that the storage time of AEAB is more than 20 h. It also means that the AEAB can maintain a uniform and stable state without

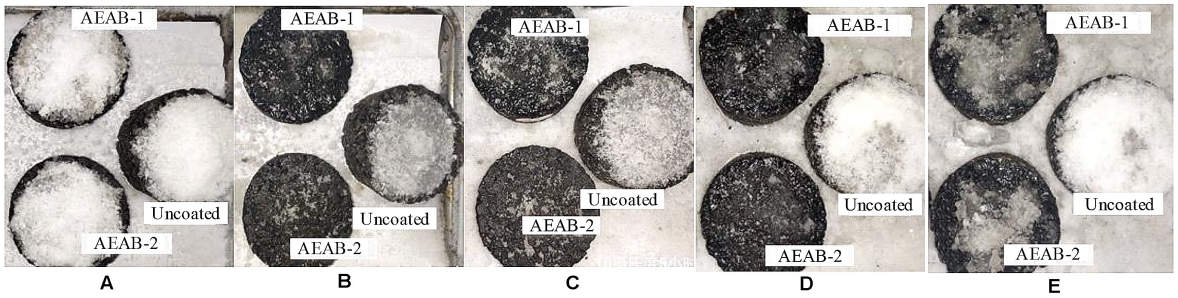

FIGURE 5 | Comparisons of ice-melting test at different temperature: **(A)** Initial state of each group. **(B)** −5°C. **(C)** −10°C. **(D)** −15°C. **(E)** −25°C.

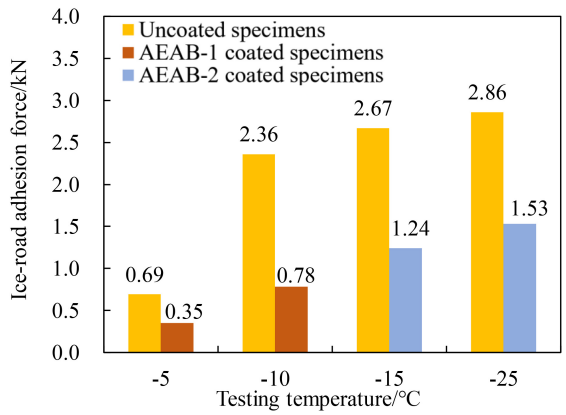

FIGURE 6 | Ice-road adhesion force of AEAB coated and uncoated specimens at different temperature.

demulsification more than 20 h. So, there is enough time for the production and construction of AEAB.

Anti-icing Performance

The surface conditions of the specimens in the environmental box are shown in **Figure 5**. It is observed that the snow-ice particles on the surface of AEAB-coated specimens are much less than that on the surface of the uncoated specimens. It means that the AEAB coating has an obvious effect on facilitating the melting of snow and ice. From **Figures 5B–E**, it can be seen that the amount of snow-ice particles on the specimen increases obviously with the decrease in temperature. It means that the effect of the AEAB decreases with decrease in temperature. But it still has the snow-melting ability when the temperature is −25C. Besides, the ice-melting condition of AEAB-1 coating and AEAB-2 coating are similar to each other at the same temperature; this may happen because the observing time is too short to show the anti-icing differences between the two types of anti-icing fillers.

The ice-road adhesion force of the uncoated specimens and the AEAB coated specimens is shown in **Figure 6**. It can be seen that, under the conditions of −5°C, −10°C, −15°C, and −25°C, the ice adhesion forces of AEAB-coated specimens have decreased by 49.3%, 67%, 53.6%, and 46.5%, respectively, compared with that of uncoated specimens. It means that AEAB

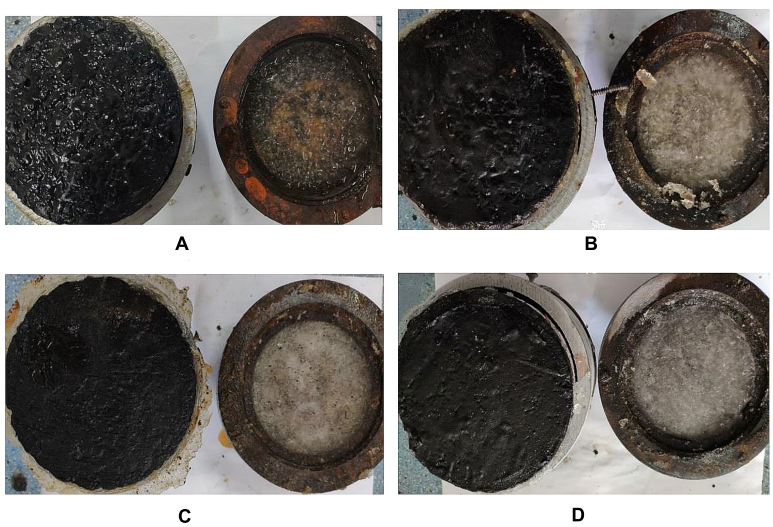

FIGURE 7 | The interface of the AEAB-coated specimens after ice-road adhesion tests: **(A)** −5°C. **(B)** −10°C. **(C)** −15°C. **(D)** −25°C.

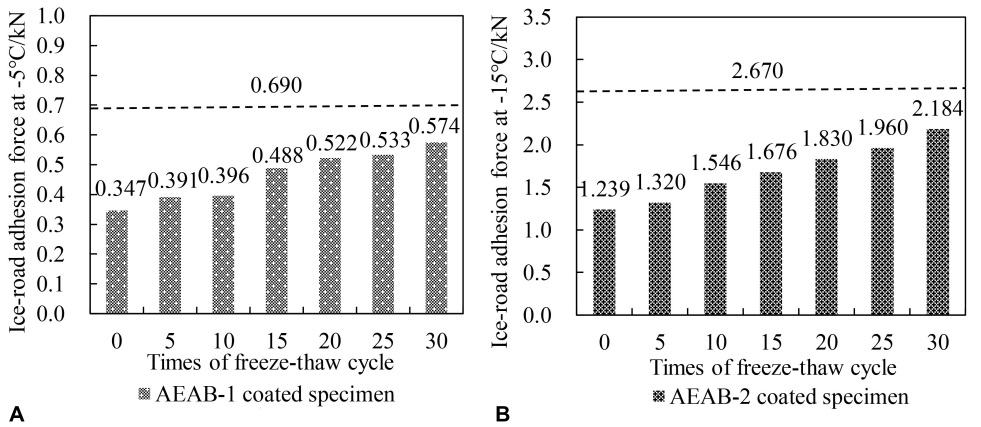

FIGURE 8 | Ice-road adhesion force of different times of freeze-thaw cycle: **(A)** AEAB-1-coated specimen. **(B)** AEAB-2-coated specimen. The dash line in the figure indicates the ice-road adhesion of uncoated specimens that do not experience the freeze-thaw cycle.

FIGURE 9 | Observation during snowing weather in Harbin China. **(A)** Snow-melting conditions after light snow in November 2019. **(B)** Snow-removing conditions after heavy snow in December 2019.

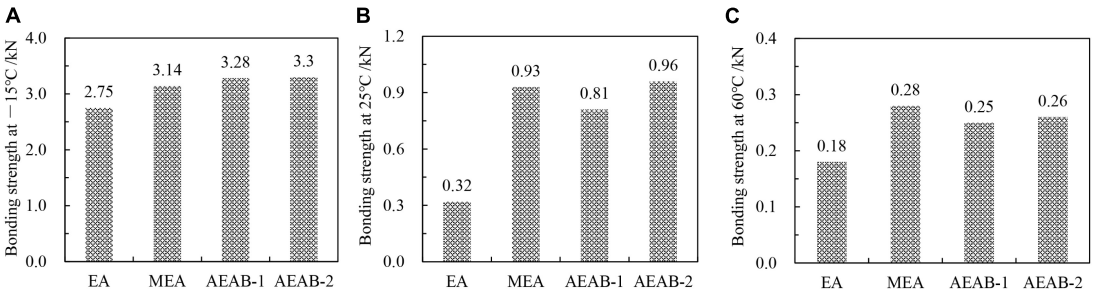

FIGURE 10 | Bonding strength of different coating materials at different temperature: **(A)** At −15°C **(B)** At 25°C **(C)** At 60°C. In the figures, EA represents the emulsified asphalt binder, and MEA represents the modified emulsified asphalt binder.

coating can dramatically reduce the adhesion force between ice and asphalt pavement, which is very helpful for the snow/ice removal. The interfaces of the specimens after ice-road adhesion test are shown in **Figure 7**. It is found that there is basically no ice covering on the surface of the AEAB-coated specimens, which proves that the ice is easy to pull off from the specimen due to the reduction of ice-road adhesion force.

The ice-road adhesion forces of the specimens experienced different times of freeze-thaw cycles are shown in **Figure 8**. It can be seen that the ice-road adhesion force of AEAB-1- and AEAB-2-coated specimen increases slightly with the increase in times of freeze-thaw cycles. It is mainly due to the constant release of anti-icing ingredients, which slowly decreases the deicing effect of AEAB. Besides, the freeze-thaw cycle can also cause an increase in the adhesion force between ice and specimen. Nevertheless, after the AEAB coated has experienced 30 times of freeze-thaw cycles, the ice-road adhesion force of AEAB-coated specimen is still lower than the ice-road adhesion of uncoated specimens that do

not experience the freeze-thaw cycle. It indicates that the release rate of anti-icing ingredients has been maintained at a moderate level and the AEAB can well keep its adhesion-reduce function.

Figure 9A shows the snow-melting conditions of the uncoated area and the AEAB-coated area on the asphalt pavement after a light snow. It can be seen that there is barely any snow covering the AEAB coated area compared with the uncoated asphalt pavement. It is direct evidence that the AEAB coating on asphalt pavement can facilitate the melting of snow to realize a self-ice-melting function. When the snow is heavy, the mechanical equipment is used to remove the snow on the asphalt pavement. **Figure 9B** shows that the snow-removing conditions of the uncoated area and the AEAB coated area on the asphalt pavement after heavy snow. It can be seen that the snow remaining on the AEAB-coated area is obviously less than that on the uncoated area. It proves that the snow/ice is easy to clear due to the reduction of ice-road adhesion force on the AEAB-coated pavement.

Bonding Properties

The bonding strengths of the emulsified asphalt binder, modified emulsified asphalt binder, and AEAB were tested, and the results are shown in **Figure 10**. It can be seen that, compared with the bonding strength of emulsified asphalt (shown as EA in the figures), the bonding strengths of modified emulsified asphalt binder (shown as MEA in the figures) increases significantly. This indicates that the compound modifier has an obvious effect on improving the bonding properties of the emulsified asphalt binder. Besides, comparing the bonding strength of modified emulsified asphalt binder with that of AEAB (shown as AEAB-1 and AEAB-2 in the figures), it shows that the bonding strengths of modified emulsified asphalt binder slightly changes after adding anti-icing fillers. It means that the participation of anti-icing filler has little effect on the bonding properties of modified emulsified asphalt binder. In a word, the bonding test proves that the AEAB has an excellent bonding state with the original pavement, which can prolong the service life of the coating.

CONCLUSION

In this paper, a kind of AEAB was developed by adding anti-icing fillers into a modified emulsified asphalt binder. The anti-icing performance and pavement performance of AEAB coating were analyzed. The major conclusions of this study can be drawn:

(1) Although the participation of anti-icing fillers can slightly affect the low-temperature performance and elastic recovery ability of modified emulsified asphalt binder, all of the performance of AEAB can still meet the requirements of the specification.
(2) The AEAB coating has excellent anti-icing performance. It can facilitate the melting of snow and ice on pavement and dramatically reduce the adhesion forces between ice and road, which is helpful for the snow/ice removal and the maintaining of skid resistance on asphalt pavement.
(3) The compound modifier has an obvious effect on improving the bonding properties of AEAB. The AEAB coating can keep an excellent bonding state with the original pavement, which can prolong the service life of the coating.
(4) The study has proved that the AEAB has the necessary storage stability for the actual construction. Future research should be conducted to develop a kind of AEAB that has a longer storage stability time, and the anti-icing mechanism of AEAB coating needs to be further studied.

DATA AVAILABILITY STATEMENT

The raw data supporting the conclusions of this article will be made available by the authors, without undue reservation.

AUTHOR CONTRIBUTIONS

LS and YT proposed the research direction and provided the funds for the research. HY wrote the first draft. DT carried out the experiments. All authors analyzed the results and contributed to writing of the manuscript.

FUNDING

The study was financially supported by the National Natural Science Foundation of China under the Grant Nos. U1633201, 51778195, and 51978218.

ACKNOWLEDGMENTS

The authors acknowledge Ms. Jianrong Wang for providing the emulsifier.

REFERENCES

Baldino, N., Gabriele, D., Rossi, C. O., Seta, L., Lupi, F. R., and Caputo, P. (2012). Low temperature rheology of polyphosphoric acid (PPA) added bitumen. *Constr. Build. Mater.* 36, 592–596. doi: 10.1016/j.conbuildmat.2012.06.011

Chen, M., Wu, S., Wang, H., and Zhang, J. (2011). Study of ice and snow melting process on conductive asphalt solar collector. *Sol. Energy. Mat. Sol. C* 95, 3241–3250. doi: 10.1016/j.solmat.2011.07.013

China Communications Press (2004). *Technical Specifications for Construction of Highway Asphalt Pavements JTG F40-2004*. Beijing: China Communications Press.

China Communications Press (2008). *Field Test Methods of Subgrade and Pavement for Highway Engineering JTG E60-2008*. Beijing: China Communications Press.

China Communications Press (2011). *Standard Test Methods of Bitumen and Bituminous Mixtures for Highway Engineering JTG E20-2011*. Beijing: China Communications Press.

China Communications Press (2018). *Deicing and Thawy Material Used in Asphalt Mixture-Part 2: Salinization-Based Material JT/T 1210.2-2018*. Beijing: China Communications Press.

Dan, H., He, L., and Xu, B. (2017). Experimental investigation on skid resistance of asphalt pavement under various slippery conditions. *Int. J. Pavement Eng.* 18, 485–499. doi: 10.1080/10298436.2015.1095901

Daniels, J. W. III, Heymsfield, E., and Kuss, M. (2019). Hydronic heated pavement system performance using a solar water heating system with heat pipe evacuated tube solar collectors. *Sol. Energy* 179, 343–351. doi: 10.1016/j.solener.2019.01.006

Han, S., Yao, T., and Yang, X. (2019). Preparation and anti-icing properties of a hydrophobic emulsified asphalt coating. *Constr. Build. Mater.* 220, 214–227. doi: 10.1016/j.conbuildmat.2019.06.021

Henry, J. J. (1991). *Highway de-Icing, Transportation Research Board. Special Report* 235. Washington, DC: National Research Council.

Huang, S., Robertson, R. E., Branthaver, J. F., and Claine Petersen, J. (2005). Impact of lime modification of asphalt and freeze–thaw cycling on the asphalt–aggregate interaction and moisture resistance to moisture damage. *J. Mater. Civil Eng.* 17, 711–718. doi: 10.1061/(asce)0899-1561200517:6(711)

Li, F., and Wang, Z. (2012). Experiment on road performance of asphalt mixture with automatic long-term snowmelt agent. *J. Highway Transport. Res. Dev.* 6, 11–17. doi: 10.1061/jhtrcq.0000002

Lin, J., Guo, P., Wan, L., and Wu, S. (2012). Laboratory investigation of rejuvenator seal materials on performances of asphalt mixtures. *Constr. Build. Mater.* 37, 41–45. doi: 10.1016/j.conbuildmat.2012.07.008

Liu, X., Rees, S. J., and Spitler, J. D. (2007). Modeling snow melting on heated pavement surfaces. Part I: model development. *Appl. Therm. Eng.* 27, 1115–1124. doi: 10.1016/j.applthermaleng.2006.06.017

Luo, S., and Yang, X. (2015). Performance evaluation of high-elastic asphalt mixture containing deicing agent Mafilon. *Constr. Build. Mater.* 94, 494–501. doi: 10.1016/j.conbuildmat.2015.07.064

Mamlouk, M. S., and Dosa, M. (2014). Verification of effectiveness of chip seal as a pavement preventive maintenance treatment using LTPP data. *Int. J. Pavement Eng.* 15, 879–888. doi: 10.1080/10298436.2014.893318

Pan, P., Wu, S., Xiao, Y., and Liu, G. (2015). A review on hydronic asphalt pavement for energy harvesting and snow melting. *Renewable Sustain. Energy Rev.* 48, 624–634. doi: 10.1016/j.rser.2015.04.029

Pan, T., He, X., and Shi, X. (2008). "Laboratory investigation of acetate-based deicing/anti-icing agents deteriorating airfield asphalt concrete," in *Asphalt Paving Technology-Proceedings*, Vol. 77 (Philadelphia, PA: Technical Session of the Association-of-Asphalt-Paving-Technologists), 773.

Peng, C., Zhang, H., You, Z., Xu, F., Jiang, G., Lv, S., et al. (2018). Preparation and anti-icing properties of a superhydrophobic silicone coating on asphalt mixture. *Constr. Build. Mater.* 189, 227–235. doi: 10.1016/j.conbuildmat.2018.08.211

Salopek, B., Krasic, D., and Filipovic, S. (1992). Measurement and application of zeta-potential. *Rudarsko-geolosko-naftni zbornik* 4, 147.

Stachurski, J., and MichaŁek, M. (1996). The effect of the ζ potential on the stability of a non-polar oil-in-water emulsion. *J. Colloid Interface Sci.* 184, 433–436. doi: 10.1006/jcis.1996.0637

Tan, Y., Hou, M., Shan, L., and Sun, R. (2014). Development of sustained release complex salt filler for asphalt pavement included salt. *J. Build. Mater.* 17, 256–260. doi: 10.3969/j.issn.1007-9629.2014.02.013

Tan, Y., Sun, R., Guo, M., Zhong, Y., and Zhou, S. (2013). Research on deicing performance of asphalt mixture containing salt. *China J. Highw. Transp.* 26, 23–29. doi: 10.19721/j.cnki.1001-7372.2013.01.004

Tan, Y., Zhang, C., Xu, H., and Tian, D. (2019). Snow melting and deicing characteristics and pavement performance of active deicing and snow melting pavement. *China J. Highw. Transp.* 32, 1–17. doi: 10.19721/j.cnki.1001-7372.2019.04.001

Tan, Z. (2018). *Research On Hardening Process and Hardening Mechanism of Cement Asphalt Composite Binder*. D. Harbin: Harbin Institute of Technology.

Tang, X., Jiao, S., Gao, Z., and Xu, X. (2008). Study of 5.8 GHz magnetron in microwave deicing. *J. Electromagnet. Wave.* 22, 1351–1360. doi: 10.1163/156939308786348901

Tian, D. (2019). *Preparation Technology and Applied Research of Anti-Icing Glutinous Emulsified Asphalt*. D. Harbin: Harbin Institute of Technology, doi: 10.27061/d.cnki.ghgdu.2019.001640

Waluś, K. J. (2017). "Driver's strategy and braking distance in winter," in *Transport Means, Proceedings of 21st International Scientific Conference* (Juodkrantė), 20–22.

Wang, H., Zhao, J., and Chen, Z. (2008). Experimental investigation of ice and snow melting process on pavement utilizing geothermal tail water. *Energy Convers. Manag.* 49, 1538–1546. doi: 10.1016/j.enconman.2007.12.008

Wang, Z., Zhang, T., Shao, M., Ai, T., and Zhao, P. (2017). Investigation on snow-melting performance of asphalt mixtures incorporating with salt-storage aggregates. *Constr. Build. Mater.* 142, 187–198. doi: 10.1016/j.conbuildmat.2017.03.070

Yehia, S., and Tuan, C. Y. (1999). Conductive concrete overlay for bridge deck deicing. *Mater. J.* 96, 382–390.

Zheng, M., Wu, S., Wang, C., Li, Y., Ma, Z., and Peng, L. (2017). A study on evaluation and application of snowmelt performance of anti-icing asphalt pavement. *Appl. Sci.* 7, 583. doi: 10.3390/app7060583

Zhou, X., Yang, Z. J., Chang, C., and Song, G. (2011). Numerical assessment of electric roadway deicing system utilizing emerging carbon nanofiber paper. *J. Cold Reg. Eng.* 26, 1–15. doi: 10.1061/(ASCE)CR.1943-5495.0000033

Conflict of Interest: DT was employed by the company CCCC Highway Consultants CO., Ltd.

The remaining authors declare that the research was conducted in the absence of any commercial or financial relationships that could be construed as a potential conflict of interest.

frontiers in Materials

ORIGINAL RESEARCH
published: 11 August 2020
doi: 10.3389/fmats.2020.00209

Preparation and Properties of Carbon Nanofiber Modified Emulsified Asphalt Based on Ultrasonication and Surfactant and the Impact of SBR and NH_4Cl

Xuhang Liu[1], Yuning An[1], Jinyan Feng[1], Xingyi Zhu[2] and Feng Li[1]*

[1] School of Transportation Science and Engineering, Beihang University, Beijing, China, [2] College of Transportation Engineering, Tongji University, Shanghai, China

Carbon nanofiber (CNF) is a nanomaterial with unique mechanical properties, which can improve the properties of composite materials effectively. Research focusses on the impact of CNF on asphalt, asphalt binders, and mixtures. Traditional emulsified asphalt presents a limited performance at both high and low temperatures. Emulsified asphalt with a better performance, is therefore required in engineering. Referring to research on CNF-asphalt, CNF is considered to improve the performance of emulsified asphalt. In this study, a preparation method for CNF modified emulsified asphalt with styrene-butadiene rubber (SBR) was proposed. Ultrasonication and surfactant were utilized to disperse the CNFs in water. The optimum dispersion surfactant percentages and ultrasonic energy density to disperse CNFs were determined through ultraviolet-visible spectra (UV-vis spectra). The modified emulsified asphalt was produced using CNFs suspension with SBR as a modifier, and the properties of the residue, with different percentages of CNFs, were tested. Gel permeation chromatography (GPC) was performed to analyze the molecular size distribution. The results indicated that CNFs significantly improved high-temperature performance of the residue but decreased low-temperature properties. The addition of SBR not only perfected storage stability but also improved low-temperature performance by introducing more small molecules.

Keywords: carbon nanofiber, dispersion, SBR, residue properties, GPC

OPEN ACCESS

Edited by:
Yiqiu Tan,
Harbin Institute of Technology, China

Reviewed by:
Qiang Yuan,
Central South University, China
Changjun Zhou,
Dalian University of Technology, China

****Correspondence:***
Jinyan Feng
fjy@buaa.edu.cn

Specialty section:
This article was submitted to Structural Materials, a section of the journal Frontiers in Materials

Received: *14 March 2020*
Accepted: *09 June 2020*
Published: *11 August 2020*

Citation:
Liu X, An Y, Feng J, Zhu X and Li F (2020) Preparation and Properties of Carbon Nanofiber Modified Emulsified Asphalt Based on Ultrasonication and Surfactant and the Impact of SBR and NH_4Cl. Front. Mater. 7:209. doi: 10.3389/fmats.2020.00209

INTRODUCTION

In the past few years, nanomaterials, especially carbon nanotube (CNT) and carbon nanofiber (CNF), have presented advantages in composite materials and has attracted extensive investigation. There are many studies on the application of CNT/CNF in civil engineering because of their extraordinary properties (Pacheco-Torgal and Jalali, 2011). For example, carbon nanofibers exhibit excellent mechanical properties with Young's modulus from 25 to 200 GPa (Lawrence et al., 2008) and tensile strength of up to 12 GPa (Mordkovich, 2003).

For CNF reinforced composite materials, it is vital to obtain a uniform dispersion of CNFs in the matrix material to take advantage of the excellent mechanical properties of CNFs. Compared to CNF, there are more studies on the dispersion of CNT that indicate the effectiveness of surfactant

and ultrasonication to disperse CNTs in water uniformly (O'Connell et al., 2002; Strano et al., 2003). Considering a similar surface structure between CNT and CNF, the dispersion principle and method for these two materials should therefore also be similar.

There are many studies that focus on CNF reinforced cement. A. Yazdanbakhsh and Zoi S. Metaxa provided a method to produce carbon nanofiber modified cement with surfactant and ultrasonication (Yazdanbakhsh et al., 2009, 2010; Metaxa et al., 2013): first, CNFs were dispersed through ultrasonication in water containing surfactant, then the suspension was added to cement instead of water, and participated in hydration. Konsta-Gdoutos MS and Shah et al. researched CNF-cement composites further. They found significant improvements in flexural strength, Young's modulus, flexural toughness, and fracture toughness (Gdoutos et al., 2016). Zhu et al. (2018) researched the effect of the interfacial transition zone on Young's modulus of CNF reinforced cement concrete. Moreover, there is also research that indicates that the addition of CNFs significantly influences resistance to corrosion, electrical conductivity, and resistivity sensibility to structural damage of the nanocomposites (Galao et al., 2014; Konsta-Gdoutos and Aza, 2014; Konsta-Gdoutos et al., 2017).

The success of CNFs-cement composites has motivated studies on CNFs modified asphalt. According to the production of CNFs-cement materials, to prepare a CNF-asphalt composite material, the CNFs can be dispersed in the solvent and then be added to the asphalt. Khattak et al. (2013a) dispersed CNFs in kerosene or acetone by ultrasonication and then added the mixture into the asphalt. Kerosene or acetone eventually evaporated by heating (Khattak et al., 2013a,b). Asphalt mixtures with nanofibers also exhibit excellent mechanical properties like enhanced stiffness, higher dynamic modulus (Khattak et al., 2013a), and higher resistance to cracking under repeated loads (Khattak et al., 2013b). Furthermore, Khattak et al. (2013a) also studied the impact of CNFs modified asphalt on asphalt binder rheology through dynamic shear rheometer (DSR). They found that visco-elastic response and fatigue life were improved, which indicated higher resistance to rutting and fatigue (Khattak et al., 2012). Goh's research demonstrated that CNFs improved moisture susceptibility performance (decrease the moisture damage potential) of the mixture in most cases, and hot-mix asphalt mixture exhibited the greatest tensile strength with 0.75 wt% nanofibers (Goh et al., 2011). Despite these achievements, there are still issues. Generally, CNFs are easy to disperse in water with the assistance of surfactant and ultrasonication (get suspension), hence, there is a relatively uniform dispersion of nanofibers in cement, of which the suspension is a composition. By contrast, it is more difficult to disperse CNFs in asphalt directly, since the ultrasonication fails to work in high viscosity and hot liquid. Although agents like kerosene facilitate dispersion, they must ultimately be removed. Additionally, incomplete removal can affect performance.

Compared to the hot asphalt, considering that emulsified asphalt consists of asphalt and water, it is possible to produce emulsified asphalt with evenly dispersed CNFs by obtaining suspension first. Moreover, emulsified asphalt and relevant materials such as cold recycled mixture and cement asphalt emulsion mortar are environmentally friendly, however, their poor properties limit further development (Ouyang et al., 2018, 2020). It is therefore necessary to improve the performance of cold recycled mixture and cement asphalt emulsion mortar, of which improving the properties of emulsified asphalt is essential.

This paper proposed a method to prepare CNF modified emulsified asphalt. According to present research, CNFs only enhance high temperature performance, so in this study, SBR was used as a modifier. Furthermore, the properties of the evaporation residue of the emulsified asphalt were investigated. Gel permeation chromatography (GPC) was performed to analyze the effect of SBR on the molecular size distribution and low-temperature properties.

PREPARATION OF CNFs MODIFIED EMULSIFIED ASPHALT

Materials

One 70# asphalt is selected as the base asphalt (**Table 1**). Carbon nanofibers are black powder (**Figure 1**) provided by Nanjing XFNANO Materials Tech Co., Ltd. All the CNFs are as-grown vapor grown carbon nanofibers (VGCNFs) produced at a high temperature with stable properties. The characteristic properties of CNFs are shown in **Table 2**. The surfactant is a kind of pale-yellow transparent liquid with a density of 0.98 g/ml provided by BASF Chemicals Co., Ltd (ID: GS8325).

TABLE 1 | Properties of asphalt.

Index	Result
Penetration (0.1 mm)	67
Softening Point (°C)	47.5
Ductility (10°C) (cm)	25
Rotational viscosity (135°C) (Pa·s)	0.48
PI (–)	−0.7

FIGURE 1 | CNFs used in this study.

TABLE 2 | Properties of carbon nanofibers (CNFs).

Commercial name	XFM60
Length (μm)	5–50
Diameter (nm)	200–600
Surface area (m^2/g)	>18
Purity (%)	>70
Density (g/cm^3)	2.1

Dispersion of CNFs

Emulsified asphalt consists of water and asphalt, so it is feasible to disperse CNFs in water and to then produce modified emulsified asphalt. The surfactant provided by BASF Chemicals Co., Ltd. was used in this study to improve the dispersion of CNFs and the stability of the suspension. VCX800 purchased from Sonics & Materials Co., Ltd. performed ultrasonication with a probe of a diameter of 25 mm. Ultrasonication caused a cavity (cavitation effect) and provided energy through a cavity burst to overcome the Van der Waals forces between nanofibers and disrupted CNFs aggregation. Surfactant attached on the surface of individual CNF enhanced the isolation. This process is exhibited in **Figure 2**. After ultrasonication, CNF aggregation was dispersed into individual CNF surrounded by surfactant molecules.

To obtain the optimum dispersion, ultrasonication energy density (KJ/L) and the amount of surfactant are significant factors (5), which should be determined in advance. In this study, the ultrasonic instrument was input energy with a constant power of 70 W. The energy density varied from 3000 KJ/L to 7000 KJ/L, and the weight ratio of CNFs to surfactant varied from 1:3 to 1:5.

UV-vis Spectra

Individual CNT is active in the UV-vis spectra and exhibits characteristic bands corresponding to additional absorption due to van Hove singularities (Saito et al., 1992). Some researchers have obtained a strong peak of UV-vis spectra at the wavelength of approximately 250 nm (Chen et al., 1998; Grossiord et al., 2005; Yu et al., 2007; Cui et al., 2017). There is a certain similarity in the microstructure between CNF and CNT, so the UV-vis spectra can also be used to evaluate the dispersion of CNFs. The relationship between absorbance and solution concentration can be determined by Lambert-Beer law as follows (Formula 1), where A is the absorbance; T is the transmissivity; K is the molar absorptivity; b is the thickness of the absorption layer (cm); c is the concentration of light-absorbing substances (mol/L). A higher peak value at a particular wavelength indicates a higher concentration of individual CNF in suspension, presenting a better dispersion state.

$$A = \lg\left(\frac{1}{T}\right) = Kbc \tag{1}$$

There is a positive correlation between absorbance and solute concentration only when absorbance ranges from 0.2 to 0.8, according to the Lambert-Beer law. The suspension was therefore diluted by 50 times its volume before measuring to control the absorbance (**Figure 3**).

UV-vis spectra of all suspension with different energy density and surfactant content were performed with a sweep of wavelength from 200 to 500 nm. The results are demonstrated in **Figure 4**. Absorbance all appears within the expected range (0.2–0.8), so the results are valid.

There is an additional absorption peak for each group at a specific wavelength of 246 nm. The highest peak in **Figure 4** indicates that the optimal dispersion method is to disperse CNFs using ultrasonication at an energy density of 5000 KJ/L, accompanied by the addition of surfactant at a weight ratio of 1:5 to CNFs. It is noticeable that ultrasonication energy

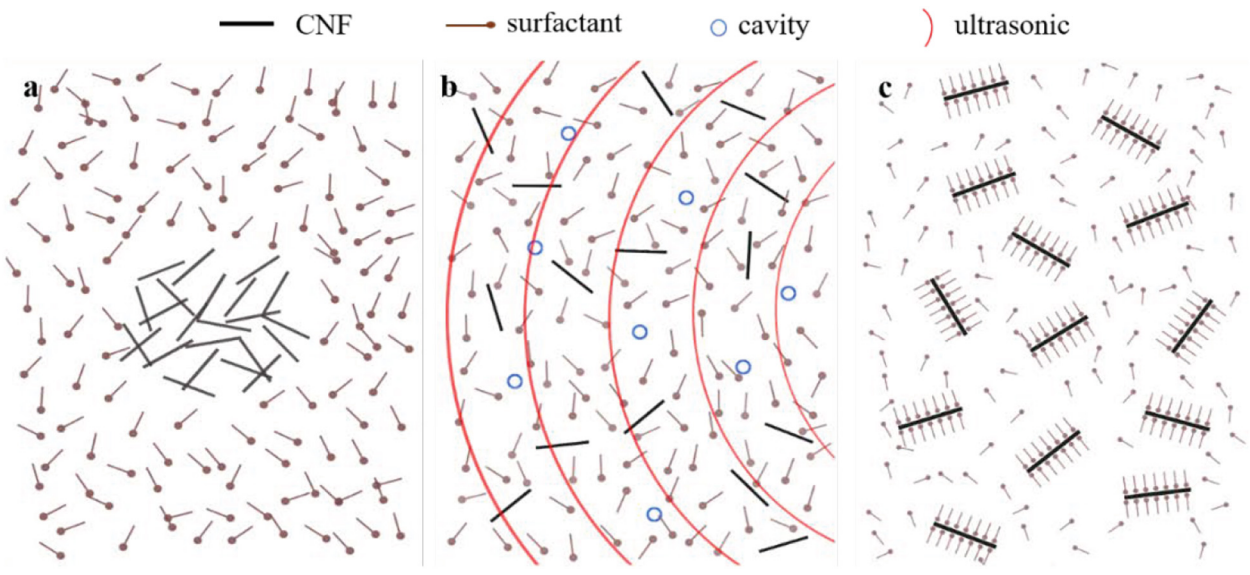

FIGURE 2 | Dispersion process: **(a)** unprocessed **(b)** during process **(c)** after process.

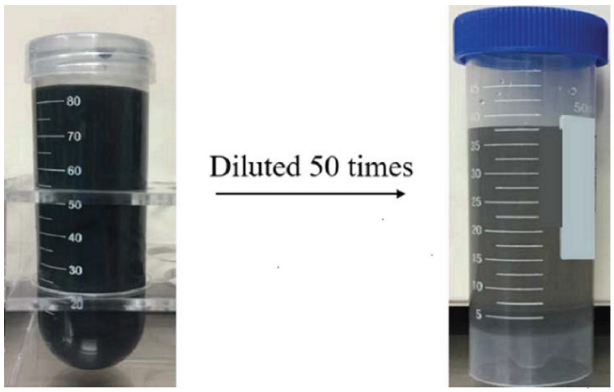

FIGURE 3 | Dilution of suspension for UV-vis spectra.

density and surfactant both impact disaggregation significantly. With the same surfactant content, the peak value of absorbance increases with the increase of energy density from 3000 to 5000 KJ/L and then decreases at a higher energy density. Similarly, under a constant energy density, more surfactant (weight ratio of CNFs to surfactant varies from 1:3 to 1:5) first contributes to a higher peak, then the absorbance decreases at the ratio of 1:6.

Preparation of Emulsion Containing CNFs and Emulsification

Colloidal mill MD-1 from Jiaxing Mide Machinery Co., Ltd. was utilized. In this study, the mass ratio of asphalt to emulsion (water and emulsifier) was 65:35. The emulsifier was SBT-50, provided by Westvaco Corporation. In this research, the emulsifier accounted for 3.9% of the mass of emulsified asphalt.

Carbon nanofibers content was determined by weight ratio to asphalt (0.1, 0.3, 0.5, and 1.0 wt%). First, CNFs were dispersed according to the optimal method above. The emulsifier was then dissolved into the suspension to obtain an emulsion. Hydrochloric acid was added to adjust pH value (pH≈2). Before production, the mill was heated, then materials were added to the colloid mill in this order: emulsion at 70°C was added and circulated for about half a minute, then hot asphalt at 135–145°C was added with a constant speed to ensure uniform mix. For example, assuming the mass of emulsified asphalt is M, and the CNFs content is 0.1 wt%, the whole process is demonstrated in **Figure 5**.

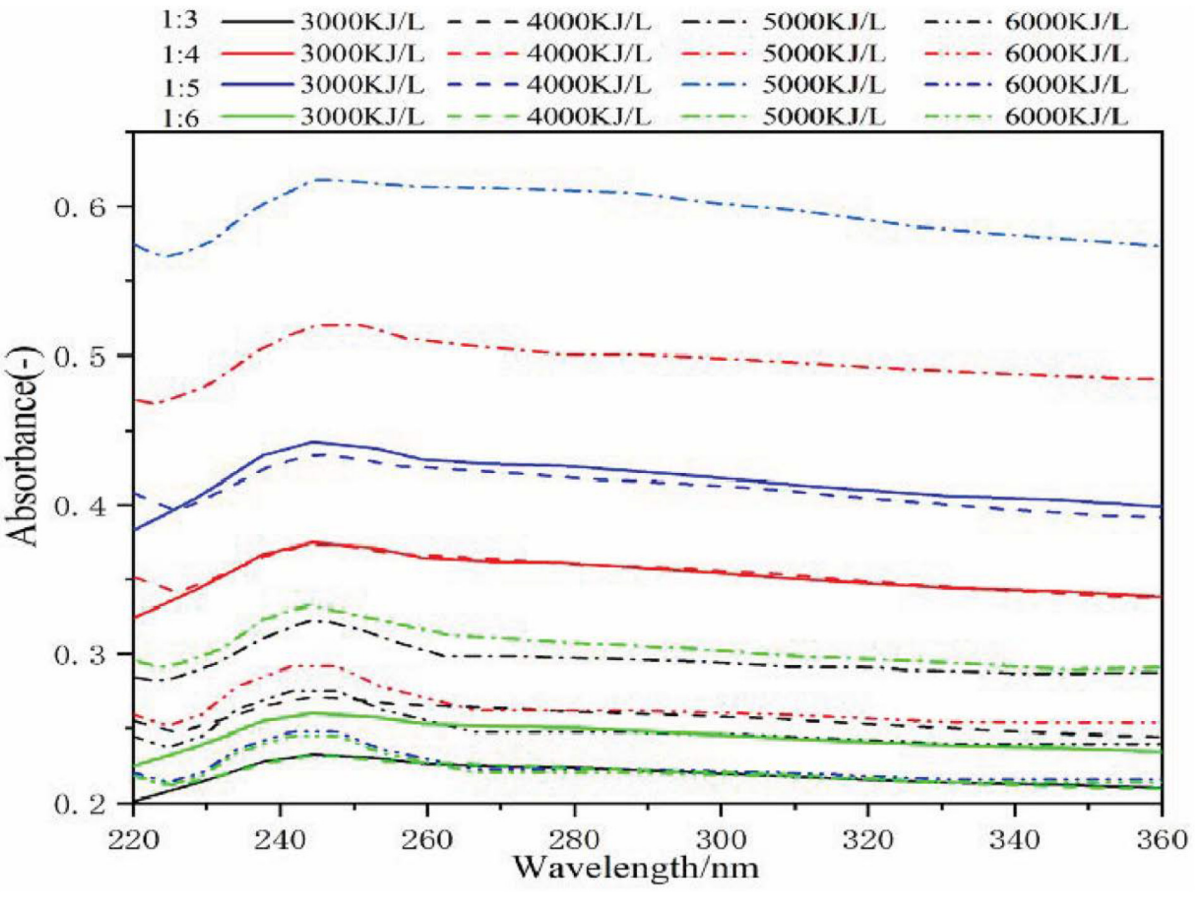

FIGURE 4 | Absorbance of CNFs suspension with different energy density and weight ratio of CNFs to surfactant.

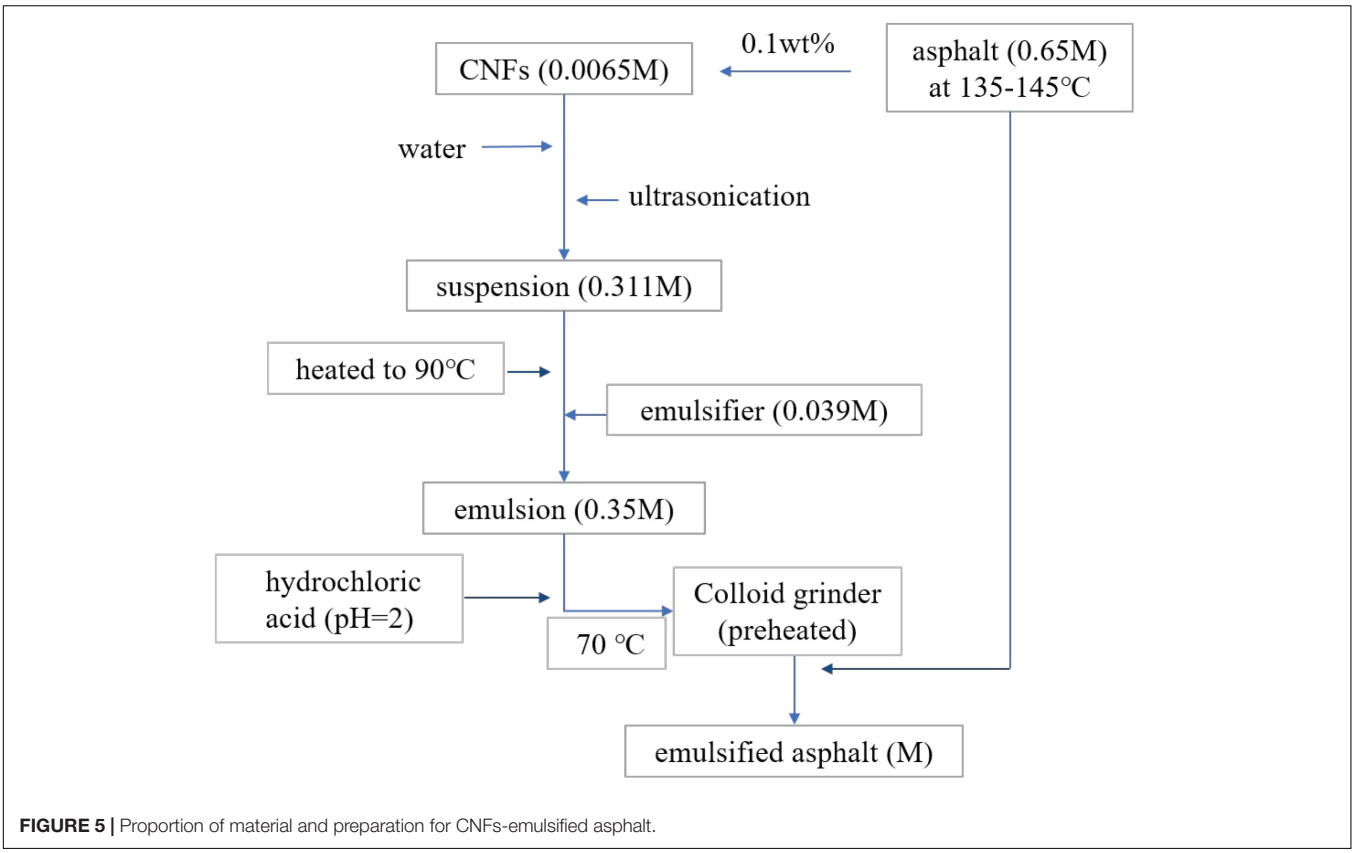

FIGURE 5 | Proportion of material and preparation for CNFs-emulsified asphalt.

TABLE 3 | Experimental group setting (0.1 wt% CNFs for example).

ID	CNFs content (wt%)	NH_4Cl content (wt%)	SBR content (wt%)
Control	–	–	–
0.1C	0.1	–	–
0.1C1N	0.1	1.0	–
0.1C3N	0.1	3.0	–
0.1C1N1S	0.1	1.0	1.0
0.1C3N1S	0.1	3.0	1.0

After production, ammonium chloride (NH_4Cl) was added as a stabilizer. NH_4Cl content varied as 0, 1, and 3 wt% (weight ratio to asphalt). 1 wt% SBR latex (weight ratio to emulsified asphalt) was added as a modifier. **Table 3** shows the ID of groups with 0.1 wt% CNFs. The ID of groups with 0.3, 0.5, and 1.0 wt% CNFs are similar.

EXPERIMENTS

Storage Stability

Storage stability (1 day) at room temperature was investigated to estimate the feasibility of this preparation method. Emulsified asphalt was settled in the storage stability tube for 1 day, then the asphalt content of the 50 ml sample from the top and the 50 ml sample from the bottom were calculated, respectively. Their difference presents storage stability. In most situations, the emulsified asphalt is used immediately after production, so the stability of 1 day is enough to prove engineering suitability.

Basic Properties of the Modified Emulsified Asphalt

In this study, to investigate the influence of CNFs and SBR, traditional experiments were performed. The emulsified asphalt was heated to remove moisture primarily. In this process, the temperature slowly increased and was below 180°C to avoid asphalt aging. Then the penetration (25°C), softening point, rotational viscosity (135°C), and ductility (5°C) were tested according to experiment specifications. Each experiment was performed three times, and the average was calculated as the final result.

Gel Permeation Chromatography (GPC) Test

Emulsified asphalt consists of components with various molecular weights, that significantly influence the properties of asphalt. In this study, the GPC test was performed to analyze the molecular weight distribution and to investigate the impact on properties. Tetrahydrofuran (THF) was selected as the solvent to dissolve the 20 mg emulsified asphalt sample. A combination of three columns was used for separating components with various molecular weights. The solution passed through the columns at a flow rate of 1 mL/min.

RESULTS AND DISCUSSION

Storage Stability and Properties

Experiment results of modified emulsified asphalt with 0.1 wt% CNFs are exhibited in **Table 4**.

Negative influence on stability is introduced by CNFs: the sample of 0.1 C presents unqualified stability that is much more than the specification requirements (<1%). However, NH_4Cl significantly improves storage stability. After adding the stabilizer, the CNFs modified emulsified asphalt exhibits excellent stability (less than 1%). The ability of group 0.1C1N1S is almost the same as group 0.1C3N1S, which indicates that the 1.0wt% stabilizer is economical. It can be thus be concluded that SBR seldomly impacts stability.

Compared to the control group, the addition of CNF improves the high-temperature properties of the residue by an increase in the softening point and rotational viscosity and a decrease in penetration. Nevertheless, on the other hand, CNFs also worsen performance under low temperatures. There is no ductility value for groups 0.1C, 0.1C1N, and 0.1C3N because specimens fractured immediately under tension at 5°C. This undesirable impact can be changed by SBR; samples with SBR show significantly higher ductility, which presents better low-temperature performance. Further, SBR also slightly improves high-temperature properties.

TABLE 4 | Properties and storage stability of modified emulsified asphalt (0.1 wt% CNFs).

ID	Properties				Storage stability (%)
	Penetration/ 0.1mm	Softening point/°C	Rotational Viscosity/ Pa·s	Ductility/ cm	
Control	65	47.5	0.48	5.0	0.5
0.1C	57	50.0	0.51	–	3.2
0.1C1N	56	50.5	0.50	–	0.6
0.1C3N	57	50.0	0.52	–	0.5
0.1C1N1S	52	52	0.55	9.5	0.6
0.1C3N1S	51	51.5	0.55	9.9	0.5

Effect of CNFs Content

To investigate the effect of CNFs content on the properties of the residue, samples with 0.3, 0.5, and 1.0wt% CNFs underwent the same experiments. The results are shown in **Figure 6**.

It can be seen from **Figure 6** that with the increase of CNFs percentages from 0 to 0.5wt%, the penetration of residual asphalt decreased remarkably, while the softening point and rotational viscosity increased, which indicates an improvement in temperature performance. However, a further increase of CNFs percentages (to 1.0wt%) induces a higher penetration value, lower softening point, and lower rotational viscosity than those of 0.5wt%. Compared to the control group, the residue asphalt with 0.5wt% CNFs exhibits the best high-temperature performance, with penetration decreasing by 22.4%,

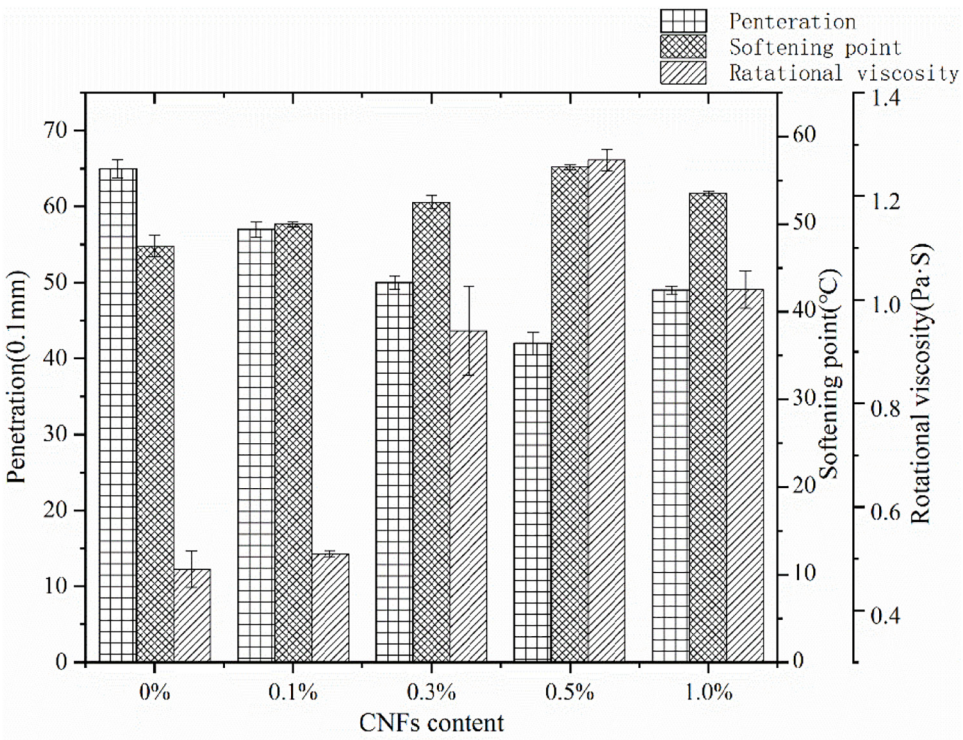

FIGURE 6 | Penetration, softening point and rotational viscosity with various CNFs percentages.

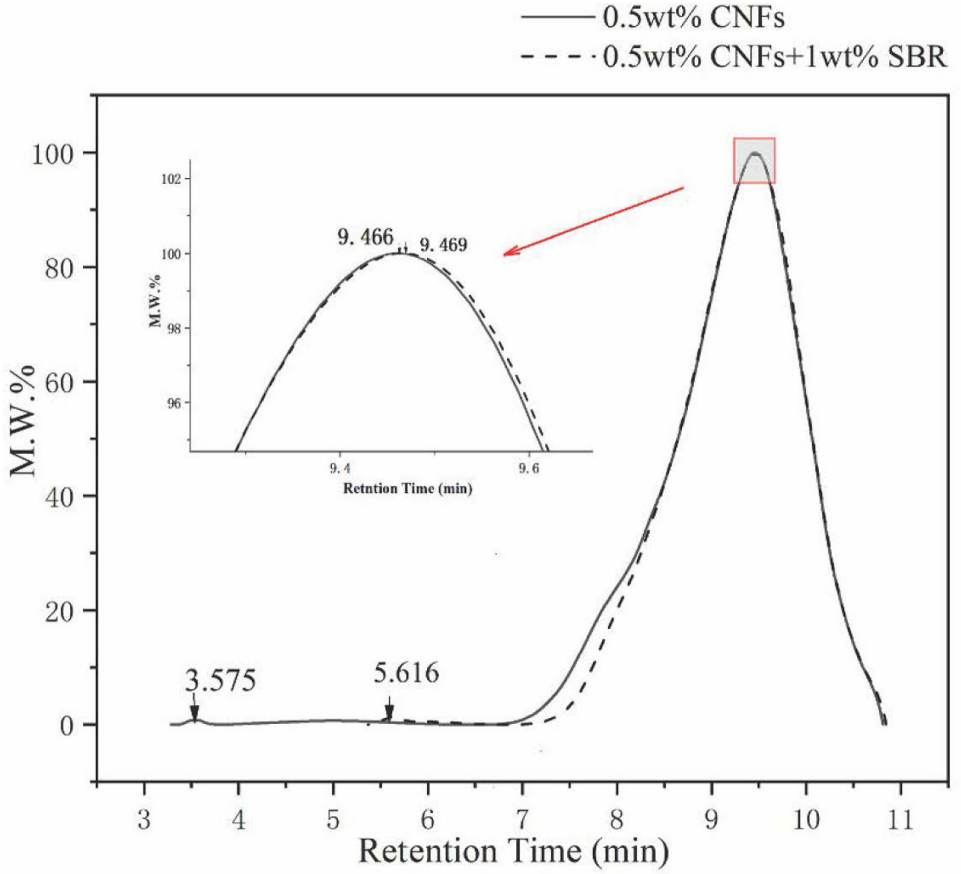

FIGURE 7 | GPC original results of modified emulsified asphalt.

the softening point increasing by 18.9%, and the rotational viscosity increasing by 164.6%.

This phenomenon may be explained by the network of CNFs. Individual CNF interconnects to form a micro-network to improve high-temperature properties. More CNFs facilitate and strengthen the network structure, which stiffens the asphalt and results in better high-temperature performance. However, excessive CNFs may interfere with network formation, and the high-temperature properties worsen to some extent.

GPC Results and the Effect of SBR

Gel permeation chromatography results of the emulsified asphalt with 0.5wt% CNFs were selected to analyze the particle size distribution and the effect of SBR. **Figure 7** shows the initial results of GPC, and relevant data are presented in **Table 5**.

In the GPC test, smaller molecules stay in columns for longer, so the peak appears later. **Figure 7** shows that before adding SBR, two peaks appear at the time of 3.575 and 9.466 min, respectively. The addition of SBR causes two peaks to shift to the right, appearing at 5.616 and 9.469 min, which indicates the proportion of smaller molecule increases.

Table 5 exhibits three primary data from GPC: Mn and Mw are average molecular weight in terms of number and weight statistics, respectively, and their ratio Mw/Mn presents the distribution width of molecules. The addition of SBR reduces Mn and Mw significantly, which means an increase in the proportion of small molecules. Moreover, the Mw/Mn value of the sample with SBR is far less than that without SBR, meaning a more concentrated distribution. It can be concluded that after adding SBR to the emulsified asphalt, more molecules are small molecules that distribute in a smaller range.

This conclusion is consistent with the results of ductility and storage stability. More small and flexible molecules enhance the elasticity of the residue asphalt, so the ductility under low temperature increases. Since smaller molecules settle more slowly, the stability is thus improved. On the other hand, even though SBR enhances the performance at a

TABLE 5 | GPC data of samples with and without SBR.

Data	0.5 wt% CNF	0.5 wt% CNFs + 1 wt% SBR
Number Average Molecular Weight (Mn)	730	698
Weight Average Molecular Weight (Mw)	15469	2833
Mw/Mn	21.18	4.06

low temperature, it seldomly influences the high temperature properties like penetration and the softening point, because the high temperature performance strongly depends on the network of CNFs but the SBR fail to interfere with the network.

CONCLUSION

A method to produce CNFs modified emulsified asphalt with NH_4Cl and SBR was proposed based on ultrasonication. The performance of CNFs modified emulsified asphalt was then evaluated. A GPC test was performed to investigate the effect of SBR on molecule distribution. The following conclusions were obtained:

(1) A combination of ultrasonication and surfactant is effective to disperse CNFs. To achieve uniform dispersion, the optimum weight ratio of surfactant to CNFs is 1:5, and the optimum energy density is 5000KJ/L.
(2) A method to produce CNF modified emulsified asphalt was proposed by dispersing CNFs in water with surfactant and ultrasonication in advance. The emulsifier was then dissolved into the suspension. Hot asphalt and emulsion were mixed in a colloidal mill to produce modified emulsified asphalt.
(3) Storage stability of CNF modified emulsified asphalt cannot meet the requirements, but the addition of NH_4Cl improves storage stability effectively, and SBR will not influence the stability.
(4) The addition of CNFs increases the high-temperature performance and decreases the low-temperature properties of the residue. Residue with a CNFs percentage of 0.5 wt% exhibit the best high temperature performance (penetration decreased by 22.4%, softening point increased by 18.9%, and rotational viscosity increased by 164.6%).
(5) GPC results indicate that SBR improves low-temperature ductility of residue asphalt significantly by increasing the proportion of small molecules.

DATA AVAILABILITY STATEMENT

All datasets generated for this study are included in the article/supplementary material.

AUTHOR CONTRIBUTIONS

JF, FL, and XZ conceived the presented study idea. XL and YA performed the experiments and collected the data. XL wrote the manuscript with support from FL. All authors discussed the results and contributed to the final manuscript.

FUNDING

This study was supported by the National Key R&D Program of China (2018YFB1600100), the National Natural Science Foundation of China (Nos. 51622805 and 51978029), and the Shandong Provincial Department of Transportation (No. 2018BZ4).

REFERENCES

Chen, J., Hamon, M. A., Hu, H., Chen, Y., Rao, A. M., Eklund, P. C., et al. (1998). Solution Properties of Single-Walled Carbon Nanotubes. *Science* 282:95. doi: 10.1126/science.282.5386.95

Cui, H. Z., Yan, X. T., Monasterio, M., and Xing, F. (2017). Effects of Various Surfactants on the Dispersion of MWCNTs-OH in Aqueous Solution. *Nanomaterials* 7:14. doi: 10.3390/nano7090262

Galao, O., Baeza, F. J., Zornoza, E., and Garcés, P. (2014). Strain and damage sensing properties on multifunctional cement composites with CNF admixture. *Cement Concrete Composites* 46, 90–98. doi: 10.1016/j.cemconcomp.2013.11.009

Gdoutos, E. E., Konsta-Gdoutos, M. S., Danoglidis, P. A., and Shah, S. P. (2016). Advanced cement based nanocomposites reinforced with MWCNTs and CNFs. *Front. Struct. Civil Eng.* 10:142–149. doi: 10.1007/s11709-016-0342-1

Goh, S. W., Akin, M., You, Z. P., and Shi, X. M. (2011). Effect of deicing solutions on the tensile strength of micro- or nano-modified asphalt mixture. *Construct. Build. Mater.* 25, 195–200. doi: 10.1016/j.conbuildmat.2010.06.038

Grossiord, N., Regev, O., Loos, J., Meuldijk, J., and Koning, C. E. (2005). Time-dependent study of the exfoliation process of carbon nanotubes in aqueous dispersions by using UV-visible spectroscopy. *Anal. Chem.* 77, 5135–5139. doi: 10.1021/ac050358j

Khattak, M. J., Khattab, A., and Rizvi, H. R. (2013a). Characterization of carbon nano-fiber modified hot mix asphalt mixtures. *Construct. Build. Mater.* 40, 738–745. doi: 10.1016/j.conbuildmat.2012.11.034

Khattak, M. J., Khattab, A., Zhang, P. F., Rizvi, H. R., and Pesacreta, T. (2013b). Microstructure and fracture morphology of carbon nano-fiber modified asphalt and hot mix asphalt mixtures. *Mater. Struc.* 46, 2045–2057. doi: 10.1617/s11527-013-0035-33

Khattak, M. J., Khattab, A., Rizvi, H. R., and Zhang, P. F. (2012). The impact of carbon nano-fiber modification on asphalt binder rheology. *Construct. Build. Mater.* 30, 257–264. doi: 10.1016/j.conbuildmat.2011.12.022

Konsta-Gdoutos, M. S., and Aza, C. A. (2014). Self sensing carbon nanotube (CNT) and nanofiber (CNF) cementitious composites for real time damage assessment in smart structures. *Cement Concrete Compos.* 53, 162–169. doi: 10.1016/j.cemconcomp.2014.07.003

Konsta-Gdoutos, M. S., Batis, G., Danoglidis, P. A., Zacharopoulou, A. K., Zacharopoulou, E. K., Falara, M. G., et al. (2017). Effect of CNT and CNF loading and count on the corrosion resistance, conductivity and mechanical properties of nanomodified OPC mortars. *Construct. Build. Mater.* 147, 48–57. doi: 10.1016/j.conbuildmat.2017.04.112

Lawrence, J. G., Berhan, L. M., and Nadarajah, A. (2008). Elastic properties and morphology of individual carbon nanofibers. *Acs Nano* 2, 1230–1236. doi: 10.1021/nn7004427

Metaxa, Z. S., Konsta-Gdoutos, M. S., and Shah, S. P. (2013). Carbon nanofiber cementitious composites: effect of debulking procedure on dispersion and, reinforcing efficiency. *Cement Concrete Compos.* 36, 25–32. doi: 10.1016/j.cemconcomp.2012.10.009

Mordkovich, V. Z. (2003). Carbon nanofibers: a new ultrahigh-strength material for chemical technology. *Theor. Found. Chem. Eng.* 37, 429–438. doi: 10.1023/a:1026082323244

O'Connell, M. J., Bachilo, S. M., Huffman, C. B., Moore, V. C., Strano, M. S., Haroz, E. H., et al. (2002). Band gap fluorescence from individual single-walled carbon nanotubes. *Science* 297, 593–596. doi: 10.1126/science.1072631

Ouyang, J., Yang, W., Chen, J., and Han, B. (2020). Effect of Superplasticizer and Wetting Agent on Pavement Properties of Cold Recycled Mixture with Bitumen Emulsion and Cement*. 32, 04020136. doi: 10.1061/(ASCE)MT.1943-5533.0003194

Ouyang, J., Zhao, J., and Tan, Y. (2018). Modeling Mechanical Properties of Cement Asphalt Emulsion Mortar with Different Asphalt to Cement Ratios

and Temperatures*. 30, 04018263. doi: 10.1061/(ASCE)MT.1943-5533.0002480

Pacheco-Torgal, F., and Jalali, S. (2011). Nanotechnology: advantages and drawbacks in the field of construction and building materials. *Construct. Build. Mater.* 25, 582–590. doi: 10.1016/j.conbuildmat.2010.07.009

Saito, R., Fujita, M., Dresselhaus, G., and Dresselhaus, M. S. (1992). Electronic structure of chiral graphene tubules. *Appl. Phys. Lett.* 60, 2204–2206. doi: 10.1063/1.107080

Strano, M. S., Moore, V. C., Miller, M. K., Allen, M. J., Haroz, E. H., Kittrell, C., et al. (2003). The role of surfactant adsorption during ultrasonication in the dispersion of single-walled carbon nanotubes. *J. Nanosci. Nanotechnol.* 3, 81–86. doi: 10.1166/jnn.2003.194

Yazdanbakhsh, A., Grasley, Z., Tyson, B., and Al-Rub, R. K. A. (2009). Carbon nano filaments in cementitious materials: some issues on dispersion and interfacial bond*. *Spec. Publ.* 267, 21–34. doi: 10.14359/51663280

Yazdanbakhsh, A., Grasley, Z., Tyson, B., and Abu Al-Rub, R. K. (2010). Distribution of carbon nanofibers and nanotubes in cementitious composites. *Trans. Res. Rec.* 89–95. doi: 10.3141/2142-13

Yu, J. R., Grossiord, N., Koning, C. E., and Loos, J. (2007). Controlling the dispersion of multi-wall carbon nanotubes in aqueous surfactant solution. *Carbon* 45, 618–623. doi: 10.1016/j.carbon.2006.10.010

Zhu, X. Y., Gao, Y., Dai, Z. W., Corr, D. J., and Shah, S. P. (2018). Effect of interfacial transition zone on the Young's modulus of carbon nanofiber reinforced cement concrete. *Cement Concrete Res.* 107, 49–63. doi: 10.1016/j.cemconres.2018.02.014

Conflict of Interest: The authors declare that the research was conducted in the absence of any commercial or financial relationships that could be construed as a potential conflict of interest.

frontiers in Materials

ORIGINAL RESEARCH
published: 14 August 2020
doi: 10.3389/fmats.2020.00182

A New Method of Mix Design for Cold Patching Asphalt Mixture

Songtao Lv, Shuangshuang Wang, Chengdong Xia and Chaochao Liu*

National Engineering Laboratory of Highway Maintenance Technology, Changsha University of Science & Technology, Changsha, China

The objective of this research was to improve the scientificity of the design method of the cold patching asphalt mixture (CPAM). Firstly, the curing temperature for CPAM was optimized. In addition, based on the traditional Marshall mix design method, the volume parameters of CPAM were converted, and the low-temperature workability index was added. This is the modified Marshall mix design method to determine the optimal asphalt aggregate ratio of CPAM. Then, the initial strength, forming strength, storage stability, water stability, and high-temperature stability of CPAM were tested. The properties of CPAM designed by using the modified Marshall mix design method were compared with those of CPAM designed by using the traditional Marshall mix design method and the empirical formula method. The test results show that the optimal asphalt aggregate ratio of CPAM is 5.38%. The recommended oven curing temperature for the CPAM specimen is 90°C. The initial strength and forming strength of CPAM meet the requirements, and the forming strength can reach about twice the initial strength. The stability of CPAM increases with an increase in storage time. High-temperature performance is good. These properties of CPAM designed by using the modified Marshall mix design method were all superior to those of the CPAM designed by using the traditional Marshall mix design method and the empirical formula method, and the water stability is similar to that of the CPAM designed by the traditional Marshall mix design method. The CPAM designed by using the modified Marshall mix design method shows better road performance, which shows that the modified procedure in this study is feasible and can be recommended as the mix design method for CPAM.

Keywords: Cold patching asphalt mixture, mix design, modified marshall mix design method, volume parameters, low-temperature workability, road performance

OPEN ACCESS

Edited by:
Yiqiu Tan,
Harbin Institute of Technology, China

Reviewed by:
Tao Ma,
Southeast University, China
Gilda Ferrotti,
Marche Polytechnic University, Italy
Haryati Yaacob,
University of Technology Malaysia, Malaysia
Ahmad Kamil Arshad,
MARA University of Technology, Malaysia

****Correspondence:***
Shuangshuang Wang
13142164380@163.com

Specialty section:
This article was submitted to Structural Materials, a section of the journal Frontiers in Materials

Received: *29 February 2020*
Accepted: *18 May 2020*
Published: *14 August 2020*

Citation:
Lv S, Wang S, Xia C and Liu C (2020) A New Method of Mix Design for Cold Patching Asphalt Mixture. Front. Mater. 7:182. doi: 10.3389/fmats.2020.00182

INTRODUCTION

Hot mix asphalt is widely used in road paving and repair because of its excellent performance as pavement (Yang et al., 2011). However, in the process of mixing, transportation, and placement of hot mix asphalt, the temperature required and its control are relatively high and strict, respectively (Li et al., 2017). High temperature causes not only great energy consumption but also severe environmental pollution (Diaz, 2016). Poor temperature control will cause aging of the asphalt mixture, which affects its fatigue performance and service life (Khan et al., 2016; Liu et al., 2020). Hot mix asphalt mixture cannot be produced at low temperature and in rainy weather. The damage to pavement in winter can only be repaired after April of the next year, which not only aggravates the damage to the road but also affects its comfort and safety (Ling et al., 2007). In view of these

problems, cold patching asphalt mixture (CPAM) is very popular in pavement repair due to its excellent characteristics such as environmentally friendliness, low energy cost, convenient placement procedure, and sustainability and the fact that is is almost always ready to be used.

At present, there are many kinds of CPAM on the market. According to the type of solution, they can be divided into three types: solvent type, emulsion type, and reaction type (Doyle et al., 2013). In the existing research on CPAM at home and abroad, the main focus is on performance improvement. Approaches include designing moisture-resistant CPAM, high-strength CPAM, and crack-resistant CPAM. Bentonite (a kind of nano clay with strong water absorption) or microbial carbonate precipitation (MCP) has been added to CPAM with the objective of improving its capacity for moisture resistance. Moreover, these additives enhance the dehumidification and water damage prevention characteristics related to CPAM (Ling et al., 2016; Dong et al., 2018; Alenezi et al., 2019; Attaran Dovom et al., 2019). Besides, the use of cementing material instead of the emulsion can achieve the same effect. Generally, cement is added to CPAM when high strength is needed from this asphalt mixture (Shanbara et al., 2018). Fiber is added to CPAM with the goal of enhancing its tensile modulus significantly (Gómez-Meijide and Pérez, 2014). The improvement of tensile properties plays a vital role in slowing down crack growth in asphalt mixture, and permanent deformation is also significantly reduced. Cold patching asphalt mixture has been widely used in actual pavement repair and has achieved some results (Guo et al., 2014; Ma et al., 2016). However, research related to CPAM is not as mature as that associated with hot patching asphalt mixture. The early performance of CPAM is worse than that of hot patching asphalt mixture. The mechanical properties of the mixture are greatly affected by the mixing sequence and the interface formed. The stability of the aggregate skeleton and the bond strength between aggregate and binder are positively related to the rutting resistance (Ma et al., 2018; Zhang et al., 2019; Chen et al., 2020). There is not an mature method for designing a set of mix proportions for CPAM (Song et al., 2014; Saadoon et al., 2017). At present, the majority of research has used the mix proportion design method of hot mix asphalt mixture (Marshall mix design method) to design CPAM (Li et al., 2010; Dash and Panda, 2018). Additionally, the empirical formula methods of California and Tongji University are also used to calculate the amount of cold asphalt binder (Song and Lv, 1998). Cold patching asphalt mixture is different from hot mix asphalt mixture, as it need not be heated during construction. The Marshall mix design method is not suitable for designing CPAM, and the parameters of Marshall mix design (stability and flow value) have a weak correlation with the road performance of CPAM (Xu et al., 2018). The empirical formula method is greatly influenced by gradation and local climate, and the design method lacks volume index control, so the durability of the mixture is difficult to guarantee (Meng et al., 2011).

Based on the characteristics of CPAM, the Marshall mix design method was modified in this study. The road performance of three kinds of CPAM designed by using the modified Marshall mix design method, the Marshall mix design method, and the empirical formula method were tested. The comparative analysis verified the usefulness of the modified Marshall mix design method, which provides a reference for designing CPAMs.

MATERIALS AND METHODS

Raw Materials

The research object of this study is the solvent used in CPAM, which is composed of neat asphalt or modified asphalt, diluent, additive, and aggregate.

Neat Asphalt

The neat asphalt used in this research is Sinopec Donghai 70PG# road petroleum asphalt; its main technical characteristics were obtained, and the results are shown in **Table 1**.

Diluent

The diluent can reduce the viscosity of asphalt so that CPAM has good workability under low temperature. The diluent should have good solubility in asphalt. Considering safety, volatility, and economy, the diluent used in this study was diesel oil.

Additive

The cold patching additives are generally patented by the manufacturer. In this research, the additive PR-JW03A was optimized. PR-JW03A was produced by Shenzhen Jiashengwei Chemical Technology Co., Ltd. This additive is a special polymer chemical product composed of a variety of polymers that can improve the properties of asphalt when added to ordinary road asphalt. Its technical indicators are shown in **Table 2**.

TABLE 1 | Test results of technical indices of base asphalt.

Index	Specification requirements	Test result	Test method
Penetration (25°C)/(0.1 mm)	60–80	71	T0604
Penetration index PI	−1.5 to +1.0	−1.16	T0604
15°C ductility (cm)	≥100	>150	T0605
Softening point (°C)	≥46	47.6	T0606
25°C density (g/cm^3)	–	1.026	T0603
60° Dynamic viscosity (Pa s)	≥180	196	T0619
Flash point (°C)	200	319	T0611
Solubility (Trichloroethylene) (%)	≥99.5	99.89	T0607
Wax content (%)	2.2	1.6	T0615

TABLE 2 | Technical indices of PR-JW03A cold patching asphalt additive.

Number	Testing items	Unit	Detection result
1	Density	g/cm^3	1.05
2	Viscosity of prepared liquid asphalt (60°C)	60°C/CST	250–1600
3	Phase state	–	Liquid
4	Color	–	Black and blue
5	Flash point	°C	>230

Coarse Aggregate

The coarse aggregate plays an important supporting role in the mixture skeleton and is the main part of the pavement bearing load. Limestone was used as a coarse aggregate in this study. According to the requirements of the specification, the relevant technical indices of the coarse aggregate were obtained; the test results are shown in **Table 3**.

Fine Aggregate

The fine aggregate fills the gaps formed by the coarse aggregate to achieve a dense skeleton structure, improving the durability of the pavement. The fine aggregate used in this research was limestone.

Mineral Filler

The mineral filler can not only fill the gap between aggregates but also improves the water stability of CPAM. Furthermore, the addition of mineral filler increases the proportion of structural asphalt, which enhances the strength of CPAM. In this study, the selected mineral filler was obtained by grinding limestone, and its main properties met the specification requirements, as shown in **Table 4**.

Preparation of Cold Patching Asphalt

The main instrument used in the preparation of cold patching asphalt is a high-speed disperser, with a speed range equal to 0–10,000 r/min. The electric furnace, thermometer, oven, electronic scale, and other auxiliary tools were also utilized.

The best ratio for cold patching asphalt finally determined in this research was additive:asphalt:diluent = 1.8:100:25. The preparation steps were as follows.

1) Heat the neat asphalt in an oven at 135°C for 2 h, then take it out and heat it in an electric furnace to maintain the temperature around 135°C.
2) Add the additive into (1), start the disperser, rotate at 200 r/min, and mix for half an hour.
3) Add diesel oil into (2), control the temperature at about 110°C, and mix for 30 min.
4) The preparation is completed.

TABLE 3 | Mechanical index of coarse aggregate.

Mechanical index	Crushed stone value (%)	Polished stone value (BPN)	Weared stone value (%)
Limestone	14.9	56.2	21.8

TABLE 4 | Mineral powder test results.

Project	Unit	Test result	Specification requirements
Apparent specific gravity	g/cm^3	2.727	≥2.50
Water content	%	0.42	≤1
Plasticity index	–	3	<4
Hydrophilic coefficient	–	0.6	<1
Appearance	–	No agglomeration	No agglomeration

The preparation of cold patching asphalt and the principle involved are shown in **Figure 1**.

MIX DESIGN OF CPAM

The Marshall mix design method was used to obtain the proportion of each element that composes hot mix asphalt mixture. By utilizing this method, researchers have accumulated a rich body of practical experience and data. Cold patching asphalt mixture should not only have good road performance in the later stage but also have excellent low-temperature workability. Based on the Marshall mix design method, the Marshall test indices of CPAM were tested. In addition, given the performance requirements of CPAM, the low-temperature workability index was considered. The volume parameters of the finished specimen were converted into those related to the initial specimen. According to the relationship between each index and the asphalt aggregate ratio, the best asphalt aggregate ratio of CPAM was determined.

Gradation

Generally, the ratio of pavement disease depth h and the maximum size D of aggregate is used to determine the nominal maximum aggregate size of CPAM. Usually, it is considered that h/D should be greater than or equal to 2. The thickness of the upper layer of asphalt pavement is designed as 4 cm, and the nominal maximum grain size of the top layer is generally 13.2 mm. Considering the interface characteristics of the new and old mixture, and according to the calculation of h/D, the nominal maximum aggregate size was determined to be 13.2 mm.

According to the *Technical Specifications for Construction of Highway Asphalt Pavements* (JTG F40–2004, 2004), LB-13 gradation was adopted in this study. The grading is shown in **Table 5**.

Marshall Specimen Preparation

In this research, the second compaction method was used to form the specimen. This involves first compacting both sides 50 times. The specimen is then put in a test mold in the oven at a certain temperature for 24 h, standing on its side. After taking the sample out from the oven, both sides are compacted 25 times immediately, and it is demolded. The height of the specimen is measured by using a vernier caliper and should meet the criterion 63.5 ± 1.3 mm. According to the *Technical Specifications for Construction of Highway Asphalt Pavements* (JTG F40–2004, 2004), the initial curing temperature of the specimen in this research was equal to 110°C, but it was found that the specimen was loose and peeled after curing. This fact shows that the curing temperature of 110°C was too high, and it was not suitable for solvent-type CPAM. Therefore, considering the volatilization rate of diluent inside the specimen, and the integrity of the specimen, four different curing temperatures were preliminary selected: 60, 75, 90, and 100°C. After curing, the Marshall stability of the specimen was obtained, and the results are shown in **Figure 2**.

As can be seen from **Figure 2**, the stability increases with the increase in temperature. The value rapidly increases from 60 to

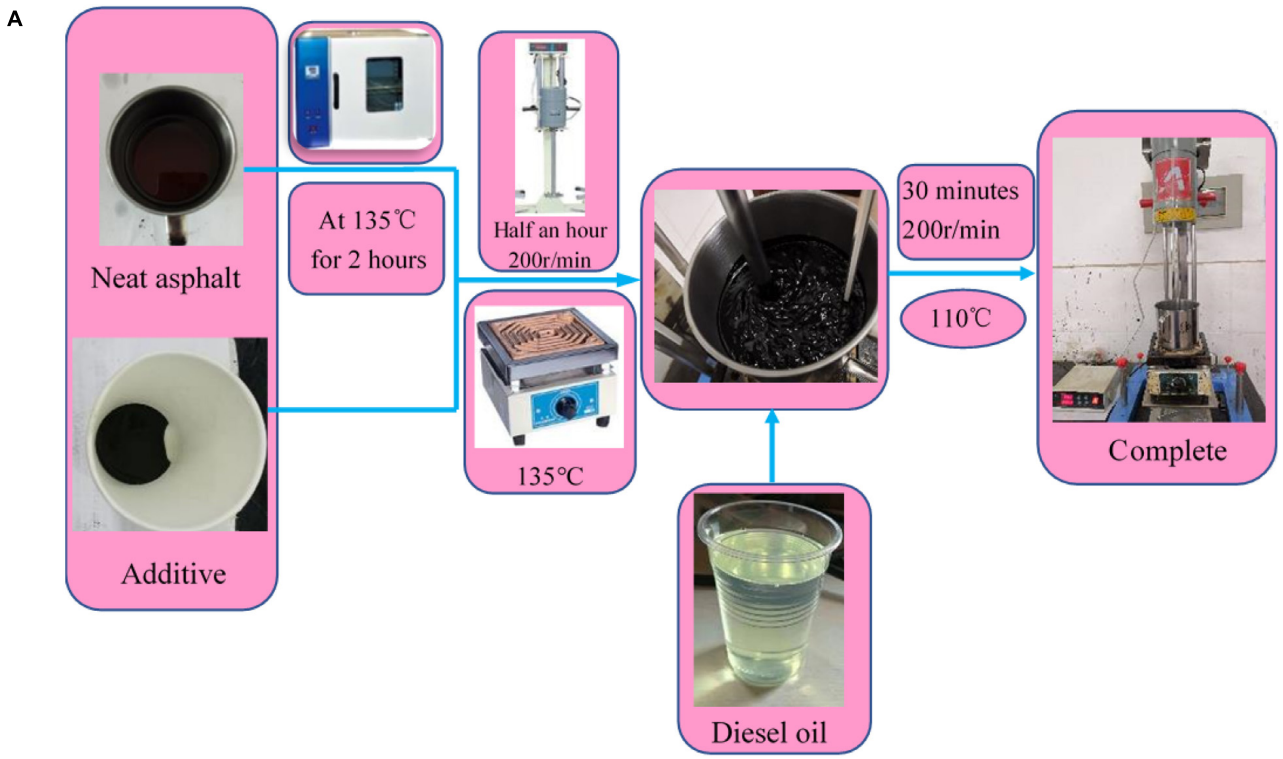

FIGURE 1 | Preparation of cold patching asphalt by disperser and the principle involved. **(A)** Flow chart of cold patching asphalt preparation. **(B)** Principle of cold patching asphalt preparation.

90°C and then slowly increases from 90 to 100°C. According to the *Technical Specifications for Construction of Highway Asphalt Pavements* (JTG F40–2004, 2004), the Marshall stability of CPAM should not be less than 3 kN, and the specimen can meet this requirement when the curing temperature is above 90°C. Considering the Marshall stability growth rate with temperature,

TABLE 5 | LB-13 gradation.

Gradation	The percentage (%) of mass passing through each sieve (mm)									
	16	13.2	9.5	4.75	2.36	1.18	0.6	0.3	0.15	0.075
Upper limit of gradation	100	100	95	60	40	20	15	12	8	5
Lower limit of gradation	100	90	60	30	10	5	0	0	0	0
Gradation median	100	95	77.5	45	25	12.5	7.5	6	4	2.5
Synthetic gradation	100	96	79	49	25	14	8	5	4	3

the integrity of the test piece, and the economic and energy-cost factors, the final curing temperature adopted in this study was equal to 90°C.

Determination of Asphalt Aggregate Ratio

According to the volatilization level of diluent in CPAM, the forming stage of CPAM can be divided into two states: the initially and finally formed states. The diluent inside the CPAM in the finally formed state has basically evaporated. However, the diluent in CPAM in the initially formed state has not yet begun to volatilize, so the CPAM in this state can be regarded as a typical hot mix. With the gradual volatilization of diluent, the volume parameters of the CPAM in the finally formed state can be obtained by using all of the volume parameters of the initially formed specimen. Therefore, the optimal binder content of CPAM can not only be determined according to the parameters of the final formed specimen. The volume parameter that should be used is that of the initially formed specimen, which can be regarded as an ordinary hot mix (Gu, 2017).

The most obvious characteristic of CPAM is that it can be elaborated under normal and low-temperature conditions. Therefore, the CPAM is required to be loose at low temperature, which is convenient for spreading and compaction. In this research, low temperature and workability indices were considered in the process of mix design.

Volume Parameter Conversion

All of the measured volume parameters of the finally formed specimen were converted into the volume parameters of the initially formed specimen. Before compacting, the quality m_p of the mixture in each test mold was recorded.

The bulk specific gravityr_{pf} of the initially formed specimen was calculated according to formula (1),

$$r_{pf} = \frac{m_p}{m_f - m_w} \tag{1}$$

where m_f and m_w are the surface dry mass of the specimen and the water mass of the specimen, respectively, g.

The theoretical maximum specific gravity r_{pt} of the initially formed specimen was calculated according to formula (2),

$$r_{pt} = \frac{r_t(m_a - m_w) + (m_p - m_a)}{(m_a - m_w) + (m_p - m_a)} = \frac{r_t(m_a - m_w) + (m_p - m_a)}{(m_p - m_w)} \tag{2}$$

where m_a is the air mass of the specimen, g and r_t is theoretical maximum specific gravity.

According to formulas (3)–(5), the percentage of voids in mineral aggregate*pvma*, percent air voids *pvv*, and percent voids in mineral aggregate filled with asphalt *pvfa* are calculated,

$$pvma = \left(1 - \frac{r_{pf}}{r_{sb}} \times p_s\right) \times 100 \tag{3}$$

$$pvv = \left(1 - \frac{r_{pf}}{r_{pt}}\right) \times 100 \tag{4}$$

$$pvfa = \frac{pvma - pvv}{pvma} \times 100 \tag{5}$$

where r_{sb} is synthetic bulk density, g/cm^3 and p_s is proportion of mineral aggregate quality to total asphalt mixture quality,%.

The volume parameters of the initially formed specimen are obtained based on the above formula. The relationship between each volume parameter and the asphalt aggregate ratio was obtained. According to the determination method of the optimal asphalt aggregate ratio of hot mix asphalt mixture, the optimal asphalt aggregate ratio of CPAM was determined.

Determination of the Optimal Asphalt Aggregate Ratio

The Marshall test results of the finished formed specimens are shown in **Table 6**.

Keeping the stability unchanged, the volume parameters of the final formed specimen were converted into the volume parameters of the initially formed specimen. The calculation results are shown in **Table 7**.

Figure 3 shows the relationship between the asphalt aggregate ratio and each index of the initially formed specimen.

To sum up, the asphalt aggregate ratio a_1, a_2,a_3, a_4 corresponding to the maximum stability, the maximumr_{pf}, the

TABLE 6 | Test results of volume parameters and mechanical indices of finished formed specimens.

Asphalt aggregate ratio (%)	r_f (g/cm^3)	VMA (%)	VV (%)	VFA (%)	Stability (KN)
4.0	2.225	21.9	15.1	31.7	4.21
4.5	2.248	21.3	13.5	36.7	4.24
5.0	2.273	20.1	11.5	42.5	4.26
5.5	2.260	22.0	13.1	45.3	4.02
6.0	2.265	21.6	10.6	47.6	3.98

TABLE 7 | Volume parameters and mechanical index results of initially formed specimens.

Asphalt aggregate ratio (%)	r_{pf} (g/cm^3)	*pvma* (%)	*pvv* (%)	*pvfa* (%)	Stability (kN)
4.0	2.243	21.3	13.4	38.4	4.21
4.5	2.255	21.0	12.8	39.4	4.24
5.0	2.258	20.7	12.4	39.9	4.26
5.5	2.291	20.9	8.6	57.2	4.02
6.0	2.269	21.4	7.1	59.4	3.98

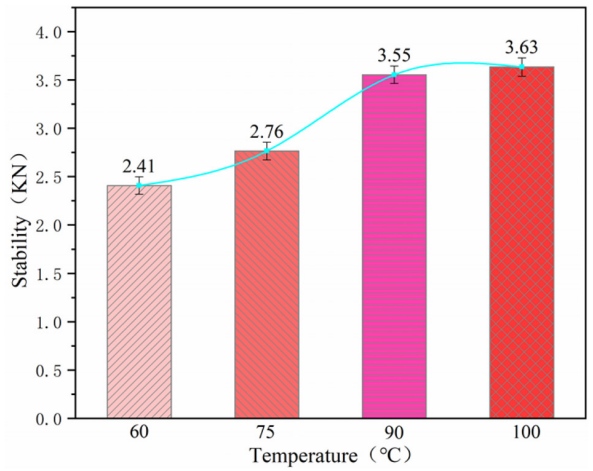

FIGURE 2 | Stability of CPAM under different curing temperatures.

median design range of*pvv*, and the median range of *pvfa* were determined from **Figure 3**. According to formula (6), the average value of the four asphalt aggregate ratios is the initial value OAC_1 of the optimal asphalt aggregate ratio.

$$OAC_1 = (a_1 + a_2 + a_3 + a_4)/4 = (5.56\% + 5.65\% + 5.43\% + 4.98\%)/4 = 5.405\% \quad (6)$$

On the basis of the test results of each index, the range of asphalt content that meets the technical standards was determined. According to the *Technical Specifications for Construction of Highway Asphalt Pavements* (JTG F40–2004, 2004), Marshall stability should be not less than 3 kN. *pvma* and *pvfa* refer to the Marshall test standard of hot mix asphalt mixture. Therefore, the asphalt aggregate ratio is required to be higher than 5.3% for *pvv*. The asphalt aggregate ratio needs to be higher than 5% for *pvfa*.

CPAM should have excellent workability at room temperature. Therefore, this research focuses on workability under low-temperature conditions. Cold patching asphalt mixture was prepared with variations of 0.2% in the asphalt aggregate ratio. According to the *Technical Specifications for Construction of Highway Asphalt Pavements* (JTG F40–2004, 2004), the CPAM was placed in a refrigerator at -10°C for 24 h. If the mixture has no obvious agglomeration phenomenon, it can be easily mixed with a shovel. Cold patching asphalt mixture was taken out from the refrigerator and showed good workability at low temperatures. The test results are shown in **Table 8**.

According to the test results shown in **Table 8**, the asphalt aggregate ratio should be 5.2–5.4% for low-temperature workability. The initial value of the optimal asphalt aggregate ratio OAC_2 was calculated from Eq. (7).

$$OAC_2 = (OAC_{\min} + OAC_{\max})/2 = (5.3\% + 5.4\%)/2 = 5.35\% \quad (7)$$

The optimal asphalt aggregate ratio of CPAM is calculated according to formula (8),

$$OAC = (OAC_1 + OAC_2)/2 = (5.405\% + 5.35\%)/2 = 5.38\% \quad (8)$$

The optimal asphalt aggregate ratio of CPAM obtained by using the modified Marshall mix design method was equal to 5.38%.

ROAD PERFORMANCE VERIFICATION

In this study, the optimal asphalt aggregate ratio of CPAM obtained by using the tradition Marshall mix design method was equal to 5.52%. In addition, the empirical formula proposed by LV Weimin of Tongji University was used to find the optimal asphalt aggregate ratio of CPAM. The calculation formula is as follows.

$$P = 0.021a + 0.056b + 0.099c + 0.12d + 1.2 \quad (9)$$

where P is the asphalt aggregate ratio,%, a is the mass percentage of aggregate with particle size greater than 2.36 mm,%, b is the mass percentage of aggregate with particle size between 0.3and 2.36 mm,%, c is the mass percentage of aggregate with particle size between 0.075and 0.3 mm,%, and d is the mass percentage of aggregate with particle size less than 0.075 mm,%.

According to Eq. (9), the asphalt aggregate ratio designed by using the empirical formula was equal to 4.5%.

In order to verify the usefulness of the modified Marshall mix design method proposed in this study, road performance tests of CPAM designed by the different methods were carried out. The test flow chart is shown in **Figure 4**.

Test Method

Initial Strength

In the early stage of CPAM, the diluent has not volatilized, and the cohesion among minerals is small. The initial strength is mainly supported by the intercalation and friction among aggregates (Nassar et al., 2016). In order to ensure that the pavement can resist the loose damage caused by the rolling of vehicles at the initial stage of repair, it should be ensured that the initial strength of CPAM reaches a specific value.

The test method of initial strength was as follows: take about 1100 g of CPAM (subject to the height of the specimen conforming to 63.5 ± 1.3 mm) and put it into a Marshall test mold. Compact the upper and lower sides respectively 75 times by using an automatic Marshall compactor. Stability can be tested after demolding.

Forming Strength

The method for testing the forming strength is as follows. Take 1100 g of CPAM (subject to the height of the specimen conforming to 63.5 ± 1.3 mm) and put it into a Marshall test mold. Compact the upper and lower sides respectively 75 times by using an automatic Marshall compactor. After that,

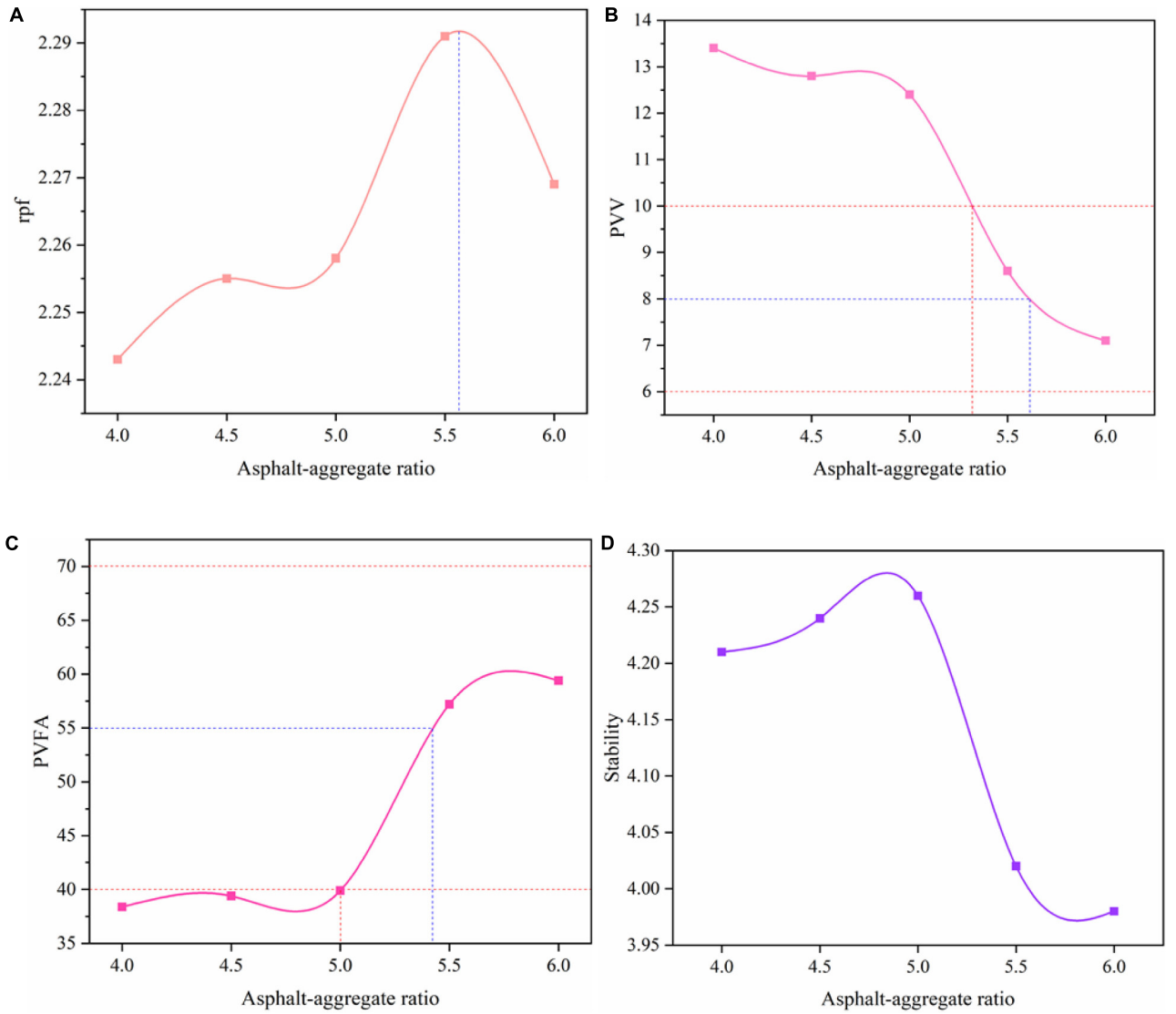

FIGURE 3 | (A) Relationship between asphalt aggregate ratio and rpf; **(B)** relationship between asphalt aggregate ratio and PVV; **(C)** relationship between asphalt aggregate ratio and PVFA; **(D)** relationship between asphalt aggregate ratio and stability.

the specimen with the test mold is kept in an oven at 90°C for 24 h, and then it is removed from the oven and compacted on both sides 25 times. A Marshall stability test is conducted after demolding.

Storage Stability

The CPAM can be divided into hot mix CPAM and cold mix CPAM according to mixing conditions. Hot mix CPAM can be stored for about two years (Dulaimi et al., 2017). During the storage process, it should be ensured that the CPAM does not experience a high degree of agglomeration to facilitate its placement and compaction during construction. In this research, the CPAM was stored and sealed for 0, 3, 7 and 28 days at normal temperature. The initial strength was then tested, and the method described above was used to judge the workability at 28 days.

Water Stability

The water stability of CPAM was evaluated by conducting an immersion Marshall test and freeze-thaw splitting test. The test should be carried out according to *Standard Test Methods of Bitumen and Bituminous Mixtures for Highway Engineering* (JTG E20–2011, 2011).

High-Temperature Performance

In this study, the Hamburg rutting test was used to evaluate the high-temperature performance of CPAM. According to the formation method of a hot mix asphalt rutting specimen, combined with the characteristics of CPAM, the formation of a rutting specimen was carried out as follows.

TABLE 8 | Test results of low-temperature workability of CPAM.

Mixture status classification	State description	Gradation	Asphalt aggregate ratio (%)
A	Most of the CPAM is agglomerated and cannot be mixed with a shovel.	5	6.0
B	There are numerous large agglomerations of CPAM that cannot be easily dispersed, and it is difficult to mix.	4	5.6,5.8
C	There are numerous small agglomerations of CPAM, but the agglomerations can be easily spread after beating.	3	5.2,5.4
D	There are small agglomerations of CPAM, and the particles can be loose when mixing with a shovel.	2	4.6,4.8,5.0
E	The CPAM has almost no agglomeration and is in a free state.	1	4.0,4.2,4.4

Take the CPAM and put it into the test mold and first conduct manual compaction. Then, roll down the CPAM two times in one direction and 12 times in the other direction using a hydraulic rutting machine. Put the CPAM with the test mold into an oven at 90°C for 24 h and then take it out and carry out a second rolling according to the first rolling method. The Hamburg rutting test should be carried out according to *Standard Test Methods of Bitumen and Bituminous Mixtures for Highway Engineering* (JTG E20–2011, 2011).

RESULTS AND DISCUSSION

Initial Strength

The initial strength of the three kinds of CPAM (empirical formula method design, Marshall mix design method, and modified Marshall mix design method) was tested. The test results are shown in **Figure 5**.

It can be seen from **Figure 5** that the CPAM with a 5.38% asphalt aggregate ratio has the largest initial strength. The initial strength of the 4.5% asphalt aggregate ratio is the lowest. This is because there is a small amount of binder and the strength of the mixture is mainly supported by the friction among the aggregates. There is no specificated requirement for the initial strength of CPAM. The United States and Song Jiansheng, China, require an initial strength greater than 2 kN. The initial strengths of CPAM with asphalt aggregate ratios of 5.38 and 5.52% are equal to 2.84 and 2.53 kN, respectively, which meet this requirement. The asphalt aggregate ratio obtained by the empirical formula method is too low, so that the initial strength is too low and fails to meet the requirement.

Forming Strength

The forming strengths of the three kinds of CPAMs were measured according to the test method in section"Forming Strength". In this section, the initial strength and the forming strength are compared; the results are shown in **Figure 6**.

The forming strength consists of cohesion and internal friction. It can be noticed from **Figure 6** that the forming strength of the three CPAMs is basically twice the initial strength. This fact is because the viscosity of the binder increases and the cohesion of CPAM increases as a result of diluent volatilization. The forming strength of CPAM with a 5.38% asphalt aggregate ratio achieves the highest value, which is equal to 6.13 kN. The forming strength of CPAM with a 4.5% asphalt aggregate ratio has the lowest value because the amount of binder is too small, and the cohesion is not sufficient. When the asphalt aggregate ratio is equal to 5.52%, the binder content of CPAM is too high, and there is a large amount of free asphalt. A larger or smaller asphalt aggregate ratio is not advantageous to the forming strength of CPAM. Compared with the other two methods, the forming strength of CPAM designed by using the modified Marshall mix design method formed faster.

Storage Stability

Three CPAMs were prepared by using the three different design methods. Then, the elaborated CPAM specimens were stored and sealed for a period of time, and afterward, their initial strength and workability were tested. The test results are shown in **Table 9**.

According to **Table 9**, the relationship between the initial strength and storage time of the three CPAM is consistent. The initial strength increases with an increase in storage time in all cases. After 28 days of storage, the strength of the three kinds of CPAM changes little; the variation is lower than 0.2 kN. The initial strength is relatively stable. The workability grade of CPAM designed by using the Marshall mix design method was equal to 4, meaning that its low-temperature workability was poor. The results show that the asphalt content of CPAM designed by using the Marshall mix design method is too high and it easily agglomerates. However, the low-temperature workability of CPAM designed by using the modified Marshall mix design method was acceptable.

Water Stability

The immersion Marshall test and freeze-thaw splitting test were carried out with the objective of testing the three kinds of CPAM with different asphalt aggregate ratios. The water damage resistance of CPAM with different asphalt aggregate ratios was studied and compared with that of hot asphalt mixture. The results of the immersion Marshall test are shown in **Figure 7**, and the results of the freeze-thaw split test are shown in **Figure 8**.

It can be seen from **Figure 7** that the residual stability of the CPAM specimens with asphalt aggregate ratios of 5.38 and 5.52% meets the requirements of the residual stability for hot asphalt mixture. The residual stability of the CPAM with a 4.5% asphalt aggregate ratio is low. This is due to the lack of binder and the large percentage of air voids. It can be noticed from **Figure 8** that the freeze-thaw splitting strength

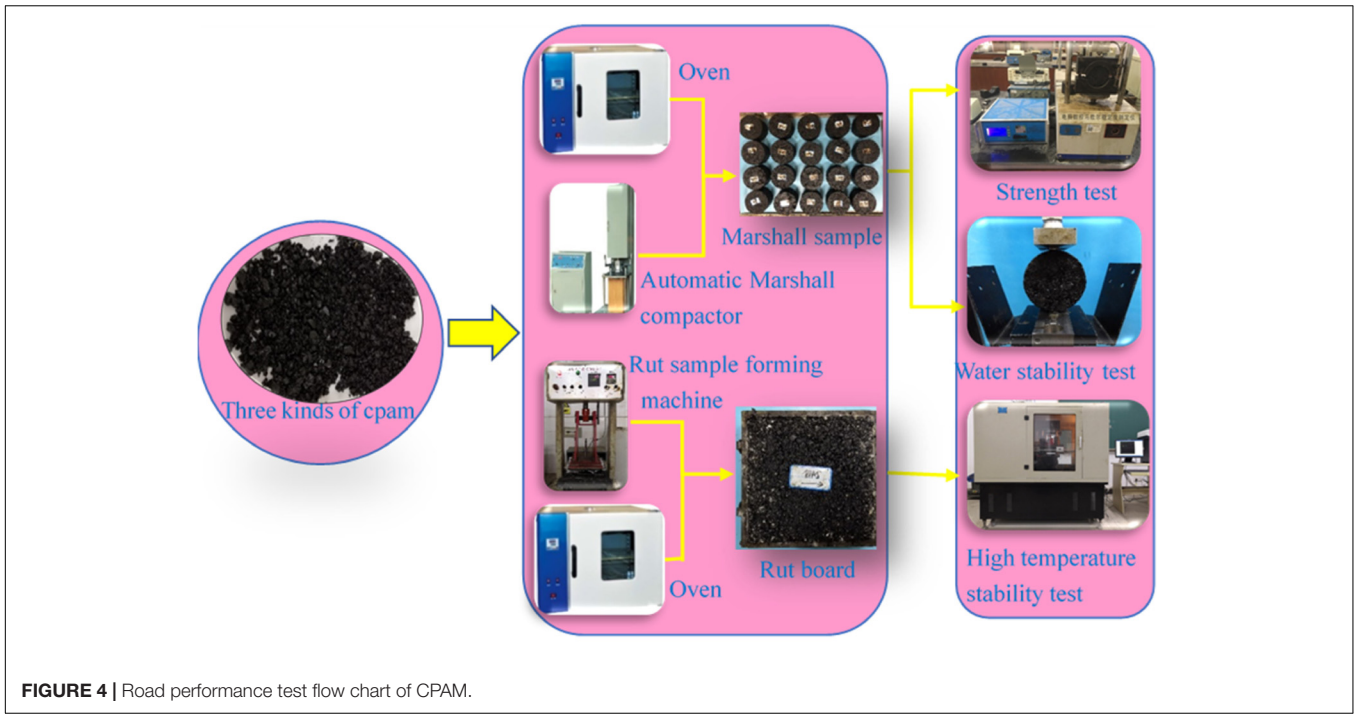

FIGURE 4 | Road performance test flow chart of CPAM.

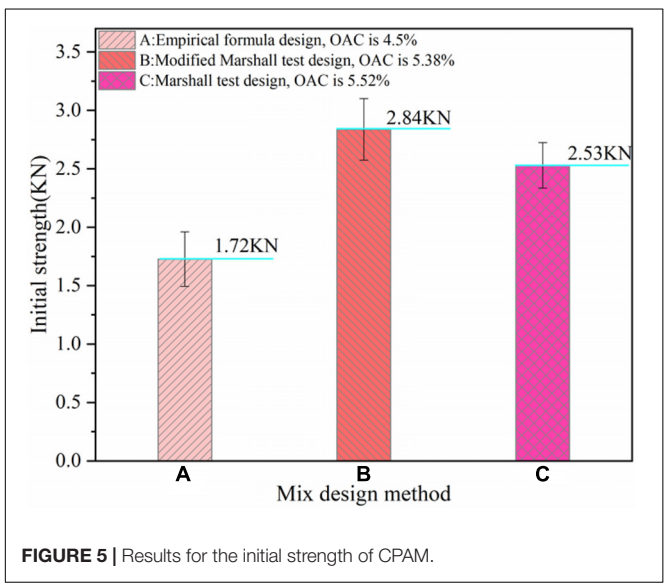

FIGURE 5 | Results for the initial strength of CPAM.

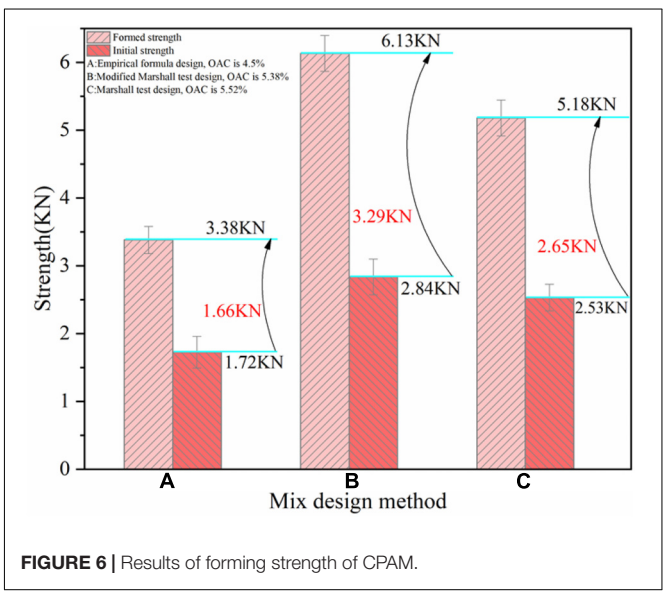

FIGURE 6 | Results of forming strength of CPAM.

ratio of the three CPAMs meets the requirements for hot asphalt mixture. The order of the freeze-thaw splitting strength ratios is as follows: 5.38% CPAM > 5.52% CPAM > 4.5% CPAM. This shows that CPAM designed by the modified Marshall mix design method has the best water stability. The residual stabilities and the freeze-thaw splitting strength ratios of the three kinds of CPAM are lower than that of the hot asphalt mixture. Because the diluent has not been completely volatilized, the CPAM has not been fully formed, and, consequently, its performance is poor.

High-Temperature Performance

Track boards were formed according to the method in section"High-Temperature Performance". The Hamburg rutting test was carried out to test the three kinds of CPAM, and the results are shown in **Figure 9**.

It can be seen from **Figure 9** that the dynamic stability of CPAM designed with the modified Marshall mix design method was slightly higher than that of CPAM designed with the other two methods. The dynamic stability of the CPAM with a 4.5% asphalt aggregate ratio shows the smallest value because the amount of binder is too small and the cohesion

TABLE 9 | Storage performance test results for CPAM.

Mix design method	Asphalt-aggregate ratio (%)	Storage time (days)				
		0	3	7	28	28
		Initial strength (kN)				Workability grade
Empirical formula	4.5	1.72	1.74	1.80	1.88	2
Modified Marshall test	5.38	2.84	2.86	2.91	3.00	3
Marshall test	5.52	2.53	2.54	2.59	2.69	4

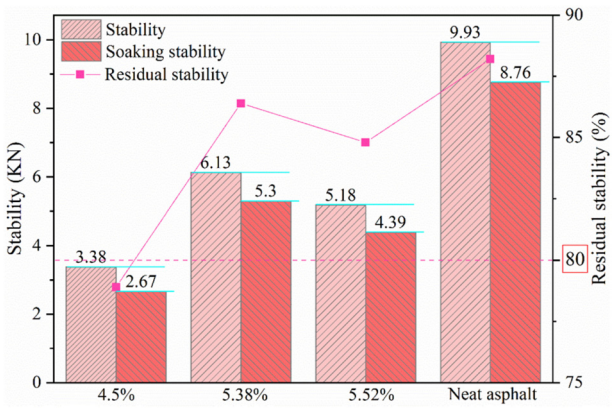

FIGURE 7 | Immersion Marshall test results for CPAM.

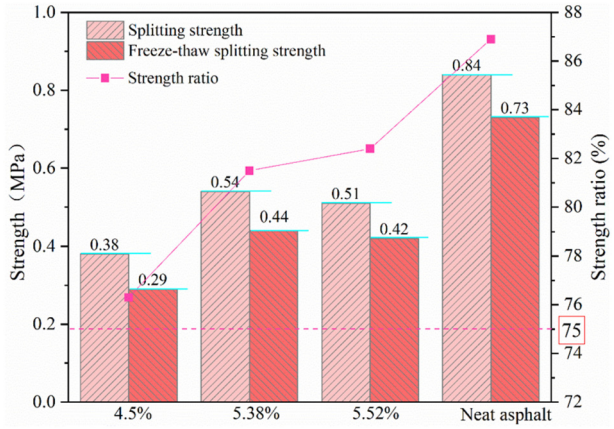

FIGURE 8 | Freeze-thaw splitting test results for CPAM.

is poor, which causes the mixture to have a dry texture. The dynamic stability of CPAM with a 5.52% asphalt aggregate ratio is lower than that of CPAM with a 5.38% asphalt aggregate ratio. This may be because the former CPAM has a larger amount of binder and thick asphalt film. The increase in free asphalt leads to move and plastic deformation at high temperature. The overall dynamic stability of CPAM is low because the strength of the mixture has not been fully formed. The rutting resistance under this condition does not represent the final performance of CPAM.

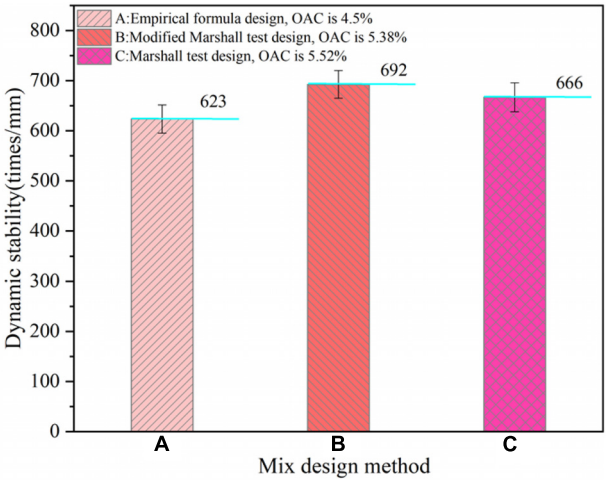

FIGURE 9 | High-temperature stability test results for CPAM.

CONCLUSION

The Marshall mix design method was modified with the objective of designing CPAMs. A series of road performance tests of CPAM designed by using the Marshall mix design method, the empirical formula method, and the modified Marshall mix design method were carried out. The tests included an initial strength test, forming strength test, storage stability test, water stability test, and high-temperature stability test. The results of comparative analysis verified the usefulness and feasibility of the modified Marshall mix design method. Based on the results of this limited laboratory investigation, the following conclusions can be drawn.

- In this paper, the recommended curing temperature for a CPAM specimen was 90°C. The optimal asphalt aggregate ratio of CPAM obtained by using the modified Marshall mix design method was equal to 5.38%. This value was between the optimal asphalt aggregate ratio obtained by using the traditional Marshall mix design method and that obtained by using the empirical formula method.
- The road performance of CPAM designed by using the modified Marshall mix design method was better than that of CPAM designed by using the traditional Marshall mix design method and empirical formula method. The modified Marshall mix design method is feasible.
- The strength of CPAM increases with time. The forming strength was about twice the initial strength.
- The mix design of CPAM should consider its own characteristics. In this paper, volume parameter conversion and the addition of the low-temperature workability requirement enable better CPAM design. It is recommended that the modified Marshall mix design method be utilized as the mix design procedure for CPAM.

DATA AVAILABILITY STATEMENT

All datasets generated for this study are included in the article/supplementary material.

AUTHOR CONTRIBUTIONS

SL directed the entire process of the manuscript. SW, CX, and CL carried out the experiments and data analysis. All authors analyzed the results and contributed in writing the manuscript.

FUNDING

This work was supported by the National Natural Science Foundation of China (51578081, 51608058), the Scientific and Technological Innovation Project of Hunan Province for University Graduate Students (CX2019B***), the National Engineering Laboratory Open Fund Project (kfh160102), Hunan Province-Transport Construction Projects of Science and Technology (201701), Inner Mongolia Autonomous Region Transportation and Transportation Department Transportation Projects of Science and Technology (NJ-2016-35, HMJSKJ-201801), the National Key R&D Program of China (2018YFB1600100), the Natural Science Foundation of Hunan Province (2018JJ3550), the Education Department of Hunan Province (18B144), and the Science and Technology Project of Henan Provincial Department of Transportation (2016Z2).

ACKNOWLEDGMENTS

We wish to thank the reviewers and editors for their advice on this article.

REFERENCES

Alenezi, T., Norambuena-Contreras, J., Dawson, A., and Garcia, A. (2019). A novel type cold mix pavement material made with calcium-alginate and aggregates. *J. Clean. Product.* 212, 37–45. doi: 10.1016/j.jclepro.2018.11.297

Attaran Dovom, H., Mohammadzadeh Moghaddam, A., Karrabi, M., and Shahnavaz, B. (2019). Improving the resistance to moisture damage of cold mix asphalt modified by eco-friendly Microbial Carbonate Precipitation (MCP). *Constr. Build. Mater.* 213, 131–141. doi: 10.1016/j.conbuildmat.2019.03.262

Chen, T., Luan, Y., Ma, T., Zhu, J., Huang, X., and Ma, S. (2020). Mechanical and microstructural characteristics of different interfaces in cold recycled mixture containing cement and asphalt Emulsion. *J. Clean. Product.* 258:120674. doi: 10.1016/j.jclepro.2020.120674

Dash, S. S., and Panda, M. (2018). Influence of mix parameters on design of cold bituminous mix. *Construct. Build. Mater.* 191, 376–385. doi: 10.1016/j.conbuildmat.2018.10.002

Diaz, L. G. (2016). Creep performance evaluation of Cold Mix Asphalt patching mixes. *Int. J. Pavement Res. Technol.* 9, 149–158. doi: 10.1016/j.ijprt.2016.04.002

Dong, Q., Yuan, J., Chen, X., and Ma, X. (2018). Reduction of moisture susceptibility of cold asphalt mixture with Portland cement and bentonite nanoclay additives. *J. Clean. Product.* 176, 320–328. doi: 10.1016/j.jclepro.2017.12.163

Doyle, T. A., McNally, C., Gibney, A., and Tabakoviæ, A. (2013). Developing maturity methods for the assessment of cold-mix bituminous materials. *Construct. Build. Mater.* 38, 524–529. doi: 10.1016/j.conbuildmat.2012.09.008

Dulaimi, A., Al Nageim, H., Ruddock, F., and Seton, L. (2017). High performance cold asphalt concrete mixture for binder course using alkali-activated binary blended cementitious filler. *Construct. Build. Mater.* 141, 160–170. doi: 10.1016/j.conbuildmat.2017.02.155

Gómez-Meijide, B., and Pérez, I. (2014). A proposed methodology for the global study of the mechanical properties of cold asphalt mixtures. *Mater. Design* 57, 520–527. doi: 10.1016/j.matdes.2013.12.079

Gu, C. (2017). *Structural Characteristics and Test Evaluation of Cold Patching Asphalt Mixture*. Master thesis, Southeast University, Nanjing.

Guo, M., Tan, Y., and Zhou, S. (2014). Multiscale test research on interfacial adhesion property of cold mix asphalt. *Construct. Build. Mater.* 68, 769–776. doi: 10.1016/j.conbuildmat.2014.06.031

JTG E20–2011 (2011). *Standard Test Methods of Bitumen and Bituminus Mixture for Highway Engineering*. Beijing: China Communications Press.

JTG F40–2004 (2004). *Technical Specifications for Construction of Highway Asphalt Pavements*. Beijing: China Communications Press.

Khan, A., Redelius, P., and Kringos, N. (2016). Evaluation of adhesive properties of mineral-bitumen interfaces in cold asphalt mixtures. *Construct. Build. Mater.* 125, 1005–1021. doi: 10.1016/j.conbuildmat.2016.08.155

Li, F., Huang, S. C., Xu, J., and Qin, Y. C. (2010). Research on composition design of cold patching asphalt mixture. *J. Wuhan Univ. Sci. Technol.* 32, 79–82.

Li, J. X., Nan, B. Z., and Gao, J. T. (2017). Study on composition and performance of cold patching asphalt mixture. *Highway Transp. Technol.* 13, 199–200, 227.

Ling, C., Hanz, A., and Bahia, H. (2016). Measuring moisture susceptibility of Cold Mix Asphalt with a modified boiling test based on digital imaging. *Construct. Build. Mater.* 105, 391–399. doi: 10.1016/j.conbuildmat.2015.12.093

Ling, J. M., Zhou, Z. F., and Peng, J. C. (2007). Preparation and performance of storage asphalt mixture for pavement repair. *J. Build. Mater.* 10, 195–200.

Liu, C. C., Lv, S. T., Peng, X. H., Zheng, J. L., and Yu, M. (2020). Analysis and comparison of different impacts of aging and loading frequency on fatigue characterization of asphalt concrete. *J. Mater. Civ. Eng.* 32:04020240. doi: 10.1061/(ASCE)MT.1943-5533.0003317

Ma, Q. H., Xing, X. T., Xu, X. S., Li, J. Z., and Feng, X. H. (2016). Preparation and performance analysis of cold patching asphalt mixture. *J. S. Univ.* 46, 594–598.

Ma, T., Zhang, D., Zhang, Y., Wang, S., and Huang, X. (2018). Simulation of wheel tracking test for asphalt mixture using discrete element modeling. *Road Mater. Pavement Design* 19, 367–384. doi: 10.1080/14680629.2016.1261725

Meng, W. Z., Yang, L., Xia, Z., Wang, X. Y., Xue, J., Wu, J. Y., et al. (2011). Preparation and properties of cold patching asphalt mixture. *J. Wuhan Univ. Eng.* 33, 49–53.

Nassar, A. I., Thom, N., and Parry, T. (2016). Optimizing the mix design of cold bitumen emulsion mixtures using response surface methodology. *Construct. Build. Mater.* 104, 216–229. doi: 10.1016/j.conbuildmat.2015.12.073

Saadoon, T., Garcia, A., and Gómez-Meijide, B. (2017). Dynamics of water evaporation in cold asphalt mixtures. *Mater. Design* 134, 196–206. doi: 10.1016/j.matdes.2017.08.040

Shanbara, H. K., Ruddock, F., and Atherton, W. (2018). A laboratory study of high-performance cold mix asphalt mixtures reinforced with natural and synthetic fibres. *Construct. Build. Mater.* 172, 166–175. doi: 10.1016/j.conbuildmat.2018.03.252

Song, J. S., and Lv, W. M. (1998). Study on composition design of storage asphalt mixture. *J. Tongji Univ.* 26, 664–668.

Song, X. F., Fan, Z. H., and Wang, Y. F. (2014). Study of the same curing condition of large volume concrete based on maturity methods. *Adv. Mater. Res.* 893, 593–596. doi: 10.4028/www.scientific.net/AMR.893.593

Xu, W., Mei, H., Luo, R., Guo, X. L., and Wang, X. (2018). Material design and mixture performance of cold patching asphalt. *J. Wuhan Univ. Sci. Technol.* 42, 1049–1054.

Yang, L., Meng, W. Z., Wang, X. H., Xia, Z., Wang, X. Y., Xue, J., et al. (2011). Effect of inorganic filler on strength of cold patching asphalt mixture. *J. Wuhan Univ. Eng.* 33, 47–51.

Zhang, Y., Ma, T., Ling, M., Zhang, D., and Huang, X. (2019). Predicting dynamic shear modulus of asphalt mastics using discretized-element simulation and reinforcement mechanisms. *J. Mater. Civil Eng.* 31:04019163. doi: 10.1061/(ASCE)MT.1943-5533.0002831

Conflict of Interest: The authors declare that the research was conducted in the absence of any commercial or financial relationships that could be construed as a potential conflict of interest.

frontiers in Materials

ORIGINAL RESEARCH
published: 06 October 2020
doi: 10.3389/fmats.2020.00231

Study on the Laboratory Mixing and Compaction Methodology of Emulsified Asphalt Cold Recycled Mixture

*Liping Liu[1], Zhanchuang Han[1], Ping Wu[2], Guangshun Zheng[1] and Lijun Sun[1]**

[1] The Key Laboratory of Road and Traffic Engineering, Ministry of Education, Tongji University Shanghai, Shanghai, China,
[2] Inner Mongolia road and Bridge Group Co., Ltd., Hohhot, China

Emulsified asphalt cold recycled mixture is commonly used in the upper base course of expressway reconstruction asphalt pavement. When the following layer is paved with hot-mix asphalt (HMA) mixture, the aging asphalt in the recycled material is activated due to the temperature conduction effect of the HMA mixture, so that the cold recycled layer produces "secondary thermal compaction" under the action of a roller. Based on this phenomenon, the present study aimed to discuss the influence of different molding methods and mixing processes on the volume parameters and mechanical properties of cold recycled emulsified asphalt mixture. The influences of Marshall compaction times, gyratory compaction times, curing time, and specimen-forming temperature on the voids and splitting strength of cold recycled mixture were studied. The field core sample was compared with the laboratory-forming method, which accords with the field compaction condition of the cold recycled upper base. first-time compaction number of large Marshall is 150 times and secondary compaction number is 75 times (Shorthand for 150 + 75), the compaction times of the gyratory specimen is "30 + 15." The curing time of the cold recycled mixture should not exceed 3 h and should not be constructed in low-temperature weather to ensure the quality of pavement construction. The use of a new stage and step laboratory mixing process simulating the plant mixing, compared with the traditional mixing process, increases the splitting strength by at least 13%.

Keywords: emulsified asphalt cold recycled mixture, forming method, curing time, mixing process, splitting strength, voids

OPEN ACCESS

Edited by:
Yiqiu Tan,
Harbin Institute of Technology, China

Reviewed by:
Changjun Zhou,
Dalian University of Technology, China
Norhidayah Abdul Hassan,
University of Technology Malaysia, Malaysia

****Correspondence:***
Lijun Sun
ljsun@tongji.edu.cn

Specialty section:
This article was submitted to Structural Materials, a section of the journal Frontiers in Materials

Received: *30 March 2020*
Accepted: *24 June 2020*
Published: *06 October 2020*

Citation:
Liu L, Han Z, Wu P, Zheng G and Sun L (2020) Study on the Laboratory Mixing and Compaction Methodology of Emulsified Asphalt Cold Recycled Mixture. Front. Mater. 7:231. doi: 10.3389/fmats.2020.00231

INTRODUCTION

Emulsified asphalt cold recycling technology is one of the recycling technologies of asphalt pavement. The mixing, transportation, and rolling of cold recycled mixture are carried out under normal temperatures and have the advantages of low carbon emission, convenient construction, and high-cost performance. It is more widely used in the reconstruction, expansion, maintenance, and repair of roads and other projects (Sondag et al., 2002; Xiao et al., 2018; Zhu et al., 2019). The reasonable design method and laboratory molding process of cold recycled mixture are the bases of the successful application of Emulsified asphalt cold recycling technology (Lu, 2001; National Cooperative Highway Research Program, 2007). In this regard, scholars at home and abroad have conducted a lot of research and practice on the application of a cold recycled

mixture and put forward some constructive theories and design methods, such as the Marshall method modified by AASHTO, Asphalt Recycling and Reclaiming Association (ARRA) design method, California method, AI method, Pennsylvania method, Oregon design method, widgets design method, and South Africa design method (Epps, 1995; Asphalt Recycling and Reclaiming Association [ARRA], 1996, 2001; Sondag et al., 2002; Asphalt Academy, 2009; Wirtgen, 2010). Lee et al. (2003) believed that the Marshall compaction method could not simulate the compaction effect of the field road compaction machinery, and proposed to use the gyratory compactor to compact and form a cold recycled mixture. Moghadam and Mollashahi (2017) thought that when the particle size was larger than 25 mm, a significant difference in the mechanical properties and water stability was found between the 4-inch and 6-inch specimens. Guo compared the Marshall compaction test with the gyratory compaction test and showed that the voids of the Marshall compaction specimen were basically the same as that of 40 50 times of gyratory compaction specimen (Guo, 2013). Wei et al. (2019) used the gyratory compaction test method to design the mix proportion of cold recycled mixture and improved the performance of cold recycled mixture by changing the times of gyratory compaction and the molding temperature of the specimen. Li et al. (2017) used the vibration method to form the specimen, and analyzed the voids of the specimen under different forming methods with the aid of computed tomography detection means, and concluded that the essential reason affecting the mechanical properties of cold recycled mixture was the characteristics of voids.

The results of the aforementioned research undoubtedly promoted the development of cold-recycling technology and laid a good foundation for the application of the subsequent cold recycled mixture. In 2007, Prof. Sun's group of Tongji University discovered the phenomenon of "secondary thermal compaction" for the first time (Jiang et al., 2008; Xu et al., 2013). The complete compaction process of the asphalt cold recycled upper base mixture is as follows: first, the cold recycled upper base is compacted at normal temperature when it is paved, and then the cold recycled layer is thermally compacted using the rolling machine when the hot recycled asphalt mixture is paved (Yang, 2010; Xu et al., 2013). However, the existing methods at home and abroad do not consider the secondary compaction process of the cold recycled upper base mixture, which results in the poor matching of volume parameters and mechanical properties between laboratory and field core samples. The second compaction temperature of the cold recycled upper base is much higher than that of the first compaction (Jiang, 2012). According to the test data of the voids of the cold recycled upper base core samples before and after HMA paving in the Chang-Jiu expressway reconstruction and expansion project, it was found that the voids of the recycled layer were reduced by about 3% by the secondary thermal compaction. Then, taking the voids of core samples before and after HMA paving as the control index, the previous study of Sun's group showed that the laboratory small Marshall compaction for 100 times + the second thermal compaction for 50 times could simulate the field compaction condition of the cold recycled upper base. However, the large-sized cold recycled mixture needs a larger-sized specimen for simulation. At present, gyratory compaction is the most common method of laboratory-forming. In addition, in the mechanical parameter tests of mixtures (such as modulus, compressive strength, uniaxial penetration test, and so forth), the size of the specimen is required, but the small Marshall specimen cannot meet the test requirements, the size of the small Marshall is Φ101.5 mm × 63.6 mm. Therefore, it is necessary to study the secondary forming method of laboratory large Marshall specimens and gyratory compaction specimens. The transportation of a cold recycled mixture from the mixing plant to the construction site takes some time. The cold recycled mixture, if placed for a long time, has a significant impact on the construction performance, compaction effect, and stability of the mixture. The study of curing time, forming temperature, and laboratory mixing process of a cold recycled mixture is essential. Therefore, on the basis of the previous research (Yang, 2010; Xu et al., 2013) on the "secondary thermal compaction" process, this study investigated the laboratory mixing and forming process of emulsified asphalt cold recycled mixture, which simulated the actual mixing and forming process.

Principle of Secondary Compaction of the Emulsified Asphalt Cold Recycled Upper Base Mixture

One of the important aspects of the asphalt cold recycled upper base mixture, which is different from the common hot asphalt mixture, is that it generally has two compaction processes. After the asphalt cold recycled upper base mixture is paved, the timely rolling of the roller is the first compaction process of the cold recycled layer, commonly known as normal temperature compaction process. This process needs to be completed before the complete demulsification of emulsified asphalt; otherwise, the demulsification of emulsified asphalt may cause the asphalt cold recycled upper base mixture to form a hard shell, making the compaction more difficult. The second compaction of the cold recycled upper base occurs in the construction process of the layer of the hot-mix asphalt (HMA) mixture. After completing the construction of the cold recycled layer, the cold recycled upper base needs to be cured for 3–7 days before the HMA is paved because, among other reasons, the water generated by the emulsion breaking of the emulsified asphalt has to be evaporated. Moreover, when the HMA layer is paved, the baking effect of the HMA mixture (paving temperature up to 160°C) also increases the temperature of the cold recycled upper base. When the layer of HMA is rolled, the temperature of the cold recycled upper base increases to nearly 60°C. The influence of HMA on the temperature distribution of the cold recycled layer is shown in **Figure 1**. The test result was obtained by Sun's group through embedding temperature sensors in a large number of cold regeneration field projects (Yang, 2010; Xu et al., 2013). The 60°C is the softening point of aged asphalt. When the temperature increases, the aging asphalt in the cold recycled mixture is reactivated and softened. This phenomenon is more pronounced during summer construction. Compared with the normal temperature state, the mixture is more likely to be compacted. The second compaction effect of the roller on the cold

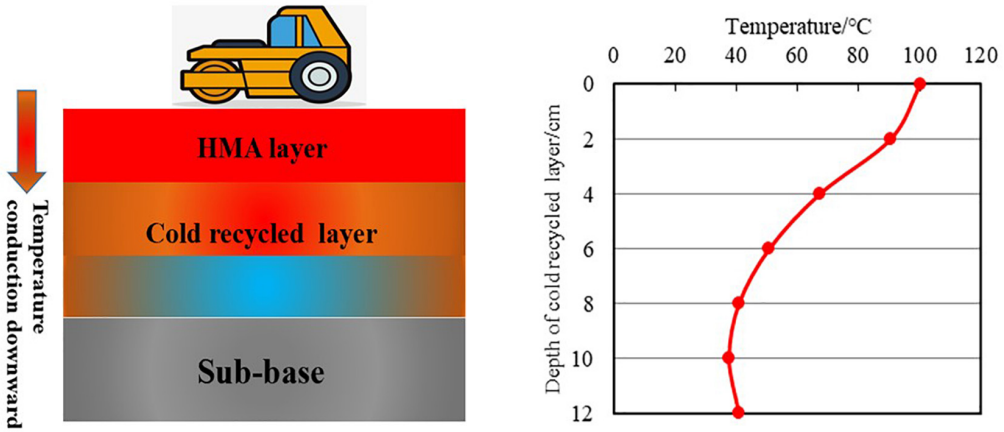

FIGURE 1 | The influence of HMA on the temperature distribution of cold recycled layer.

recycled layer is obvious. The voids of the cold recycled upper base after the second thermal compaction were reduced by 2–3% (Jiang et al., 2008; Yang, 2010; Xu et al., 2013). Current research shows that the compaction effect of the cold recycled mixture is related to the thickness and temperature of the HMA layer and cold recycled layer, as well as the rolling technology (Zheng et al., 2016; People's Communications Press, 2019). Considering the secondary thermal compaction process in the design of cold recycled mixture, the amount of emulsified asphalt can be reduced, which is of great economic value. The performance of cold recycled mixture will also be greatly improved, which could replace the asphalt concrete layer and be used in heavy traffic conditions, and even play the role of hot asphalt mixture (Yang, 2010; Xu et al., 2013).

MATERIALS AND TEST SCHEME

Materials

Emulsified Asphalt

The specific indexes of emulsified asphalt used in this test are shown in **Table 1**.

RAP and New Aggregate

The RAP source used in this study was the old asphalt surface milling material of an expressway reconstruction and expansion project, which was divided into three grades: 0–5, 5–10, and 10–30 mm; and the new aggregate was limestone, with a specification of 10–20 mm. The bituminous pavement had been used for 12 years before milling, and AH-70 asphalt was used. The asphalt content of RAP was 3.92%. Three indexes of asphalt were tested, the penetration at 25℃ was 41.4 (0.1 mm), softening point was 55.4℃, and ductility at 15℃ was 23.2 cm.

Mineral Powder, Cement, and Water

Mineral powder and cement were produced by a material company in the Jiangxi Province, and their technical indicators met the technical specifications for the construction of highway asphalt pavement (JTG F40-2004) of China; tap water was used as water.

Gradation, Optimum Moisture Content, and Optimum Emulsified Asphalt Content

The composition of recycled mixture was as follows: RAP (0–5 mm): RAP (5–10 mm): RAP (10–30 mm): new aggregate (10–20 mm): mineral powder = 26: 20: 40: 12: 2; the cement content was 1.5%. The optimum moisture content determined by the compaction test recommended in the technical code for road asphalt pavement regeneration and code for highway geotechnical test was 3.8%. According to the China's regeneration standard (People's Communications Press, 2019), the optimal amount of emulsified asphalt was 3.5% using splitting strength and voids as control indexes.

Test Scheme

Effect of Different Molding Methods on Voids and Splitting Strength of Cold Recycled Mixture

A marshall compactor and gyratory compactor were used to form a large Marshall specimen and a gyratory compaction specimen, respectively. The specimens were compacted (rotated) for the first time and compacted (rotated) for the second time. The size of the large Marshall specimen was Φ152.4 mm × 94.5 mm, and the size of the gyratory specimen was Φ100 mm × 63.5 mm.

For the large Marshall specimens, in the test code for asphalt and asphalt mixture of highway engineering, it is mentioned that the number of compaction of large Marshall specimens is 112, corresponding to the 75 of the small Marshall standard (Ministry of transport of the people's Republic of China, 2011), the weight of the small Marshall compactor was 4536 g, the falling distance of the hammer was 457 mm, and the size of the specimen was 101.5 × 63.6 mm^2. Moreover, the weight of the large Marshall compactor was 10,210 g, the falling distance of the hammer is 457 mm, and the size of the specimen was 152.4 × 94.5 mm^2. For the work on a unit volume of a single specimen, the work done by a small Marshall specimen in one compaction is about 1.5 times of that of a large Marshall

TABLE 1 | Test results of emulsified asphalt properties.

Test item		Unit	Experimental value	Technical requirement
Residue on sieve (1.18-mm sieve)		%	0.03	⩾0.1
Particle charge		–	Cation (+)	Cation (+)
Demulsification speed		–	Slow crack	Slow crack or middle crack
Viscosity (Engla viscosity e25)		–	–	2–30
Viscosity (cyberviscosity VS)		s	24.98	7–100
Evaporation residue content		%	62.6	⩽62
Residue	Penetration (25°C)	0.1 mm	71.1	50–300
	Ductility (15°C)	cm	56.8	⩽40
	Softening point (5°C)	°C	45.8	–
	Solubility	%	–	⩽97.5
Room-temperature storage stability: 1 d		%	0.8	⩾1
Room-temperature storage stability: 5 d		%	–	⩾5
Adhesion to coarse aggregate		–	> 2/3	⩽2/3

specimen. Therefore, in order to find the appropriate compaction times of large Marshall specimens, the compaction work per unit volume of small Marshall specimens was referred. The number of the first-time compactions were designed to be 75, 112, 150, and 187. The large Marshall specimens with similar voids after the initial compaction of the cold recycled upper-base pavement were selected to determine the appropriate number of the first-time compaction. The number of second-time compactions were designed to be 15, 40, 75, and 100 considering the actual compaction work. After the first-time compaction, the specimens with mold were placed in the laboratory for 24 h at room temperature, and then placed in the Drying Oven (60°C) for 48 h, and finally compacted for the second-time. After the samples were formed, the voids and splitting strength were measured. And it was compared with the voids and splitting strength after the primary compaction of the cold recycled upper base and after the layer of HMA were paved and compacted.

For the gyratory specimens, the number of first-time gyrations were designed to be 20, 30, 50, 75, 100, and 150. The specimens with similar voids after the initial compaction of cold recycled upper base pavement were selected to determine the appropriate number of first-time gyratory compactions. On this basis, the number of second-time gyrations were designed to be 5, 10, 15, and 25 considering the actual compaction work. The pressure of the gyratory compactor was controlled by 600 MPa, and the gyratory angle was 1.16°. The curing conditions of the specimens after the first-time gyrations was the same as that of the large Marshall specimen. After the samples were formed, the voids and splitting strength were measured and compared with the voids and splitting strength after the first compaction of a field cold recycled upper base pavement and the compaction of the upper HMA.

Effect of Different Curing Times and Temperatures on Voids and Splitting Strength of Cold Recycled Mixture

The cold recycled mixture was placed in the boxes (constant temperature and humidity) at 5, 15, 25, and 35°C and maintained for 0, 1, 2, and 3 h until the small Marshall specimens were, respectively, formed 6 h later, and the number of compaction was "100 + 50" (after 100 times of compaction, the side of the specimen with the mold was put into a 60°C air blast oven for curing for 48 h, and the specimen with the mold was taken out from the oven and immediately put into the Marshall compactor 50 times on both sides). After the sample was formed, the voids and splitting strength were measured, and the effects of different molding temperatures and curing time on the voids and splitting strength of cold recycled mixture were compared.

The Influence of Laboratory Mixing Technology on Voids and Splitting Strength of Cold Recycled Mixture

At present, the laboratory mixing process of the cold recycled mixture in China is basically fixed. The recommended mixing process is shown in **Figure 2**, which is defined as the traditional mixing process. The improved mixing process is shown in **Figure 3**, which is defined as the new mixing process. The traditional mixing process includes the following steps: (1) the RAP material prepared according to the design proportion was added to the mixer; (2) water was added according to the calculated amount of water and mixed evenly for 60 s; (3) emulsified asphalt was added according to the calculated amount of emulsified asphalt and mixed evenly for 60 s. The new mixing process includes the following steps: (1) RAP (10–30 mm), new aggregate (10–20 mm), water (1/3 of the external water), and emulsified asphalt (1/2 of the total amount) were added to the mixing pot according to the design proportion and mixed for 45 s; (2) fine RAP (0–5 mm), medium RAP (5–10 mm), mineral powder, cement, water (1/3 of the external water), and the asphalt (one half of the total amount) were added to the mixing pot according to the design proportion and mixed for 45 s; (3) water (one third of the external water) was added to the mixing pot and mixed for 30 s.

Two mixing processes were used to mix emulsified asphalt cold recycled mixture, and then small Marshall specimens were formed indoors. In this study, the small Marshall specimens were all shaped twice, and the number of compactions were "100 + 50." The curing conditions of the specimens was

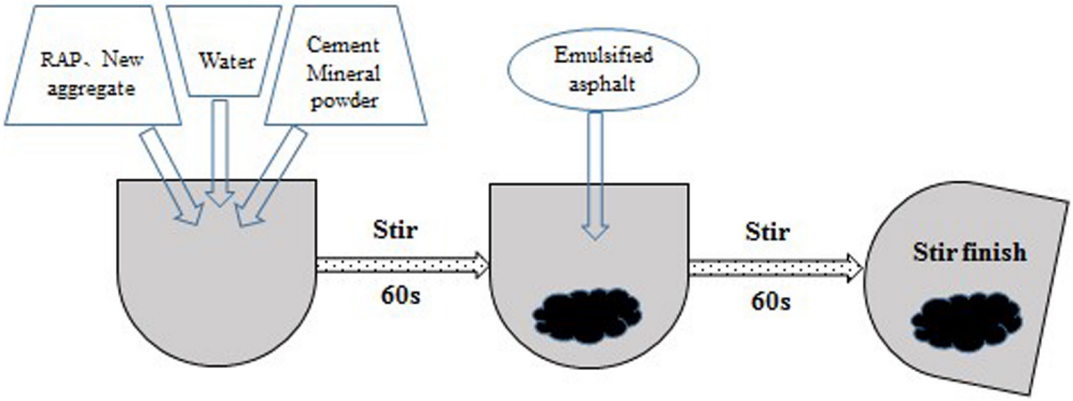

FIGURE 2 | Traditional mixing process.

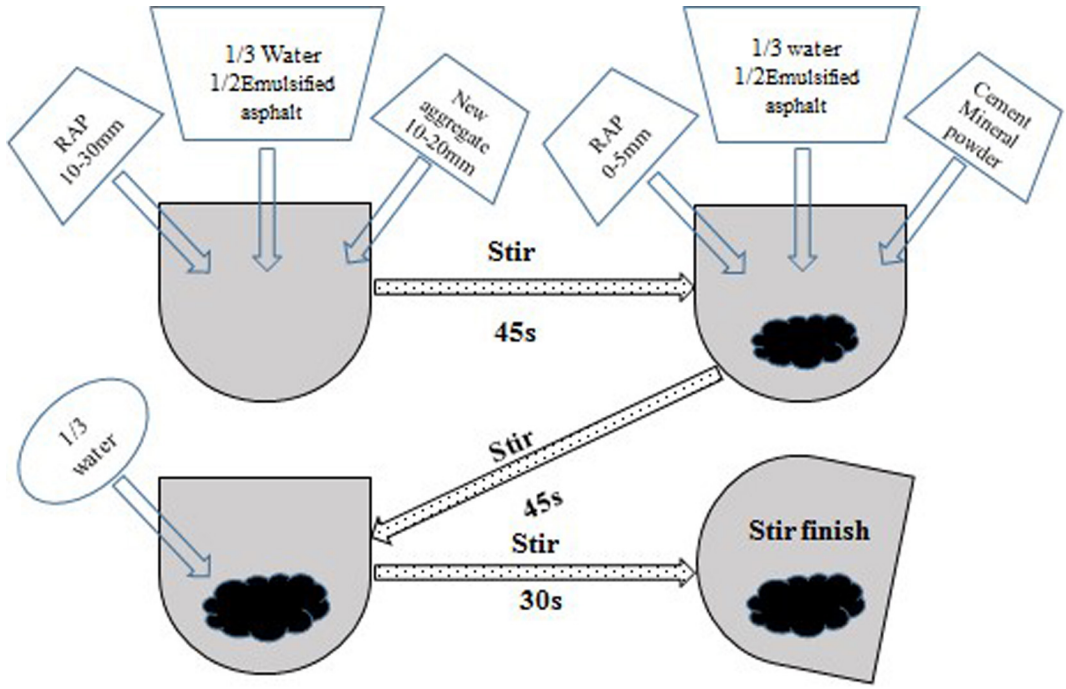

FIGURE 3 | New mixing process.

the same as that of the large Marshall specimen. After the specimens were formed, the voids and splitting strength were measured, and the voids and splitting strength of the specimens formed in the cold recycled mixture chamber under the traditional mixing process and the new mixing process were compared.

All the data in this paper are the averages of the test data of six parallel specimens tested by the Grubbs method. The Grubbs test is one of the statistical methods to test outliers. In the statistical calculation method of eliminating outliers, the Grubbs test is not only applicable to the abandonment of one or more suspicious values in a group of data, but also applicable to the limited number of determinations. It is the most reliable test method for the determination of suspicious values (Adikaram et al., 2015).

Test Results and Analysis

Effect of Different Forming Methods on Voids and Splitting Strength of Cold Recycled Mixture

Formation of large Marshall specimens

The test results of the voids and splitting strength of large Marshall specimens under the first-time compaction and before paving HMA in the test section of the cold recycled upper base course are shown in **Figure 4A**. The test results of voids and splitting strength of specimens under second-time compaction

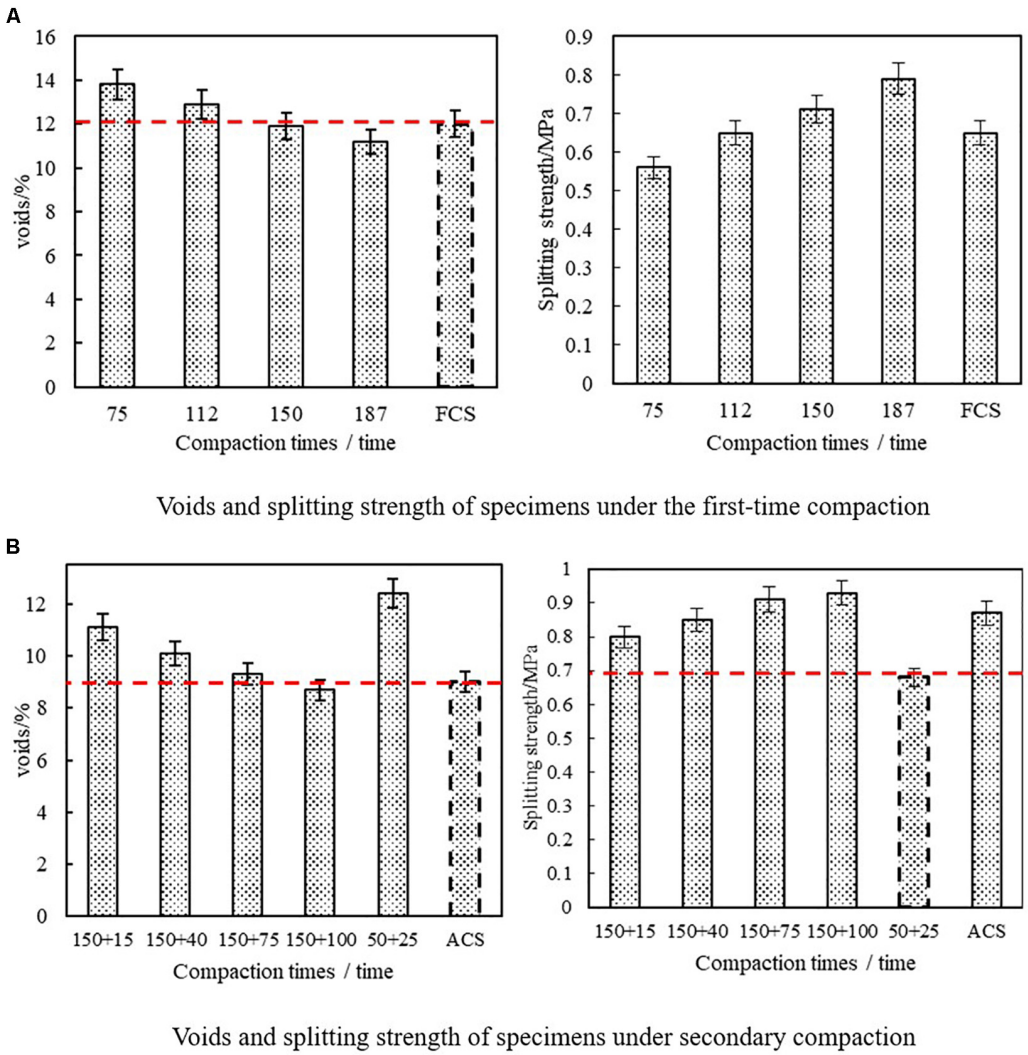

FIGURE 4 | Voids and splitting strength of large Marshall specimens under different compaction times: **(A)** voids and splitting strength of specimens under the first-time compaction; **(B)** voids and splitting strength of specimens under secondary compaction.

and after paving HMA in the test section of the cold recycled upper base course are shown in **Figure 4B**. FCS and ACS represent the core samples before and after the HMA was paved on the cold recycled upper base.

Figure 4A shows that the voids of laboratory specimens decreased with an increase in compaction times. When the large Marshall specimen was compacted 150 times, the voids were 11.9%. Before paving HMA, many core samples in the field were drilled and the volume parameters were tested. The results show that the voids of core samples were 12% ± 0.7% in the 95% confidence interval (This is basically consistent with the core sample test results accumulated by the Sun group in different cold regeneration field projects) (Yang, 2010; Xu et al., 2013). Therefore, it was concluded that the laboratory large Marshall specimen was compacted 150 times. The voids of the specimen were similar to that of the field cold recycled upper base course pavement after the initial compaction at room temperature. This indicated that the 150 times compaction of the laboratory large Marshall specimen could simulate the initial compaction state of the cold recycled upper base course pavement after paving on the site. This compaction level was equivalent to the 100 times compaction of laboratory small Marshall specimens, which could simulate the initial compaction state of the cold upper base course pavement after paving on the site. The reason for this phenomenon was that China's standard Marshall test method was established in the early 1980s and adapted to the compaction level (rubber roller was lower than 20*t*, vibration roller was 2–6*t*, and double-wheel steel cylinder roller was 6–8*t*) and traffic conditions at that time. The laboratory compaction times recommended in the technical code for the recycling of highway asphalt pavement refer to the standard Marshall test method. The current Marshall standard compaction work has lagged behind the production practice with the improvement in the technology level, compaction machinery level (generally, 10–14*t* vibrating

roller and 25–30*t* rubber wheel roller) and the development of modern traffic in the construction work. Therefore, the number of compactions of large Marshall specimens in first-time laboratory forming should be 150.

Figure 4B shows that after the completion of the first compaction, the second compaction was carried out in real time, and the voids of the specimen decreased with the increase in the second compaction. When the large Marshall specimen was compacted 75 times, the voids of the specimen were 9.3%. The voids of the specimen were 9.0% measured from the core sample drilled from the site after the HMA was paved on the cold recycled upper base pavement. Therefore, it was concluded that the voids of laboratory large Marshall specimen after compaction for "150 + 75" times was similar to that of the cold recycled upper base pavement after the HMA was paved and compacted, so that the laboratory large Marshall specimen compaction for "150 + 75" times could simulate cold-recycling on-site compaction state of raw road surface after the HMA was paved. The reason for this phenomenon was that when the asphalt cold recycled mixture was used as the upper base course of the road, two compaction processes occurred: after the cold recycled asphalt mixture was paved, the compaction of the normal-temperature mixture under the action of the roller was the first compaction process of the cold recycled upper base course, called the normal-temperature compaction (or cold compaction) process. When the HMA have been spread, the paved HMA had a further heating effect on the cold recycled upper base due to its high temperature, causing the cold recycled layer to reach a higher temperature, thereby reactivating and softening the old asphalt in the mixture. The obvious second compaction process occurred under the action of the roller, called the thermal compaction process. The first compaction was carried out for the laboratory-formed specimens, and the second compaction was carried out after 48-h curing in an oven at 60°C, which to some extent simulated the two

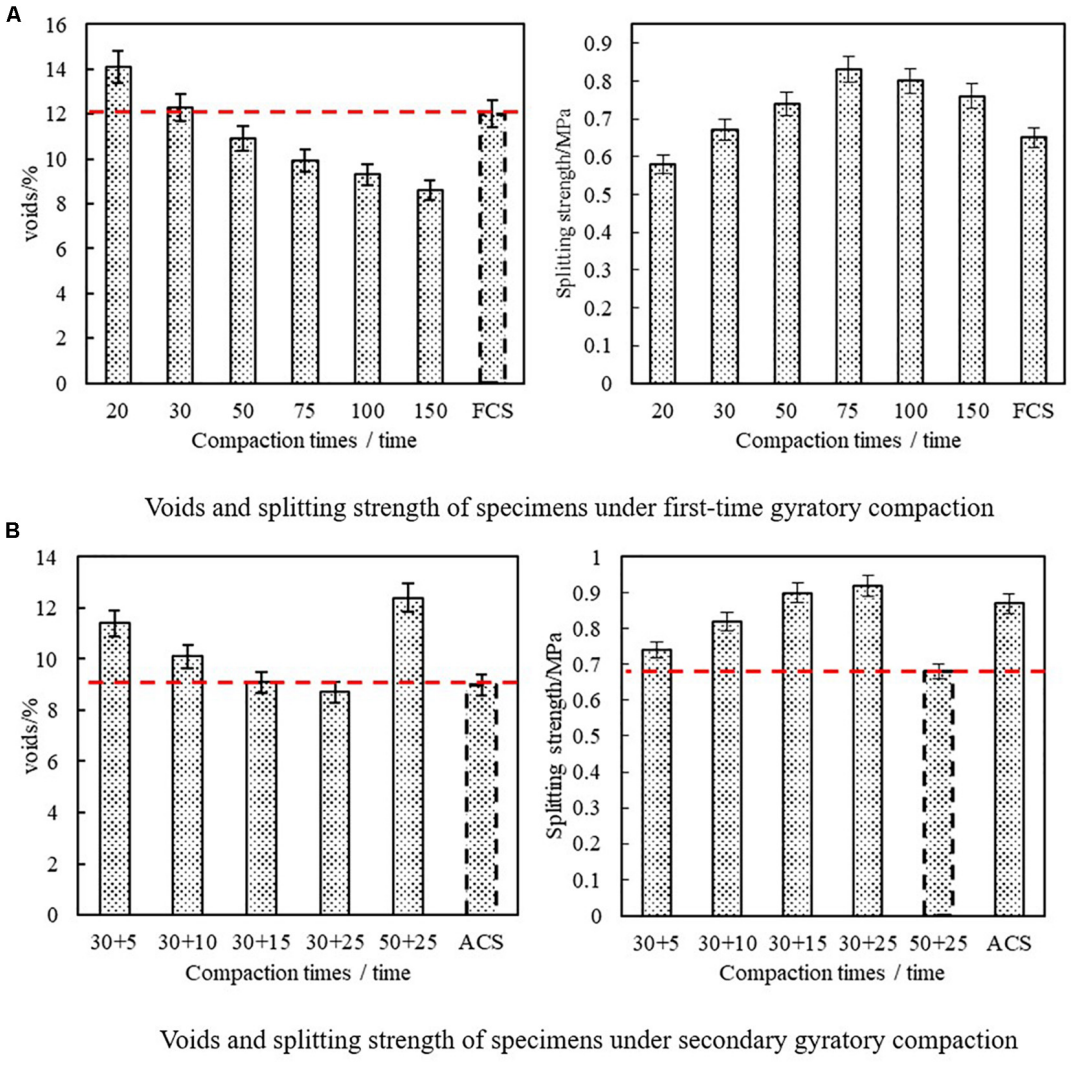

FIGURE 5 | Voids and splitting strength of specimens under different times of gyratory compaction: **(A)** voids and splitting strength of specimens under first-time gyratory compaction; **(B)** voids and splitting strength of specimens under secondary gyratory compaction.

compaction processes of the cold recycled upper base. Therefore, the compaction times of large Marshall specimens should be "150 + 75" times to better simulate the compaction condition of the field. However, the type and tonnage of the roller used in different practical projects and the compaction work during construction may be different, leading to the difference in the voids of the cold recycled mixture. Hence, the conclusions need to be confirmed in the future.

Figure 4 shows the splitting strength of the large Marshall specimens compacted 150 times and "150 + 75" times were roughly the same as that of the core samples before and after the HMA was paved on the cold recycled upper base course. However, the splitting strength of the small Marshall specimens was less than 0.7 MPa, which was far lower than that of the field core samples by adopting the method recommended in the technical code for road asphalt pavement regeneration. The splitting strength (0.9 MPa), which was basically the same as the aforementioned voids phenomenon, showed that the large Marshall specimens compacted 150 times and "150 + 75 times" could better simulate the compaction mechanism and mechanical properties of the cold recycled upper base pavement.

Formation of gyratory compaction specimens

The test results of voids and splitting strength of gyratory specimens under first-time gyratory compaction are shown in **Figure 5A**. The test results of voids and splitting strength of specimens under secondary gyratory compaction are shown in **Figure 5B**.

Figure 5A shows that the voids of the laboratory specimen decreased with the increase in compaction times. When the gyratory compaction specimen rotated 30 times, the voids of the specimen were 12.3%. Before paving HMA, many core samples in the field were drilled and the volume parameters were tested. The results show that the voids of core samples were 12% ± 0.7% in the 95% confidence interval (This is basically consistent with the core sample test results accumulated by the Sun group in different cold regeneration field projects) (Yang, 2010; Xu et al., 2013). Therefore, it was concluded that the laboratory gyratory compaction specimen rotated 30 times, and the voids of the specimen were similar to that of the field cold recycled upper base pavement after the initial compaction at room temperature, indicating that the compaction specimen rotated 30 times, simulating the initial compaction state after the cold recycled upper base pavement was paved on the site. Therefore, the number of rotations of the laboratory first-time-forming gyratory compaction specimen should be 30.

Figure 5B shows that after the first compaction, the second compaction was carried out in real time, and the voids of the specimen decreased with the increase in the second compaction. When the rotating compaction specimen rotated 15 times, the voids of the specimen was 9.1%. The small Marshall specimen was double-sided compacted 50 times and then double-sided compacted 25 times after the completion of the curing, as recommended in the technical code for road asphalt pavement regeneration. The voids of the specimen were 12.4%. The voids of the specimen were 9.0% as measured from the core sample drilled from the site after the HMA was paved on the cold recycled upper base course pavement. Therefore, it was concluded that the voids of the laboratory gyratory compaction specimen after rotating "30 + 15" times were similar to that of the cold recycled upper base pavement after the HMA was paved and compacted. The conclusion was consistent with the discussion in "Formation of large Marshall specimens."

Figure 5 shows that the splitting strength of 30 times of compaction and 30 + 15 times of gyratory compaction specimen were roughly the same as that of the core samples before and after the HMA was paved on the cold recycled upper base course, indicating that the forming mode of 30 times of compaction and

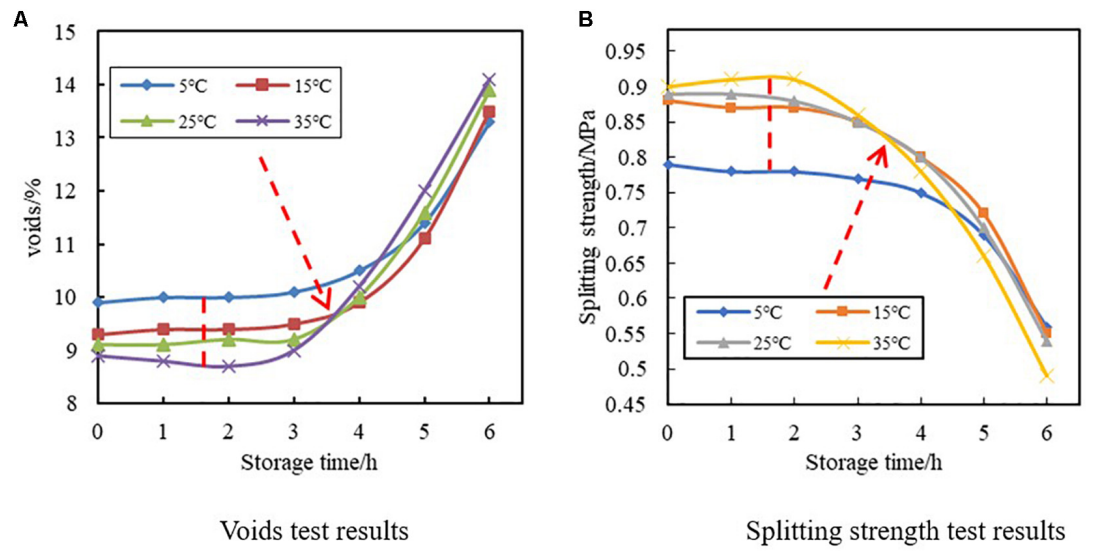

FIGURE 6 | Voids and splitting strength of cold recycled mixture under different molding temperature and curing time: **(A)** voids test results; **(B)** splitting strength test results.

30 + 15 times of gyratory compaction specimen could better simulate the compaction mechanism and mechanical properties of the cold recycled upper base course pavement. In addition, the voids of the gyratory compaction specimen (100 times of compaction) were similar to that of the gyratory compaction specimen (30 + 15 times of compaction), but the splitting strength was different to some extent. This was mainly because a large amount of excess water in the specimen flowed out in the process of the specimen formed by 100 times of rotation at one time due to the extremely dense gyratory compaction, accompanied by the loss of more emulsified asphalt. As a result, the asphalt solid content of the 100 times rotated specimens decreased, thereby decreasing the splitting strength.

Effect of Curing Time and Temperature

The cold recycled mixture after laboratory mixing was placed in boxes (constant temperature and humidity) at 5, 15, 25, and 35°C and maintained for 0, 1, 2, and 3 h until the small Marshall specimens were formed 6 h later. The test results of voids and splitting strength of the formed small Marshall specimens are shown in **Figure 6**.

Figure 6 shows that the voids of the formed specimen first remained unchanged and then presented a gradually increasing trend at 5, 15, 25, and 35°C with the extension of cold recycled mixture placing time, while the splitting strength first remained unchanged and then presented a gradually decreasing trend. When the cold recycled mixture was placed for 3 h, the voids and splitting strength of the specimen did not change. After 3 h, the voids and splitting strength of the cold recycled mixture at 35°C first changed, then the voids and splitting strength of the cold recycled mixture at 25, 15, and 5°C changed in turn, and with the extension of the curing time, the voids and splitting strength changed. A growing trend of change was noted. This was because the emulsified asphalt gradually began to demulsify with the extension of the curing time. The emulsified asphalt after demulsification selectively adhered to the fine materials in the aggregate to form the mastic micelle, which was difficult to be compacted in the forming process. Therefore, it presented more porosity and less splitting strength. The demulsifying time of emulsified asphalt was related to the temperature during the forming process. Because the higher the temperature, the more intense the Brownian motion of the molecule, and the greater the probability of the asphalt particles colliding with each other, the more unstable the emulsified asphalt, and the more likely it is to break the emulsion. Therefore, the voids of

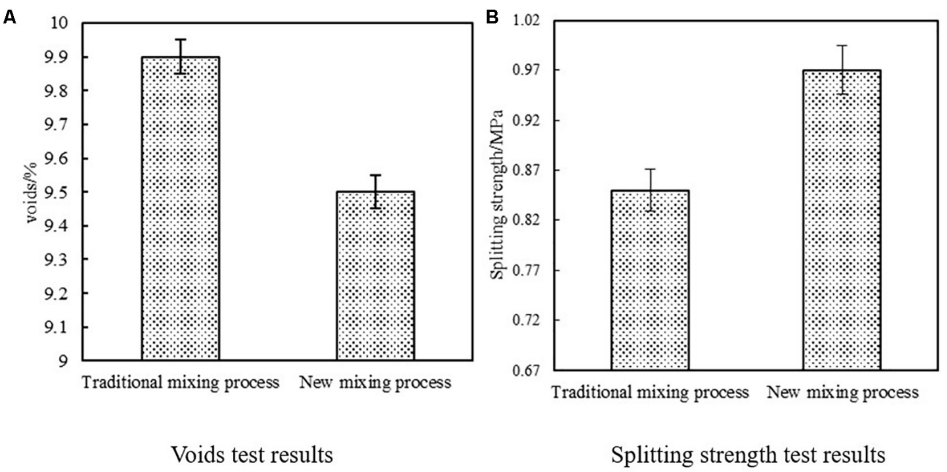

FIGURE 7 | Test results of the voids and splitting strength of cold recycled mixture under different mixing processes: **(A)** voids test results; **(B)** splitting strength test results.

TABLE 2 | Independent sample test.

Item		Levene's test for equality of variance		*t*-test for equality of means						
		F	Sig.	t	df	Sig.(2-tailed)	Mean difference	Std. error difference	95% confidence interval of the difference	
									Lower	Upper
Splitting Strength	Equal variances assumed	1.709	0.212	4.53	14	0.000	0.1125	0.02485	0.059	0.1658
	Equal variances not assumed			4.53	12.36	0.001	0.1125	0.02485	0.059	0.1667
Voids	Equal variances assumed	3.036	0.103	−3.19	14	0.007	0.4250	0.1333	0.711	0.139
	Equal variances not assumed			−3.19	8.89	0.011	0.4250	0.1333	0.727	0.123

the cold recycled mixture at 35°C began changing first during the specimen-forming process. Therefore, from the engineering point of view, the cold recycled mixture should be transported to the construction site and spread as soon as possible after mixing in the mixing plant. When the construction is carried out in high-temperature and extreme weather, the transportation distance should be shortened and the spreading and rolling speed of the mixture should be accelerated so as to improve the compactness and strength of the pavement.

New Laboratory Mixing Process for Emulsified Asphalt Cold Recycled Mixture

The test results of voids and splitting strength of cold recycled mixture under different mixing processes are shown in **Figure 7**. The results of *t*-test analysis are shown in **Table 2**.

Figure 7 shows that for the cold recycled mixture under the traditional mixing process, the voids of the twice-formed Marshall specimen were 9.9%, the splitting strength was 0.85 MPa, the voids of the formed specimen under the new mixing process were 9.5%, and the splitting strength was 0.97 MPa. Using SPSS statistical software, the voids and splitting strength test results under different mixing processes are analyzed by *t*-test, the significance (2-tailed) is less than 0.05. It can be seen from the test results of independent samples that different mixing processes have significant differences in voids and splitting strength. From the test results in **Figure 7**, compared with the traditional mixing process, the new mixing process had higher strength; the splitting strength increased by at least 13%. This was because the new mixing process adjusted with the sequence of aggregate addition: first, the RAP (10–30 mm) and the new aggregate (10–20 mm) were put into the mixing pot; then the fine material, the intermediate material, the ore powder, and the cement were added; water and emulsified bitumen were added separately to make the mixing of the mixture more complete, thus improving the uniformity of the emulsified asphalt on the surface of different aggregates. In addition, the coating effect of aggregates and emulsified asphalt significantly improved. Therefore, the strength of laboratory-formed specimens of the mixture was relatively large. For the conclusion that the new mixing process can improve the compaction and splitting strength, we will use more RAPs from different projects to further verify this in the future.

CONCLUSION

The construction process of the cold recycled upper base included the normal-temperature compaction and secondary thermal compaction. The conclusions of this study on the influence of different laboratory molding methods, molding temperature, curing time, and molding process on the volume parameters and mechanical properties of emulsified asphalt cold recycled mixture were as follows:

(1) The paper puts forward that the compaction times of the laboratory large Marshall specimen was "150 + 75" and that of the gyratory compacted specimen was "30 + 15," which could accurately simulate the field compaction conditions of the cold recycled upper base pavement.
(2) The curing time and forming temperature of emulsified asphalt cold recycled mixture greatly influenced the compactness and strength of the mixture. The longer the curing time and the lower the compaction temperature, the more difficult the mixture was to be compacted and the lower the pavement strength.
(3) Compared with the traditional mixing process, the new mixing process exhibited higher strength. The splitting strength of the new mixing process increased by at least 13%.

DATA AVAILABILITY STATEMENT

The raw data supporting the conclusions of this article will be made available by the authors, without undue reservation, to any qualified researcher.

AUTHOR CONTRIBUTIONS

LL and LS: study conception and design. ZH, GZ, and PW: data collection. LL, LS, and ZH: analysis and interpretation of results. LL and ZH draft manuscript preparation. All authors reviewed the results and approved the final version of the manuscript.

FUNDING

This research was supported by the National Natural Science Foundation of China (No. 51978521).

ACKNOWLEDGMENTS

We gratefully acknowledge the financial support.

REFERENCES

Adikaram, K. K. L. B., Hussein, M. A., Effenberger, M., and Becker, T. (2015). Data transformation technique to improve the outlier detection power of grubbs' test for data expected to follow linear relation. *J. Appl. Math.* 2019, 1–9. doi: 10.1155/2015/708948

Asphalt Academy (2009). *Technical Guideline : Bitumen Stabilized Materials a Guideline*. Lexington, KY: Asphalt Academy.

Asphalt Recycling and Reclaiming Association [ARRA] (1996). *Mixture and Structural Design of Cold Recycled Pavements*. Annapolis, MD: Asphalt Recycling and Reclaiming Association.

Asphalt Recycling and Reclaiming Association [ARRA] (2001). *Basic Asphalt Recycling Manual*. Annapolis, MD: Asphalt Recycling and Reclaiming Association (ARRA).

Epps, J. A. (1995). *Cold-Recycled Bituminous Concrete Using Bituminous Materials*. Washington, DC: Transportation Research Board

Guo, C. (2013). *Mix Proportion Technology and Road Performance of Emulsified Asphalt Cold Recycled Mixture for Asphalt Pavement*. Tongji University, Shanghai. (In Chinese).

Jiang, T. (2012). *Research on some key Problems of cold Recycled Asphalt Mixture in Reconstruction of Heavy Pavement*. Shanghai: Tongji University. (In Chinese).

Jiang, T., Lijun, S., Liping, L., and Bin, S. (2008). Study on composition of cold recycled upper base materials based on structural performance. *J. Build. Mater.* 11, 666–672. (In Chinese)

Lee, K. W., Brayton, T. E., and Harrington, J. (2003). *New Mix-Design Procedure of ColdIn-Place Recycling for Pavement Rehabilitation*. Transportation Research Record 954, Washington, DC: National Research Council.

Li, Z., Peiwen, H., and Zhiwu, C. (2017). Forming method of foamed asphalt cold recycling mixture. *J. Compos. Mater.* 34, 2038–2046.

Lu, W. (2001). *) Design Principle and Method of Asphalt Mixture*. Shanghai: Tongji University Press.

Ministry of transport of the people's Republic of China (2011). *JTG f40-2011 asphalt and asphalt mixture test procedures*. Beijing: People's Communications Press. (In Chinese).

Moghadam, B. B., and Mollashahi, F. H. (2017). Suggesting a simple design method for cold recycled asphalt mixes with asphalt emulsion. *J. Civil Eng. Manag.* 23, 966–976. doi: 10.3846/13923730.2017.1343200

National Cooperative Highway Research Program (2007). *Superpave Mix Design: Verifying Gyration Levels in the N-design Table*. Washington, DC: National Cooperative Highway Research Program.

People's Communications Press (2019). *Technical Specifications for Highway Asphalt Pavement Recycling: JTG / 5521-2019*. Quitman, TX: People's Communications Press.

Sondag, M. S., Chadbourn, B. A., and Drescher, A. (2002). *Investigation of Recycled Asphalt Pavement (Rap) Mixtures*. Minnesota, MN: Department of Civil Engineering University of Minnesota.

Wei, H., Xianping, B., Feiyue, W., Wei, L., and Jiao, J. (2019). Mix design of emulsified asphalt cold recycled mixture based on gyratory compaction method. *J. Cent. South Univ.* 26, 759–767. doi: 10.1007/s11771-019-4045-3

Wirtgen (2010). *Wirtgen Cold Recycling Technology*, 3th Edn. Windhagen: Wirtgen GmbH, 2010.

Xiao, F., Yao, S., Jingang, W., Xinghai, L., and Amirkhanian, S. (2018). A literature review on cold recycling technology of asphalt pavement. *Constr. Build. Mater.* 180, 579–604.

Xu, Y., Lijun, S., and Liping, Y. (2013). Study on design method of emulsified asphalt cold recycled mixture considering hot compaction process. *Highway Eng.* 38, 72–76+89. (In Chinese)

Yang, J. (2010). *Study on Design method of Emulsified Asphalt cold Recycled Mixture*. Shanghai: Tongji University doctoral dissertation. (In Chinese).

Zheng, G., Liping, L., and Jian, W. (2016). Study on rolling technology of emulsified asphalt cold recycling upper base. *Traffic Sci. Eng.* 32, 39–44. (In Chinese)

Zhu, C., Zhang, H., Guo, H., Wu, C., and Wei, C. (2019). Effect of gradations on the final and long-term performance of asphalt emulsion cold recycled mixture. *J. Clean. Prod.* 217, 95–104.

Conflict of Interest: PW was employed by the company Inner Mongolia road and Bridge Group Co., Ltd.

The remaining authors declare that the research was conducted in the absence of any commercial or financial relationships that could be construed as a potential conflict of interest.

Advantages of publishing in Frontiers

OPEN ACCESS
Articles are free to read for greatest visibility and readership

FAST PUBLICATION
Around 90 days from submission to decision

HIGH QUALITY PEER-REVIEW
Rigorous, collaborative, and constructive peer-review

TRANSPARENT PEER-REVIEW
Editors and reviewers acknowledged by name on published articles

Frontiers
Avenue du Tribunal-Fédéral 34
1005 Lausanne | Switzerland

Visit us: www.frontiersin.org
Contact us: info@frontiersin.org | +41 21 510 17 00

REPRODUCIBILITY OF RESEARCH
Support open data and methods to enhance research reproducibility

DIGITAL PUBLISHING
Articles designed for optimal readership across devices

FOLLOW US
@frontiersin

IMPACT METRICS
Advanced article metrics track visibility across digital media

EXTENSIVE PROMOTION
Marketing and promotion of impactful research

LOOP RESEARCH NETWORK
Our network increases your article's readership